Single-cycle exhaust soot measurement from internal combustion engines

by

Pooyan Kheirkhah

B.Sc. Mechanical Engineering, University of Tehran, 2012

M.A.Sc. Mechanical Engineering, University of British Columbia, 2015

A THESIS SUBMITTED IN PARTIAL FULFILLMENT
OF THE REQUIREMENTS FOR THE DEGREE OF

Doctor of Philosophy

in

THE FACULTY OF GRADUATE AND POSTDOCTORAL STUDIES

(Mechanical Engineering)

The University of British Columbia

(Vancouver)

December 2020

The following individuals certify that they have read, and recommend to the Faculty of Graduate and Postdoctoral Studies for acceptance, the thesis entitled:

Single-cycle exhaust soot measurement from internal combustion engines

submitted by **Pooyan Kheirkhah** in partial fulfillment of the requirements for the degree of **Doctor of Philosophy** in **Mechanical Engineering**.

Examining Committee:

Steven Rogak, Mechanical Engineering
Supervisor

Patrick Kirchen, Mechanical Engineering
Co-supervisor

Rudolf Seethaler, Mechanical Engineering
Supervisory Committee Member

Mu Chiao, Mechanical Engineering
University Examiner

Milind Kandlikar, School of Public Policy and Global Affairs (SPPGA)
University Examiner

William Northrop, Mechanical Engineering, University of Minnesota
External Examiner

Additional Supervisory Committee Members:

Boris Stoeber, Mechanical Engineering
Supervisory Committee Member

Gary Schajer, Mechanical Engineering
Supervisory Committee Member

Abstract

The black carbon particulate matter (soot) emissions from internal combustion engines have negative health and climate impacts. PM emissions are typically characterized with modest temporal resolutions; however, in-cylinder investigations have demonstrated significant variability and the importance of individual cycles. Detecting such variations in the exhaust requires measurements close to the exhaust valve, which are not possible with the current sensors. Here, a methodology for characterizing the cycle-specific PM concentration at the exhaust-port of a single-cylinder research engine is developed using a light-scattering sensor, the Fast Exhaust Nephelometer (FEN).

The FEN light scattering is converted to soot mass concentration (C_m) and mass-mean mobility diameter ($d_{m,g}$) using an inversion algorithm based on the Rayleigh-Debye-Gans model for fractal aggregates (RDGFA). The model incorporates the external mixing hypothesis (EMH) to correlate the diameter of primary particles with the aggregates. The inversion parameters are obtained from Transmission Electron Microscopy (TEM) and literature, resulting in C_m and $d_{m,g}$ that are within $\pm 10\%$ of the reference methods. The results could vary by $\pm 40\%$ due to uncertainties in the RDGFA parameters; however, by incorporating the EMH morphology model, the variations are reduced to within $\sim \pm 25\%$ of the reference measurements.

The response time of the FEN, determined from a “skip-fired” scheme by disabling the fuel injection, is on average 55 ms. This is well below the engine cycle period ($\sim$100 ms) for the considered engine speeds. A cycle-specific PM mass averaging method was developed based on the characteristics of the exhaust-port signals. Using this cycle-resolved method, it is shown that the cycle-to-cycle coefficient of variation of C_m is 40%, while the in-cylinder gross indicated mean effective pressure (GIMEP) varies by 2%. Despite their different ranges of variation, the cycle-specific C_m and GIMEP are negatively correlated with $R^2 \sim 0.2$ - 0.7, where cycles with low GIMEP emit more soot. The physical causes of this association deserve further investigation, but are expected to be caused by local fuel-air mixing effects. The methods and findings of this work can further our understanding of the engine variability under transient conditions, and assist the interpretation of the in-cylinder variations observed in optical engine experiments.

Lay Summary

Direct-injection internal combustion engines are major sources of black-carbon particulate matter (soot) pollution. Complex engine calibrations, needed to meet the emissions regulations and fuel-efficiency targets, can benefit from high-speed sensors for time-varying emissions. Variations can even occur during a constant operating point, which is investigated here.

A method is developed to characterize single-cycle soot emissions at the exhaust port, using a high-speed light-scattering sensor, the Fast Exhaust Nephelometer (FEN). The soot concentrations can be quantified to ±25%, similar or better than available slow-response light-scattering sensors, and is achieved using a signal inversion algorithm based on the physics of soot.

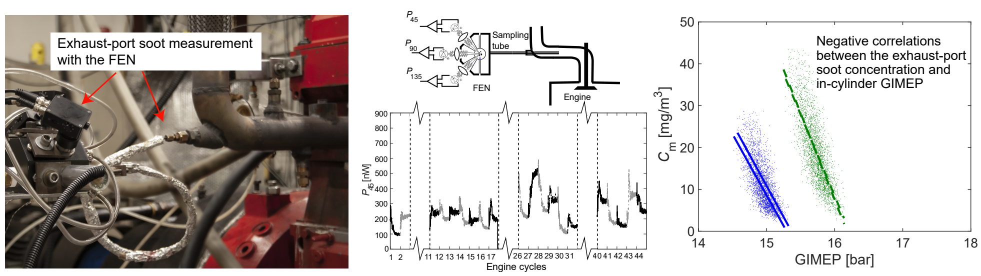

Using these methods, large variations in soot concentration are, for the first time, correlated to small variations in combustion energy. This demonstrates the impact of engine variability on soot emissions, which can enhance our understanding of the in-cylinder optical diagnostics results, and be utilized to reduce emissions during transient engine calibrations.

Preface

The work presented in this dissertation is the original work of the author, Pooyan Kheirkhah, with guidance and inputs from my supervisors Dr. Steven Rogak and Dr. Patrick Kirchen during the ideation and design of the experiments, analysis of results, and preparation of the ensuing scholarly publications.

The Fast Exhaust Nephelometer (FEN), described in Chapter 3 and used throughout this investigation, is designed by Dr. Steven Rogak and fabricated at the UBC Mechanical Engineering Machine Shop. Darren Sutton contributed to the initial design and testing of the FEN laser system, Jeff Yeo created a SolidWorks™ CAD computer model and fabricated the FEN in the UBC-MECH machine shop, and Jay Hope upgraded the laser circuitry and carried out preliminary particle measurements with the FEN. I further upgraded the FEN photodetection, temperature controls, and purge air systems, and incorporated the FEN with a research engine instrumentation for crank-angle-resolved signal acquisition. A summer intern student, Jeff Farnese helped me upgrading the FEN for engine exhaust-port measurements. I carried out the engine measurements, developed signal inversion toolkits, and performed all of the data analysis.

This thesis is an integration of conference proceedings and presentations, and published or accepted articles in scholarly journals. The results and discussions in Chapter 4 is published in Aerosol Science and Technology, and the material in Chapters 5 and 6 is accepted for publication in the International Journal of Engine Research. The introduction in Chapter 1 and the description of the experimental systems in Chapter 3 are based on the corresponding material in the two manuscripts, and a technical paper for the Society of Automotive Engineers (SAE). Below is a list of published or accepted work in the scholarly journals:

- Kheirkhah P., Kirchen P., and Rogak S. 2016. Fast Exhaust Nephelometer (FEN): A new instrument for measuring cycle-resolved engine particulate emissions. SAE Technical Paper. 2016-01-2329.

- Kheirkhah P., Baldelli A., Kirchen P., and Rogak S. 2020. Development and validation of a multi-angle light scattering method for fast engine soot mass and size measurements. *Aerosol Science and Technology.* 54(9): 1083-1101.

- Kheirkhah, P., Kirchen P., and Rogak S. Measurement of cycle-resolved engine-out soot concentration from a diesel-pilot assisted natural gas direct-injection compression-ignition engine. Accepted for publication in the International Journal of Engine Research on November 24, 2020.

The experiments, including designing the test matrices, operating the engine and the PM instrumentation, developing the light scattering inversion model, and processing the collected data is carried out by myself. Dr. Alberto Baldelli collected samples for Transmission Electron Microscopy (TEM) and processed the TEM images discussed in Chapter 4. Una Trivanovich helped with the TEM imaging of the engine soot samples in Chapter 6, and I carried out all the image-processing work. Complementary image analysis is done by a co-op student, Lawrence Zhou, supervised by Dr. Timothy Sipkens to compare the automatic pair-correlation (PCM) results with the manual image processing method.

I was the lead author and wrote the three manuscripts. Dr. A. Baldelli provided the information and the data related to the TEM analysis for the second paper. Dr. S. Rogak and Dr. P. Kirchen were involved during the design of the experiments, provided insight for developing the data inversion methodology, and critically reviewed the papers.

Chapter 5 consists of the experimental measurements and analyses conducted in 2019 by the author. The experimental measurements are compared to an earlier experimental and modeling work published as a Master's thesis by Patrick Steiche during the spring of 2017. In the 2017 campaign, Patrick Steiche carried out the GT-Power™ modeling work and conducted the experimental data processing related to the pressure and flow modeling of the engine exhaust system, while I ran the experiments and analyzed the FEN light scattering data.

Table of Contents

List of Tables

List of Figures

List of Symbols

Latin symbols

A	Surface area [m^2] or [nm^2]
a	Radius [m] or [nm]
C_m	Mass concentration [mg/m^3]
C_c	Cunningham slip correction factor
CH_4	Methane
CO	Carbon monoxide
CO_2	Carbon dioxide
d	Diameter of an object (frequently referring to particles) [m] or [nm]
D	Correlation exponent
e	Elementary charge (1.602×10^{-19} C), Euler's number: 2.718
$\mathbf{E}$	Electric component of an electromagnetic field
E	Rayleigh absorption function
f	Friction coefficient
F	Rayleigh scattering function [-], Force [N]
g	Density auto-correlation function
G	Gain of an amplifier [dB]
h	Density auto-correlation cut-off function
$\mathbf{g}$	Observed or measured values in an inverse problem
I	Intensity of electromagnetic radiation [W/m^2]
k	Wave number (nm^{-1}), Pre-factor of a correlation
$\mathbf{k}$	Wave vector
k_{ext}	Extinction coefficient [m^{-1}]
$\mathbf{K}$	Kernel matrix of an inverse problem
K	Longitudinal (Taylor) diffusivity [m^2/s]
KL	Optical thickness of in-cylinder soot cloud
Kn	Knudsen number
L	Length of an object, Geometric length scale [m] or [nm]
$\mathbf{m}$	Complex refractive index
$\dot{m}$	Mass flow rate [kg/s]
m or M	Mass of a particle
n	Real part of the complex refractive index
N	Number
NaCl	Sodium chloride
NO	Nitric oxide

NO_2	Nitrogen dioxide
O_2	Oxygen
OH	Hydroxyl radical
P	Bayesian probability, Pressure [kPa], Optical power [nW]
q	Magnitude of scattering wave vector [nm^{-1}]
R	Gas constant [$\frac{J}{kgK}$], Radius [nm], Light-scattering ratio
R_λ	Responsivity of a photodiode at wavelength λ
Re	Reynolds number
r	Distance from a reference point or a particle
S	RDGFA structure factor
$\mathbf{S}$	Light scattering matrix
St	Stokes number
t	Time [s] or [ms]
T	Temperature [°C] or [K]
u or U	Flow velocity [m/s]
V	SCRE cylinder volume, FEN measurement chamber volume
$\mathbf{x}$	Matrix of unknowns in an inverse problem
x	Normalized diameter
Z	Electrical mobility

Greek symbols

α_{pol}	Polarization angle of electromagnetic radiation
γ	Specific heat ratio
δ	Time constant [CAD]
Δ	Perturbation of a parameter in sensitivity analysis
ε	Inversion error function
ζ	Characteristic length in density auto-correlation function
η	PM sampling efficiency
θ	Light scattering angle, Engine crank-shaft angular position
θ_{50}	Crank angle for mid combustion phasing [CAD]
κ	Imaginary part of refractive index
λ	Wavelength of light [nm]
λ_{air}	Mean free path of air molecules [m or nm]
Λ_{FEN}	Optical coefficient of FEN [Wm]
μ	Dynamic viscosity [N/m^2s]
ρ	Particle density [kg/m^3]

ρ'	RDGFA optical phase-shift parameter
σ	Optical cross section [nm^2], Standard deviation of a distribution
τ	Time constant [ms]
ϕ	Combustion equivalence ratio
Ω	Solid angle [sr]

Subscripts

0	Related to FEN laser beam, sampling delay, or ambient condition
1	Conditions at the inlet of sampling tube
135	Related to light-scattering in 135° direction
2	Conditions at the outlet of sampling tube
45	Related to light-scattering in 45° direction
90	Related to light-scattering in 90° direction
a	Property of an aggregate, Projected-area properties
ad	Aerodynamic
asp	Related to aspiration sampling losses
b	Related to bends in sampling tube
$inert$	Related to inertial sampling losses
cyl	Related to or measured inside the engine cylinder
d	Related to aerodynamic drag
eff	Effective value of a quantity
exh	Related to or measured at the exhaust
ext	Light-extinction parameter
f	Fractal properties
g	Gyration properties
GT	Based on GT-power model
int	Related to or measured at the intake
IT	Based on an iso-thermal model
m	Related to mobility diameter or mass-mobility relations
m,g	Geometric mass-mean value
p	Property of a primary particle
$p,100$	Referring to primary particles in a 100-nm aggregate
$peak$	Light scattering signal peak
$poly$	Property of polydisperse samples
$resp$	Exhaust-port measurement response
sc	A single-cylinder parameter
SF	Based on skip-firing measurements

tail	Light-scattering signal tail
TEM	Properties derived from TEM images
α	Related to a 2D aggregate projection image
θ	Related to light scattering measurement at angle θ
λ	Related to or measured at wavelength λ

List of Abbreviations

aEVO	after exhaust valve opening
AFR	Air fuel ratio
BC-PM	Black carbon particulate matter
BDC	Bottom dead center
CAD	Crank-angle degrees
CCV	Cycle-cycle combustion variation
CERC	Clean energy research center
CEV	Cycle-cycle emissions variation
CFD	Computational fluid dynamics
COV	Coefficient of variation
CPC	Condensation particle counter
D/G	Ratio of disordered to graphitic carbon Raman spectra
DAQ	Data acquisition
DDA	Discrete dipole approximation
DI	Direct injection
DLCA	Diffusion-limited cluster aggregation
DM	Dobbins and Megaridis (RDGFA structure factor)
DMA	Differential mobility analyzer
DMM	Dekati mass monitor
DMS	Differential mobility sizer (spectrometer)
DOC	Diesel oxidation catalyst
DPF	Diesel particulate filter
DR	Dilution ratio
EC	Elemental carbon
EDM	Euclidian distance mapping
EEPS	Engine exhaust particle sizer
EGR	Exhaust gas recirculation
ELPI	Electrical low-pressure impactor
ELS	Elastic light scattering
EM	Electromagnetic
EMH	External mixing hypothesis
EVO	Exhaust valve opening
EXP	Exhaust-port (referring to sampling location)
FEN	Fast exhaust nephelometer
FFID	Fast flame ionization detector
FID	Flame ionization detector
GDI	Gasoline direct-injection

GHG	Green-house gas
GIMEP	Gross indicated mean effective pressure
GMM	Generalized multi-sphere Mie
GPF	Gasoline particulate filter
H:C	Hydrogen to carbon ratio
HACA	Hydrogen abstraction - C_2H_2 addition
HD	Heavy-duty
HEPA	High-efficiency particulate absorption
HPDI	High-pressure direct injection
HR-TEM	High-resolution transmission electron microscopy
HRR	Heat release rate
ICE	Internal combustion engine
IHR	Integrated heat release
IVC	Intake valve closing
LII	Laser-induced incandescence
LSE	Least-square estimation (estimator)
LTC	Low-temperature combustion
MAC	Mass-absorption cross-section
MAP	Maximum a posteriori probability
MSC	Mass scattering cross-section
MSS	Micro soot sensor
MSTM	Multi-sphere T-matrix
NO_x	Oxides of nitrogen, collective NO and NO_2 vehicular emissions
NTE	Not-to-exceed
OPC	Optical particle counter
PAH	Poly-cyclic aromatic hydrocarbons
PASS	Photo-acoustic soot sensor
PCM	Pair-correlation method
PEMS	Portable emissions measurement system
PFI	Port fuel injection
PIDING	Pilot-ignited direct-injection natural gas
PM	Particulate matter
PPCI	Partially-premixed compression ignition
PSS	Pegassor soot sensor
PST	Post surge-tank (referring to sampling location)
QCM	Quartz crystal microbalance
RDE	Real-drive emissions
RDGFA	Rayleigh-Debye-Gans fractal aggregates
RI	Refractive index
RPM	Rotations per minute

SCRE	Single-cylinder research engine
SMPS	Scanning mobility particle sizer (spectrometer)
SPN	Solid particle number
SVOC	Semi-volatile organic compounds
TEM	Transmission electron microscopy
TEOM	Tapered element oscillating microbalance
TPS	Thermophoretic sampler
uHC	Unburned hydrocarbons
VOC	Volatile organic compounds
VPR	Volatile particle remover
WALS	Wide-angle light scattering
WHO	World Health Organization

Acknowledgments

This work would not be possible without the guidance and mentorship of my supervisors Dr. Steven Rogak and Dr. Patrick Kirchen at the University of British Columbia. I have greatly benefited from their critical evaluation of my work and many in-depth discussions of, at times, perplexing experiments. I would also like to thank Dr. Sandeep Munshi, Dr. Gordon McTaggart-Cowan, and Dr. Jim Huang at Westport Fuel Systems Inc. for financially and technically supporting this project, and regularly providing their feedback on my work.

During my time at UBC, I have had the chance of getting to know many amazing people. The fellow graduate students at the Clean Energy Research Center (CERC), Jeremy Rochusen, Jeff Yeo, Michael Karpinski-Leydier, Mahdiar Khosravi, Rene Zepeda, Aditya Prakash Singh, and Jeff Meiklejohn thank you all for being there to help. I also would like to thank Dr. Alberto Baldelli, Una Trivanovic, and Dr. Timothy Sipkens for their help with operating the TEM facility and image-processing.

Over these years, I have come to know people whose company has always been a pleasure. My dear friends, Arman Abtahi, Yasaman Foolad, Sima Motiee, Pouyan Jahangiri, Amin Engarnevis, Hoda Talebiyan, Sarah Crosby, and Keyhan Babaee, thanks for your company. I owe a great debt of thanks to Mahnaz Khanavi, Syamak Shahsavari, and Kasra Shahsavari, who were like family for me during my early years at UBC. I miss you dearly!

This journey had a great many ups and downs, and it was the unconditional support and love from my family, my mother, Maryam, and my brother, Peyman, who were always there for me and gave me the strength

to carry on. Thank you!

Chapter 1

Introduction

Black carbon particulate matter (BC-PM) is a byproduct of the combustion of hydrocarbons. The pyrolysis of hydrocarbon fuels generates, among other chemical species, solid carbonaceous particulate matter (PM), called soot, ranging from less than 10 nm to larger than 1 μm. Internal combustion engines (ICE) are major sources of anthropogenic soot due to incomplete combustion in the locally fuel-rich regions inside their combustion chamber. The engine-emitted soot particles can penetrate deep into the respiratory tract and even enter the bloodstream due to their small size. Chronic exposure to soot is linked to asthma, heart attack, and respiratory infections [23, 189]. Diesel soot is also categorized as a group 1 carcinogen by the World Health Organization (WHO) [16]. Moreover, soot particles warm the climate by directly absorbing the solar radiation, and by reducing the reflectivity of the ice and cloud nuclei (surface albedo effect) [21]. Therefore, the ICE soot emission, and its measurement and mitigation warrant further research.

1.1 Soot emissions from internal combustion engines

Direct injection (DI) engines of diesel, gasoline, or alternative fuels power more than 75% of the on-road commercial vehicles [2, 41]. The spark ignition (SI) gasoline direct-injection (GDI) engines can be operated under a wider range of air-fuel ratios, and have lower unburned hydrocarbon (uHC) emissions compared to port fuel injection (PFI) SI engines, especially during the low- and part-load operation [208]. Compression ignition (CI) engines, predominantly powered by diesel fuel, are operated with higher compression ratios and have near-zero throttling losses, making them more fuel-efficient than SI engines. The benefits in fuel economy and reduced green-house gas (GHG) emissions generated a shift towards the light-duty diesel passenger cars in Europe [74], and rapid market adoption of the GDI technology worldwide [84]. Diesel and GDI engines are the largest mobility and transportation-related sources of BC-PM emission [21]. The DI engines running on diesel or alternative fuels are especially widespread in heavy duty transportation, and off-road applications such as in mining, construction, marine applications, and power generation [119]. Therefore, their emissions are under further scrutiny, as they can put the public at greater PM exposure and bear higher costs on the health care system.

The graphitic carbon is a strong absorber of the solar radiation; therefore, soot particles heat up the atmosphere and affect the properties of clouds [138]. The reduction of engine-emitted soot offers co-benefits in public health and climate change. Especially, it might be that the reduction of BC-PM produces fast climate-cooling effects due to its short atmospheric lifetime, and thus is of much interest [66]. The complex properties of soot and the challenges in the source-appointment of emissions, nonetheless, generate a large uncertainty in the assessment of its role in epidemiological and climate studies [21].

1.1.1 Engine PM Regulations

Regulations are put in place to curb the "tail-pipe" emissions of fine and ultrafine PM from vehicles or engines, which are measured during controlled steady and transient test cycles [43]. The most recent European standards require heavy-duty diesel engines to meet the 0.01 g/kWh limit for PM mass in addition to the recently introduced $8{\times}10^{11}$ #/kWh for the solid particle number (SPN) [42, 61]. The emissions are measured by testing the engines (heavy-duty) or vehicles (light-duty) on a dynamometer which controls the load, speed, or both.

Certification test cycles are transient and include idling, stop-starts, and frequent engine speed-load variations. The exhaust is sampled for the entire duration of the transient cycle, diluted with clean air, and measured for the number and mass of particles [61]. Engines generate more pollution during real-world driving compared to stationary tests [159]. Hence, measuring the real-drive emissions (RDE) using portable emissions measurement systems (PEMS) is added in the European type-approval tests since 2017 [127].

1.1.2 PM mitigation and control

To meet the challenging PM standards, DI engines are equipped with particulate filters (DPF's and GPF's) that remove more than 90% of the particles [68]. The filters are regenerated by increasing the exhaust temperature to oxidize the accumulated soot that builds up over time on the particle traps [95]. This is an energy-intensive process. In order to alleviate the fuel consumption penalties associated with the DPF regeneration, the "engine-out" soot must be minimized. Reducing the engine-out soot is even more crucial in applications where DPF is uncommon or impractical, and the emitted PM is directly released into the surrounding environment, such as in rail or marine applications.

Engines are calibrated over steady and transient test cycles, where the control parameters are tuned for optimized in-cylinder combustion to reduce harmful emissions with minimum fuel efficiency penalty. Off-cycle emissions tend to be more significant, as such, even transient test cycles do not accurately represent real-world driving [127]. A simplified demonstration of a transient engine load-speed trajectory on a steady-state emission map is shown in Figure 1.1. During the transition between the steady-state points A and B, the combustion conditions (air-fuel ratio, combustion timing, etc.) are nonoptimal, resulting in soot concentration spikes [63, 70].

It is known that the soot emission from diesel combustion is a delicate

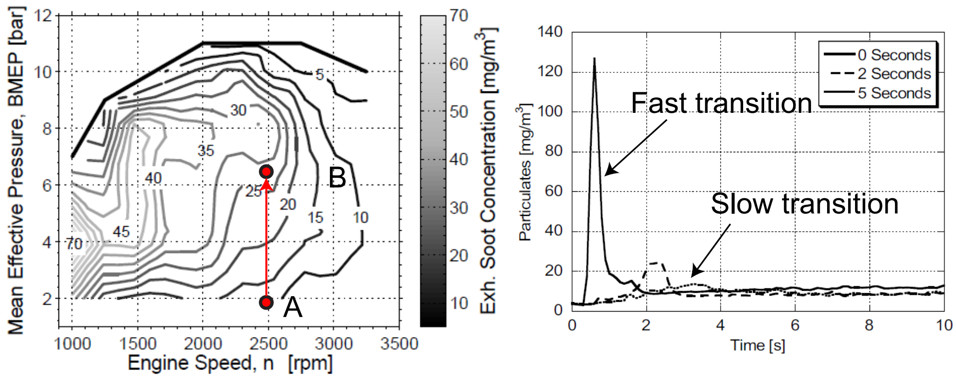

Figure 1.1: An illustration of engine exhaust soot concentration time series (right, adapted from [70], permission obtained from SAE) when transitioning between two steady-state operation points on the load-speed map (left, adapted from [102], by permission of author). The peak of the soot concentration in a fast-transition trajectory exceeds the steady-state concentrations by a factor of 10.

balance between the formation and oxidation reactions [191], which are very sensitive to the injector, fuel-oxidizer mixture, and the combustion conditions. Cycle-resolved measurements of in-cylinder air-fuel ratios suggest that soot emissions can be substantially reduced if the high-emitting cycles are detected and mitigated [69]. This requires optimizing the in-cylinder combustion using fast engine controls based on cycle-resolved inputs.

The combustion cyclic variability (CCV) may be characterized based on in-cylinder pressure measurements or from optical diagnostics. Over the last two decades, fast instruments for cycle-resolved exhaust measurement of gaseous pollutants have been used to study the cyclic emissions variability (CEV). The study of CCV-CEV correlations reveals patterns in engine emissions the are obscure to lower-speed instruments [10, 37, 110]. In-cylinder natural luminosity measurements have also indicated that soot formation and oxidation are highly sensitive to the combustion properties [87]. Despite the advances in the in-cylinder techniques, cycle-resolved soot emissions have not been characterized in the exhaust; hence, the correlations between the cycle-resolved combustion and the exhaust soot variations are not fully understood. This information is highly useful and a critical gap in the engine soot literature, which is tried to be addressed in this work.

1.2 ICE PM measurement

To determine whether engines meet the regulatory limits on PM pollution, their diluted exhaust is measured during a transient test cycle. The regulatory procedures require that particles smaller than 2.5 μm ($PM_{2.5}$) be collected on filters and gravimetrically weighed for PM mass, and the number of solid particles (SPN) larger than 23 nm measured after removing the volatile and semi-volatile contents [61]. To determine the effect of rapid changes to the engine operation throughout a transient test, faster measurement methods are desirable for research and development. Respectively, indirect particle mass and size measurement techniques are developed to address such need for transient time-resolved data.

1.2.1 Exhaust measurements

Time-resolved quantitative soot volume or mass concentrations may be measured indirectly using optical techniques, or by measuring particle electrical charge. Photo-acoustic soot sensors (PASS) [160], or laser induced incandescence (LII) sensors [169] measure the acoustic and thermal radiation from soot particles by laser heating. Opacimeters and aethalometers [88] measure light attenuation of soot or other light-absorbing particles suspended in air or loaded on filters. These instruments, however, have limited time resolution because of pressure, temperature, or flow rate restrictions inside their optical cavity, or due to the time needed for filter loading [14, 171]. Non-optical methods, such as Electrical Low-Pressure Impactor (ELPI) [125], Engine Exhaust Particle Sizer (EEPS) [89], or Differential Mobility Sizer (DMS) [163] rely on generating unipolar charge distribution on particles, classifying them based on their aerodynamic or electrical mobility diameter, and subsequently measuring the size-classified particles with electrometers.

The measurement response time with such instruments is practically limited by the flow transport and mixing in the exhaust pipe and sampling lines; faster response times require carrying out measurements upstream in the exhaust system, with short sampling tubes. The techniques discussed here, however, strongly depend on the pressure and flow of the sample into the instrument [144]. As a result, measurements close to the exhaust valve would be affected by the rapid variations in exhaust pressure and flow rate close to the manifold or at the exhaust port [173, 207].

For these instruments, samples are collected downstream in the exhaust system, such as after the turbocharger or at the tail-pipe, and might require dilution with clean dry air prior to measurement. Considering the mixing time in the exhaust train and dilution tunnel, or residence time in the sampling lines and pressure damping chambers, the time resolution of the mentioned instruments is at best 0.5 s [196], not sufficient for cycle-resolved measurements.

1.2.2 In-cylinder measurements

The cycle-specific soot emissions may be estimated from the in-cylinder pressure and natural flame luminosity traces. Semi-empirical models, such as the well-known two-step soot model of Nishida and Hiroyasu, can be made to estimate the soot mass concentration from the in-cylinder pressure trace [141]. Optical measurements of natural or stimulated light emissions are also used to obtain measurements of in-cylinder soot. Two-colour-ratio pyrometry is commonly used to study the in-cylinder soot formation and oxidation from the crank-angle-resolved optical thickness of the soot cloud (KL) [11, 102, 104, 197]. The pyrometry KL is determined from the thermal light emission from soot, which diminishes long before the opening of the exhaust valve and is prone to noise due to weak signal late in the cycle [81].

It is not clear, to what extent the low-temperature late-cycle oxidation contributes to the variation of KL for cycles with seemingly similar pressure and heat-release traces [87, 102, 197]. Given such cycle-to-cycle variability, estimating the quantitative rates of in-cylinder soot formation and oxidation requires an exhaust-value datum, which requires measuring engine-out soot at the exhaust port.

1.2.3 Exhaust-port measurements

Optical techniques are fast and can be adapted for undiluted measurements upstream of the exhaust system. An application of the LII method introduced in Section 1.2.1 is demonstrated for raw exhaust measurement upstream of turbocharger for a light-duty diesel engine. Despite sampling upstream of the turbocharger, the transient response times reported for this LII system are limited to ~ 0.5 s, due to its distance from the exhaust valve [196]. Application of elastic light scattering (ELS) for in- and ex-situ exhaust-port soot measurements for light- and heavy-duty DI engines is shown in the literature [99, 154], demonstrating the possibility of single-cycle measurements. Nonetheless, such studies are limited to qualitative demonstrations rather than quantitative measurements. ELS is a promising method for fast, possibly cycle-resolved exhaust-port soot measurement, but requires proper data inversion for the accuracy needed to characterize the cycle-to-cycle variations.

Light scattering is implemented in commercial instruments such as the Dusttrak by TSI Inc. [29] or research instruments such as the SootTrack demonstrated in [77]. As it is sensitive to the morphological and optical properties of particles, factory calibrations based on standard dust may not be suitable for measuring soot. PM mass measurement with different instruments, including the TSI-Dusttrack, demonstrated discrepancies in the range of 30% due to dissimilar measurement principles and the complex physicochemical properties of ICE-generated PM [123, 143].

Much of soot light scattering research in the literature is limited to stationary flames and not transient engines [6, 38]. Furthermore, converting the measured light-scattering signals into soot mass and size, also called "inversion", is not trivial as it requires complex models for solving inverse problems containing ill-posed system of non-linear equations [24]. The Rayleigh-Debye-Gans model for fractal aggregates (RDGFA) is commonly used to model the light scattering from combustion soot [182]. Holve used a two-angle light scattering RDGFA model to measure the exhaust soot from a diesel engine and a gas-turbine [78]. Their results suggest that using the literature-based soot properties creates large uncertainties in the concentration and particle sizes obtained from the measured light intensities. Furthermore, the RDGFA models in the literature assume that the primary particles are mono-disperse [6]. Even when the primary particle polydispersity is considered, its distribution parameters are assumed independent of the aggregate size distribution [148]. These assumptions should be reconsidered given the observations that the soot primary particle size is correlated to the aggregate size [33], recently explained by external mixing hypothesis (EMH) [146].

The Fast Exhaust Nephelometer (FEN) is a multi-angle light scattering instrument, developed for sampling near the exhaust valve and measuring raw exhaust [99]. Quantitative soot measurement with the FEN requires a methodology that considers the soot morphology and optical properties, as well as the FEN optical and geometrical characteristics. Furthermore, light scattering signals generated during exhaust-port sampling contain complex features due to the exhaust transient flow and pressure waves that must be analyzed for single-cycle soot concentrations. Similar approaches were demonstrated in the past, for example, for a fast flame ionization detector (FFID) used to measure single-cycle unburned hydrocarbon emissions [31]. No work, however, has been reported for quantitative, single-cycle, engine-out soot measurement near the exhaust valve.

It is desired to characterize the FEN, such that it can be used to measure the engine-out soot concentration in order to explore the variation of cycle-resolved soot emission and its correlation with the in-cylinder processes.

1.3 Research objectives

Quantitative measurement of cycle-resolved exhaust-stream soot concentration has not been reported in the literature, yet it is highly useful for understanding the effects of cycle-to-cycle combustion variability on the emissions. Obtaining such measurements is impeded partly by the lack of instruments that can sample and measure the exhaust-port soot, but is also affected by a lack of methodology to interpret the light-scattering signals acquired during the process of exhaust-port measurement. Light-scattering inversion models that consider the effects of exhaust-port pressure and flow variations on the measurements are needed to determine the cycle-specific PM concentration from light-scattering traces.

Motivated by the lack of means and methods for characterizing the single-cycle exhaust-stream soot, FEN is used to carry out such measurement on a pilot-ignited direct-injection natural gas (PIDING) single-cylinder research engine (SCRE). To achieve this, the measured light-scattering signals must be processed to determine the single-cycle soot concentration and its cycle-to-cycle variations, and to examine its correlations with the in-cylinder combustion parameters. The inversion of light-scattering into soot concentration and size is inherently ill-posed [24]; thus, measurement noise and errors embedded in light-scattering models used for signal-processing are amplified in the inversion process [80]. To alleviate such uncertainties, a morphology model that considers the wide range of soot sizes present in the engine exhaust must be incorporated in the inversion process.

Correspondingly, the objectives of this research are to:

- develop and characterize a method for measuring the concentration and size of soot from its light scattering (inversion).
- develop a single-cycle soot measurement methodology based on the FEN exhaust-port light-scattering measurements.
- demonstrate the utility of the new method for characterizing the cycle-resolved variation of engine-out soot and its correlations with in-cylinder combustion processes.

The first objective is tackled by developing a three-angle light-scattering inversion algorithm that takes the measured FEN signals and produces the soot concentration and mean diameter as outputs. The inversion scheme is based on the RDGFA light scattering model, modified to include the variation of soot primary particle sizes based on the EMH model. The inverted light scattering soot measurements are validated against the reference gravimetric mass and mobility diameter measurements and its sensitivity to the light-scattering model and the inversion process is characterized.

Furthermore, a methodology is developed to determine the cycle-specific soot concentration and size based on the measured PM light scattering at the exhaust port. Features in the crank-angle-resolved FEN signals are studied in relation to the exhaust pressure and flow variations. A crank-angle signal averaging procedure is developed based on the response time of the FEN to represent the cycle-specific soot concentration. To determine the response time of the exhaust-port measurement system, engine combustion is disrupted with the intention of generating rapid changes in exhaust soot concentration. The FEN light-scattering traces during this "skip-firing" operation is analyzed to determine the sample transfer delay in the exhaust pipe and the FEN sampling tube.

Hence, the key objectives of this work are to develop a method for exhaust-port light-scattering soot measurement, quantitatively validate it against reference standard methods, and utilize it to characterize the cycle-to-cycle variation of soot emissions. The utility of this method is demon-

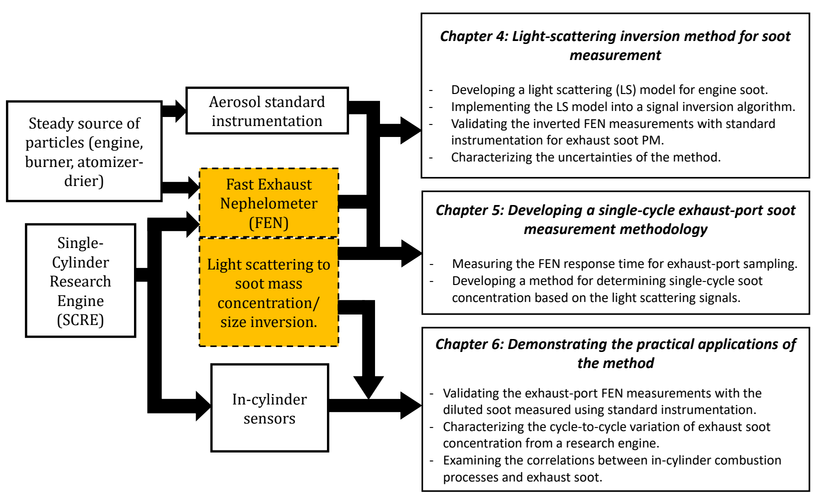

Figure 1.2: The research objectives and thesis organization.

strated by exploring the correlations between the engine-out soot concentration and the in-cylinder combustion parameters, assess the statistical significance and repeatability of these correlations, and their differences for different operating points.

The thesis is structured so that these objectives are addressed in chapters, as shown in Figure 1.2 and explained below.

1.4 Thesis layout

This thesis is divided into 7 chapters, including this introductory chapter, and finishes with the conclusions of this study and provides recommendations for future research. A chapter-by-chapter description is provided here.

In Chapter 2, the literature vis-á-vis the ICE PM emission measurement, particularly, the time-resolved methods for exhaust soot are reviewed. A discussion on the physics of in-cylinder soot formation, and the resulting soot properties, pertinent to light-scattering measurements, is provided. The chapter is concluded by a discussion on the gaps in the literature and the ways they are addressed in this work. The experimental facility is introduced in Chapter 3. A detailed description of the FEN is provided and its optical properties are examined. The SCRE, the PM sampling and measurement instrumentation, and the methods of soot mass, size, and morphology characterization are elaborated.

Chapters 4, 5, and 6 discuss the results and findings of this work. In chapter 4, the RDGFA+EMH model employed in the light-scattering inversion software is introduced. Diluted FEN exhaust soot measurement is validated with gravimetric PM mass and mobility instruments, and its variations due to uncertainties in the inversion model are discussed. In chapter 5, a method for determining the single-cycle soot concentration from exhaust-port measurements is explained. Particularly, the crank-angle-resolved FEN light-scattering traces are characterized, and the response time of the measurement system is experimentally determined. In chapter 6, the applications of the single-cycle exhaust soot measurement method vis-á-vis cycle-to-cycle soot concentration variability and its correlations with the in-cylinder combustion processes are explored.

In chapter 7, the main results and findings from the previous chapters are reviewed and their implications for engine soot measurement are highlighted. Recommendations for future research are provided, and design modifications meant to enhance the capabilities of the FEN or other similar light scattering instruments are presented.

Chapter 2

Review of engine PM emission and measurement methods

Techniques and procedures have been developed over the years to characterize different aspects of PM emissions from internal combustion engines (ICE), and are continuously evolving to meet the needs of the industry, and guide the environmental policy and regulations. Most regulations require a cumulative PM measurement for the entire duration of tests; while, high-speed techniques are more common in research and development to resolve transient emissions. There are, however, fewer cases of cycle-resolved soot measurement in literature, which are almost exclusively limited to in-cylinder optical diagnostics, and not carried out in the exhaust of metal engines. The in-cylinder studies have shown that single-cycle soot emissions are important, especially during transient engine operations which is prevalent in real-world applications.

This chapter starts with a brief review of the in-cylinder soot formation processes and pathways, and the resulting physical properties of soot formed inside DI engines. Different techniques and the corresponding instrumentation for PM measurement are described, and some strategies developed to mitigate the in-cylinder or exhaust PM emissions are reviewed. A considerable portion of this chapter is dedicated to models for PM light scattering and their applications and limitations. Particularly, the Rayleigh-Debye-Gans model for fractal aggregates (RDGFA) is explained in more detail, as it is reasonably simple and widely used and characterized in the literature, and can be implemented with modest computational costs. Following this, the inversion of light scattering measurements into soot concentration and size are briefly discussed, and its implications for soot measurements with the FEN are highlighted. The chapter ends with a summary of the reviewed literature and the critical gaps therein, that are addressed in upcoming chapters.

2.1 Formation and properties of particulate matter from engines

Properties of soot strongly depend on its formation processes inside the engine, which, in turn, depend on the combustion conditions. A detailed description of the formation and transport of in-cylinder soot is still elusive due to the complex chemical kinetics of soot precursors and the nucleation processes, and the intricacies of particle-flow interactions in the highly turbulent reacting fuel jets. Hence, experimental measurements play a major role in the soot emission research. Here, the in-cylinder processes relevant to soot formation and oxidation are reviewed, and the resulting properties of the ICE-generated soot are discussed.

2.1.1 Chemical mechanisms and phenomenology in engines

Soot is formed in hot, locally fuel-rich regions, inside the combustion chamber, and is mostly oxidized when passing the stoichiometric flame front. Poly-cyclic aromatic hydrocarbon (PAH) species, formed during the fuel pyrolysis, are considered the gaseous precursors to soot. Based on the current models, these precursor molecules grow by absorbing more carbon atoms through the hydrogen-abstraction-C_2H_2-addition (HACA) mechanism until they form a distinct condensed phase, the nascent soot primary particles [56]. These primary spherules agglomerate to form chain-like aggregates which

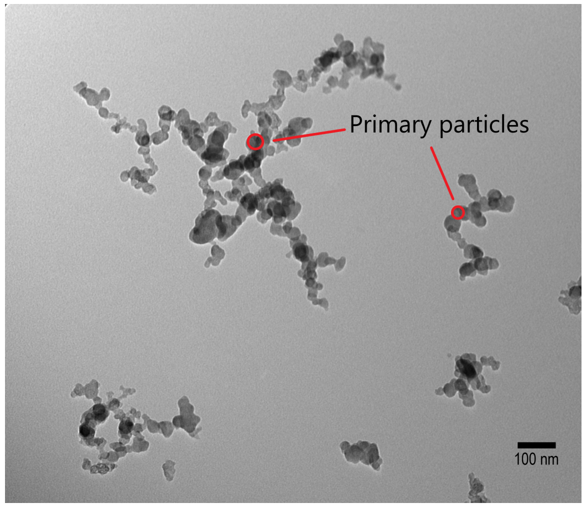

Figure 2.1: Transmission electron microscopy (TEM) image of soot from the pilot-ignited direct-injection natural gas (PIDING) engine used in this work. Primary particles are marked with red circles

contain between a few to several hundred or thousands of primary particles. Soot particles sampled from the exhaust of the pilot-ignited direct-injection natural gas (PIDING) research engine used in this work are shown in Figure 2.1, demonstrating the structure of aggregates and their primary particles.

Much of the freshly formed soot undergoes simultaneous oxidation reactions by O_2 and OH radicals [191], resulting in a significantly lower net concentration than initially formed inside the flame. A complete modeling of soot evolution inside an engine demands using computational fluid dynamics (CFD), including the PAH chemistry, and modeling the transport and population balance of the particles [150]. Such an implementation is demonstrated by Mosbach et al.. This is a computationally expensive process and requires complex validation, such as with the in-cylinder rapid sampling mechanism implemented in [135], which provided a qualitative baseline for validation of the model, but was insufficient for a quantitative validation. Thus, simpler models, such as the empirically-based two-step soot formation-oxidation mechanism of Nishida and Hiroyasu are still pop-

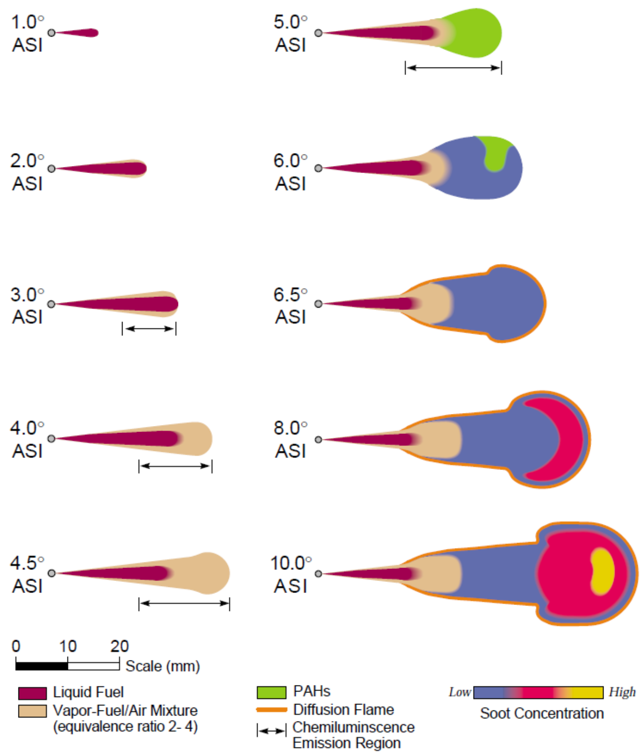

Figure 2.2: A conceptual model for the progression of soot formation reactions including the precursor PAH species in DI diesel combustion based on in-cylinder laser-sheet imaging, adapted from [40] with permission from SAE.

ular for engine soot modeling [11, 12, 97, 103].

Breakthrough progress was made by using in-cylinder laser diagnostics to develop a conceptual understanding of the DI diesel soot formation [40]. This study demonstrated that soot formation starts shortly downstream of the fuel spray in the hot carbon-rich zones, shown in Figure 2.2, and is mostly oxidized near the stoichiometric flame front. Similar techniques are used to study the formation of soot in other combustion regimes ever since, such as in the low-temperature combustion (LTC) of diesel [137], or in the dual-fuel natural gas diesel combustion [101, 164].

The properties of soot depend on the underlying formation-oxidation processes inside the combustion chamber. Therefore, particles emitted during different combustion conditions can differ substantially, as discussed below.

2.1.2 Structure of soot including results from TEM

PM from DI engines consists of small (10 - 60 nm) primary particles, made of elemental carbon (EC), forming a fractal-shaped aggregate, shown in Figure 2.1. This solid core may be coated with condensed volatile and semi-volatile organic compounds (VOC and SVOC)[1] in the exhaust [61]. It might also contain small amounts of inorganic material, such as sulfates and metal oxides, from oil and fuel additives [96, 122, 139]. For the purpose of this study, the exhaust-port PM is considered to be free of VOC or SVOC coatings, justified by the high exhaust-port temperatures, exceeding 250 °C - 300 °C that prevents semi-volatile condensation. Such liquid coatings might be generated as the exhaust cools down or mixed with cold air, which affects diluted exhaust measurements as discussed in Chapter 4 and Chapter 6.

The optical properties of soot depend on its morphology, chemical composition, and nano-structure. The morphology of soot may be studied from its projected transmission electron microscopy (TEM) images, such as the sample in Figure 2.1. TEM images provide detailed information about the aggregate length scales, such as projected area diameter (d_a) or radius of gyration (R_g), and their correlations with the number and size of primary particles (N_p and d_p respectively) [22]. The particle-cluster and cluster-cluster aggregation of primary particles inside the flame produces ramified structures, observed in figure 2.1, obeying the mass-fractal relation [132, 182].

$$N_p = k_f \left(\frac{2R_g}{d_p} \right)^{D_f} \tag{2.1}$$

Here, D_f and k_f are the fractal dimension and pre-factor. Particles formed

[1] Here, we follow the definitions of Giechaskiel et al.; in that, the VOC species are those that condense below 100 °C, and SVOC are material that condense between 100 °C and 350 °C [61].

in diffusion-limited cluster aggregation (DLCA) regime are shown to have D_f in the range 1.6 - 1.8 [108]. Other factors, such as the primary particle overlap and necking due to surface growth reactions, affect the aggregation process, resulting in a higher fractal dimension in the range 1.9 - 2.2 [145].

More recently, TEM analysis of soot aggregates has revealed that primary particles are relatively uniform within an aggregate, but vary between aggregates [32]. By considering soot from various sources, a first-order power-law correlation between the diameter of primary particles and aggregates is established,

$$d_p = d_{p,100}\left(\frac{d_a[\text{nm}]}{100}\right)^{D_{\text{TEM}}} \tag{2.2}$$

where $d_{p,100}$ is the mean primary particle diameter of 100 nm aggregates, d_a is the projected-area diameter, and D_{TEM} is an exponent based on TEM image analysis [146]. These observations suggest that each aggregate is formed in a small region with relatively uniform conditions, and is later externally mixed with other aggregates formed in different regions, also called the external mixing hypothesis (EMH) [146]. It suggests that larger aggregates are formed in more fuel-rich regions, resulting in larger primary particles and possibly different physicochemical properties.

The chemical composition and nano-structure of soot, too, depend on its formation history inside the flame. Incipient and young soot contains higher amounts of organic carbon due to the existing PAH molecules. As the formation reactions progress in the high-temperature fuel-rich regions, the ratio of hydrogen-to-carbon atoms (H:C) decreases, and the carbon atoms start to form small graphitic crystallites [20]. High-resolution TEM (HR-TEM) images of flame soot from various fuels suggest that residence inside the high-temperature fuel-rich regions produces larger, structured graphitic carbon domains, yielding highly light-absorbing soot, while short residence times and lower combustion temperatures promote amorphous carbon structures. Examples of such structures are illustrated in Figure 2.3 [195].

The structure of carbon atoms determines the refractive index (RI) of

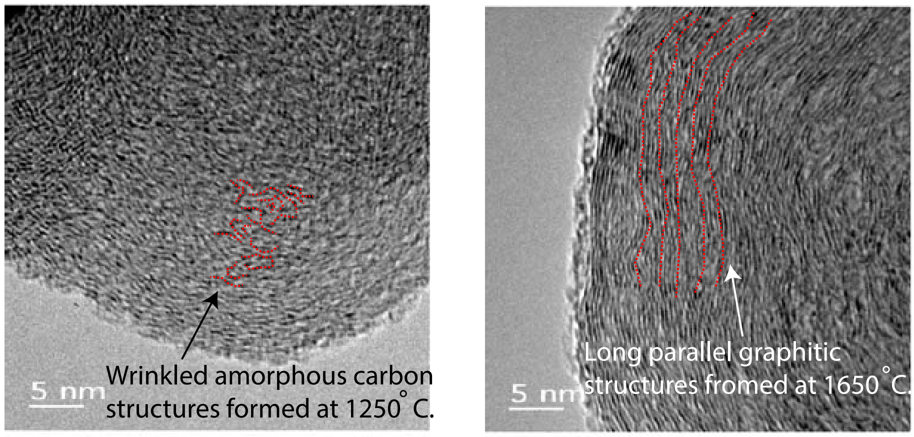

Figure 2.3: High-resolution TEM (HR-TEM) images of soot from acetylene flames at 1250 °C (left) and 1650 °C (right), showing the nano-structure of primary particles. Soot produced at higher temperatures (right) has a more graphitic carbon structure, resulting in a higher absorption coefficient (κ). Figure is adapted from [195], with permission from Elsevier.

soot, $\mathbf{m} = n + i\kappa$[2], and affects its light absorption and scattering behaviour. The large range of reported RI in the literature can be attributed to the variation of soot chemical composition and nano-structure due to different combustion conditions. A refractive index of $\mathbf{m}$ = 1.9 + 0.79i was recommended in a review paper by Bond and Bergstrom based on the data published until 2006 [20]. It is, however, shown that this value must be modified to account for recent measurements and modeling results of soot mass-absorption cross section (MAC) from various flames [94, 118]. Raman spectroscopy of soot from research burners indicate the ratio of disordered-to-graphitic (D/G) carbon bonds decreases for larger aggregates [8, 36], resulting in higher MAC values for larger particles presumably due to more graphitic structures. Soot refractive indices from various sources in literature are summarized in Appendix B, and is revisited in Chapter 4.

Optical measurements rely on physical and morphological properties of

[2] The real part, n, is the ratio between the speed of light in vacuum and inside a material. The imaginary part, κ, is related to the light absorption coefficient of the material.

soot. Therefore, the effects of these properties on soot light absorption and scattering must be considered when interpreting their measurements. Below, various models for describing the interaction of particles with light are elaborated, and their implications for soot measurement are discussed in Section 2.4.4 and Chapter 4.

2.2 Interaction of particles with light

Aerosols interact with light and scatter or absorb the incident electromagnetic (EM) radiation. The interactions between the particles and the incident electric field may be described by the scattering matrix **S**, with components S_1 - S_4 in Equation 2.3, relating the components of the scattered electric field (denoted by $\mathbf{E}_s$) to the incident electric field (denoted by $\mathbf{E}_i$).

$$\begin{pmatrix} \mathbf{E}_{s,l} \\ \mathbf{E}_{s,r} \end{pmatrix} = \frac{e^{ik(r-z)}}{-ikr} \begin{pmatrix} S_2 & S_3 \\ S_4 & S_1 \end{pmatrix} \begin{pmatrix} \mathbf{E}_{i,l} \\ \mathbf{E}_{i,r} \end{pmatrix} \tag{2.3}$$

Here, r is the particle-photodetector distance, z is the projected distance along the propagation direction of the incident wave (Z axis), and k is the wave number ($2\pi/\lambda$) of the incident light. Subscripts "l" and "r" represent the components of the electric field paralle**l** and perpendicula**r** to the scattering plane, schematically shown in Figure 2.4. In this demonstration, a photodetector is positioned on the scattering plane, at angle $\boldsymbol{\theta}$ relative to the incident wave vector, this direction defines the scattered wave vector ($\mathbf{k}_s = \frac{2\pi}{\lambda}\hat{\mathbf{k}}_s$). The light scattering strongly depends on the size and shape of particles; therefore, different models are needed to describe the wide-ranging PM geometries and sizes, as briefly described here.

2.2.1 Particles with simple geometries

A small particle inside an electromagnetic field may be modeled as a dipole oscillating with the field and producing light scattering patterns based on the Rayleigh model. The components of the Rayleigh scattering matrix are shown in Equation 2.4,

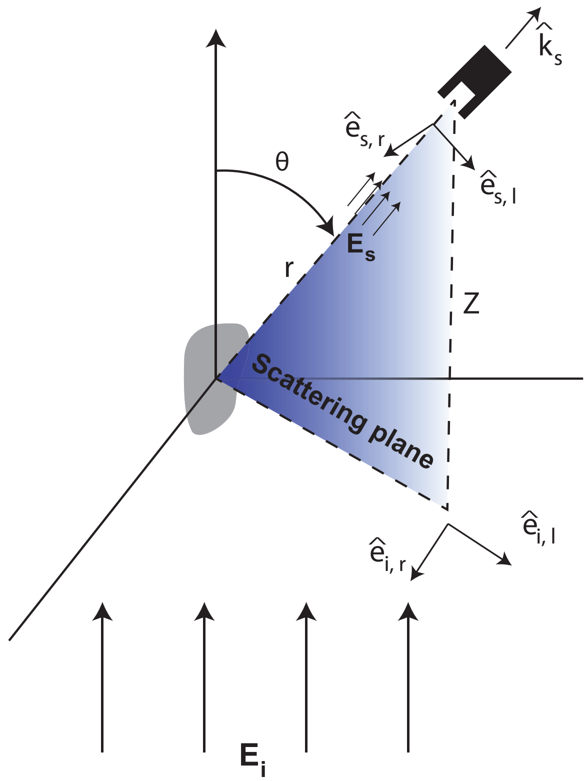

Figure 2.4: The incident and scattered light propagation vectors ($\mathbf{E}_i$ and $\mathbf{E}_s$), the scattering plane, and the normal and parallel unit vectors are shown. The incident rays are in Z-direction, the scattering angle is $\boldsymbol{\theta}$, and the subscripts r and l represent the parallel and perpendicular directions to the scattering plane.

$$S_1 = -ix_p^3\left(\frac{\mathbf{m}-1}{\mathbf{m}+2}\right) \tag{2.4a}$$

$$S_2 = -ix_p^3\left(\frac{\mathbf{m}-1}{\mathbf{m}+2}\right)\cos(\theta) \tag{2.4b}$$

where S_3 and S_4 are zero, $\mathbf{m}$ is the complex refractive index, and x_p is the normalized diameter of the particle [82].

$$x_p = ka_p = \frac{\pi d_p}{\lambda} \tag{2.5}$$

In Equation 2.5, $k = 2\pi/\lambda$ is the wave number of the incident light with wavelength λ. The intensity of the scattered filed parallel and perpendicular to the scattering plane are,

$$I_l = \frac{|S_2|^2}{k^2r^2} I_{l,0} = \frac{x_p^6}{k^2r^2} \left| \frac{\mathbf{m}^2-1}{\mathbf{m}^2+2} \right|^2 \cos^2(\theta)\cos^2(\alpha_{pol}) I_0 \tag{2.6a}$$

$$I_r = \frac{|S_1|^2}{k^2r^2} I_{r,0} = \frac{x_p^6}{k^2r^2} \left| \frac{\mathbf{m}^2-1}{\mathbf{m}^2+2} \right|^2 \sin^2(\alpha_{pol}) I_0 \tag{2.6b}$$

where r is the distance from the particle to the detector (e.g. a photodiode), I_0 is the intensity of the incident light, and α_{pol} is the angle of polarization of the incident light relative to the scattering plane. The total intensity of the scattered light is the sum of the two components in Equation 2.6. It is common to use the "differential scattering cross section", $\frac{d\sigma_s}{d\Omega}$, instead of intensity,

$$\frac{d\sigma_{s,R}}{d\Omega} = \frac{x_p^6}{k^2} F(\mathbf{m}) \left(\cos^2(\theta)\cos^2(\alpha_{pol}) + \sin^2(\alpha_{pol})\right) \tag{2.7}$$

where $F(\mathbf{m})$ is the Rayleigh scattering function defined in Equation 2.8.

$$F(\mathbf{m}) = \left| \frac{\mathbf{m}^2-1}{\mathbf{m}^2+2} \right|^2 \tag{2.8}$$

The Rayleigh light absorption cross section, too, depends on x_p, k, and $\mathbf{m}$ [82],

$$\sigma_{abs} = \frac{4\pi}{k^2} x_p^3 E(\mathbf{m}) \tag{2.9}$$

where $E(\mathbf{m})$ is the Rayleigh absorption function.

$$E(\mathbf{m}) = \mathrm{Im}\left(\frac{\mathbf{m}^2-1}{\mathbf{m}^2+2} \right) \tag{2.10}$$

Light absorption is proportional to the volume of particles, due to the x_p^3 factor. This is utilized to measure the volume concentration (or mass concentration given a known density) from light absorption, further explained in Section 2.4.3.

The formulation given in Equations 2.7 - 2.10 depends on the size and refractive index of particles and is valid for $|\mathbf{m}|x_a << 1$. Outside this limit, more elaborate light scattering models are needed. Solutions to the Maxwell's equations exist for light scattering from spheres, ellipsoids, and other simple geometric shapes. Here, Mie's solution for light scattering of a sphere is discussed [19]. Using the mathematical formulation of Bohren and Huffman, the diagonal components of the scattering matrix (S_1 and S_2) are

$$S_1 = \sum_n \frac{2n+1}{n(n+1)}(a_n \pi_n + b_n \tau_n) \tag{2.11a}$$

$$S_2 = \sum_n \frac{2n+1}{n(n+1)}(a_n \tau_n + b_n \pi_n) \tag{2.11b}$$

where, π_n and τ_n are functions of $\cos(\theta)$ and are related to the Legendre function,

$$\pi_n(\cos(\theta)) = \frac{1}{\sin(\theta)} P_n^1(\cos(\theta)) \tag{2.12a}$$

$$\tau_n(\cos(\theta)) = \frac{d}{d\theta} P_n^1(\cos(\theta)) \tag{2.12b}$$

while the coefficients a_n and b_n depend on the normalized particle diameter x_p and the refractive index $\mathbf{m}$.

$$a_n = \frac{\mathbf{m}\psi_n(\mathbf{m}x_p)\psi_n'(x_p) - \psi_n(x_p)\psi_n'(\mathbf{m}x_p)}{\mathbf{m}\psi_n(\mathbf{m}x_p)\xi'(x_p) - \xi_n(x_p)\psi_n'(\mathbf{m}x_p)} \tag{2.13a}$$

$$b_n = \frac{\psi_n(\mathbf{m}x_p)\psi_n'(x_p) - \mathbf{m}\psi_n(x_p)\psi_n'(\mathbf{m}x_p)}{\psi_n(\mathbf{m}x_p)\xi_n'(x_p) - \mathbf{m}\xi_n(x_p)\psi_n'(\mathbf{m}x_p)} \tag{2.13b}$$

Here, $\psi(x)$ and $\xi(x)$ are defined based on the spherical harmonic Bessel functions of the first and second kind, with details provided in [19]. The matrix obtained based on the series provided in Equations 2.11 describes the light scattering intensity around a spherical particle.

Mie formulae are sometimes used to approximate the light scattering from irregularly-shaped particles too. Jaggard et al. measured the light scattering from sodium chloride aerosols, where their measurements for $\boldsymbol{\theta} < 90^{\circ}$ were in close agreement with the Mie results, deviating mildly only for larger angles [85]. We later employ this approximation to calculate the optical coefficient of FEN by measuring NaCl aerosols, described in Chapter 3, with details provided in Appendix A. For soot aggregates, however, the Mie light scattering model based on an aggregate-equivalent spherical diameter produces inaccurate results [180]. Such applications require proper superposition strategies based on the geometric features of fractal aggregates.

2.2.2 Light scattering from fractal aggregates

The aggregation processes inside a flame result in soot structures that resemble fractals; in that, they demonstrate fractal-like size-invariant properties, such as in Equation 2.1 [55, 132]. The Rayleigh-Debye-Gans model for fractal aggregates (RDGFA), describes the light scattering by considering individual primary particles as Rayleigh scatterers ($x_p \sim 0.2$ - 0.3), assuming they are unaffected by light-scattering from other primaries. The scattering wave vector $\mathbf{q}$ with the magnitude expressed in Equation 2.14 describes the RDGFA angular light scattering distribution around an aggregate.

$$q = 2k \sin\left(\frac{\theta}{2}\right) \tag{2.14}$$

The net scattering field from an aggregate may be approximated as the sum of light scattering from individual primary particles. This is formulated as a double sum based on the distances between all primary particles, called the structure factor $S(\mathbf{q})$,

$$S(\mathbf{q}) = N^{-2} \sum_{i}^{N} \sum_{j}^{N} e^{i\mathbf{q}.(\mathbf{r_i}-\mathbf{r_j})} \tag{2.15}$$

where $\mathbf{r}_i$ and $\mathbf{r}_j$ are the positions of any primary particle pairs inside the aggregate. This sum can be simplified in terms of the density autocorrelation function, $g(r)$ [26],

$$g(r) = Ar^{(D_f-3)}h\left(\frac{r}{\zeta}\right) \tag{2.16}$$

where D_f is the fractal dimension, A is an appropriate scaling constant, and $h(r/\zeta)$ is a cutoff function, wherein ζ is a characteristic length of the aggregate. Structure factors obtained based on different density auto-correlations are reviewed by Sorensen, and compared in Figure 2.5. The structure factors based on a Gaussian cutoff function (G), and the models of Dobbins and Megaridis (DM) [44] and Lin et al. (L) [114] in Equation 2.17 are quite similar, with the maximum differences of up to 20% occurring at $qR_g \sim 2$, shown in Figure 2.5.

$$S_G(qR_g) = {}_1F_1\left[\frac{D_f}{2}, \frac{3}{2}; -\frac{(qR_g)^2}{D_f}\right] \tag{2.17a}$$

$$S_{DM}(qR_g) = \begin{cases} \exp\left(-\frac{q^2R_g^2}{3}\right) & q^2R_g^2 \leq 1.5D_f \\ \left(\frac{3D_f}{2e}\right)^{\frac{D_f}{2}}(qR_g)^{-D_f} & q^2R_g^2 > 1.5D_f \end{cases} \tag{2.17b}$$

$$S_L(qR_g) = \left[1 + \sum_{s=1}^{4} C_s(qR_g)^{2s}\right]^{-D_f/8} \tag{2.17c}$$

In Equation 2.17, ${}_1F_1$ is the hypergeometric function describing the structure factor with a Gaussian density auto-correlation cut-off. The coefficients C_1 - C_4 in the model of Lin et al. are $\frac{8}{3D_f}$, 2.5, -1.52, and 1.02, respectively, and e is the Euler's number in the model of Dobbins and Megaridis. The simpler DM formulation highlights that for small qR_g, the Guinier regime, one can measure the aggregate size from the light scattering ratios in multiple angles [98], as the structure factor depends only on qR_g.

The differential light scattering cross-section of an aggregate is calculated based on the cross sections of individual primary particles, $d\sigma_p/d\Omega$, corrected with the aggregate structure factor,

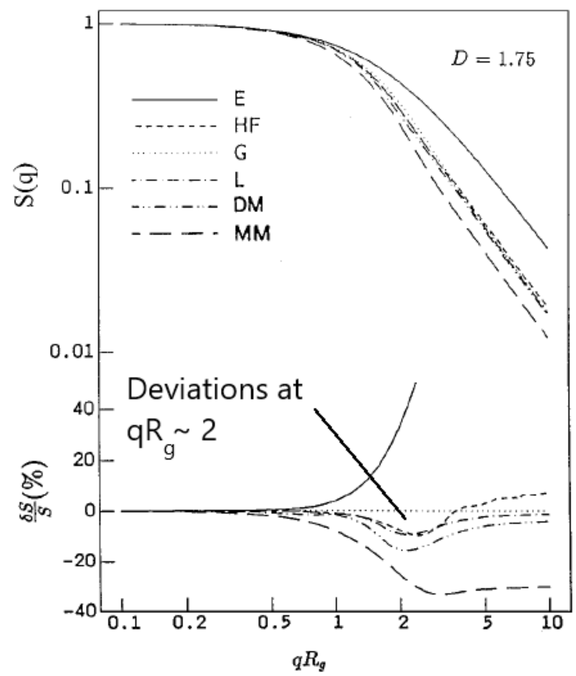

Figure 2.5: Aggregate light scattering structure factors, $S(qR_g)$, for different structure models. The structure factors based on the Gaussian auto-correlation cut-off (G), and the models of Dobbins and Megaridis (DM), and Lin et al. (L) are in close agreement. Figure is adapted from [182], with permission of Taylor and Francis.

$$\frac{d\sigma_{agg}}{d\Omega} = N_P^2 \frac{d\sigma_p}{d\Omega} S(qR_g) \tag{2.18}$$

where N_p is the number of primary particles. Combining Equations 2.17-2.18, one can calculate the magnitude and angular dependency of the light scattering intensity around a fractal aggregate.

2.2.3 Considerations for polydisperse samples

The RDGFA light scattering model formulated in Equation 2.18 is for a single aggregate size. For polydisperse aggregates, the size distribution has to be considered. Lognormal [73] and self-preserving scaling [57] size distributions are proposed for polydisperse combustion soot. In this work, we use the lognormal distribution assumption, as it models the whole size range, and is demonstrated for engine soot in various studies [73], such as for the research engine used in this work [65]. More detailed discussion of the lognormal distribution and its integration into the light scattering calculations are presented in Chapter 4.

The aggregates in a polydisperse sample span over a size range of 10 - 1000 nm. Since light scattering from an aggregate depends on d_p^6 (Equation 2.7), the variation of primary particle diameter is important and must be considered. It is, however, common in the literature to assume a constant primary particle diameter for all soot in a polydisperse sample. A more appropriate description is one that considers the scaling correlations between the size of primary particles and the aggregates, modeled in Equation 2.2 based on the EMH mode [146].

The theoretical background presented here provides a simple framework to understand and interpret the light scattering and absorption measurements, used in a range of instruments. Below, further considerations from regulatory and research and development standpoints are presented, and together with the material discussed in this section, provide a framework to evaluate different ICE PM measurement methodologies.

2.3 Emission standards

The properties of engine-out PM may change in the exhaust system. The particles coagulate, and as they grow larger, their number concentration decreases. The VOC and SVOC compounds, such as unburned fuel, water vapour, and engine oil form nucleation-mode PM or condense onto the existing soot [61]. Therefore, the condition of the exhaust-port sampling and its location are important for reproducibility of the measurements, and is further discussed here.

2.3.1 Regulations

Exhaust PM emissions are controlled by legislations in response to their adverse health effects. Since the introduction of the motor vehicle air-pollution standards in the 1970's, the regulations have become stricter and allow lower PM emission for type approval. The standards differ based on the vehicle application, weight, and sometimes the method of ignition. The heavy duty (HD) on-road vehicles, relevant to this work, are tested on engine-dynamometer setups, and their emissions are normalized by the engine output work in units of bhp.hr or kWhr. The HD PM mass emission limits have decreased over the years from higher than 0.6 g/kWhr in the 80's to less than 0.01 g/kWhr in the most recent regulations, as shown in Figure 2.6 [59]. Heavy-duty engines (primarily diesel) have been required to meet these emissions standards based on their production year and intended market. The recent EURO-VI standard includes a limit of 6×10^{11} #/kWhr on solid particle number (SPN) emissions, and a not-to-exceed (NTE) limit for real-drive emission tests (RDE), as well [42].

In early standards, engines were required to run on steady-state load-speed modes, with enough dwell at each mode allowing for engine stabilization [59]. Emissions during steady-state operation, however, grossly under-represent the real-world emissions dominated by transient events. Soot, in particular, is sensitive to sudden increases in engine load, with peak concentrations many times higher than the steady levels [70]. Recent standards require transient engine-dyno testing to model the real-drive operations.

PM mass during a transient test is measured by extracting tail-pipe exhaust sample, transferred to a dilution tunnel to mix with particle-free air, and collected onto filters for subsequent gravimetric weighing. To measure the SPN, a diluted sample is passed through a volatile particle remover (VPR) to remove the liquid volatile and semi-volatile material by heating [25] or catalytic oxidation [1, 106], and the solid particles are measured by a condensation particle counter (CPC). For consistency, particles larger than 2.5 μm are removed before the mass measurement, and particles smaller

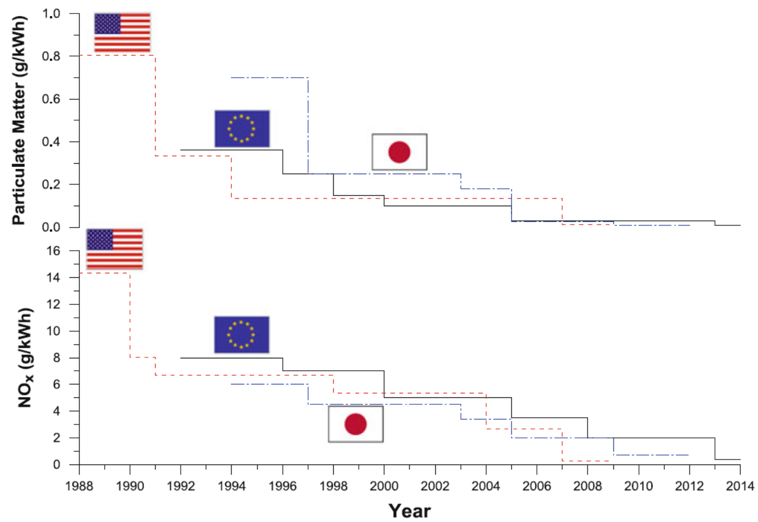

Figure 2.6: The evolution of the PM and NO_x emission limits for heavy-duty on-road engines (primarily diesel) between the years 1988 and 2015 for the North American, European, and Japanese standards [59]. Reprinted by permission from Springer Nature - Springer International Publishing, 4901030933623.

than 23 nm are not counted during the SPN measurement[3] [60]. To further enhance the reproducibility of the results, limits are set on the range of dilution ratios, and on the temperatures of the dilution air. A 20% interlaboratory variability in mass and number measurements are still reported, possibly due to artifacts related to rapid dilution or different sampling locations [61, 71].

2.3.2 PM mitigation

The exhaust emission limits are met by inhibiting the pathways of in-cylinder soot formation and physically removing the PM from the exhaust stream. A diesel particulate filter (DPF) removes 90-99% of the engine-out PM, thereby significantly reducing its tail-pipe concentration [95]. Continuous

[3]A CPC for regulatory SPN measurement is required to have a counting efficiency of less than 50% for 23-nm particles [60].

PM loading on the filters increases the exhaust back pressure; hence, the DPF-deposited soot has to be oxidized using continuous (passive) or programmed (active) regeneration mechanisms. The excess O_2 in lean diesel exhaust or the NO_2 generated in the diesel oxidation catalyst (DOC) are used to burn the deposited soot at exhaust temperatures of 250°C - 450°C [68]. Often, passive methods are aided by active mechanisms, such as delaying the combustion timing, injecting excess fuel into the exhaust, or electrically heating the exhaust gases, to facilitate the DPF regeneration [7].

Much attention is directed towards reducing soot inside the combustion chamber to alleviate the DPF regeneration penalties. High diesel injection pressures possible with the modern common-rail systems reduces the in-cylinder soot formation. Moreover, multiple-injections [49, 79] and partial premixed combustion (PPCI) [50, 137] strategies are shown to further reduce PM. Alternative fuels, such as natural gas with lower C-to-H ratio, are less susceptible to high soot emissions [129]. Dual fuel combustion strategies, such as port-fuel injected natural gas assisted with direct injection of diesel reduces PM, but its application is limited by the reduced intake volumetric efficiency and high CH_4 emissions [92]. Direct-injection of natural gas assisted with a pilot diesel injection (pilot-ignited direct-injection natural gas or PIDING) is a promising method that has lower CH_4 emissions than port-injected dual-fuel natural gas engines, preserves the high torque and fuel efficiency of diesel engines, while offering lower PM and CO_2 emissions, and allowing flexible fueling ratios [130].

2.4 PM measurement methods for engine research and certification

PM emissions are characterized based on the different methods tailored to the property being measured. Here, we review the measurement techniques for PM number, mass, size, and optical properties and their relevance to the research carried out in this work. Indirect optical measurements provide fast response times, and are of interest for high-speed sensors. Particularly, the light scattering method utilized in the FEN is elaborated in detail, and its application for exhaust PM measurement is discussed.

2.4.1 Number

Particle number emissions are important from a health perspective. While the small nucleation-mode particles, formed in large numbers, do not significantly contribute to the total mass, they can penetrate deep into lungs and carry carcinogenic material [112]. To characterize the number concentrations, particles are either counted optically when crossing a beam of light, or electrically by counting charged particles with an electrometer. In the optical method, the main sample is diluted with clean air and the stream is focused using sheath air to reduce the coincidence error. Small particles scatter very little light, due to the d^6 scattering dependency in the Rayleigh regime (Equation2.7). Therefore, particles smaller than $\sim$ 300-500 nm are not detected with regular optical particle counters (OPC). This size range is very important for engine measurements, as it constitutes the soot accumulation and nucleation modes [61].

Smaller detection limits are achievable by growing particles through condensation of supersaturated volatile vapour. A condensation particle counter (CPC) can detect PM smaller than 10 nm, thereby measuring the nucleation and accumulation modes of the exhaust PM [134]. The CPC-3025 by TSI Inc. is an example of a commercially available CPC and is used along a particle mobility classifier for size-resolved number concentrations in this work. The CPC-3025 accepts PM concentrations of up to 10^5 #/cm^3, and counts particles larger than 3 nm [193].

PM number may also be measured by measuring the charges imparted on particles with a unipolar particle charger, such as a high-voltage corona needle. The charged particles are collected onto impactors or electrodes that are connected to sensitive electrometers for measurement. This method is less sensitive than the CPC, even with the 1 femto Ampere resolution of modern electrometers. Moreover, the unipolar PM charging depends on particle size and morphology [174], which must be considered when post-processing the raw signals. The diffusion charging and electrical counting methods are coupled with size classifiers to produce PM size distribution, as further discussed below.

2.4.2 Size distribution

Measuring PM size is common in air pollution, nanomaterial synthesis, and PM epidemiological research. The 3D geometric properties of soot may be determined from TEM images. The primary particle diameter (d_p) is a key geometric parameter in light scattering modeling, which can be determined from manual processing of projected TEM images. This method, despite its robustness and accuracy, is extremely time consuming. Therefore, automatic algorithms such as the Hough transformation [67], Euclidian distance mapping (EDM) [39], and pair-correlation method (PCM) [34] are developed for this task. These algorithms are calibrated against the manual method, yet variations as large as 10% or more in d_p are reported between different methods [3]. The PCM method of Dastanpour et al. is calibrated for the PIDING engine soot used in this work, and is employed for the analysis of TEM images in Chapter 4 and Chapter 6.

The TEM image-processing method gives detailed morphological information about the aggregates, as discussed in Section 2.1.2, yet it is too time consuming for most applications. Most often, a PM mobility or inertial classifier coupled with a particle counter are used to resolve the PM size distribution. As the classification process relies on the aerodynamic or electrical forces on particles, it results in different classifications for particle size. Here, these methods are reviewed and their differences are highlighted.

Mobility diameter

The mobility diameter (d_m) is perhaps the most commonly used characteristic size of PM, as it is directly related to the aerodynamic drag on particles, F_d,

$$F_d = \frac{3\pi\mu U d_m}{C_c} \tag{2.19}$$

where the numerator is the Stokes drag force on a sphere with diameter d_m, as a function of the particle-gas relative velocity (U) and the dynamic viscosity of the surrounding gas (μ). In the denominator, C_c is the slip correction factor, accounting for deviations from the continuum gas behaviour for small particles [54].

$$C_c = 1 + Kn\left[1.257 + 0.40\exp\left(-\frac{1.10}{Kn}\right)\right] \tag{2.20}$$

The size of particles relative to the mean-free-path of the surrounding air molecules is characterized by the Knudsen number (Kn).

$$Kn = \frac{2\lambda_{air}}{d_m} \tag{2.21}$$

Small particles with large Kn (free molecular regime) are affected by the thermal motion of air molecules, and behave differently from large particles in the continuum regime (small Kn). The relationship between the mobility diameter (d_m) of soot and the number and size of its primary particles depends on the Knudsen number. Mobility diameter is similar to the projected-area diameter (d_a) in the free molecular regime and well into the transition regime, while it becomes considerably larger than d_a in the continuum regime [183].

The mobility diameter is practically determined from measuring the trajectory of charged particles inside an electric field, such as in the scanning mobility particle spectrometer (SMPS) used in this work. Electrically charged PM enters a differential mobility analyzer (DMA), where it drifts in a cylindrical electric field used to separate particles in a narrow range of electrical mobility (Z) which are subsequently counted [53]. In order to convert Z into d_m, the electric charge on particles must be known. Charging of PM takes place inside a radioactive Kr-85 or a soft X-ray neutralizer (such as TSI 3054 and 3088) placed before the DMA, producing a bipolar PM charge distribution, determined based on the Fuchs-Wiedensohler model [200]. The strength of the electric field inside the DMA is changed with time to scan different d_m. This method provides a finely resolved size distribution with up to 64 size bins per decade. The trade-off, however, is the long scan time which is in the order 30 s to few minutes for a full spectrum [192].

The measurement response time may be improved by simultaneously measuring different particle sizes. This is often achieved by using a number of fixed electrodes connected to electrometers measuring the PM electric charge. The differential mobility spectrometer (DMS-500) by Cambustion Ltd. and the engine exhaust particle sizer (EEPS) by TSI Inc. utilize this method to resolve the PM size distribution with a sub-second time resolutions. The unipolary charged particles enter a voltage trap where excess gaseous ions are removed, then migrate across an electric field and impact on electrodes where their electric charge is measured [89, 163]. The inversion of the electrometer signals into d_m is complex, as it relies on the size-dependent efficiency of the unipolar diffusion charger [174].

The DMS 500 and EEPS contain 26 - 32 size channels, and resolve particle sizes in the ranges of 5 - 1000 nm and 5 - 560 nm, respectively. Here, the much faster response time, needed for transient engine measurements, comes at the cost of lower resolution and less accurate signal inversion compared to the SMPS.

Aerodynamic diameter

The motion of a particle in a changing flow, such as in a bend or an impinging jet on a plate, depends on particle inertia. The inertial behaviour of a particle is described by the Stokes number.

$$St = \frac{\rho d^2 C_c U}{18 \mu L} \tag{2.22}$$

The parameters d and ρ are the diameter and the density of the particle, and L is the geometric length scale of the flow. Since ρ might change with the particle size, the aerodynamic diameter, d_{ad}, is defined as the diameter of a unit-density (1 g/cm^3) sphere with the same Stokes number. The aerodynamic diameter is used to characterize the particle sampling losses [46] and deposition in human longs and other surfaces [187].

The electrical low-pressure impactor (ELPI) uses unipolar particle charging and a cascade impactor to measure PM based on its aerodynamic diameter (d_{ad}). The ELPI+ by Dekati Inc. contains 14 impactor stages which collect particles in the 16 nm - 10 μm d_{ad} range [86]. This wide size range comes at the cost of poor resolution, especially for the ultrafine PM in engine exhaust. The inversion of the electrometer signals to concentration is an intricate process, as the unipolar charging efficiency is a function of d_m, while the particle classification is based on d_{ad} [125]. This is partially addressed in the Dekati Mass Monitor (DMM) by including a mobility analyzer column to measure particles with d_m <30 nm, while the rest of the sample is classified with cascade impactors similar to the ELPI+ [121]. The information obtained from the number and size measurement of soot can be used to indirectly calculate its mass, for example, by determining the soot effective density from combined d_m and d_{ad} measurements [124].

2.4.3 Mass

The exhaust PM mass is collected on filters during regulatory tests, and is gravimetrically weighed to check the emissions compliance. This, however, requires a long sampling time to collect detectable mass and does not resolve changes in the PM concentration during transient events.

Time-resolved PM mass concentration may be obtained from tapered element oscillating microbalance (TEOM) [62] or quartz crystal microbalance (QCM) [75], where PM mass loading changes the oscillation frequency of a filter. The time resolution of these methods depends on the concentration, and is too slow to resolve fast engine transients. Indirectly, the measurements of PM size and number, described in Section 2.4.2, can be converted to mass based on the particle density. The effective density of soot is size-dependent and may be obtained from simultaneous particle mobility and aerodynamic diameter measurement [124], or from direct particle mass coupled with d_m classification [47, 65]. A power-law correlation between the soot effective density and mobility diameter is evident based on these methods. The diffusion charging process, too, is size-dependent, and may be used as a surrogate for PM mass, such as in the Pegassor soot sensor (PSS) [144]. The limited accuracy of this method is offset by its fast response time and ability to continuously sample the raw exhaust flow [4]. Higher time resolutions are possible with optical methods, and further discussed below.

Particles, depending on their chemical makeup, absorb and scatter light. The BC-PM is strongly light-absorbing, a property that is harmful for environment, but useful for its measurements! The light absorption by soot aggregates may be correlated to their mass (see Section 2.4.4, Equation 2.9). The laser-induced incandescence (LII) and the photo-acoustic soot sensing (PASS) are techniques for measuring soot mass concentration from light absorption. In LII, the soot particles are heated to 2000-4000 K, their mass concentration is measured from the thermal light emission intensity, and their primary particle size is obtained from the decay of light intensity signal due to cooling [169, 170]. In the photoacoustic method too, modulated laser heating of soot and the subsequent thermal expansions and contractions of the surrounding air generates acoustic waves which are correlated to the soot mass concentration [160, 168]. The PASS signal may be generated with lower laser powers, since unlike the LII, milder temperatures are acceptable.

The LII-300 by Artium Scientific Inc. and the micro soot sensor (MSS) by AVL are commercially available LII and PASS sensors, respectively. The PASS method is sensitive to acoustic noise in the environment and variations in the sample flow rate, and cannot be used for engine exhaust-port measurements. LII, on the other hand, is not affected by acoustic noise, and thus, is used for direct raw exhaust sampling, even before the turbocharger where large excursions exist [196, 202]. The inversion of the LII signal, however, is complex and is prone to variations of soot optical properties [116, 178].

Mass concentration may also be obtained from light attenuation. Particles can be collected onto filters, where the filter blackness indicates the amount of accumulated mass [72, 142], This is a slow process due to the time required for sufficient loading of optically detectable soot. The particle-in-air light attenuation, however, is faster and can resolve sub-second variations of the soot extinction coefficient (k_{ext}) for transient engine measurements

[111, 176].

Light scattering in nephelometers and photometers is yet another technique for indirect PM mass concentration measurement. The light scattering of soot depends on the its refractive index, size, and morphology, as discussed in Sections 2.1.2 and 2.2. Therefore, calibrated instruments with standard dust may not be suitable for engine soot measurement. The Dusttrak by TSI Inc., calibrated with A1 Arizona test dust (ISO 12103-1) [194], is a single-angle photometer frequently used for engine PM [29]. The changing PM size and morphology between different engine operating points, however, affects light scattering and can produce inaccurate results from single-angle light-scattering instruments such as the Dusttrak [123]. The multi-angle light scattering addresses some of these shortcomings when the effects of soot morphology are considered in data inversion, but it requires involved calibration procedures for the light scattering models used for the inversion.

2.4.4 Optical methods and the challenge of data inversion

The RDGFA model, introduced in Section 2.2.2, is simple and computationally fast, but as a first-order approximation, it does not consider multiple scattering inside an aggregate. Solving the Maxwell's equations for light scattering of a particle, on the other hand, is highly accurate but computationally intractable. To enhance the computational performance, without sacrificing the accuracy, complex particles are modeled based on the superposition of accurate EM solutions for simple geometries. The multi-sphere T-matrix (MSTM) [120] and the generalized multi-sphere Mie (GMM) [204] models, for example, compute the light scattering of primary particles using the superposition of harmonic spherical functions (e.g. Equation 2.12) to determine the near and far-field light scattering. These models give accurate scattering and absorption cross sections by considering multiple scattering from primary particles inside an aggregate.

The MSTM and GMM models are suitable for aggregates with point-touching spherical primary particles. Real aggregates with overlapping primary particles, necking around the connecting edges, and liquid coatings cannot be modeled with these methods. In such cases, particles are modeled as an ensemble of oscillating dipoles, in a method called the discrete dipole approximation (DDA) [45]. Here, each primary particle is divided into polarizable sub-volumes affected by the incident EM field (E_i) and a secondary field due to the oscillation of other dipoles (E_d). The DDA may be used to model more complex geometries and internally mixed aerosols, such as soot with overlapping primary particles [205] or with liquid coating due to condensation [117, 181]. Its result, however, are not exact as they approximate the EM field, and are sensitive to the density of dipoles and their polarizability [115].

The optical cross sections of randomly oriented particles encountered in experimental measurements require averaging many MSTM and DDA realizations based on different aggregate orientations. The number of operations in the MSTM light scattering computations for each aggregate realization scales with N_p^{α}, where α is between 2 and 3 [45, 120]. This computational time is prohibitive especially when computing the light scattering of polydisperse aggregates. The computational cost of DDA is even higher due to the number of dipoles needed to model each primary particle [115]. Furthermore, implementing the DDA method for point-touching aggregates introduces errors in the range of 10% due to sharp changes in the EM field near the touching points. The MSTM method is, therefore, preferred due to favourable computational cost and accuracy when modeling point-touching aggregates. The effects of primary particle overlap, necking, and coating, on the other hand, cannot be modeled in MSTM and requires the DDA simulations [117, 205].

The RDGFA model, despite its shortcomings, is popular thanks to its simplicity and low computational cost. Errors in the RDGFA model can be characterized based on the results of the orientationally-averaged MSTM or DDA computations, and used to improve its accuracy. For point-touching fractal aggregates, the error depends on the normalized primary particle diameter, x_p, the refractive index $\mathbf{m}$, and the number of primary particles N_p. The contours shown in the left panel of Figure 2.7 demonstrate the

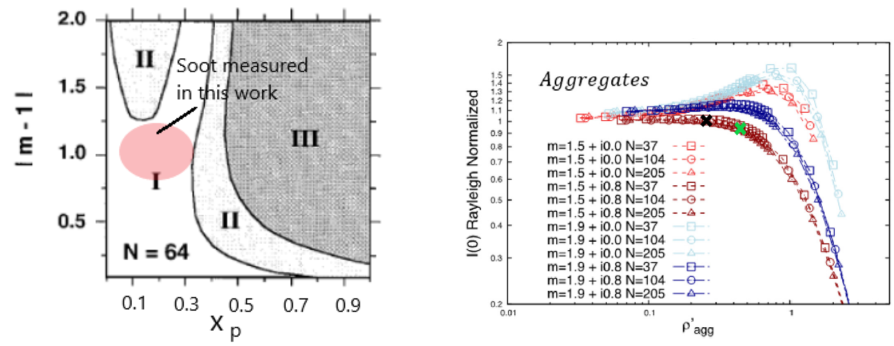

Figure 2.7: Errors in the RDGFA based on more accurate light scattering models. Left panel: Error of the RDGFA total scattering cross section in regions I, II, and III, are less than 10%, between 10% and 30%, and more than 30%, respectively. The red ellipse marks the range of soot encountered in this work. Figure is adapted from [51], by permission of the Optical Society of America. Right panel: The forward light scattering intensity ratio between the MSTM and the RDGFA. The black and green crosses mark a 100 nm and 400 nm soot aggregate respectively. Figure is adapted from [184], by permission of Elsevier.

RDGFA errors in the $|\mathbf{m}-1|$ - x_p space for an aggregate containing 64 primary particles [51]. More recently, Sorensen et al. studied the deviations of the RDGFA from the MSTM model for numerically generated fractal aggregates as a function of the optical phase shift ρ', shown in the right panel of Figure 2.7. The ranges of engine soot encountered in this work are marked on both panels, and the structural RDGFA errors are further discussed in Appendix F.

$$\rho'_{agg} = kd_p \left| \frac{\mathbf{m}^2 - 1}{\mathbf{m}^2 + 2} \right| N_p^{0.08} \tag{2.23}$$

In light scattering experiments, soot properties such as the total concentration, the moments of size distribution, or the fractal properties are usually unknown, while the light scattering intensities at multiple angles or different wavelengths are measured. The relation between the measured light scattering and the size and concentration is convoluted into an integral equation,

$$\mathbf{g}(\theta) = C\int_0^\infty P(\mathbf{x}, R_g)\mathbf{K}(\mathbf{x}, R_g, \theta)dR_g \tag{2.24}$$

where $\mathbf{x}$ is the vector of unknowns, such as the size distribution or fractal parameter, $\mathbf{K}$ is the convolution kernel constructed based on a light scattering model (e.g. RDGFA or MSTM), $\mathbf{g}$ is the vector of measured values, such as light scattering intensities at multiple angles, and C is a calibration coefficient modeling the characteristics of the light scattering instrument. The deconvolution of $\mathbf{x}$ from the integral equation based on the measured $\mathbf{g}$ and the kernel K is called the light scattering inversion. It is more constructive to write Equation 2.24 in a discretized matrix form $\mathbf{Kx} = \mathbf{g}$ and solve it numerically. This, however, results in an ill-posed system of equations, since the number of unknowns is typically more than the measured intensities [24]. Additional constraints based on prior information about the population or morphology of aggregates has to be introduced to stabilize the inversion.

Methods based on least square estimation (LSE) may result in a large set of solutions that are equally likely based on the minimization criteria, and cannot be distinguished from one another considering the measurement uncertainties. Instead, methods based on maximum a posteriori probability (MAP) use the Bayesian statistics to find the unknowns $\mathbf{x}$ based on the measurements $\mathbf{g}$, i.e. $P(\mathbf{x}|\mathbf{g})$ in Equation 2.25.

$$P(\mathbf{x}|\mathbf{g}) = \frac{P(\mathbf{g}|\mathbf{x})P(\mathbf{x})}{P(\mathbf{g})} \tag{2.25}$$

Here, $P(\mathbf{g}|\mathbf{x})$ is the likelihood of obtaining the light scattering measurements $\mathbf{g}$ given known polydisperse parameters $\mathbf{x}$, $P(\mathbf{x})$ is the prior information about the PM sample such as its morphology or the shape of size distribution, and $P(\mathbf{g})$ is a scaling factor. The effects of measurement noise, and systematic errors in the light scattering model embedded in the kernel $\mathbf{K}$, are considered in the likelihood function $P(\mathbf{g}|\mathbf{x})$ [133], while the prior information, such as smoothness and non-negativity of the size distribution are implemented in $P(\mathbf{x})$ [24].

The Bayesian method accepts general priors such as the ones mentioned above; however, often this is not sufficient to converge to a concentration, and specific information, such as lognormal size distribution assumption, are necessary. This is demonstrated in the inversion of measurements from a wide-angle light scattering (WALS) instrument, where the Bayesian technique is employed to determine the mean size and standard deviation ($d_{m,g}$ and $\sigma_{m,g}$) of lognormal polydisperse soot, along with the fractal dimension and pre-factor (D_f and k_f in Equation 2.1) [80]. When a lognormal polydispersity is assumed and $P(\mathbf{x})$ is enhanced by tandem morphological data from TEM, the results of the Bayesian inversion are close to the LSE method [24]. One could argue that the Bayesian MAP has the advantage of determining the uncertainty bounds based on the probability distribution of the recovered results. While true, it can be shown that similar information may be recovered from the LSE method, coupled with a sensitivity analysis based on the perturbation of inputs [98]. The latter is used to characterize the uncertainty of light scattering inversion method employed in this work, and is discussed in Chapter 4.

2.4.5 Summary of PM measurement techniques

The methods reviewed in the previous sections are frequently used in literature to characterize the engine exhaust PM. Their results, however, might differ depending on the methodologies, range, resolution, and the response time of the instruments used to carry out the measurements. Differences of a factor of 2 or more in the concentration of PM is observed in simultaneous measurements during engine transient tests with an ELPI, DMS-500, and an EEPS [167]. Lower ELPI PM mass concentrations compared to the gravimetric TEOM and light-absorption LII measurements are reported in other studies [161, 201], most likely due to uncertainties in the soot effective density and low size resolution of ELPI for the accumulation-mode diesel soot. Further complications might also arise due to different transient response times of different instruments.

The response time of an instrument largely depends on its internal volume and flow rates. The ELPI, for instance, has a response time of 1 s, and instruments such as the DMS-500 and EEPS have response times in the range 0.2 - 0.5 s [163, 167]. This does not consider the effects of mixing inside the engine exhaust path, or inside the sampling lines. The combined effects of the instrument and sampling location may be determined from the rate of change of the measured signal to controlled changes in the PM concentration. Using this approach, the response times of a DMS-500, a PASS (AVL micro soot sensor), an opacimeter (AVL), and an LII sensor (Artium) are compared. The opacimeter and the PASS were shown to have similar 50% - 100% response times close to 1 second, and where slightly slower than the DMS-500 which had a 50%-100% response time of 0.6 - 0.9 s. The LII was the only instrument able to measure PM before the turbocharger and had the shortest (0.3 - 0.6 s) response time [196]. This case study demonstrates the combined effects due to the specifications of the instruments, and their ability to sample close to the source of emission for faster response times. Fast ex situ and in situ exhaust LII measurements are reported elsewhere too [202], as highlighted in Table 2.1. A summary of the instruments and the methodologies reviewed in this chapter is provided in Table 2.1.

Evidently, the optical methods such as LII and light scattering could be used for fast measurements at the exhaust port. The in-situ exhaust measurements by Witze et al. revealed large fluctuations in the LII signal, but the underlying causes for the variations were not explained nor investigated. The light scattering method, too, is used for ex- and in-situ exhaust measurements. The application of a two-angle light scattering instrument with fast exhaust dilution, soottrack, is demonstrated for diesel exhaust measurements [78]. Moreover, in situ raw exhaust light scattering measurements by Parks et al. demonstrated cycle-resolved and cylinder-specific data, their results, however, were limited to qualitative demonstrations rather than quantitative comparisons [154]. These optical methods could potentially be utilized for quantitative cycle-resolved engine-out PM, a potential that is explored in this work using the method of light scattering with the FEN, and demonstrated on an engine-dynamometer test facility at different operating conditions.

Table 2.1: Comparison of the different instruments for engine PM measurement reviewed in this chapter.

Quantity	Instrument	Measurement method	Response time
Number	OPC	Optical particle counting	1 s
	CPC	Condensation growth and optical counting	1 s
Mobility diameter	SMPS	Electrostatic mobility classification and counting with CPC	0.5 - 3 min
	DMS-500	Diffusion charging, electrical mobility classification, and electrometer charge measurement	0.5 - 1.0 s*
	EEPS	Similar to DMS-500	0.5 - 1.0 s*
Aerodyn. diameter	ELPI	Diffusion charging, inertial classification, and electrometer measurement	1 s
Projected diameter	TEM	Thermophoretic sampling, TEM image processing for d_a, d_p, and R_g	30 s - 1 min
Gravimetric mass	Filters	Filters are gravimetrically weighed	$\sim$ 30 mins
	TEOM	Filter oscillation frequency	10 s - 1 min
Indirect mass	PASS	Laser light absorption, subsequent acoustic pressure measurement	1 s*
	LII‡	Laser light absorption, subsequent thermal emission measurement	0.3 - 0.6 s*
	Smokemeter	Light attenuation due to BC filter loading	10 - 30 s
	Opacimeter	Light attenuation in particle-laden gas	1 s*
	Light scattering	Single or multi-angle elastic light scattering	0.1 - 1 s†
	PSS‡	Diffusion charging, and measuring the escaped current	0.5 s

* Response times are based on [163, 167, 196]

† The range is due to the different LS instruments in literature.

‡ Can measure raw exhaust soot.

2.5 Outlook

The complex in-cylinder soot formation-oxidation processes are difficult to model, and require expensive and complex optically accessible engines for experimental validation. The soot formation and oxidation depend on mixture formation and combustion, which vary during transient operation of an engine, and produce highly variable soot emissions that cannot be resolved with current exhaust PM instruments.

In this chapter, methods commonly used for measuring the number, size, and mass of PM are discussed, and the conversion between different measurements are explained. The mass concentration is a common proxy for the health and climate impacts of the engine-emitted PM, and is measured directly (gravimetric) or indirectly. The indirect methods tend to have faster response times, such as in the optical instruments. Nonetheless, the inversion of the optically-measured mass is non-trivial, as it depends on the size, morphology, and physical properties of PM. Multi-angle light scattering is a promising method to measure the PM mass, while simultaneously providing information about its size and morphology.

The RDGFA model predicts the soot light scattering for a wide range of aggregate sizes and optical properties, and is computationally efficient. The simplicity of the RDGFA model compared to the elaborate MSTM or DDA models is especially critical for the polydisperse soot calculations encountered in most measurements. Further improvements can be made by incorporating the EMH morphology model to account for the enlargement of the primary particles with the aggregate size. Such improvements can be crucial, considering that the model errors are amplified in the process of inversion.

The response time of the current PM instrumentation is insufficient to resolve the cycle-by-cycle variations of emissions. Fast response times, necessary for the cycle-resolved measurements, require sampling close to the exhaust valve, using a short sampling tube. Due to the high PM concentrations, high exhaust temperature, and strong fluctuations in the flow, the raw exhaust-port soot measurement has been limited to a few qualitative studies in the literature. To fill this gap, a new methodology with a reasonable quantitative accuracy is demonstrated in Chapter 4, and implemented on a single-cylinder research engine (SCRE) for measuring the cycle-resolved exhaust soot and its correlations with the in-cylinder pressure in Chapter 5 and Chapter 6. The single-cycle capability of this method makes it a useful tool for characterizing the transient emissions, where single cycles can affect the engine calibration results. More advanced inline engine controls applications, e.g. by virtual soot sensors [11, 12], might also benefit from our proposed method during the tuning process, but require considerable research efforts and is outside the scope of this work.

Chapter 3

Experimental research facility

The research carried out in this work takes an experimental approach to characterize single-cycle engine-out soot emissions based the light scattering technique. The exhaust-port soot generated by a research engine on a dynamometer test-bed is sampled and measured with the Fast Exhaust Nephelometer (FEN). The FEN is characterized based on reference instruments for PM size, mass, and morphology. Here, a detailed description and the operating procedures for the FEN, the research engine, and the PM instrumentation are laid out. The characteristics of the FEN as a PM sensor for steady and transient samples are briefly demonstrated, and the engine operating points used throughout this study are summarized.

3.1 Fast Exhaust Nephelometer (FEN)

The FEN consists of an aluminum block with two perpendicular internal bores for the flow of the soot-laden sample and the passage of a laser beam. The light passes through the exhaust sample at the center of the FEN block, and the scattered light from the polydisperse sample in this intersection volume is recorded using photodetectors, as shown in Figure 3.1. A 250 mW, 405 nm laser beam is collimated with a lens. Moreover, five successively finer aperture disks are used to trim the beam cross section to avoid stray light reflections, especially at the beam entrance and exit of the measurement chamber. The aperture disks also act as spacers between the laser diode and the sampled flow (which might be hot, polluted or both) inside the FEN measurement chamber.

The scattered light is measured at three cone angles of 30° positioned at 45°, 90°, and 135° relative to the beam path, as shown in Figure 3.1. At the end of each cone, the scattered light is focused using two successive biconvex lenses with focal lengths of 50 mm and 25.4 mm (Thorlabs LB1471 and LB1761) onto silicon photodetectors (Throlabs PDA36A). The FEN measurement chamber has an internal volume of 20 cm^3 for the passage of the sampled flow, of which, 0.2 cm^3 is illuminated by the 405-nm laser beam called the optical volume. The optical components are protected against the hot engine exhaust and soot fouling by continuously purging the FEN with clean air. When making measurements, the purge air is temporarily shut off to avoid disturbing the exhaust flow inside the FEN, and is re-enabled after the measurement is completed.

The power of the laser beam is measured using a handheld power meter (Sper scientific) between the engine measurement campaigns, and indicated a stable 250±20 mW beam power. The temperature of the FEN is kept constant at 65-70 °C using a cartridge heater and a thermocouple inserted into the aluminum block, and the temperature of the exhaust sample (T_{sample}) is measured at the outlet of the FEN with an exposed-tip thermocouple and varies between 190 °C and 230 °C. The pressure inside the FEN chamber is kept near-atmospheric using an excess-port at its outlet, and the effect of temperature on the density of the sample is factored in by multiplying the measured soot concentrations by $\frac{T_{sample}+273}{298}$.

3.2 Research engine facility

The research conducted in this work is carried out using the facility in the Clean Energy Research Center (CERC) at the University of British Columbia (UBC). The CERC clean combustion facility includes advanced

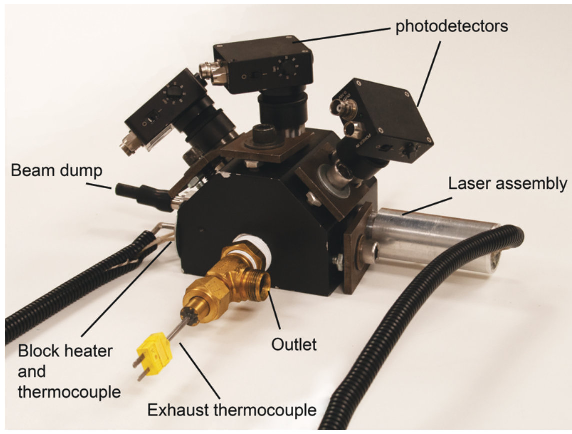

(a) FEN hardware

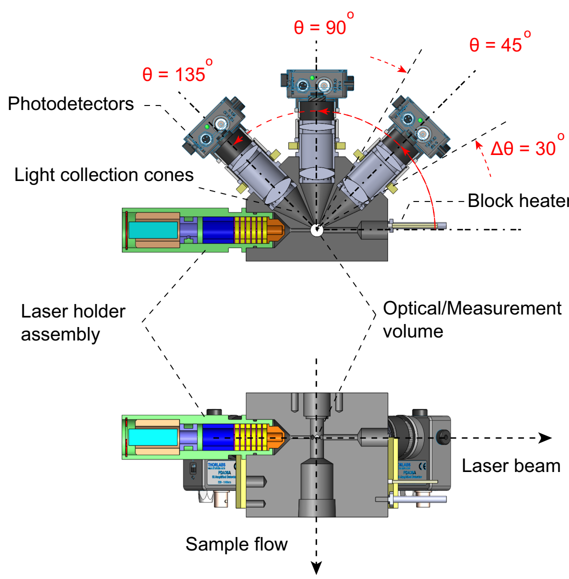

(b) FEN computer model

Figure 3.1: A photo of the FEN showing its key components (top), and a computer model demonstrating its internal features (bottom). The particles in the measurement chamber are illuminated with a laser beam and their scattered light is focused on the three photodetectors.

engine diagnostics to research alternative fuels and advanced combustion strategies, and to characterize engine emissions. Here, the details of the research engine and the supporting instrumentation for characterizing the combustion, fuel-air thermochemistry, and exhaust emissions are laid out.

3.2.1 Single-cylinder research engine (SCRE)

The soot particles studied here are generated by a pilot-ignited direct-injection natural gas (PIDING) single-cylinder research engine (SCRE) on a dynamometer test-bed. The SCRE is based on a production 6-cylinder, 2.5 L/cyl. Cummins-ISX-451 engine, modified to fire only one cylinder (closest to flywheel). Engine torque and speed are controlled with a water-cooled eddy current dissipation GE dynamometer, also linked to a variable frequency drive (VFD) electric motor to assist during cold start. The facility utilizes a first-generation Westport Fuel Systems high-pressure direct-injection (HPDI) injector to enable direct injection of natural gas that is ignited by a pilot diesel [48, 131]. The majority of fuel energy (95% or more) is from natural gas, and the diesel pilot serves as an ignition source. Elevated exhaust and intake air pressures simulate turbocharged operation, and the engine is equipped with a cooled exhaust gas recirculation (EGR) system, similar to modern compression ignition engines. This configuration allows more flexibility in setting the combustion air and the EGR flow rates independently, allowing to operate the engine in conditions meant for research, which are generally different from standard production engines.

Direct injection of natural gas leads to relatively low, but non-negligible, formation of particulate matter [90]. Especially at high loads, the combustion process can be altered from its optimal configuration to generate higher levels of engine-out soot, for example by reducing injection pressure or lowering the air-fuel ratio [155]. In this configuration, the FEN is mounted near the SCRE exhaust and connected to its exhaust-port with a sampling tube, shown in Figure 3.2.

The SCRE is also equipped with a water-cooled Kistler model 6067C piezo-electric sensor connected to a charge-amplifier for high-speed in-cylinder

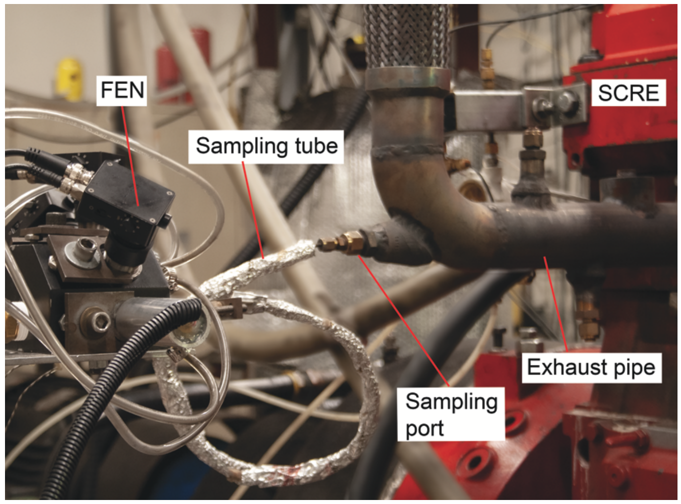

Figure 3.2: The FEN mounted for SCRE exhaust-port sampling.

Table 3.1: Specifications of the high-speed pressure sensors implemented for SCRE measurements.

Sensor make and model	Application	Specifications
Kistler 6067C	Piezo-electric sensor for in-cylinder pressure measurement.	0 - 250 bar range, -25 pC/bar sensitivity, natural frequency of 90 kHz, water-cooled with an operating temperature range of -50 - +350 °C [105].
PCB 1501C02EZ	High-speed intake manifold pressure measurement.	0 - 170 kPa range, faster than 1 ms response time, compensated operating temperature range of -20 - +80 °C, and an accuracy of ±0.25% FS [157].
Omega PX4201-100GV	Silicon-on-sapphire sensor for high-speed exhaust-port pressure measurement.	0 - 690 kPa range, 0.2 ms response time (63%), 0.25% FS accuracy including linearity and hysteresis, and a temperature range -50 - +120 °C [149].

pressure measurements. The amplified signal from the in-cylinder sensor is equalized with an intake manifold pressure (piezo-resistive PCB piezotronics 1501C02EZ), at the intake stroke bottom dead center (BDC) of each cycle [105, 157, 177]. This enables measuring the quantitative in-cylinder pressure between the intake valve closing (IVC) and exhaust valve opening

(EVO), which is crucial for engine load, efficiency, and combustion calculations. The exhaust manifold pressure is also measured with a fast-response Omega PX4201-100GV pressure sensor, used to assist the interpretation of FEN light scattering signals, discussed in Chapter 5. Specifications of the pressure sensors used for the intake and exhaust manifold and the in-cylinder pressure measurements are summarized in Table 3.1.

3.2.2 Instrumentation and data acquisition

To monitor and control the engine operating condition, characterize the in-cylinder combustion, and measure exhaust emissions, SCRE is instrumented with various sensors, wired to a National Instruments NI CDAQ-9188 chassis. The data acquisition (DAQ) chassis is equipped with several boards listed in Table 3.2, to accommodate the various types of sensors and different data acquisition speeds required to characterize the engine operation. The pressures, temperatures, and flowrates of air, fuel lines, exhaust, and EGR are needed to monitor the engine condition and determine the combustion air-fuel ratio (AFR). These are marked with light blue colour in Figure 3.3, and recorded on boards NI-9205 and NI-9213 with a 1 Hz acquisition rate.

Signals which require high-speed acquisition, such as the PDA36A FEN photodetectors and the index signal for the laser diode are recorded on high-speed DAQ boards (NI-9215), synchronous with 0.5° pulses of an optical crank-shaft encoder. Other crank-angle-resolved signals include the in-cylinder, intake- and exhaust-port pressures (P_{cyl}, P_{int}, and P_{exh} in Figure 3.3), used for calculating the cycle-resolved in-cylinder pressure and heat-release parameters, explained in Section 3.2.4, and determine the effects of exhaust pressure fluctuations on FEN light scattering traces, discussed in Chapter 5. Details about the instrumentation and DAQ system is provided in Table 3.2.

When the FEN is mounted for SCRE exhaust-port measurements, shown in Figures 3.2 and 3.3 (with black outline), its sampling tube protrudes into the exhaust pipe for head-on ($\theta = 0$) PM sampling. In this mode, the

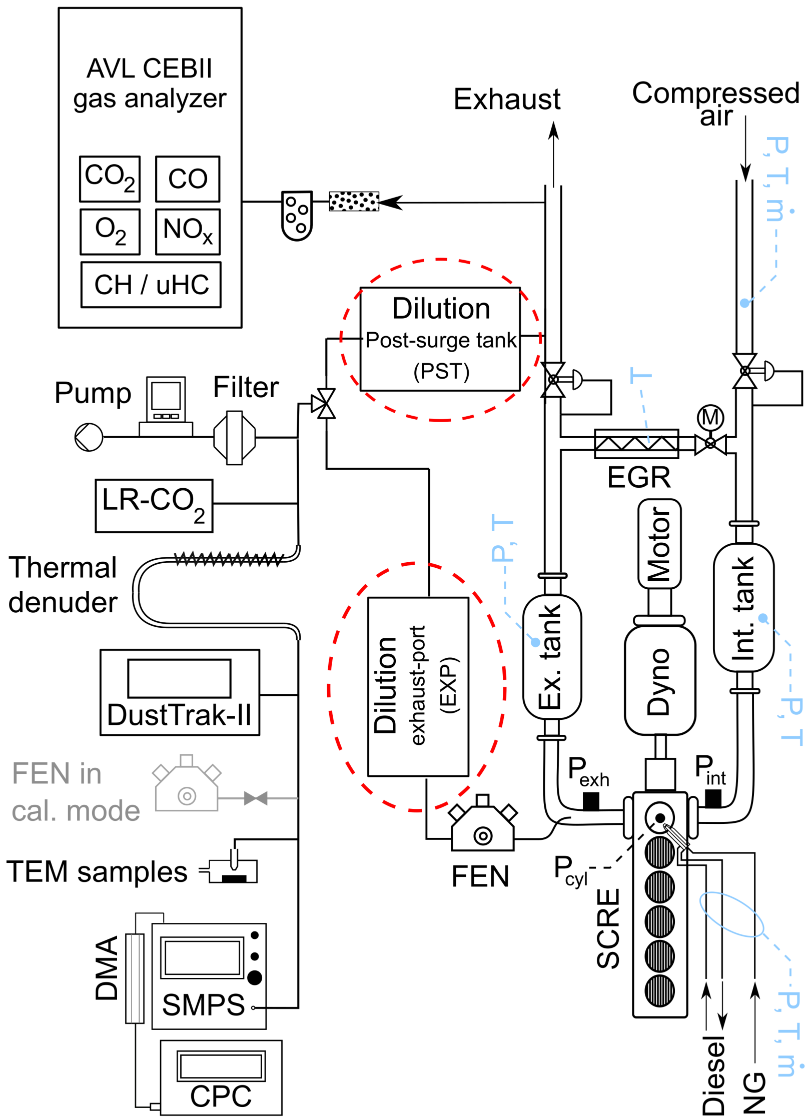

Figure 3.3: The SCRE and PM emissions measurement layout. The post-surge-tank (PST) and the exhaust-port (EXP) PM sampling locations are marked with dashed ellipses. Crank-angle-resolved sensors for in-cylinder, intake- and exhaust-port measurements (black outline), and time-resolve sensors for engine monitoring and control (light blue) are shown.

Table 3.2: Specifications of the data acquisition system.

DAQ board/module	Specifications	Signals acquired
NI-9205 (1 Hz temporal resolution)	16 differential analog inputs, 250 kS/s, does not support simultaneous sampling at clock ticks, 16 bits resolution.	Intake air and exhaust surge tank pressures, intake air flowmeter differential pressure, fuel rails pressures and mass flowrates (light blue colours in Figure 3.3).
NI-9213 (1 Hz temporal resolution)	16 thermocouple inputs, 75 S/s, supports all standard thermocouples, nominal accuracy 0.77 °C.	Intake air, EGR, and exhaust temperatures. Fuel line, engine oil, and coolant temperatures (light blue colours in Figure 3.3).
NI-9215 (0.5° crank-angle resolution)	4 differential analog inputs, 100 kS/s/ch, supports simultaneous sampling at clock ticks, 16 bits resolution.	Crank-angle-resolved signals: In-cylinder, and intake- and exhaust-port pressures (P_{cyl}, P_{int}, and P_{exh} in Figure 3.3), the FEN PDA36A photodetector voltage and the laser diode electric current signals.
NI-9375	16 digital input-only, and 16 digital output-only channels, 7 μs maximum update rate.	SCRE emergency shut-down input signals.

FEN crank-angle-resolved light scattering intensities are processed to determine the cycle-specific soot concentrations, discussed in Chapter 5 and Chapter 6 in detail. In the calibration mode, the FEN (shown with gray outline in Figure 3.3) measures steady samples of diluted exhaust, and its signals are recorded on a separate DAQ (National Instruments BNC-2120). The recorded light-scattering signals are averaged, post-processed with an inversion algorithm, and compared against the low-speed reference PM instruments introduced in Section 3.3.

3.2.3 Gaseous emissions

The exhaust gaseous emissions of SCRE are measured with an AVL CEB-II gas analyzer bench. Water vapour is removed from the sample, so the measured concentrations are on a dry basis. The engine EGR and equivalence ratio (ϕ) are calculated based on the intake and exhaust CO_2 and O_2 concentrations measured with the AVL CEB-II. The exhaust CO_2 is also used for calculating the dilution ratio of the PM samples, explained in Section 3.3.1.

The gaseous pollutants, namely the concentrations of CO, NO_x, CH_4, and other unburned hydrocarbons (collectively labeled uHC) are also measured with the CEB-II analyzer. The CO, similar to CO_2, is measured using a non-dispersive infrared (NDIR) cell. The concentrations of CH_4 and uHC are measured inside a flame ionization detector (FID), based on the electric current generated by carbon atoms of unburned hydrocarbon molecules in an otherwise carbon-free hydrogen flame [186]. The oxides of nitrogen (NO and NO_2, collectively called NO_x) are measured in a chemiluminescence cell based on the photochemical reactions between nitric oxide (NO) and ozone [13]. The emissions from the engine operating points tested in this study are reported in Section 3.5 and monitored for engine repeatability.

3.2.4 Combustion characterization

In-cylinder combustion is characterized using the crank-angle-resolved cylinder pressure. Gross indicated mean effective pressure (GIMEP) is calculated based on the work done by the in-cylinder gases on the piston during the IVC to EVO period.

$$GIMEP = \frac{1}{V_d} \int_{\theta_{IVC}}^{\theta_{EVO}} P_{cyl}(\theta) dV(\theta) \tag{3.1}$$

Here, P_{cyl} is the cylinder pressure, measured with the piezo-electric sensor, and $V(\theta)$ is the combustion chamber volume at the crank-shaft angular position θ. Other metrics for characterizing the combustion are the net heat release rate (net HRR), the rate of fuel energy conversion obtained from the cylinder pressure, and the net integrated heat release (net IHR), the cumulative energy released during the combustion. HRR and IHR quantities are defined in Equations 3.2 - 3.3,

$$HRR(\theta) = \frac{\gamma}{\gamma - 1} P_{cyl}(\theta) \frac{dV(\theta)}{d\theta} + \frac{1}{\gamma - 1} V \frac{dP_{cyl}(\theta)}{d\theta} \tag{3.2}$$

$$IHR(\theta) = \int_{\theta_{IVC}}^{\theta} HRR(\theta^*) d\theta^* \tag{3.3}$$

where, γ is the specific heat ratio of the cylinder gases [76]. The crank-angle at which half of the total fuel energy is released, θ_{50}, is defined so that $IHR(\theta_{50}) = \frac{IHR(\theta_{EVO})}{2}$ and used to characterize the phasing of combustion. GIMEP, and θ_{50} are used in the subsequent chapters to study the combustion, characterize its cyclic variability, and investigate its correlations with cycle-resolved soot emissions.

3.3 PM characterization

PM emission from SCRE is characterized based on steady measurements of diluted samples, as well as with the exhaust-port FEN light scattering. Below, the conditions of the exhaust sampling and dilution, and the details of PM instruments and their layout during SCRE measurements are presented.

3.3.1 Exhaust sampling and dilution

To characterize the soot measurement methodology developed for the FEN, diluted samples from exhaust-port and down-stream of the exhaust system are measured and compare with the raw exhaust-port FEN measurements. The SCRE exhaust passes through 10 m long, 5 cm nominal diameter piping, and a 500 L surge tank before sampled for gaseous and the down-stream PM emissions measurements. For exhaust-port diluted measurements, the exhaust of the FEN is quickly routed to a dilution tunnel, where it is mixed with HEPA-filtered air as shown in Figure 3.3. The diluted sample from this point represents the exhaust-port soot more closely and is better-suited for the validation of the FEN during exhaust-port measurements.

The sample extracted down-stream of the surge tank (post-surge-tank or PST) is mixed with heated (60 °C) clean air using an ejector that provides an initial dilution ratio of ~ 5. The diluted sample from the ejector is further diluted with extra air (at room temperature) introduced in a tee branch to provide a suitable PM concentration for instruments. The dilution ratio of the PST sample can vary between 5 to more than 100, which is particularly useful when calibrating the FEN for mass concentration measurement, as it allows a wider range and more control over the measured concentrations, necessary for exploring the dynamic range of the FEN, elaborated in Chapter 4. The exhaust-port sample (EXP), on the other hand, is diluted in a single step using an ejector nozzle with a fixed dilution ratio of 20:1. This sample is used for validating the exhaust-port FEN measurements, and characterizing the morphology and size of the exhaust-port PM, and is also compared with the down-stream soot samples.

The dilution ratio (DR) is calculated from Equation 3.4,

$$DR = \frac{[CO_2]_{r,d}\,(1-[H_2O]_{exh}) - [CO_2]_{BG}}{[CO_2]_{dl,w} - [CO_2]_{BG}} \tag{3.4}$$

where the CO_2 concentration of the diluted (dl) sample is measured on a wet (w) basis, and in the raw (r) engine exhaust stream is measured on a dry (d) basis (from AVL CEB-II), and a background (BG) CO_2 concentration of 420 ppm is assumed for the dilution air. The diluted CO_2 concentrations from the EXP and the PST samples are measured with LI-COR LI-820 and California Analytical model-100 CO_2 analyzers, respectively (schematically represented by the LR-CO_2 block in Figure 3.3). Both sensors are calibrated at the beginning of each test day with zero (high-purity N_2), 2500 ppm (for LI-820), and 8000 ppm (for California Analytical) CO_2 concentration gases. The wet CO_2 concentration of the raw exhaust is calculated based on the CEB-II dry CO_2 measurement, corrected for the exhaust water concentration, hence the (1 - $[H_2O]_{exh}$) factor in the numerator of Equation 3.4. The exhaust water concentration is calculated based on the fuel composition (assuming H:C ratio of 1.79 and 3.83 for diesel and natural gas) and the combustion equivalence ratio (ϕ) [131, 156].

The diluted sample is thermally denuded by heating to 200 °C - 250 °C, and then cooling it down to ambient temperature. The thermodenuder used here is based on the design of [25], and has been extensively characterized in our laboratory [156]. During the heating process, the condensed VOC and SVOC contents are evaporated, which are subsequently condensed or adsorbed onto the walls of the cooling secition. Due to the flowrate restrictions of the thermodenuder, gravimetric filters are collected from the undenuded sample. The gravimetric mass concentrations, thus, might be affected by the SVOC and VOC material in the sample and could differ from the denuded measurements due to PM losses in the thermodenuder. The effect of the VOC and SVOC removal is discussed in Chapter 4 and Chapter 6, and the thermodenuder losses are characterized in Appendix C, and discussed in Chapter 4.

3.3.2 PM instrumentation

The FEN light scattering measurements are validated against reference methods and commercial instruments with traceable calibrations, used for measuring diluted exhaust. In particular, particle mass, number, size, morphology, and light scattering are characterized for the SCRE PM emissions. Gravimetric mass concentration is measured by collecting PM on PTFE filters which are subsequently weighed in an automated micro-balance device (Mettler-Toledo MT5, accurate to $\pm$ 6 μg). Instruments such as the AVL micro soot sensor (MSS) or smoke meter (AVL 415S) are commonly used in automotive applications to measure the mass concentration of black carbon particles. Unfortunately, we did not have access to such instruments, and limited our mass measurements to the total PM mass concentration based on gravimetric filter method, further explained in Chapter 4 and Chapter 6.

The mobility diameter distribution is measured with a TSI SMPS-3080 equipped with a custom-made DMA, set for 180 s scan times. Moreover, soot aggregates are collected onto 3 mm carbon-coated copper grids (Ted Pella Inc.) using a thermophoretic sampler for transmission electron microscopy (TEM) imaging. Soot projected area and radius of gyration are measured from the TEM images based on the method of [22], the primary particle diameters are determined based on the automated algorithm of [34] and verified with manually sized primary particle diameters. A TSI Dusttrak photometer is used to measure light scattering PM mass concentration. The condensed liquids are removed from the samples of the SMPS, Dusttrak, and the TEM thermophoretic sampler streams using the thermodenuder introduced in Section 3.3.1. Further details about the PM instrumentation is provided in Table 3.3.

Table 3.3: Specifications of the PM instrumentation for diluted exhaust soot measurements.

Instrument	Purpose	Specifications
Emfab Filters, Pall Co.	Collecting PM for gravimetric mass measurement	Fiber-reinforced Teflon. Sample flow rate controlled with an orifice and measured with a MB-50SLPM Alicat Scientific mass flow meter.
SMPS 3080, TSI Inc.	Soot mobility diameter measurement	Uses a custom-made Differential Mobility Analyzer (DMA), with sheath and sample flow rates set up for 14-680 nm particle diameter range, and a CPC-3025 for particle counting.
TEM H7600, Hitachi	Imaging soot aggregates for morphological analysis	Using an AMX XR50 CCD camera, it has 0.35 nm point-to-point resolution and 50-200 kx magnification. Samples collected on 3 mm copper grids (Ted Pella Inc.) using a thermophoretic sampler.
Dusttrak-II, TSI Inc.	PM mass concentration from light scattering	Calibrated with Arizona road-dust, produces 1-Hz concentration time series.
Thermodenuder	Removing condensed semi-volatiles	Heats the sample to 200 °C and then cools it to remove the semi-volatiles.

3.4 Practical considerations for PM measurement with the FEN

Measuring PM mass concentration and size with the FEN depends on the optical and morphological properties of particles, the optical characteristics of FEN, and the thermomechanical conditions of the engine exhaust. The key parameters and considerations related to these measurements are introduced here, and detailed discussions are ensued in the next chapters.

3.4.1 FEN as an optical PM sensor

FEN measures the scattered light from the particles crossing the laser beam in its measurement chamber. Three silicon-based photodetectors measure the scattered light in the 350 - 1100 nm range. The responsivity of the photodiodes, i.e. the ratio of the generated photocurrent to the incident light power (P_0) [190], varies across this range, as shown in Figure 3.4. At the laser wavelength (405 nm) used in the FEN, the responsivity of the photodetectors is low (~0.16 A/W) and highly sensitive to the wavelength, due to the steep slope of the graph shown in Figure 3.4 at 405 nm. The output voltages from the amplified photodetectors (V) are converted to optical power, based on the responsivity and amplifier gain,

$$P[\mathrm{nW}] = \frac{V[\mathrm{V}]}{1500 \times 10^{\frac{G}{20}} \times R_\lambda} \times 10^9 \left[\frac{\mathrm{nW}}{\mathrm{W}}\right] \tag{3.5}$$

where G is the amplifier gain (nominally set at 70 dB), R_λ is the photodiode responsivity (Figure 3.4) at a wavelength λ, and P is the optical power in nW.

The scattered light power depends on the mass concentration of PM (C_m) and probe volume viewed by each photodetector (V_θ, only a few percent of the total 0.2 cm^3 optical volume). The product of the laser beam intensity and the probe volume ($I_0 V_\theta$), or equivalently the product of the laser beam power P_0 and the probe length viewed by each detector ($P_0 L_\theta$), is the FEN-specific parameter in Equation 3.6, relating the measured scattered light to the soot mass concentration.

$$P_\theta = P_0 L_\theta \left(MSC_\theta\right) C_m \tag{3.6}$$

The mass scattering cross-section (MSC) is defined as the ratio between the light scattering cross section (σ_{scat}) and particle mass, further discussed in Chapter 4. The probe length L_θ scales with $1/\sin(\theta)$ and therefore is slightly different for each detection angle [148]. Moreover, correction factors are needed due to the FEN walls partially blocking the scattered light rays, and the effects of light collection optics, such as the responsivity of

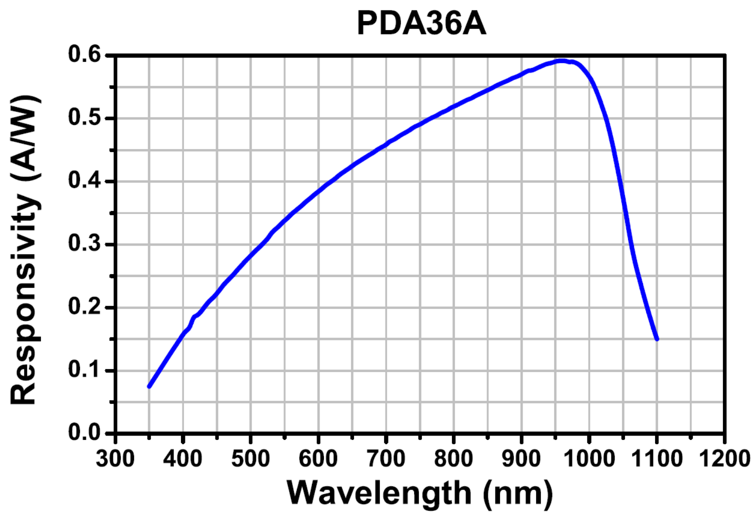

Figure 3.4: The responsivity (R_λ) of the PDA36A photodiode in the wavelength range 350-1100 nm [190]. At 405 nm, R_λ is 0.16 and very sensitive to the wavelength.

the photodiodes, the transmission losses of the lenses, and imperfect light focusing (e.g. due to aberration) on photodiodes. These parameters are independent of the aerosols measured and hardly vary over time. Namely, the effective beam path length, L_θ, depends on the geometric specifications of the FEN, the laser beam power is measured with a handheld power meter (Sper Scientific pocket laser power meter – 840011) before and after the engine measurements and shows a stable beam power of 250 mW. Soot fouling on lenses can deteriorate the optical performance, but a purge air system in the FEN is designed to prevent that.

The compounded effect of these parameters, rather than the effect of each individual factor, is important in the conversion of light scattering into mass concentration. The FEN optical coefficient, Λ_{FEN}, introduced in Equation 3.7, models the effect of these instrument-related parameters in mass concentration calculations.

$$P_\theta = \Lambda_{FEN,\theta}\,(MSC_\theta)\,C_m \tag{3.7}$$

This coefficient was determined by simultaneously measuring the PM mass, MSC, and light scattering of sodium chloride aerosols. The mass concentration (C_m) of an NaCl aerosol stream was measured by collecting filters for gravimetric analysis, its MSC was characterized based on mobility measurements with SMPS and Mie light scattering calculations similar to the method of [85], and P_θ was measured by FEN. Details of the calibration procedures employed for determining Λ_{FEN} are discussed in Appendix A, resulting in optical coefficient values of 8.6×10^{-5}, 7.2×10^{-5}, and 9.3×10^{-5} Wm for $\Lambda_{FEN,45}$, $\Lambda_{FEN,90}$, and $\Lambda_{FEN,135}$, respectively. The optical coefficient might change over time, due to soot fouling on the lenses or deterioration of the laser diode. Using purge-air during engine tests (when not making measurements), and cleaning the focusing lenses after raw exhaust-port measurements prevents the deterioration of Λ_{FEN}. Moreover, drifts in the performance of the laser diode may be detected and accounted for by measuring the laser beam power regularly, and re-calibrating the FEN in intervals or 3 - 6 months or 100 hours of raw exhaust measurements.

3.4.2 FEN as an exhaust soot sensor

To demonstrate the utility of the FEN for soot measurement, it is first compared to another light scattering instrument. To this end, preliminary proof-of-concept tests are carried out, where diluted SCRE exhaust is simultaneously measured with a Dusttrak-DRX alongside the FEN, and its results are shown in Figure 3.5.

The thermodenuded PST exhaust sample is used for this comparison, where the PM concentration at a given operating point is varied by changing the dilution ratio, possible with the PST system. The Dusttrak-DRX works based on 90° light scattering measurement and is factory-calibrated with A1 Arizona test dust (ISO 12103-1), and has a user-adjustable calibration constant for other particles [194]. The data in Figure 3.5 demonstrates that the light scattering response on the 45° and 135° photodetectors, P_{45} and P_{135} respectively, vary linearly with the Dusttrak light scattering soot mass concentration. The small offset in the least-square regression lines suggests

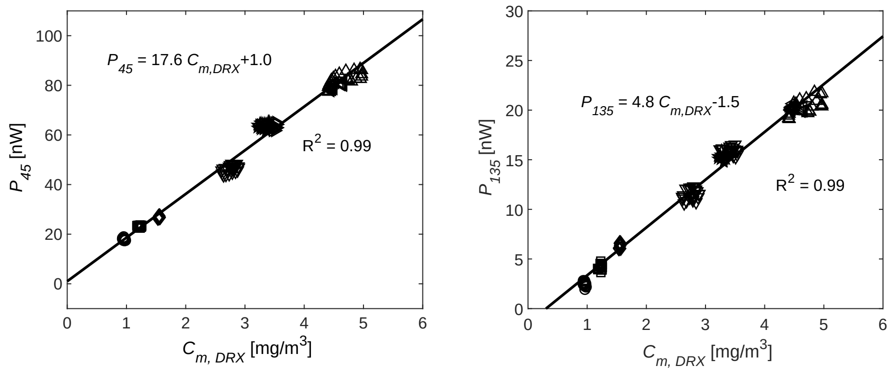

Figure 3.5: The FEN light scattering (vertical axes) produced due to diluted SCRE exhaust soot, measured on the 45° (left) and 135° (right) photodetectors, and compared with concentrations measured with the Dusttrak-DRX photometer. Figure adapted from [99].

that concentrations below 1 mg/m^3 cannot be accurately measured with the FEN, as the light scattering is too weak and might be affected by background and noise on the photodetectors [99].

The preliminary results show that the response of the FEN is similar to the light-scattering Dusttrak-DRX mass concentration measurements, which is widely used in the literature. Nonetheless, the correlation between light scattering and gravimetric soot mass concentration is complex and requires information about the morphology and properties of soot. This is evident from the deviations in the Dusttrak-measured soot concentrations and the gravimetric method for diesel soot, and particularly for PIDING-HPDI soot [156]. Therefore, a methodology for inversion of the FEN three-angle light scattering signals into soot concentration is developed and elaborated in Chapter 4, which considers the variations in the morphology and size of aggregates, and characterizes the uncertainties in the inverted results.

While FEN can measure steady soot concentrations, the cycle-resolved measurements require fast response-times and is affected by the conditions of the exhaust port. Preliminary, proof-of-concept data during exhaust-port measurement is shown in Figure 3.6. Here, light scattering traces from 45

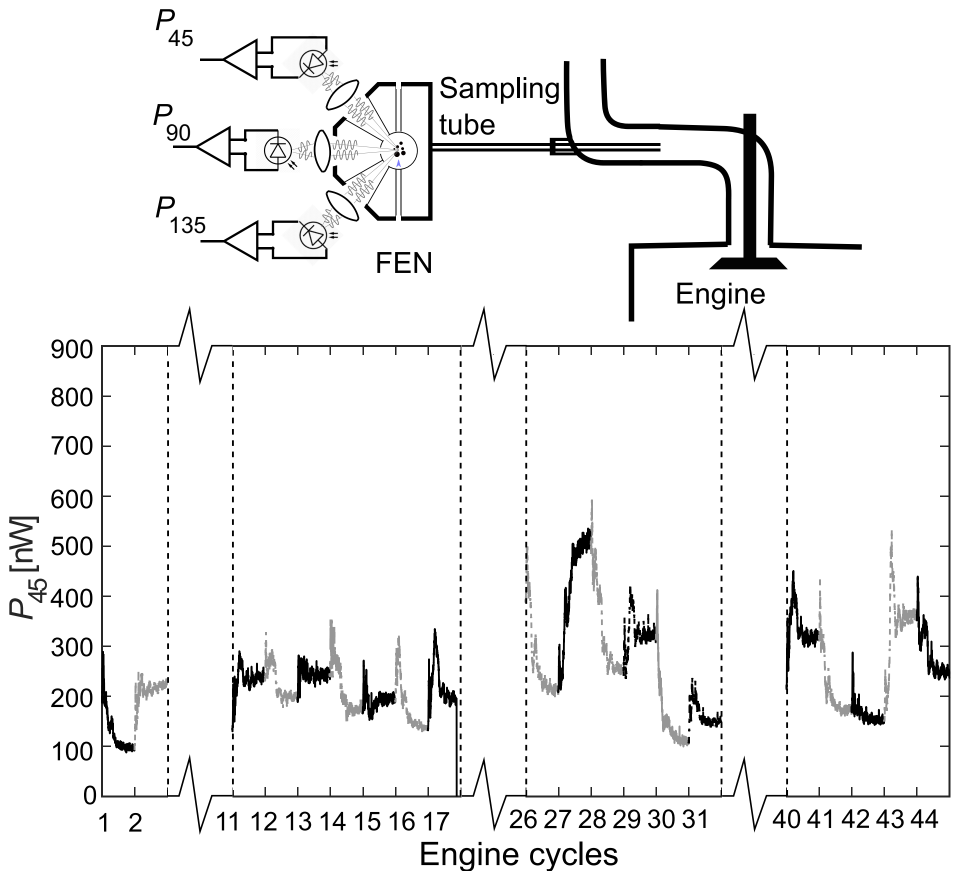

Figure 3.6: The FEN three-angle light scattering measurement of engine-out exhaust-port PM. The crank-angle-resolved 45° photodetector signal is plotted during 45 engine cycles. Individual cycles are highlighted by alternating black and grey traces, the cycle numbers are shown on the horizontal axis, and the laser-off periods are bounded by vertical dashes. [98].

consecutive engine cycles are shown, where cycle indices are marked on the horizontal axis, and the alternating black and grey colours are employed to separate the successive cycles.

The FEN traces, shown in Figure 3.6, have dynamic intra-cycle features, as well as significant cycle-cycle variations. These preliminary light scattering measurements suggest large cycle-to-cycle variations can exist, even during a fixed operating point, and are further discussed Chapter 5 and Chapter 6. Background light-scattering signals, collected by motoring the engine and measuring clean air, were stable and in the range of 0-20 nW as demonstrated in an earlier work [99], and are subtracted from the measured light intensities during fired tests, such as in Figure 3.6.

3.5 Engine operating points

Cycle-resolved exhaust soot emission and its correlations with in-cylinder combustion are investigated for the engine operating points listed in Table 3.4. The test matrix provided here is designed for an exploratory investigation, rather an engine parametric study. The points in Table 3.4 are operated in steady-state modes to validate the FEN results with diluted soot measurements, and study the cycle-cycle variabilities. Some points are also repeated in an intermittent "skip-firing" mode to explore the transient response time of the FEN. The former is discussed in Chapter 4 and Chapter 6, and the latter is presented in Chapter 5.

Table 3.4: SCRE operating points tested for the FEN calibrations and the single-cycle exhaust-port measurement.

Engine point	Engine speed [RPM]	GIMEP [bar]	θ_{50} [°aTDC]	ϕ [-]	EGR [%]	P_{exh} [kPa-a]
1	1335	16.0	12.7	0.65	19	276
2	1350	16.0	12.7	0.55	12	285
3	1350	15.5	15.5	0.54	13	270
4	1350	15.5	20.0	0.75	22	275
5	1350	16.0	20.0	0.65	15	268
6	1500	11.8	11.2	0.55	20	222
7	1200	12.2	10.0	0.70	0	196
8	890	9.9	11.3	0.53	46	223
9	1350	13.0	21.5	0.90	20	227

To produce sufficient amounts of soot for detection with the FEN, all operating points have mid-high ϕ compared to standard lean-burn diesel operation and have a range of EGR, shown in Table 3.4. For this exploratory study, only limited sweeps of ϕ, EGR, and θ_{50} are considered. Point 9 has an excessively high ϕ of 0.9, meant to generate very high soot concentrations needed for calibrating the FEN with diluted exhaust in Chapter 4, and is not tested during the exhaust-port measurements.

The concentration of the gaseous and particulate pollutants for these engine points are reported in Table 3.5 to highlight the differences between the operating points. A detailed discussion of the gaseous emissions is outside the scope of this research, and the data in Table 3.5 are only meant to provide insight into the operating conditions explored here. The PM emissions, however, are extensively studied for these operating points, and their results are discussed in the subsequent chapters.

Table 3.5: The concentration of gaseous and particulate exhaust emissions. Numbers are the mean values from multiple repetitions of each operating point. Further details about the PM concentrations are provided in Chapter 4 and Chapter 6.

Engine point	CO_2† [%]	CH_4† [ppm]	uHC† [ppm]	CO† [ppm]	NO_x† [ppm]	PM‡ [mg/m^3]
1	7.85	223	95	3840	182	65
2	6.72	129	48	1030	326	19
3	6.53	137	60	750	228	9.5
4	9.48	137	58	3015	72	27
5	8.10	95	42	809	140	9.5
6	6.85	224	98	1578	182	29
7	8.27	50	62	2235	740	18
8	8.65	410	178	4914	29	96
9	11.03	148	53	10843	59	80

† Measured with AVL CEB-II on a dry basis.

‡ Measured from the PST sample based on the gravimetric method.

3.6 Summary

The experimental facility, the key apparatus, and the instruments used to carry out the research presented in this work are introduced and elaborated in this chapter. This investigation is conducted with the FEN implemented to measure the exhaust soot from a single-cylinder research engine (SCRE) equipped with the HPDI fueling system and operated under the PIDING combustion. The SCRE is equipped with high-speed sensors enabling single-cycle in-cylinder combustion characterization using standard thermodynamic metrics, such as GIMEP and θ_{50}, to be compared with the single-cycle exhaust-port FEN results. The instrumentation and its setup for characterizing diluted SCRE soot is introduced, and its results are used to validate the FEN light scattering measurements in the next chapters.

Preliminary proof-of-concept results demonstrate the feasibility of the FEN as a PM sensor. FEN responds to changes of soot concentration similarly to a commercial light scattering instrument, the Dusttrak. Moreover, early demonstrations suggest that cycle-resolved information might be retrievable from exhaust-port FEN light scattering traces, a novel feature that is further explored in this work. Measurements conducted with the FEN are intended to provide quantitative concentrations, utilized to characterize the cycle-resolve engine-out soot and its correlations with the underlying in-cylinder combustion performance.

Chapter 4

Development and validation of a three-angle light scattering method for soot measurement[1]

4.1 Overview

The FEN simultaneously measures the light scattering intensity at three angles to infer the mass concentration (C_m), the geometric mass mean mobility diameter ($d_{m,g}$), and the geometric standard deviation ($\sigma_{m,g}$) of polydisperse soot. A kernel is used to determine C_m, $d_{m,g}$, and $\sigma_{m,g}$ based on lookup tables generated with the RDGFA model. The model incorporates the variation of the primary particle size (d_p) with aggregate size (d_a), and nine parameters related to the soot properties, and one to the FEN optics. These parameters are determined a priori from literature and TEM. The inverted C_m and $d_{m,g}$ are within ±10% of the gravimetric mass concentration and SMPS mobility

[1]This chapter is based on the work published in *Aerosol Science and Technology* Kheirkhah P, Baldelli A, Kirchen P, and Rogak S. 2020. "Development and validation of a multi-angle light scattering method for fast engine soot mass and size measurements" [98], with minor modifications for the continuity of the thesis.

diameter. This, however, largely depends on the choice of the parameters used to generate the lookup tables. A parametric study shows the inferred mass is most sensitive to uncertainties in the soot refractive index, the primary particle size, and the fractal pre-factor k_f. Considering the wide range of soot refractive indices in the literature and the sensitivity of the morphological parameters to the processing of soot images, the uncertainty in mass concentration would be over 40%. Because of this, a novel approach of relating the size of primary particles to the size of aggregates is incorporated for the first time in the light scattering model, and reduces the uncertainty to ±25-30%.

4.2 Introduction

While it was shown in Chapter 3 that the response of the FEN photodetectors correlates linearly with the Dusttrak measurements, converting light scattering intensities based on such linear calibrations can introduce large errors in the recovered concentrations. Indeed, it is shown that discrepancies could exist between the measurements of the Dusttrak compared to the gravimetric diesel or HPDI soot concentrations [123, 156]. Light scattering from soot and other agglomerated PM strongly depends on their size, morphology, and optical properties. Therefore, multi-angle measurements coupled with light scattering models that consider the soot morphology and optical properties are needed for accurate soot concentration measurements with the FEN.

Multi-angle light scattering ratio has been used in the past to infer the size and concentration of combustion soot in experiments [38, 83, 91]. These systems, however, are developed for stationary laboratory flames, not transient engines, and are validated with information recovered from TEM micrographs. Complex systems such as the Wide-Angle Light Scattering (WALS) apparatus developed by Oltmann et al., or the rotating arm goniometer configurations employed by Caumont-Prim et al. can provide detailed information about the mean soot radius of gyration and fractal dimension, but their use has been limited to stationary laminar or weakly turbulent flames and not engines [27, 147, 148].

The SootTrack demonstrated by Holve et al. can measure the exhaust soot from practical combustion power plants, such as diesel engines or gas turbines, based on a 2-angle light scattering principle using two fixed photodetectors [78]. Nonetheless, simplified assumptions regarding the properties and morphology of soot was shown to produce uncertainties in the recovered concentrations and particle sizes. In particular, the polydispersity of primary particles is rarely addressed in the light scattering literature, while research suggests that it affects the light scattering cross section of aggregates [36]. This issue is addressed here based on a model that correlates the size of the primary particles with the aggregates, suggested by Olfert and Rogak based on the EMH model[146].

Here, a methodology that can be used for FEN or other multi-angle light scattering instruments is illustrated and validated with reference PM measurements. The three-angle light scattering is used to obtain the mass concentration (C_m), the mass-averaged geometric mean mobility diameter ($d_{m,g}$), and the geometric standard deviation ($\sigma_{m,g}$) of polydisperse soot. The data inversion relies on tabulated kernel functions generated using the RDGFA light scattering model with the EMH morphology model, incorporating a correlation between the primary particle and aggregate diameters [146]. The forward or direct counterpart to this data inversion problem is to calculate the light scattering for many given soot populations, characterized by different $\sigma_{m,g}$ and $d_{m,g}$, using the RDGFA+EMH model, and store the light scattering data in lookup tables. The tables are used to post-process the FEN light scattering measurements, particularly to solve the inverse problem of finding soot concentration and mean diameter based on the measured light scattering intensities.

The current approach relies on 9 parameters to describe soot properties, and one that models the FEN optics. Four of the soot parameters are experimentally determined with TEM. The FEN optical coefficient, Λ_{FEN} introduced in Chapter 3, is determined from the gravimetric mass and mobility measurements of sodium chloride particles, and the rest are taken from the most recent literature. Based on the light scattering measurements, the inversion algorithm searches the lookup tables to find the proper $\sigma_{m,g}$, $d_{m,g}$, and C_m. To determine the accuracy of the method, the inverted light scattering results are compared with the gravimetric filter mass and the SMPS measurements. As C_m and $d_{m,g}$ are sensitive to the choice of the RDGFA+EMH soot parameters, a sensitivity study is undertaken, where new lookup tables are generated for perturbations of each parameter and the resulting C_m and $d_{m,g}$ are compared with the baseline inversion results.

4.3 Research methodology

The inversion of FEN signals requires a model for the morphology of particles, as well as a related model for light scattering. With this information, mass concentration, mass-median diameter, and geometric standard deviation can be determined iteratively. These quantities are compared with standard methods for diluted aerosols produced by the SCRE operating at steady state.

4.3.1 Soot morphology modeling

The particle morphology affects light scattering and also the relation between mobility diameter and mass, which are the researched parameters. Soot typically exhibits a fractal-like structure as an aggregate of primary particles. Figure 4.1 shows a TEM image of a soot aggregate sampled from PIDING SCRE engine used in this work. The geometric properties of soot aggregates can be obtained from their 2D projected images, such as the sample in Figure 4.1 [9, 22].

The aggregate projected area and its equivalent diameter (d_a) can be determined from images. The number of the primary particles in an aggregate (N_p) is correlated to the diameter of the primary particles (d_p), obtained from the method of [34], and the diameter of the aggregate (d_a),

$$N_p = k_\alpha \left(\frac{d_a}{d_p}\right)^{2D_\alpha} \tag{4.1}$$

where D_α and k_α are the projected-area exponent and the pre-factor obtained

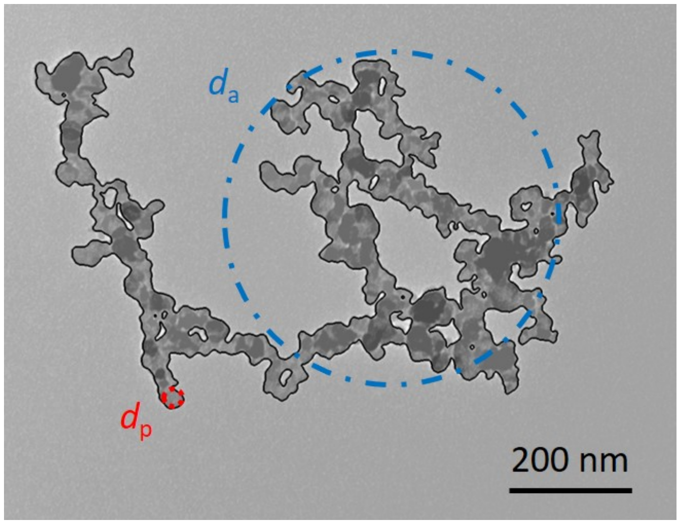

Figure 4.1: TEM image of a soot particle from the SCRE. The solid (black) line marks the boundary of the soot. The dash-dotted (blue) line marks the projected area equivalent diameter, d_a, and the dashed (red) line marks the primary particle diameter, d_p.

numerically or experimentally [22, 108]. Here, they are taken as 1.1 and 1.13 respectively, based on previous soot measurements from the same research engine [35].

It has been observed that larger aggregates tend to have larger primary particles, but only recently it has been proposed to use a power-law relation to describe the variation of the primary particle size with the aggregate diameter [146],

$$d_p = d_{p,100} \left(\frac{d_a[\mathrm{nm}]}{100} \right)^{D_{TEM}} \tag{4.2}$$

where some deviations from the correlation might occur at the very small aggregate size limits, as discussed in Section 4.5.1 (Figure 4.4). Here, $d_{p,100}$ is the average primary particle diameter for a 100 nm aggregate, and D_{TEM} is the correlation exponent. These parameters vary little over a wide range of soot sources [146], but in the present work they are determined from soot samples obtained from the SCRE. The resulting soot mass concentrations and sizes based on the variable primary particle model in Equation 4.2 are compared with constant primary particle morphology models in Sections 4.5.3 and 4.5.4. Equations 4.1 and 4.2 can be used to calculate the size and number of the primary particles in an aggregate of known d_a. The projected-area diameter is nearly equal to the mobility diameter (d_m, which can be measured with an SMPS) in the free molecular and well into the transition regimes [165]. Using the correlations recommended by Sorensen, the difference between d_a and d_m is negligible for mobility diameters below 200 nm, and might reach to up to 20% (underestimating d_m) for aggregates in the range 400-500 nm. It is, however, shown in Section 4.5.4 that errors in the light scattering inversion due to the $d_m \sim d_a$ assumption are in the order of 10% and have little influence on the validation process.

From the relations above and the model developed by Eggersdorfer et al., the relation between particle mass and mobility can be determined [47].

$$m_{agg} = \frac{\pi}{6} \rho_{eff} d_m^3 \tag{4.3}$$

$$\rho_{eff} = \frac{6 k_m}{\pi d_m^{D_m - 3}} \tag{4.4}$$

The soot effective density (ρ_{eff}) decreases with aggregate size for mass mobility exponents (D_m) less than 3 (which is the case for soot). Based on Equations 4.1 - 4.4, D_m and the mass-mobility pre-factor (k_m) are expressed in terms of the previously-introduced exponents and pre-factors,

$$D_m = 2D_\alpha (1 - D_{TEM}) + 3D_{TEM} \tag{4.5}$$

$$k_m = \frac{\pi}{6} \rho_p k_\alpha \left(\frac{d_{p,100}[\mathrm{nm}]}{100^{D_{TEM}}} \right)^{(3-2D_\alpha)} \tag{4.6}$$

where ρ_p is the density of the primary particles and is in the range of 1700 - 1800 kg/m^3 (1790 kg/m^3 is used here) [17, 151].

The relationship between the number of primary particles and the radius of gyration (R_g) of the aggregate is given by Meakin based on the fractal theory [132],

$$N_p = k_f \left(\frac{2R_g}{d_p} \right)^{D_f} \tag{4.7}$$

where D_f and k_f are the fractal dimension and pre-factor of an aggregate, respectively, and are determined here from TEM image analysis. Using Equations 4.1 - 4.7, the radius of gyration can be calculated for each mobility diameter. The numerical values of these parameters can change for different combustion regimes, fuels, or engines; thus, source-specific morphological characterization may be necessary for accurate light-scattering calculations. Further details about the soot sizing parameters are provided in Appendix B and Appendix D.

4.3.2 Soot light scattering modeling

The light scattering from soot aggregates (the main constituent of the diesel exhaust PM) is often modelled with the RDGFA model [44]. Compared to more detailed soot light scattering models such as the multi-sphere T-Matrix (MSTM) or the discrete dipole approximation (DDA), the RDGFA model can result in errors, as discussed in Chapter 2 with details in Appendix F, but has a significantly lower computational cost [133]. On average, a difference of 15% in the differential scattering cross section between the RDGFA and the MSTM calculations is expected based on the FEN laser wavelength (405 nm) and the soot sizes studied in this work (see Chapter 2 Figure 2.5). The light scattering cross section of an aggregate (σ_a) is expressed in terms of the light scattering cross sections of its constituent primary particles (σ_p),

$$\sigma_p(\theta) = \frac{x_p^6}{k^2} F(\mathbf{m}) \left(\sin^2\alpha + \cos^2\alpha \cos^2\theta \right) \Omega \tag{4.8}$$

$$\sigma_a(\theta) = N_p^2 \sigma_p(\theta) S(qR_g) \tag{4.9}$$

where the scattered light in a solid angle Ω positioned at angle θ relative to the incident light beam is considered. The scattering wave vector q is related to the incident wave number k and the scattering angle θ according to $q = 2k\sin(\theta/2)$. The light scattering cross section of the primary particles is based on the Rayleigh model assuming a linear polarization of the incident light (typical for laser diodes, as used here) at angle α out of the scattering plane (α was $\sim 45°$ for the FEN laser assembly), and x_p is the normalized particle size, i.e. $\frac{\pi d_p}{\lambda}$. In Equation 4.9, F is the Rayleigh scattering function, defined in Chapter 2 (Equation 2.8), where $\mathbf{m} = n + i\kappa$ is the complex refractive index of the soot primary particles [19, 82].

The structure factor S, described in Chapter 2 Equations 2.15 - 2.17 depends on the product qR_g and describes the angular distribution of the scattered light from an aggregate. Based on the model of Dobbins and Megaridis, S decreases exponentially with $q^2R_g^2$ For small qR_g, i.e. the Guinier regime, and is in the power-law regime for large qR_g. Assuming a smooth transition between the two regimes, the structure factor is described by Equation 4.10, where e is the Euler's number.

$$S(qR_g) = \begin{cases} \exp\left(-\frac{q^2R_g^2}{3}\right) & q^2R_g^2 \leq 1.5D_f \\ \left(\frac{3D_f}{2e}\right)^{\frac{D_f}{2}} (qR_g)^{-D_f} & q^2R_g^2 > 1.5D_f \end{cases} \tag{4.10}$$

Other functional forms that describe the soot structure factor are reviewed in Chapter 2. In this work, Equation 4.10 is used in the baseline RDGFA model and its results are compared with the structure factor proposed by Lin et al. (see Chapter 2 Equation 2.17) in Sections 4.5.3 and 4.5.4.

For comparison with experimental results, the light scattering cross section (σ_a) is converted into the mass scattering cross-section (MSC),

$$MSC_a(\theta) = \frac{\sigma_a(\theta)}{m} \tag{4.11}$$

where m is the mass of the aggregate. For polydisperse soot, the scattering cross section and mass for all aggregate sizes has to be considered. Previous studies of soot from the SCRE suggest a lognormal function describes the soot polydispersity reasonably well [65]. The light scattering, similar to particle mass, depends on the higher moments of the particle number distribution; thus, FEN light scattering inversion is characterized by the mass distribution parameters, namely the total mass concentration (C_m), the geometric mass mean diameter ($d_{m,g}$), and the geometric standard deviation ($\sigma_{m,g}$) in Equation 4.12,

$$\frac{dM}{d\ln d} = \frac{C_m}{\sqrt{2\pi}\ln\sigma_{m,g}} \exp\left(-\frac{(\ln d - \ln d_{m,g})^2}{2\ln^2\sigma_{m,g}}\right) \tag{4.12}$$

where $\frac{dM}{d\ln d}$ and C_m are the mass distribution function and the total mass concentration. It must be noted that when subscript "m,g" is used, σ refers to the geometric standard deviation of the mass distribution, and otherwise to the light scattering cross section. Samples of soot number distribution and their corresponding mass distribution for an engine point measured in this work are provided in Appendix D, and support the lognormal hypothesis.

The MSC of polydisperse soot, $MSC_{poly} = \frac{\sigma_{poly}}{m_{poly}}$, depends on the lognormal distribution parameters, $d_{m,g}$ and $\sigma_{m,g}$, and contains angular light scattering information. The scattered light power at angle θ, $P(\theta, d_{m,g}, \sigma_{m,g})$, is related to MSC_{poly}, the mass concentration C_m, and the FEN optical coefficient, Λ_{FEN}.

$$P(\theta, d_{m,g}, \sigma_{m,g}) = \Lambda_{FEN,\theta}[MSC(\theta, d_{m,g}, \sigma_{m,g})]_{poly} C_m \tag{4.13}$$

The ratio of the scattered light in directions θ_1 and θ_2, R_{θ_1/θ_2} is equal to the ratio of MSC's in the two angles (Equation 4.14), and hence is a function of $d_{m,g}$ and $\sigma_{m,g}$. Two such ratios, R_{θ_1/θ_2} and R_{θ_1/θ_3} can be obtained by measuring the scattered light at three angles, and utilized for determining $\sigma_{m,g}$ and $d_{m,g}$.

$$R_{\theta_1/\theta_2}(d_{m,g}, \sigma_{m,g}) = \frac{P(\theta_1, d_{m,g}, \sigma_{m,g})}{P(\theta_2, d_{m,g}, \sigma_{m,g})} = \frac{MSC(\theta_1, d_{m,g}, \sigma_{m,g})}{MSC(\theta_2, d_{m,g}, \sigma_{m,g})} \tag{4.14}$$

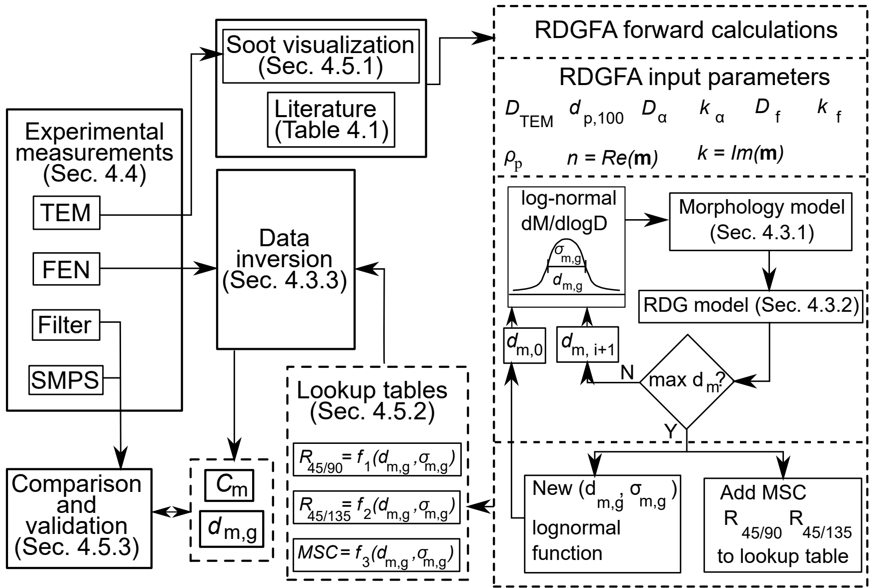

Figure 4.2: The three-angle light scattering inversion process for obtaining the soot mass concentration (C_m), the mass-weighted geometric mean mobility diameter ($d_{m,g}$), and standard deviation ($\sigma_{m,g}$). The lookup tables are generated with the RDGFA+EMH model.

4.3.3 Inversion algorithm

A method is proposed to convert light scattering measurements from the FEN into C_m, $d_{m,g}$, and $\sigma_{m,g}$. The light scattering ratios, $R_{45/90}$ and $R_{45/135}$, are used to find $d_{m,g}$ and $\sigma_{m,g}$ of polydisperse soot from the lookup tables.

The process of generating the lookup tables is shown in Figure 4.2. The parameters D_α, k_α, ρ_p, $\mathbf{m} = n + i\kappa$ were obtained from the literature as summarized in Table 4.1. The complex refractive index is a key parameter in the model and reported values vary widely. It may be that larger aggregates have higher mass-specific absorption cross-sections (MAC) and lower disordered-to-graphitic ratio (D/G) in their Raman spectra [8, 36], although these results are considered too preliminary to apply here. Studies in the past adopted the soot refractive index value of 1.95 + 0.79i suggested by [20]. This value, however, is recently shown to be inaccurate by review-

Table 4.1: The mean value and uncertainty of the soot parameters D_α, k_α, n, κ, ρ_p based on the literature. The literature sources considered for calculating the mean and uncertainty of each parameter is provided in Appendix B.

Morphology/RDGFA parameters	Mean value $\pm$ σ
D_α	1.1 $\pm$ 0.05
k_α	1.13 $\pm$ 0.1
n	1.6 $\pm$ 0.1
κ	0.8 $\pm$ 0.1
ρ_p [kg/m^3]	1790 $\pm$ 50

ing the experimental soot MAC measurements and the RDGFA absorption functions [118]. Hence, a value of $\mathbf{m}$ = (1.6$\pm$0.1) + (0.8$\pm$0.1)i, located in the valid range proposed by Liu et al. with uncertainties similar to those of their work, is adopted for the RDGFA calculations. This value is also shown to be in good agreement with DDA calculations for mature soot [94], and is similar to the values obtained in other studies [17, 205]. A summary of the literature reported parameters is provided in Appendix B.

The parameters D_{TEM}, $d_{p,100}$, D_f and k_f are obtained by analyzing the TEM images collected here (Section 4.5.1). Using these 9 parameters, the RDGFA model calculates the light scattering from polydisperse soot with size distribution parameters $d_{m,g}$ and $\sigma_{m,g}$ (forward process). The calculated $R_{45/90}$, $R_{45/135}$, and the MSC are tabulated as a function of $d_{m,g}$ and $\sigma_{m,g}$ (table row and column headers respectively). This process is repeated for different $d_{m,g}$ and $\sigma_{m,g}$ until $R_{45/90}$, $R_{45/135}$, and the MSC are calculated for the desired range of $d_{m,g}$ and $\sigma_{m,g}$ (80 - 700 nm and 1.4 - 2.0 respectively) and listed in the tables.

The measured scattered light intensities are converted into the absolute scattered light power (P_{45}, P_{90}, or P_{135}), and the ratios, $R_{45/90}$ and $R_{45/135}$, which are inputs to the data inversion block (center of Figure 4.2). The $\sigma_{m,g}$ and $d_{m,g}$ that minimize the difference between the measured (FEN) and tabulated $R_{45/90}$ and $R_{45/135}$ (i.e. minimize the ε function below) are determined. The step-by-step procedure for retrieving $\sigma_{m,g}$, $d_{m,g}$, and MSC is thus:

- Find a $d_{m,g}$ that, for each $\sigma_{m,g}$ column in the $R_{45/90}$ lookup table, has the closest $R_{45/90}$ value to the measured $R_{45/90}$, thereby construct the function $d_{45/90}(\sigma_{m,g})$.
- Repeat step 1 for $R_{45/135}$ and construct the function $d_{45/135}(\sigma_{m,g})$.
- Construct the error function $\varepsilon(\sigma_{m,g}) = \left|d_{45/90}(\sigma_{m,g}) - d_{45/135}(\sigma_{m,g})\right|$.
- Find the $\sigma_{m,g}$ for which the error function ε is minimized. This is assumed to be the geometric mean standard deviation of the sample.
- For this $\sigma_{m,g}$, the $d_{m,g}$ is taken as the average value of $d_{45/90}(\sigma_{m,g})$ and $d_{45/135}(\sigma_{m,g})$. The $d_{45/90}$ and the $d_{45/135}$ are ideally similar if the error function is zero, but in reality, due to measurement noise and the RDGFA approximations, the two are different.

The MSC is then calculated and used to convert the scattered light power (P_{45}) into the mass concentration C_m using

$$C_m = \frac{P_{45}}{\Lambda_{FEN,45} MSC_{45}} \tag{4.15}$$

where $\Lambda_{FEN,45}$ is the FEN optical coefficient for the 45° cone, and accounts for laser beam power, the probe length, and the optical efficiencies of the lenses and photodetectors. The numerical value of Λ_{FEN} for the 45°, 90°, and 135° is 8.6×10^{-5}, 7.2×10^{-5}, and 9.3×10^{-5} Wm respectively, and details of its measurement is provided in Appendix A.

4.4 Experimental setup

The performance of the FEN and the inversion method are assessed based on experimental soot measurements. The experiments are designed to generate engine soot over a range of conditions, characterize particle morphology, and validate the mass and sizes inferred from the light scattering signals.

The source of the soot particles is the SCRE, described in detail in Chapter 3. Samples from the post-surge-tank (PST) sampling point, with dilution ratios in the range 6 - 45, are measured with the instruments shown in Figure 4.3. The dilution ratio is measured based on the exhaust CO_2 concentration from the AVL CEB-II bench and the diluted CO_2 concentration is from the low-range CO_2 analyzer (LR-CO_2), as explained in Chapter 3. Part of the diluted sample is thermally denuded to remove the VOC and SVOC compounds before measurements with the FEN and the SMPS, and introduction to a thermophoretic TEM sampler.

Particle samples are collected onto fiber-reinforced PTFE filters (47 mm, Emfab by Pall Co.) for gravimetric weighing using a MTL filter weighing system (MT5, Mettler-Toledo). Prior to weighing, the filters were stored for 48 hours inside the device in a room with stabilized environmental conditions with relative humidity of 35% (±5%), pressure of 100 kPa (±5 kPa), and temperature of 23 °C (±2 °C). Details about the microbalance, the storage room, and the weighing process can be found in the supplemental information of [175]. Gravimetric filters were collected from an undenuded stream, due to the flowrate restrictions of the thermodenuder. Moreover, ex-situ TEM visualization is carried out to obtain more representative and source-specific soot parameters for the RDGFA model. In particular, the parameters D_f, D_{TEM}, k_f, and $d_{p,100}$ are obtained from the soot TEM images. Detailed specifications of the PM instruments are provided in Chapter 3, Table 3.3.

The mass concentration of the undenuded sample is slightly higher than the denuded one. Measurements with a Dusttrak-II before and after the thermodenuder, however, show the difference in mass concentration is small, only 10%, at the lowest dilution rates (∼7:1), largely due to the diffusion and thermophoretic particle losses (see Appendix C for details). The mass of VOC and SVOC contents removed from the PM sample in the thermodenuder is expected to be less than 5% as measured by [65] for SCRE mid-high combustion loads and high EGR rates, similar to the engine operating points in this study. Such low amount of volatile material does not affect the light scattering of engine soot based on [117]; however, undenuded soot light scat-

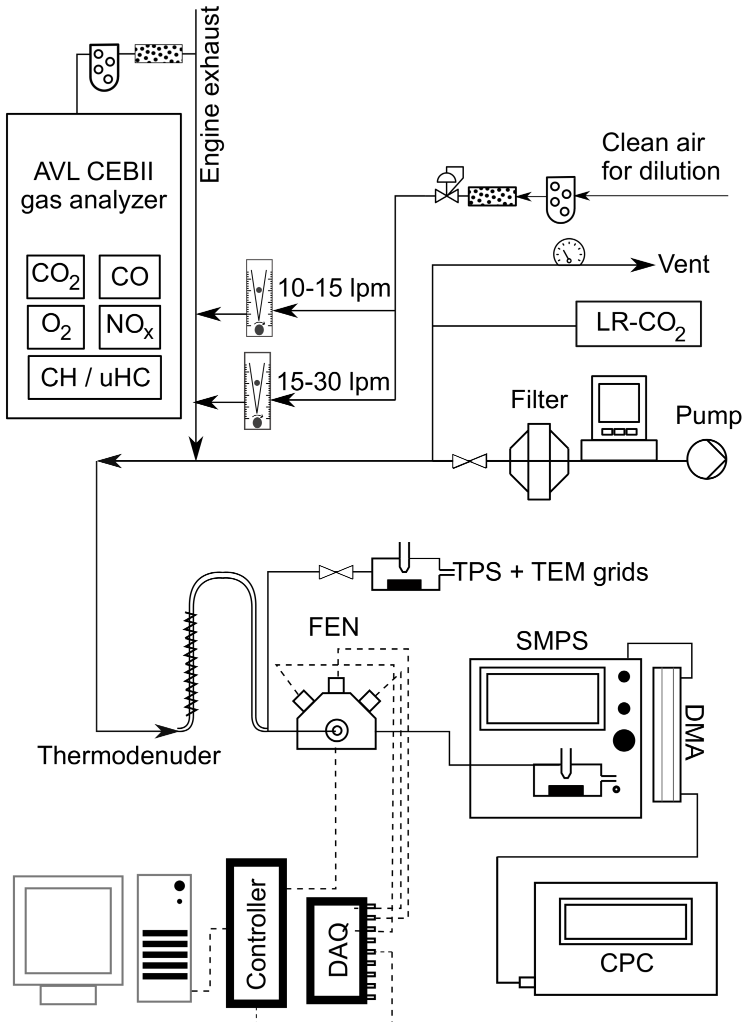

Figure 4.3: Experimental layout for characterizing the soot light scattering and morphology parameters and validating the inversion results. The SMPS and the filter assembly are used for the size and mass validation.

tering is not measured in this work, and the effect of the condensed volatiles on soot light scattering cannot be directly assessed.

4.5 Results and discussion

Here, the specifications of the engine operating points, the TEM soot analysis, and the obtained RDGFA parameters and the lookup tables are explained. The inverted FEN mass concentration and the mean mobility measurements are compared with the filters and the SMPS, and the sensitivity of the inverted results are discussed.

The measurements are conducted at four SCRE operating points (points 1, 2, 4, and 9 in Table 3.4, Chapter 3) with a range of sample dilution ratios, shown in Table 4.2, to generate a broad range of soot concentrations. The SCRE operating points selected for this investigation are intentionally designed to emit high soot concentrations. Namely, the baseline operating point, “Base-soot” in Table 4.2 (point 1), emits a soot concentration of about 75 mg/m^3 before dilution. The “High-soot” point (point 9) is designed to emit the highest soot concentration by increasing the combustion equivalence ratio to $\sim$ 0.85. The last two points “Low-soot-1” and “Low-soot-2” (points 4 and 2, respectively) have lower soot concentrations, 30 and 17 mg/m^3 respectively, by utilizing higher gas injection pressure ($\sim$ 230 bar), or lower equivalence ratio ($\phi \sim 0.55$) which were shown to reduce soot in previous works [128]. Up to 8 dilution rates are used at each of the operating points, where filters and TEM samples are collected at different dilution ratios for each engine point. The “Low-soot-2” point (point 2) has the lowest soot concentration before dilution; therefore, only one mild dilution rate is attempted so that the concentration of the sampled soot stays above the FEN detection limit ($\sim$1 mg/m^3).

4.5.1 TEM soot morphology results

The TEM soot images were used to evaluate the d_p, d_a, and R_g of each aggregate. Images of more than 1000 soot aggregates were analyzed to obtain the projected area and the average primary particle diameter in each

Table 4.2: The specifications of the experimental data points for diluted exhaust measurements.

Test ID	SCRE operating condition	Dilution ratio (DR)
1^a, 2^b, 3^a, $4^{a,b}$, 5^a, 6, 7^a, 8^a	Base-soot (point 1)	6.9^a, 8.0^b, 10^a, $13.6^{a,b}$, 14.3^a, 17.2, 20.8^a, 43.7^a
9^b, 10, $11^{a,b}$, 12, 13	High-soot (point 9)	9.2^b, 11.7, $17.7^{a,b}$, 14.5, 25.6
$14^{a,b}$, $15^{a,b}$, 16^a, 17, 18, 19	Low-soot-1 (point 4)	$8.3^{a,b}$, $10.5^{a,b}$, 11.3^a, 12.2, 12.6, 15.4
20^a	Low-soot-2 (point 2)	6.3^a

[a] Filters are collected for gravimetric measurements.
[b] TEM grid samples are collected.

aggregate using a pair correlation method [34]. On each grid, five different locations are selected to avoid size/morphology bias due to a single spot. The results of the soot image processing for the Base-soot point is shown in Figure 4.4 with circles. A least-square regression analysis of the d_p - d_a data in Figure 4.4, using the power-law type objective function in Equation 4.2 gives D_{TEM} and $d_{p,100}$. The D_{TEM} and $d_{p,100}$ values from the least-square regression and the resulting d_p - d_a correlation (solid line [blue]) is compared with the results of Graves et al. (dashed line [red]) which was obtained from the same engine but for a wider range of operating points. The TEM points follow the fit based on Equation 4.2 for the medium and large aggregate sizes, while a divergence from the fit occurs for small aggregates. This might be due to the fact that the correlation proposed in Equation 4.2, with D_{TEM} and $d_{p,100}$ parameters obtained from least-square regression shown in Figure 4.4, predicts a minimum d_a of 8.5 nm (assuming an aggregate with a single primary particle, and solving Equation 4.2 for d_p or d_a); thus, aggregates with d_p close to or less than 8.5 nm inevitably deviate from the fit. This, however, is not a major concern for the light scattering calculations, as the contribution of the small aggregates to the light scattering cross section and MSC of the whole sample is negligible.

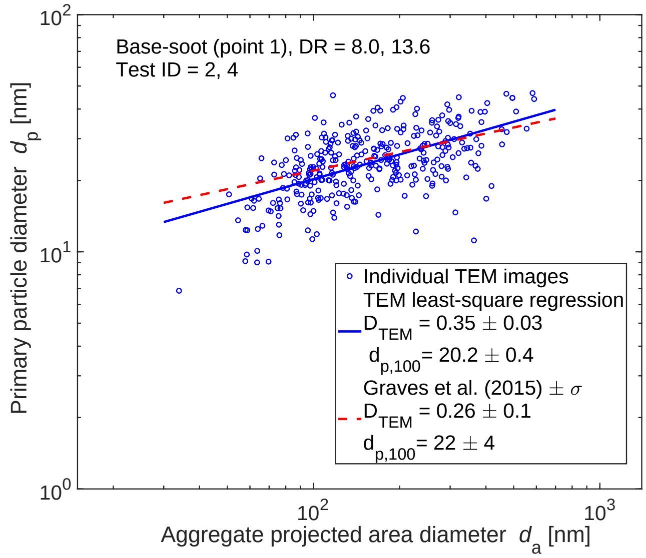

Figure 4.4: The variation of the soot primary particles with the aggregate projected area diameters for the "Base-soot" point (point 1). The circles represent individual soot TEM images. The d_p - d_a correlation based on Equation 4.2 is shown as the solid (blue) line with D_{TEM} and $d_{p,100}$ from the least-square regression of the TEM data in this study, and the dashed (red) line with D_{TEM} and $d_{p,100}$ from [65].

The variation of N_p vs $\frac{2R_g}{d_p}$ is shown in Figure 4.5, where the number of primary particles, calculated from Equation 4.1, vary with $\frac{2R_g}{d_p}$ according to Equation 4.7. The parameters D_f and k_f are obtained from least square regression fitting of an objective function shown in Equation 4.7 to the TEM data (circles [blue]), resulting in the solid (blue) line. The mean value and the uncertainties (1 sigma – 68% confidence interval) of the least-square fitting coefficients, i.e. the parameters D_{TEM}, $d_{p,100}$, D_f, and k_f, are compared with their corresponding mean value and range based on the literature in Figures 4.4 and 4.5. Here, the quantities $\frac{2R_g}{d_p}$ and N_p are calculated for each individual aggregate based on its projected area, radius of gyration, and primary particle diameter. It is, however, common in the literature to use the average primary particle diameter for all aggregates to calculate $\frac{2R_g}{d_p}$ and

N_p [47], which is observed to results in $\sim 5\%$ over-prediction of D_f (Table 4.3 footnotes). We expect that in order to determine the structure factor of each aggregate, as needed in the RDGFA model, it is more appropriate to use the average d_p from each aggregate, not the overall average. Inconsistent use of the correct averages may explain some discrepancies in the previously reported D_f values. Larger uncertainties in extracting D_f and k_f from projected soot images are still conceivable due to primary particle overlap [145] or using different image processing methodologies [3]. These artifacts are not investigated in this work; nonetheless, the sensitivity of the light scattering inversion to variations in fractal parameters due to low-mid levels of particle overlap described by Oh and Sorensen and different image-processing software reported by Altenhoff et al. are examined by artificially increasing the uncertainty bounds of k_f and D_f in Section 4.5.4.

Average values, either from TEM imaging (D_{TEM}, $d_{p,100}$, D_f, and k_f) or from the literature (D_α, k_α, n, κ, ρ_p), are used to generate the RDGFA lookup tables. The parameter values obtained from TEM imaging are listed in Table 4.3 for the "Base-soot", "High-soot", and "Low-soot-1" SCRE operating points, where the average of the three points is listed in the last column and considered for making the lookup tables. This is to ensure that the light scattering inversion is consistent throughout the data set. The mean values and the range of the rest of the parameters, namely D_α, k_α, n, κ, and ρ_p are obtained from the literature (Table 4.1).

4.5.2 The RDGFA lookup tables

The light scattering inversion is based on the $R_{45/90}$, $R_{45/135}$, and the MSC lookup tables generated using the RDGFA+EMH model with the soot parameters listed in Tables 4.1 and 4.3. The graphical representation of the lookup tables for $R_{45/90}$ and the MSC are shown in Figures 4.6 and 4.7, where each line in these figures represents a constant value of $\sigma_{m,g}$. Figure 4.6 shows that larger particles have higher $R_{45/90}$. This ratio also increases with $\sigma_{m,g}$ approximately up to the ratio of 4, at which point the trend is reversed. The elliptic markers in Figure 4.6 are placed to represent the range

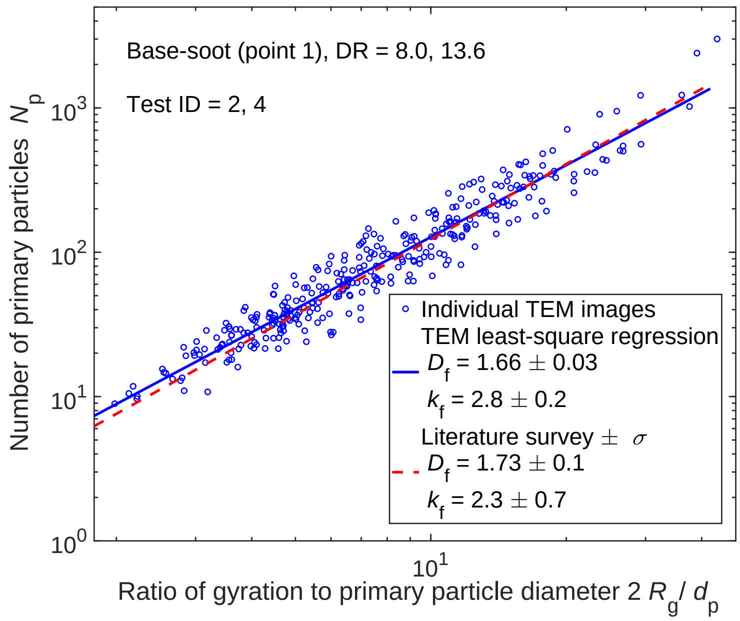

Figure 4.5: The variation of the number of primary particles vs $2R_g/d_p$ for the aggregates from the "Base-soot" point (point 1). The circles represent individual TEM soot images. The solid (blue) line shows the regression least-square fit to the TEM data. The dashed (red) line is the fractal correlation based on the average D_f and k_f compiled from various literature sources listed in Appendix B.

of ratios and corresponding $d_{m,g}$ values at each engine point. There are overlapping regions between different operating points in Figure 4.6, suggesting that similar soot diameters belonging to different SCRE points could be observed. When $R_{45/90}$ is close to 4, the $\sigma_{m,g}$ lines converge and the calculated mean mobility diameter is not dependent on $\sigma_{m,g}$; therefore, variations in the inverted $\sigma_{m,g}$ does not affect the inversion of $d_{m,g}$, indicating more robust size measurement is possible in this region. The ratios and diameters have a similar behavior in the $R_{45/135}$ table (not shown here).

Figure 4.7 shows the MSC lines for four different $\sigma_{m,g}$, which essentially overlap for $d_{m,g}$ larger than 200 nm. This indicates that the light scattering-

Table 4.3: The mean value and uncertainty of the soot parameters based on the least-square regression of the TEM data for D_{TEM}, $d_{p,100}$, D_f and k_f. The average value of each parameter based on the three SCRE points are shown in the last column, and used to generate the RDGFA lookup tables.

	SCRE points			Average
	Base-soot	High-soot	Low-soot-1	
D_{TEM}	0.35 ± 0.03	0.36 ± 0.02	0.38 ± 0.02	0.36 ± 0.03
$d_{p,100}$ [nm]	20.2 ± 0.4	19.5 ± 0.3	19.3 ± 0.3	19.7 ± 0.4
D_f	1.66[a] ± 0.03	1.67[a] ± 0.02	1.67[a] ± 0.03	1.67 ± 0.03
k_f	2.8 ± 0.2	2.8 ± 0.15	2.7 ± 0.15	2.8 ± 0.2

[a] Values are calculated by considering the d_p of each aggregate in the $2R_g/d_p$ ratio. If the average d_p of all aggregates is used instead, the calculated D_f is slightly higher, namely 1.72, 1.78, and 1.76 for the Base, High, and Low-soot-1 cases.

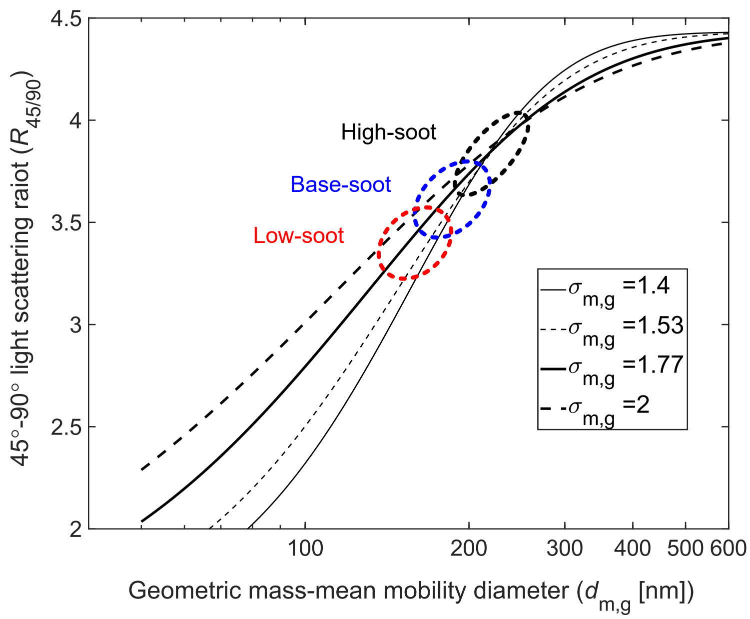

Figure 4.6: Graphical demonstration of the $R_{45/90}$ lookup table with four $\sigma_{m,g}$ values. The approximate range of the observed ratios from different SCRE points are marked with ellipses.

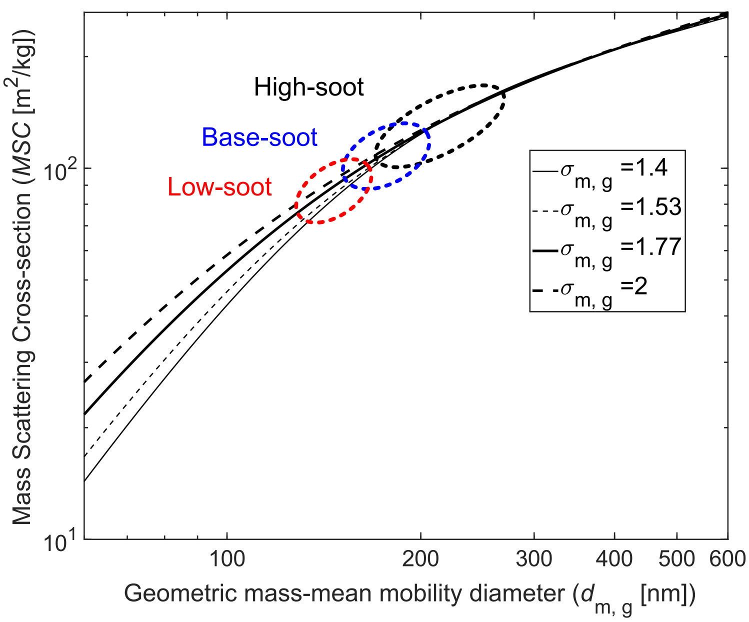

Figure 4.7: A graphical demonstration of the MSC lookup table with four $\sigma_{m,g}$ values. The approximate range of $d_{m,g}$ estimated from the light scattering ratios is marked with ellipses.

to-mass inversion is not directly affected by variations in $\sigma_{m,g}$. Nonetheless, errors in $\sigma_{m,g}$ affect the calculated mobility diameter and therefore propagate to mass inversion. The elliptical markers show the estimated MSC for each SCRE point based on a crude estimation of the expected $d_{m,g}$ from Figure 4.6. The detailed treatment of the results from the light scattering inversion are presented in the next section, and the marked regions here are only to highlight more crucial parts of the lookup tables. The MSC decreases rapidly at small $d_{m,g}$; thus, measuring polydisperse soot with mass-median mobility diameters less than 60 nm is not feasible, and re-optimized FEN hardware is necessary to extend the FEN detection range for smaller particles.

4.5.3 Validation of the FEN mass and size measurements

The light scattering is inverted to C_m and $d_{m,g}$ using the RDGFA+EMH kernels explained in Section 4.5.2. The inverted C_m and $d_{m,g}$ are compared with mass concentrations measured gravimetrically and mobility sizes measured with the SMPS (mass-based geometric mean size, calculated based on the SMPS scans and soot effective density). The RDGFA+EMH model which incorporates Equation 4.2 with the parameters listed in Tables 4.1 and 4.3, and the structure factor in Equation 4.10, generates the baseline lookup table used for the inversion (denoted as the baseline inversion). Extra lookup tables based on RDGFA with constant d_p , different physical and morphological parameters, or alternative RDGFA structure factors are generated too, and their inverted C_m and $d_{m,g}$ are compared with the baseline to evaluate the sensitivity of the FEN light scattering inversion.

Figure 4.8 shows the soot mass concentration inferred from light scattering and the gravimetric methods. The inversion is first carried out with the baseline RDGFA+EMH lookup table, shown with the symbols. A least-square regression linear fit (without an intercept) to the experimental data points is shown in Figure 4.8 as the thick solid (black) line and its slope is 0.9. As discussed earlier, the thermodenuder removes up to 10% of the mass before the FEN (particle loss to the walls), and considering this, a lower mass measurement with the FEN is expected. At test points where a filter sample is collected, several FEN light scattering and SMPS data are collected during the soot mass loading on the filters (10 to 20 minutes). The vertical error bars in Figure 4.8 are the standard deviation of the inverted C_m from the repeated FEN light scattering samples during the filter loading, and the horizontal error bars are based on the accuracy and repeatability of the gravimetric method. The accuracy of the microbalance machine, introduced in Section 4.4, is ± 6 μg and the repeatability of the gravimetric weighing process is ± 10 μg based on reweighing the filters 6 months to one year after the initial weighing. The accuracy and precision of the microbalance machine and the sample flowrate (measured with an Alicat Scientific MB-50SLPM-D/M5 mass flow meter), and variations in the dilution ratio account for $\sim$5-8% of the mean measured values. These artifacts constitute the horizontal error bars in Figure 4.8. Further details about the microbalance facility and the filter storage and weighing processes can be found in [175].

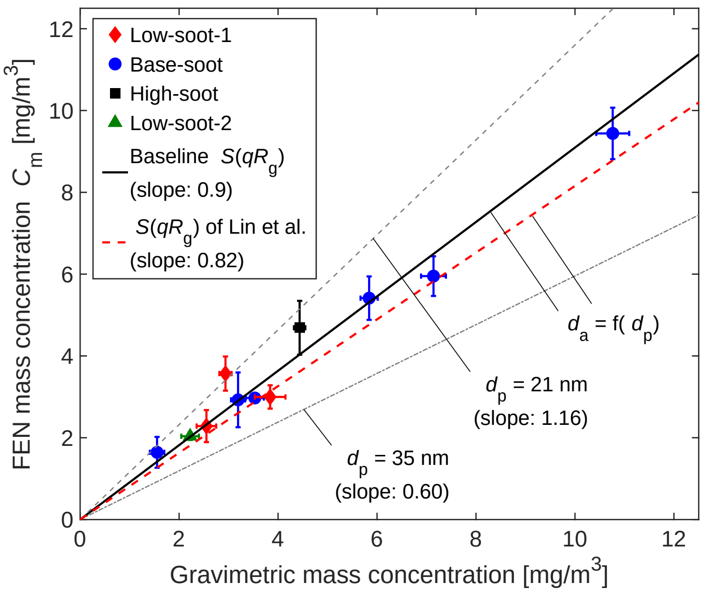

Figure 4.8: FEN C_m compared with the filter mass concentration. The symbols show the results with the baseline RDGFA structure factor [44] and the EMH morphology model. The thick solid (black) and dashed (red) lines are the linear least-square fits to the inverted results with the baseline and the Lin et al. models for $S(qR_g)$ respectively [114]. The thin dashed lines are linear fits for the inverted results with constant primary particle morphology models.

Lines fitted to constant-d_p inversions (omitting individual points for clarity) are also shown in Figure 4.8. Noting the large variation of d_p reported in the literature, here a d_p value of 35 nm from the work of Holve and Holve et al. is used, as it was based on engine-generated soot [77, 78]. Using this d_p, the inverted mass concentrations are, on average, 30% less than the baseline method (the dash-dotted least square fit with slope 0.6 compared to the baseline solid line with slope 0.9). A second inversion is done using the averaged d_p for all aggregates, 21 nm, as is calculated from Equation 4.16,

$$\bar{d}_{p,1} = \frac{\int d_p dN}{\int dN} \tag{4.16}$$

where d_p of aggregates is weighted by their number dN in the sample. Using a RDGFA kernel with a constant d_p of 21 nm ($\bar{d}_{p,1}$ obtained from Equation 4.16) results in inverted mass concentrations that are, on average, 28% higher than the baseline (the dashed least square linear fit with slope 1.16 compared to the baseline solid line with slope 0.9). Alternatively, a mean d_p can be evaluated by considering the number of primary particles of each aggregate,

$$\bar{d}_{p,2} = \frac{\int d_p N_p dN}{\int N_p dN} \tag{4.17}$$

where N_p and d_p are the number and diameter of primary particles in each aggregate. Using this method, the average d_p is shifted higher since larger aggregates contain more primary particles and contribute more to the average. The average primary particle diameter, $\bar{d}_{p,2}$ calculated based on Equation 4.17, is 25 nm, and results in closer C_m to the baseline (not shown), suggesting it might be a more representative value for constant-d_p RDGFA mass calculations. It, however, results in large differences in $d_{m,g}$ compared to the $d_{m,g}$ from the baseline lookup tables, and is further explained in the discussion of Figure 4.9.

In order to investigate the sensitivity of the results to the structural errors in the RDGFA model, inversion with a more elaborate structure factor, namely that of Lin et al. based on the formulation provided by Sorensen is carried out, and the results are shown as the thick dashed (red) lines in Figures 4.8 and 4.9 (symbols not shown). The trend lines in both figures are close to the baseline inversion with the structure factor of Dobbins and Megaridis in Equation 4.10. Variations due to using different RDGFA structure factors do exist; however, they result in minor changes compared to the variations when constant-d_p RDGFA models are used. The sensitivity of the FEN inverted mass concentration to d_p when the d_p - d_a correlation is ignored, is very large ($\pm$ 30%). This is important, as it simply indicates using a single value of d_p, either from the literature or the TEM data, can result in $\sim$ 30% difference in the inverted mass concentrations, due to the variations of d_p.

The $d_{m,g}$ measurement with the FEN light scattering is compared with the SMPS in Figure 4.9. The detailed SMPS scans, measured in a mobility diameter range of 14-680 nm, indicate unimodal lognormal number and mass distribution (the latter based on effective density), and are provided in Appendix H. There is qualitative agreement between the $d_{m,g}$ measured with the FEN and the SMPS, indicating that larger soot is produced at the higher sooting engine conditions (e.g. black squares). The light scattering inversion is also carried out with the constant-d_p lookup tables, but similar to Figure 4.8, only the least square linear fits (the gray thin dashes, omitting the symbols to avoid cluttering the figure) are shown. In the case of d_p = 35 nm, there is a noticeable difference with the baseline case. The least-square linear fit for d_p = 25 mm, calculated based on Equation 4.17, is located between the dashed lines for the 21 nm and the 35 nm primary particle diameters in Figure 4.9. This indicates that choosing a constant primary particle diameter of 25 nm for the RDGFA model results in errors in the inverted $d_{m,g}$, even though it produces inverted mass concentrations close to the baseline model. The trend line for the inverted $d_{m,g}$ using the lookup tables based on the RDGFA structure factor of Lin et al. is close to inversion with the baseline model. This is consistent with the observation in Figure 4.8 that the inversion is less affected by the RDGFA structure factor than the primary particle diameter in a constant-d_p RDGFA model.

Figure 4.9 contains the data corresponding to the repeats of the same point (i.e. fixed engine point and dilution factor) to show the variation of the data around the linear fit. The changes in the $d_{m,g}$ measured by the SMPS for a given operating condition indicates a changing sample, likely due to the variability of engine operation, and has been observed before [99]. The variation of the soot sample observed by the SMPS and FEN while loading a filter are also shown with the vertical error bars in Figure 4.8.

The slope of the linear trend line in Figure 4.9 is less than unity ($\sim$0.9); however, this cannot be explained by the presence of the thermodenuder as

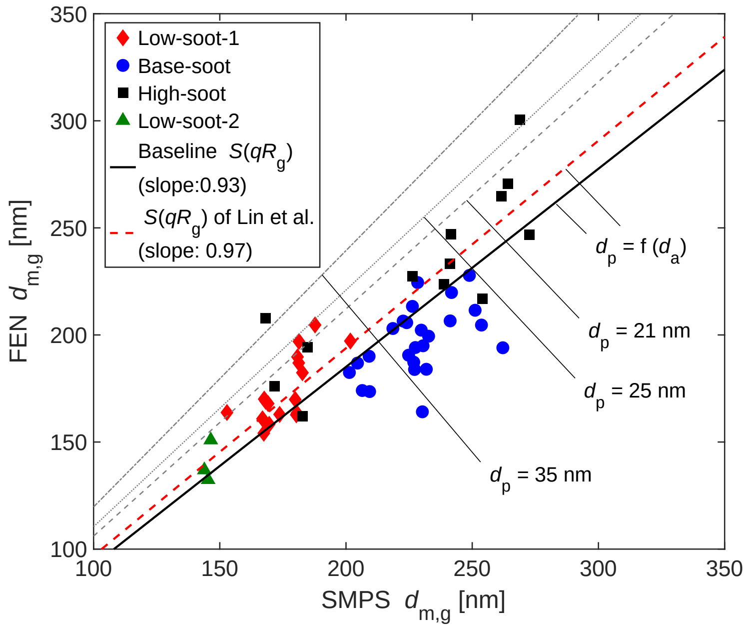

Figure 4.9: The $d_{m,g}$ from the FEN light scattering inversion compared with the $d_{m,g}$ from the SMPS. Different symbols (and colors), consistent with Figure 4.8, show different engine operating conditions. The thick solid (black) and dashed (red) lines are the least-square linear fits to the inverted results using the structure factor of Dobbins and Megaridis (baseline) and Lin et al. with slopes 0.93 and 0.97 respectively. The thin dashed lines are the linear fits to the inverted data with the constant-d_p lookup tables (symbols not shown).

both the FEN and the SMPS are placed after the thermodenuder. The low-soot points are located higher than the overall trend line, indicating that the FEN inversion produces more accurate $d_{m,g}$ for soot samples with smaller mass-median mobility diameters. The $d_{m,g}$ for the base and high-soot samples is under-predicted since the contributions of the larger aggregates is difficult to model accurately due to the increased uncertainty in the $d_m = d_a$ approximation outside of molecular flow regime [206], noisy SMPS measurements for large particles (an example is provided in Appendix H), and the sparsity of the TEM images for large aggregates. It is noteworthy that a nucleation peak (4-10 nm) due to condensed SVOC may emerge in the cooling section of the thermodenuder [188]. Such artifacts were not observed in our SMPS scans (see Appendix H), likely due to the its set size range (> 14 nm). It is, nevertheless, shown that the nucleated particles in a thermodenuder have a very minor effect on the mass distribution (and hence $d_{m,g}$) [5].

The results in this section demonstrate that FEN can provide quantitative soot mass concentration and qualitative mass-median mobility soot size measurements using the light scattering inversion method developed here. The inversion process also results in an estimate of $\sigma_{m,g}$. For the conditions here, the average value is $\sigma_{m,g} = 1.5 \pm 0.15$. While this range overlaps with $\sigma_{m,g}$ measured with the SMPS (1.65 ± 0.1), it appears to be sensitive to noise, and its measurement with the FEN is poor and likely not physically meaningful. Nonetheless, errors in $\sigma_{m,g}$ are cancelled due to averaging $d_{m,g}$ from the $R_{45/90}$ and $R_{45/135}$ ratios in step 5 of the inversion process (Section 4.3.3), resulting in more reliable and physically meaningful mass-median mobility diameters from light scattering measurements. The inverted results for $\sigma_{m,g}$ and a detailed discussion on the sensitivity of FEN $d_{m,g}$ and C_m to $\sigma_{m,g}$ are provided in Appendix E, and its summary is provided in Table 4.4 in the next section.

4.5.4 Sensitivity analysis

To characterize the sensitivity of the data inversion, new lookup tables are generated with perturbed RDGFA parameters (18 new tables). The mean value of the RDGFA parameters (used in the baseline kernel), and their variability ranges are shown in the third column of Table 4.4. The variability of $\mathbf{m} = n + i\kappa$ is $\pm$ 0.1 for the real and the imaginary parts of the refractive index, as listed in Table 4.1, and is obtained from the recent review paper by Liu et al. [118]. The nominal values of D_f, k_f, D_{TEM}, and $d_{p,100}$ are from TEM image analysis, as discussed in Section 4.5.1. It is shown, however, that these parameters inferred from TEM are subject to assumptions about the 3D structure of the aggregates, affected by overlap or sintering of primary particles [22, 145], and sensitive to image processing methods [3]. The range of variability of D_f and k_f is based on the results of Altenhoff et al. comparing different projected image processing methods, variations in D_{TEM} are based on the range reported by Olfert and Rogak for HPDI engine soot, and $d_{p,100}$ is based on the difference between d_p from manual sizing and the automatic PCM algorithm, similar to [3]. It might also be possible to obtain D_α and k_α from the projected 2D soot images; however, the uncertainties in the absence of stereo TEM images are too large. Instead, the values of D_α and k_α measured by Dastanpour et al. from SCRE HPDI soot are adopted, and their variations are considered for the sensitivity study in Table 4.4. The inversion sensitivities due to the approximation $d_m = d_a$ may also be examined by changing D_α, as different values of D_α change the relation between the aggregate projected-area diameter (d_a) and the number of primary particles (N_p) (Equation 4.1), hence change the exponent x in $d_m = N_p^x$ resulting in the variation of d_m for a given d_a. This could possibly bring the d_m values closer to the model given by Sorensen for large aggregates [183].

The FEN light scattering data are re-processed with each new look-up table, the inverted C_m and $d_{m,g}$ are compared with the baseline case, and the percentage changes in C_m and $d_{m,g}$ are listed in the corresponding rows and columns in Table 4.4. Here, Δ^+ and Δ^- are the percentage root mean square (RMS) variations of C_m or $d_{m,g}$ due to an increase or decrease (respectively) in each of the parameters in the second column of Table 4.4. The effects of perturbations are studied using two different methods. Firstly, the morphology parameters are varied independently and the resulting changes are grouped in the first rows of the table. Secondly, the morphology parameter pairs k_α–D_α and $d_{p,100}$–D_{TEM} are changed simultaneously. The soot effective density depends on D_α and k_α, and D_{TEM} and $d_{p,100}$ based on Equations 4.3 - 4.6, and varying these parameters independently can produce large discrepancy between the calculated mass concentration from the SMPS and the gravimetric filters. Thus, the suitability of the mean value and variations of D_α, k_α, D_{TEM}, and $d_{p,100}$ are evaluated by analyzing the SMPS mass concentration error function defined as, $E_{SMPS} = C_{m,SMPS} - C_{m,filter}$.

The contours of E_{SMPS} as a function of the morphology parameters are shown in Figure 4.10, confirming that the chosen morphology parameters for the RDGFA+EMH model are suitable (errors of $\sim$ -10% are consistent with the thermodenuder losses). The FEN light scattering inversion sensitivity to variations of D_α, k_α, D_{TEM}, and $d_{p,100}$ are first processed by independently varying one parameter at a time, shown with the asterisk (green) and cross (blue) symbols in Figure 4.10 along the horizontal and vertical axes, and the results are summarized in the first rows of Table 4.4. Secondly, the k_α-D_α and $d_{p,100}$-D_{TEM} pairs are varied along the iso-E_{SMPS} lines, shown with + symbols (black) in Figure 4.10, and the resulting variations in the FEN inverted C_m and $d_{m,g}$ are summarized in the second group of rows in Table 4.4. Independent variations produce larger changes in the FEN light scattering mass and mobility diameter. The information provided by the tandem SMPS and filter mass concentrations can be utilized to narrow the range of variations of the fractal parameters, thereby reducing the FEN light scattering inversion sensitivity.

The variations in k_f and independent variations in D_{TEM} produce considerably large variations in the inverted C_m in Table 4.4. The largest variation in C_m, however, is due to the imaginary part of the refractive index, κ, and the largest variation in the inverted $d_{m,g}$ is due to independent variations of D_α. The large variability of the inverted results is mainly caused by the wide range of literature values (e.g. for κ) for the RDGFA parameters, and the uncertainties in the image processing techniques. FEN C_m inversion sensitivity to the primary particle diameter in the constant-d_p RDGFA models are even larger, even if the TEM average (Equation 4.16) is used. In contrast, the perturbation of $d_{p,100}$ produces smaller variations in the inverted C_m and $d_{m,g}$ as the uncertainty of $d_{p,100}$ is less than the uncertainty of the average d_p of all aggregates (e.g. $\bar{d}_{p,1}$ and $\bar{d}_{p,2}$ in section 4.5.3). The sensitivity to $\sigma_{m,g}$ is also considered in the analysis and reported in Table 4.4, as its inversion from FEN light-scattering is particularly poor. Changes in C_m or $d_{m,g}$ due to uncertainties in $\sigma_{m,g}$, however, are modest, as any errors in the size recovered from one light scattering ratio (either $R_{45/90}$ or $R_{45/135}$) is partially corrected when averaged with the diameter recovered from the second ratio (details in the Appendix E). The structure factor in different RDGFA models is also considered, but does not affect the inverted results

Table 4.4: Sensitivity of the inverted mass concentration and mass-median mobility diameter to parameters used and assumptions made in the RDGFA+EMH light scattering calculations.

Sensitivity source	Symbol	Range	$\Delta^{-}C_m$ [%]	$\Delta^{+}C_m$ [%]	$\Delta^{-}d_{m,g}$ [%]	$\Delta^{+}d_{m,g}$ [%]
Morphology	D_f	1.67 ± 0.05	+6.9	-7.7	+8.6	-5.9
	k_f	2.8 ± 0.3	+15.0	-11.8	-5.4	+5.6
	D_{TEM}	0.36 ± 0.1	+10.2	-10.7	+2.1	-6.4
	$d_{p,100}$ [nm]	19.7 ± 1	+7.8	-7.0	-1.3	+1.4
	D_α	1.1 ± 0.05	-5.0	+4.8	+10.9	-9.0
	k_α	1.13 ± 0.1	-2.8	+2.0	+5.1	-4.0
Morphology (iso-E_{SMPS})	D_{TEM} ($d_{p,100}$ [nm])	0.36 ± 0.1 (20.7 - 18.7)	+2.8	-7.8	+3.1	-6.8
	D_α (k_α)	1.1 ± 0.05 (1.4 - 0.94)	+0.2	+1.0	-0.7	-1.5
Physical properties	n	1.6 ± 0.1	+3.4	-4.1	-	-
	κ	0.8 ± 0.1	+18.2	-14.8	-	-
	ρ_p [g/cm^3]	1.79 ± 0.05	-2.8	+2.8	-	-
Constant-d_p	$\bar{d}_p$ [nm]	21 - 35	+29	-35	+8.5	+20
$dM/d\ln d_m$	$\sigma_{m,g}$	1.4 - 2.0	±4.6		±6.3	
RDGFA	$S(qR_g)$	-	±5.3		±2.8	
Δ_{rms}, independent morphology parameters			-26, +29		-16, +17	
Δ_{rms}, D_{TEM} and D_α vary on iso-E_{SMPS}			-24, +26		-13, +13	
Δ_{rms}, constant d_p morphology model			-42, +39		-14, +26	

substantially.

The overall sensitivity is calculated based on the RMS of all ΔC_m and $\Delta d_{m,g}$ perturbations listed in Table 4.4. Based on this analysis, a 25% - 28% overall sensitivity in mass and 13% - 16% in size can be achieved with the FEN light scattering inversion using the lookup tables generated with the variable-d_p RDGFA+EMH model introduced in this work. When the d_p - d_a correlation is ignored, an additional 30% ΔC_m is introduced to the inverted mass concentration; adding this to the root mean square sum would increase the overall variability of the light scattering inversion to up to 40%.

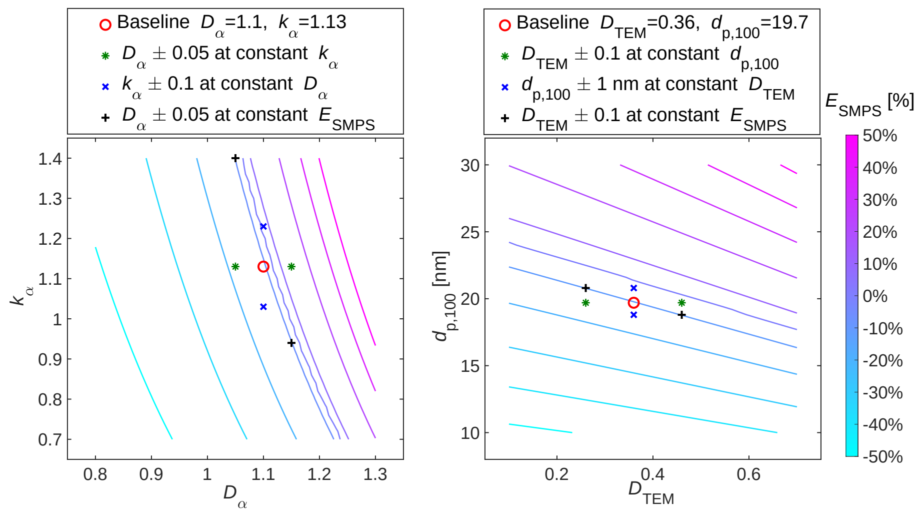

Figure 4.10: The SMPS mass concentration error (E_{SMPS}) contours for different values of k_α and D_α (left), and D_{TEM} and $d_{p,100}$ (right). The baseline parameters, obtained from the TEM analysis or the literature, are marked with circles (red). The asterisks (green) and crosses (blue) are variations of each parameter keeping the other one constant, and the + (black) symbols are variations along E_{SMPS} iso-lines.

4.6 Summary and conclusions

Soot measurement with the three-angle light scattering method of FEN is studied and an inversion methodology for obtaining the soot mass concentration (C_m) and mobility diameter ($d_{m,g}$) from the measured light scattering is developed. The FEN is made for fast engine-out soot measurement but the focus here is extending the method to provide quantitative measurements and validate it for steady, diluted exhaust concentrations. The inversion algorithm relies on lookup tables generated with the Rayleigh-Debye-Gans light scattering model for fractal aggregates (RDGFA) with a morphology model based on the external mixing hypothesis (EMH). The RDGFA+EMH model, for the first time, considers a correlation between the size of the primary particles and the aggregates on the soot light scattering, instead of using an average primary particle diameter to characterize all aggregates.

In the new approach, the mean primary particle diameter of 100 nm aggregates ($d_{p,100}$), and an exponent (D_{TEM}) are needed to model the primary particle size variation. Characterizing the soot by $d_{p,100}$ and D_{TEM} significantly reduces the sensitivity of inverted C_m and $d_{m,g}$ to the large range of primary particle diameters reported in the literature. Furthermore, using the observed primary particle size correlation produces more self-consistent results for both the mass and aggregate size, with no adjustments to any of the RDGFA parameters obtained from the literature.

The use of scaling relations between d_p and d_a allows one to estimate effective density, which connects the parameters used in the light scattering model (R_g) to the mobility diameter which is easily measured. Using suitable RDGFA parameters for generating the lookup tables, the inverted FEN mass concentration and mean mobility diameter compare closely with the reference instruments, where the average ratio of C_m to the gravimetric mass, or $d_{m,g}$ to the SMPS mobility diameter, is close to 1. A sensitivity analysis, however, shows that this ratio can vary by $\pm 25\%$ due to uncertainties in soot properties, most notably the wide range of soot refractive indices reported in the literature. In other light scattering instrumentation too, large sensitivities can arise from unknown physical properties. Here, by inverting the multi-angle light scattering measurements with the RDGFA+EMH model, this sensitivity is reduced significantly. In the next chapters, by combining this data inversion scheme with FEN's capability to sample soot after the engine exhaust valve, fast engine-out soot measurements can be obtained. This enables assessing the impacts of real-world engine transients and the cylinder-to-cylinder variability on PM emission and guide the environmental impact policy and engine development decisions.

Chapter 5

Characterization of the exhaust-port sampling system and FEN measurements[1]

5.1 Overview

The intended measurement of engine-out soot concentration with a single-cycle resolution requires a methodology to process the acquired FEN light-scattering traces, that considers the exhaust-port sampling conditions. To minimize measurement delays, soot is sampled near the exhaust-valve and transferred to the FEN using a sampling tube. The response time of such a measurement system depends on the transit time of gases in the exhaust pipe and inside the sampling tube into the FEN, and the mixing processes in between. The measured light-scattering signals are also affected by the

[1] Parts of this chapter are presented in a manuscript authored by Kheirkhah P, Kirchen P, and Rogak S., entitled "Measurement of cycle-resolved engine-out soot concentration from a diesel-pilot assisted natural gas direct-injection compression-ignition engine", accepted for publication in the International Journal of Engine Research. Necessary modifications are made for proper flow of the thesis.

thermo-mechanical conditions of the exhaust-port, such as fluctuating flow rates and strong pressure pulses. In this chapter, the effects of such phenomena are characterized to develop a signal-processing method for obtaining single-cycle soot concentrations based on FEN measurements.

We start by reviewing some key characteristics of flow in the exhaust of internal combustion engines and their effects on particle sampling. Similar studies of exhaust-port emissions measurement are reviewed and their methodologies for response-time characterization are compared with the methods employed in this study. The experimental techniques and the supporting analytical post-processing methods are explained in Section 5.4. A discussion of the FEN light scattering signatures and its response time is presented in Section 5.5, and is followed by a signal averaging scheme for representing single-cycle soot concentrations based on the FEN light scattering traces. The chapter ends with a summary of findings and conclusions of this investigation.

5.2 Introduction

The flow inside the engine exhaust path is intermittent, periodic, and contains strong pressure waves due to the opening and closing of exhaust valves [18, 173]. The temperature of the exhaust gases, their complex composition, fast flow fluctuations, and flow reversals makes direct velocity and flow measurements challenging, if not impossible. Limited applications of raw exhaust flow measurement using an ultrasonic velocimeter [15], and high-frequency pitot tubes [64, 140] are demonstrated in the literature, but are not suitable for crank-angle-resolved velocities. To provide cycle- and crank-angle-resolved exhaust velocity measurements, optical techniques, such as high-speed schlieren imaging, are used in literature. Using this technique, four distinct intra-cycle flow phases are identified and studied [207].

- Propagation of a pressure pulse from the valve throttle after the exhaust-valve opening (EVO).
- Expulsion of the high-pressure cylinder gases into the exhaust pipe

(blow-down).

- Reflection of the pressure waves, inducing a fluctuating pressure trace along the pipe.
- Backflow due to the piston downward motion before the bottom dead center (BDC).
- Slow outflow of the cylinder gases due to the piston upward motion, and attenuation of the pressure pulses due to reflections.

Effects of the exhaust flow and their interference with exhaust-port emission measurements deserves attention. The unburned hydrocarbon (uHD) measurement with fast flame ionization detectors (FFID), for example, depends on both the uHD concentration and flowrate [52]. Therefore, a sub-atmospheric constant-pressure chamber in the FFID demonstrated by Collings and Willey, is devised to filter the pressure and flow pulsations, and its sensitivity is assessed using a one-dimensional compressible plug-flow model [28, 31, 52]. Such models are commonly used to determine the response time of exhaust-port instruments, and are discussed in Sections 5.3.1 and 5.5.2.

The FEN light scattering signal depends on the PM concentration, and is theoretically independent of the sample flow rate inside the measurement chamber. Nonetheless, insights into the characteristics of the FEN sampling system, improves our understanding of its crank-angle-resolved light scattering signals, and facilitates the development of a cycle-resolved data-reduction procedure. Moreover, sampling of PM, unlike gaseous species, depends on the flow conditions at the inlet and inside the sampling tube. Here, the characteristics of the FEN exhaust-port light scattering traces are investigated from experimental measurements, and is compared with the results of flow modeling from literature.

5.3 Background

Better control and flexibility over a measurement demands physically distancing the measuring instruments from the emission source. In high-speed applications, however, a trade-off is required to maintain an acceptable time resolution by keeping the distances as short as possible. In such applications, a sample is extracted near the exhaust valve and quickly transported to an instrument using a short sampling tube. The gas dynamics considerations in the exhaust and their bearing on sample flow and the FEN PM measurements are briefly reviewed based on similar applications in the literature.

5.3.1 Exhaust-port gas sampling

The response time of an instrument for exhaust measurement depends on the spatial and temporal exhaust flow patterns, which requires highly instrumented exhaust pipes or complex optical measurements. Therefore, gas dynamics models, validated against high-speed pressure sensors placed along the exhaust path, are common [158]. The flow transit time (t_0) and the time constant (τ) are key parameters characterizing a fast exhaust-port instrument. Measurements may be considered cycle-resolved, if the combined effects of t_0 and τ does not reduce the response time of the system to below the single-cycle time threshold, t_{sc}, equal to 2 crank-shaft rotations or 720 crank-angle degrees (CAD) for a four-stroke engine such as the SCRE used here.

$$t_{sc}[\mathrm{ms}] = \frac{120,000}{N[\mathrm{rpm}]} \tag{5.1}$$

One-dimensional compressible plug flow models are suitable for describing the temporal and spatial features of flow along pipes and sampling tubes. The sample flowrate to the FFID described earlier, for instance, is determined based on a one-dimensional iso-thermal compressible flow model, resulting in [28],

$$\frac{\dot{m}}{A} = \sqrt{\frac{P_1^2 - P_2^2}{2RT\left(\frac{fL}{2d} + \ln\frac{P_1}{P_2}\right)}} \tag{5.2}$$

where, f is the friction coefficient, and P_1 and P_2 are the pressures at the inlet and outlet of the sampling tube. Using this model, and integrating the velocity along the tube, the sample transfer time may be computed,

$$t_0 = \frac{2d}{fu_1}\left(1-\left(\frac{P_2}{P_1}\right)+\frac{RT}{3u_1^2}\left[1-\left(\frac{P_2}{P_1}\right)^3\right]\right) \tag{5.3}$$

where, u_1 is the entrance velocity, assuming the flow is unchoked. Using the iso-thermal model, a total transfer duration of 80 - 300 CAD for pressure ratios between 2 and 3 are calculated at an engine speed of 900 rpm. In addition to this transit time, such measurements constitute a time constant due to mixing of the sample in axial direction (Taylor diffusion), considering a longitudinal diffusivity K in equation 5.4.

$$K\frac{\partial^2 C}{\partial x^2} = \frac{\partial C}{\partial t} \tag{5.4}$$

For a turbulent flow inside the sampling line, K depends only on the flow velocity, tube diameter, and the friction coefficient. Using this model, a 10% - 90% response time to a step change in concentration at the tube inlet may be determined using Equation 5.5.

$$\tau = 1.44Re^{-\frac{3}{16}}\frac{L}{\sqrt{RT}}\sqrt{\frac{P_1^2+P_2^2}{P_1^2-P_2^2}} \tag{5.5}$$

For the FEN sampling tube, considering the temperatures and pressures typically observed at the engine exhaust, a time constant of 8 ms is calculated from Equation 5.5. This model is revisited in Section 5.5 and compared to an experimentally-measured time constant.

More accurate results may be obtained from numerical models, such as with the commercial software GT-Power by Gamma Technologies [58], previously used to model the SCRE exhaust [185]. A schematic of the piping diagram used in this model is shown in the left panel of Figure 5.1, with the model components marked on the SCRE exhaust in the right panel. The fluctuating pressure traces observed with a fast exhaust sensor (PT in Figure 5.1) were successfully predicted by this model, although the magnitude of the GT-Power pressure peaks were slightly higher than measured. Mass flow rates of 0.8 - 0.9 kg/hr and velocities in the range of 70 - 90 m/s inside the

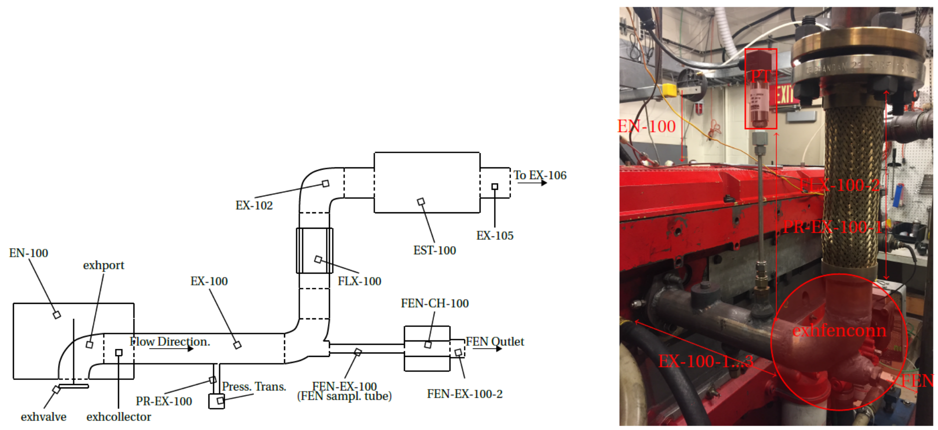

Figure 5.1: A schematic of the SCRE exhaust for GT-Power modeling (left). Components of the model are marked on a photo of the SCRE presented on the right panel showing the engine block, the exhaust pipe, the fast-response pressure sensor, and the FEN sampling port. Figure is adapted from [185], with author's permission.

FEN sampling tube are established from the model, resulting in t_0 of 10 - 12 ms and τ of 12 - 13 ms [185]. These figures, too, are compared with the experimental results of this work, the plug-flow model of [28], and the single-cycle time threshold (t_{sc}) in Section 5.5.

5.3.2 PM sampling considerations

Large flow rates and steep velocity gradients inside the SCRE exhaust and the FEN sampling tube impose losses on the sampled PM. To determine the effects of sampling losses on the FEN measurements, different PM loss mechanisms are reviewed. The inertial losses at the point of sampling (aspiration), and inside the sampling tube (wall impaction) are relevant in this application, due to the high velocities anticipated during the exhaust-port sampling. Other mechanisms, such as diffusion and thermophoretic losses, are relatively insignificant due to the short residence times in the sampling tube, but were considered for the diluted measurements in Appendix C .

At the point of sampling, large particles might be over or under-sampled, due to velocity gradients and curved streamlines. The aspiration efficiency is the ratio of PM concentration at the inlet of the sampling tube relative to the concentration in the main flow, and may be obtained from Equation 5.6 for a sampling tube positioned at 0° (head-on) relative to the flow [198].

$$\eta_{asp} = 1 + \left(\frac{U_0}{U} - 1\right)\left(1 - \frac{1}{1 + \left(2 + 0.617\frac{U}{U_0}\right) St}\right) \tag{5.6}$$

The Stokes number, St in Equation 5.6, is defined earlier in Equation 2.22, Chapter 2, and U_0 and U are the velocities in the main flow and the sampler. The compounded transmission efficiency of the sampling system also depends on the inertial losses inside the sampling tube. The inertial sampling efficiency in a bent turbulent flow is relevant to the sampling configuration implemented here, and is computed based on the correlation suggested by Pui et al.,

$$\eta_{\text{bend,inert}} = 10^{(-0.963 N_b St)} \tag{5.7}$$

where, the efficiency is expressed as a function of the Stokes number and the number of 90° bends, N_b, in the sampling tube [162]. The sampler used here is a 360° coiled tube; thus, N_b is 4.

PM loss factors for different particle diameters are calculated based on Equations 5.6 - 5.7 for a baseline SCRE exhaust condition, presented in Section 5.5, where its effects on the light scattering traces and FEN mass calculations are discussed.

5.4 Methodology

Here, the methods developed for characterizing the exhaust-port FEN light-scattering signals are elaborated. These include the experimental and analytical procedures employed to determine the response-time of the FEN, and used for single-cycle data reduction based on the phenomenology of the exhaust-port sampling.

5.4.1 Experimental procedures

The experiments are conducted with the FEN sampling at the SCRE exhaust-port shown in Figure 3.2. The sampling tube used here has an outer diameter of 3.18 mm, a wall thickness of 0.65 mm, and is 0.8 m long. A high-speed pressure transducer (Omega PX4201-100GV), with a response time of 0.2 ms is mounted at the end of a 20 cm, 6.35 mm nominal outer diameter stainless steel tube connected to the exhaust pipe 25 cm downstream of the engine exhaust valve, as shown in Figure 5.1. This arrangement is adopted to protect the sensor against the hot exhaust gases. The pressure phase shift due to the length of the mounting tube is 0.4 ms, equal to 4 - 6 CAD at a 1500 rpm engine speed (maximum speed in this study). The phasing of the pressure measured with this sensor is roughly similar to its phasing at the inlet of the FEN sampling tube, as both are similarly distanced from the exhaust valve. The FEN light scattering and the exhaust pressure are synchronously recorded with a 0.5 CAD resolution on the same DAQ described in Chapter 3.

Here, the engine points 2, 3, 5, 6, 7, and 8 of the main matrix (Table 3.4, Chapter 3), are first operated in continuous mode to characterize the crank-angle-resolved FEN light scattering signatures, and are repeated in “skip-firing” mode for response time measurement. In the latter, a decaying light scattering signal due to disrupted fuel injection is processed to calculate the flow transit time and the time constant of the measurement system. The SCRE operating points in Table 5.1 are tested during the fall of 2019, points 6 and 8 are repeated from earlier measurements for a GT-Power model validation in 2017 [185], with point 8 originally tested in 2016 to demonstrate the concept of FEN (Figure 3.6 in Chapter 3 [99]).

5.4.2 Characterization of the crank-angle-resolved exhaust measurements

To better understand the relation between the acquired FEN signals and the exhaust sampling conditions, the crank-angle-resolved light-scattering and exhaust pressure traces are analyzed. A stable background light intensity

Table 5.1: SCRE operating points for characterizing the light scattering signatures of the FEN and measuring its response time.

Engine point	Engine speed [RPM]	GIMEP [bar]	θ_{50} [°aTDC]	ϕ [-]	EGR [%]	P_{exh} [kPa-a]
2	1350	16.0	12.7	0.55	12	285
3	1350	15.5	15.5	0.54	13	270
5	1350	16.0	20.0	0.65	15	268
6†	1500	11.8	11.2	0.55	20	222
7†	1200	12.2	10.0	0.70	0	196
8†‡	890	9.9	11.3	0.53	46	223

† Previously tested for GT-Power model validation of [185].

‡ Previously operated for the FEN proof-of-concept [99].

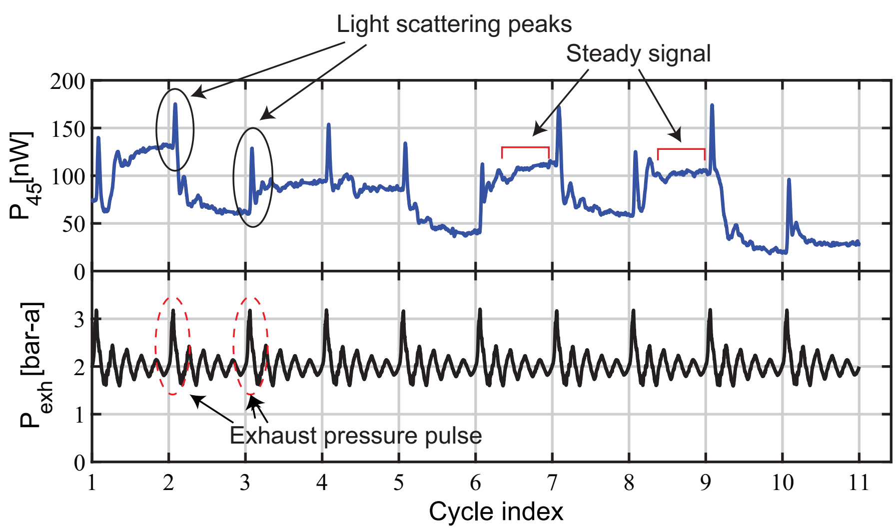

Figure 5.2: P_{45} and P_{exh} crank angle series for 10 consecutive engine cycles. Repeatable features, such as strong consistent peaks in the light scattering and the pressure traces, and flat tails in light scattering signals are marked.

signal during motored engine operation was noted [99], and subtracted from the signals acquired during fired operation, presented here. The background-corrected FEN light scattering intensity on its 45° photodetector, P_{45}, and the exhaust port pressure, P_{exh} from the Omega PX4201 sensor, are shown for 10 consecutive cycles in Figure 5.2, where the EVO occurrences are

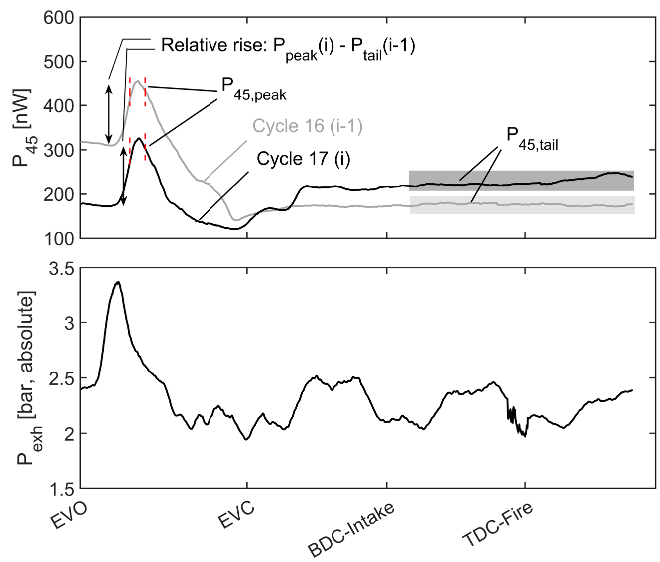

Figure 5.3: P_{45} and P_{exh} for cycles 16 (grey) and 17 (black) during a point 6 test, shown on a 720 CAD engine cycle interval, starting at EVO. The consecutive cycles have identical P_{exh}, but different P_{45} traces. The intervals corresponding to the peaks and tails of the light scattering signatures are marked.

marked with vertical dashes. The exhaust pressure fluctuations are very similar among cycles, the light scattering, too, has consistent features such as strong peaks after each EVO; nevertheless, its magnitude can vary from one cycle to the next. Similar features were also observed in a preliminary proof-of-concept study on the same engine [99]. The light scattering peaks after each EVO are shortly ($\sim 20°$) after the P_{exh} peaks. This suggests that the peaks are due to a strong pressure pulse generated by the EVO, and not the engine exhaust gases which arrive at the FEN much later (as discussed below), and not due to artifacts such as electrical noise from the injector driver which only occurs close to the combustion top dead center (TDC), nearly 500 crank-angle degrees (CAD) after the light-scattering and pressure peaks (injector electrical noise can be spotted on the P_{exh} trace close to TDC in Figure 5.3).

Details of the light scattering signals are better addressed on a 720 CAD interval, starting from EVO. The crank-angle-resolved signatures for two consecutive cycles (16 and 17) from point 6 are shown in Figure 5.3. As observed, the signals demonstrate a unique signature with a strong peak shortly after EVO followed by a trough and a constant flat tail for the remainder of the cycle. The mechanism by which the pressure pulse generates a peak in the scattering intensity may be explained by several phenomena which are explored in Section 5.5.1. The signal intensity prior to the peak is similar to the tail of the previous cycle. For example, the before-the-peak P_{45} for cycle 17 in Figure 5.3 is approximately 180 nW, similar to the magnitude of the tail of cycle 16. Moreover, the relative increase of the light intensity during the peaks (rise from the previous tail, as shown in Figure 5.2) is seemingly repeatable between different cycles for a given engine operating condition, and is further discussed in Section 5.5.1. Despite early variations after the EVO, light scattering traces are steady for the remainder of the cycle (marked with horizontal boxes), indicating a constant soot concentration inside the FEN volume during this period.

To gain a better insight into the characteristics of the light scattering traces, and the effects of exhaust and sampling tube conditions on the signals, the response of the FEN to sudden and deliberate changes in exhaust soot concentration is analyzed. These controlled changes are brought about by operating the SCRE in ”skip-firing” mode, by temporarily disabling and then re-enabling the fuel injection. Through this process, it is possible to separate the effects of the current engine cycle from the previous cycles, and thereby calculating the sample transfer delay and time constant.

During the skip-firing operation, the FEN signal decreases shortly after the fuel injection is terminated, as clean air displaces the old combustion gases in the SCRE exhaust pipe (roughly 40 cm), and enters and travels inside the sampling tube to reach the FEN. The effect of this transition on the light scattering signals is shown in Figure 5.4. By disabling the injection at cycle 1264, the light scattering signal starts to decrease after a short delay (t_0). The characteristic peak is absent during the motored cycles, presumably due to low in-cylinder pressure, and the signal decreases to zero

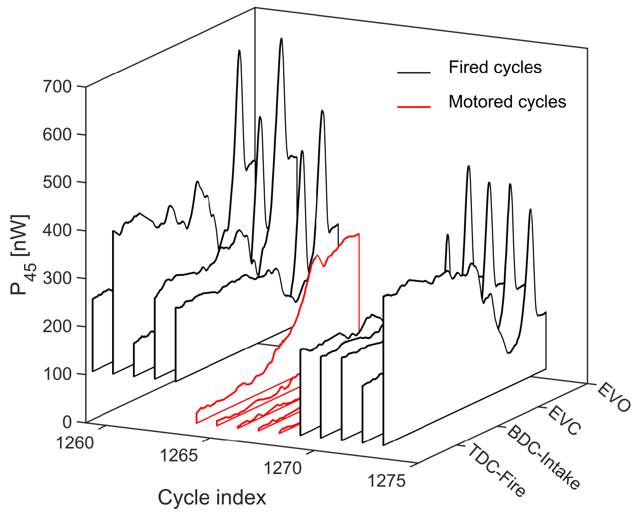

Figure 5.4: The FEN light scattering traces during a point 2 test, showing a sequence of cycles containing a skip-firing event, cycles 1264 - 1268 shown in red.

(which correspond to clean air due to background correction), resembling a first-order decay. The initial non-zero signal tail during the first few motored cycles is likely due to the EGR flow rate, which produces light scattering above the clean air background levels. During the motored cycles 1264 - 1268, this DC offset gradually decays to zero, as clean air displaces the stale EGR gases, and slowly reappears after resuming the fuel-injection. The skip-firing sequences are repeated multiple times to obtain sufficient statistics for the response-time calculation at each operating point.

Results of the intra-cycle light-scattering correlations are presented in Section 5.5.1, and are explained based on the exhaust-port phenomena. An analysis of the skip-firing results are provided in Section 5.5.2, and is compared with the GT-Power results of [185].

5.5 Results and discussion

Here, the FEN light scattering traces are analyzed with the purpose of devising a method of representing single-cycle soot concentrations based on the measured crank-angle-resolved data. Correlations between the peaks and tails of the signals are used to examine the underlying mechanisms producing the light scattering patterns seen here. Following this, the results of the skip-firing tests are presented, the procedures for extracting the transfer time and time constant from the light-scattering traces is explained, and their results are presented and discussed.

5.5.1 Phenomenological description of the exhaust-port FEN measurements

The characteristics of the FEN exhaust-port measurements may be better understood by considering the intra-cycle correlations in the signals. Namely, correlations between the peaks and tails of the light-scattering traces for neighbouring cycles can provide some insight into the underlying mechanisms affecting the exhaust-port sampling. The light scattering traces are first filtered using a 10 CAD moving average to remove noise. The signal peak after the EVO, labeled $P_{45,peak}$ in Figure 5.3, is detected using the "findpeaks" function in MATLAB. The tails are characterized by averaging the light scattering traces between $\theta = 500$ CAD aEVO until the end of the cycle at 720 CAD aEVO, labeled $P_{45,tail}$. This averaging window is chosen to remove the effects of the early variations, and is consistent with the results of response time measurements in Section 5.5.2.

To understand the causes of the repeating light-scattering peaks, we, first, examine the prominence of $P_{45,peak}$, i.e. its rise relative to the light scattering tail of the preceding cycle, which seems to be invariant from Figure 5.3. This is further examined by considering the correlations between $P_{45,tail}$ and $P_{45,peak}$ for all consecutive cycles "i-1" and "i" shown on the left panels of Figure 5.5 for SCRE points 6 and 8. Here, the dots represent individual cycles, and the lines are the least-square regression fits to the points during each test. The black solid lines show the regression results

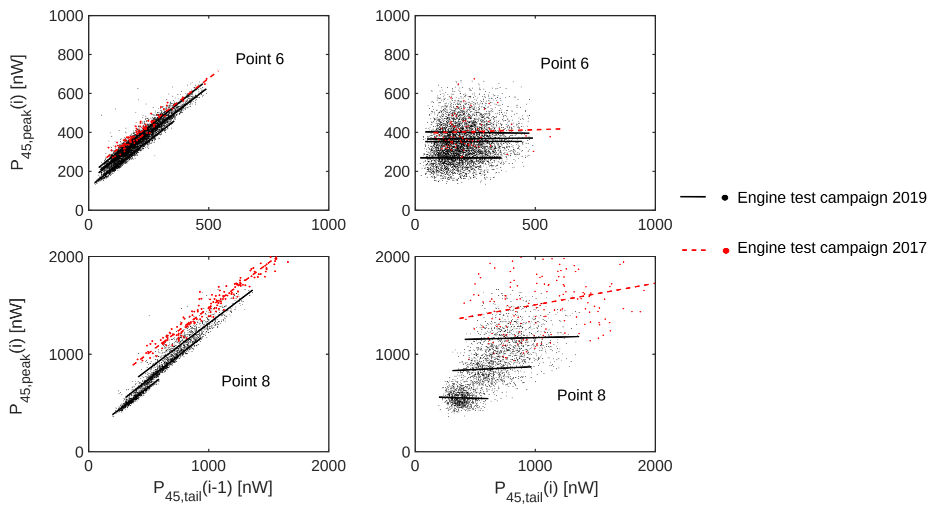

Figure 5.5: The correlations between the light scattering peak from cycle "i", and the averaged background tail from the previous cycle "i-1" (left), and the averaged tail from the current cycle "i" (right), shown on the abscissa. The plotted data belong to points 6 (top) and 8 (bottom) run in 2017 (red-dashed) and 2019 (black-solid).

from the campaign of 2019, where each engine operating point contains at least 1500 cycles. Different lines in Figure 5.5 represent repetitions of each operating point to ensure repeatability of the data. The red dashed lines are from engine tests during the campaign of 2017, each containing only 45 - 50 cycles due to the limitations of data acquisition hardware. The regression parameters, namely the R^2, the slope, and the y-intercept of the lines are summarized Table 5.2.

As shown in Figure 5.5 and Table 5.2, the correlations between $P_{45,peak}(i)$ and $P_{45,tail}(i-1)$, where "i" symbolically denotes the cycle index, are particularly strong with R^2 in the range 0.86 - 0.96. The slopes of the lines are very close to unity (0.95), and do not change much between the repeated tests. The results of the 2017 campaign indicate similar trends. The regression R^2 values, however, were slightly weaker for this dataset, likely due to the smaller population of cycles per operating point. The correlations between

Table 5.2: The correlation parameters between the crank-angle light scattering peaks and tails of successive cycles (columns on the left) and the same cycles (columns on the right) for SCRE points 6 and 8. The last column denotes the mean light scattering for each operating point. Numbers in brackets are from the measurement campaign of 2017 (red dots in Figure 5.5).

Engine point	$P_{45,peak}(i)$ - $P_{45,tail}(i-1)$			$P_{45,peak}(i)$ - $P_{45,tail}(i)$			$\bar{P}_{45}$ [nW]
	R^2	slope	y-int. [nW]	R^2	slope	y-int. [nW]	
6	0.95 (0.79)	0.96 (0.96)	120-177 (195)	< 0.001 (0.44)	-0.01 (0.04)	270-400 (394)	200±25
8	0.86 (0.87)	0.95 (0.93)	195-380 (547)	0.002 (0.46)	0.03 (0.22)	570-1100 (1284)	600±180

$P_{45,peak}(i)$ and $P_{45,tail}(i)$ for a same cycle, on the other hand, are significantly weaker, with R^2 in the range 0.001 - 0.002, and near-zero slopes, indicating that the two quantities are simply not correlated.

Since the slopes of $P_{45,tail}(i-1)$ - $P_{45,peak}(i)$ lines are close to one, the difference between $P_{45,peak}(i)$ and $P_{45,tail}(i-1)$ (the relative rise, shown in Figure 5.3) is similar for different cycles and is equal to the y-intercept of the regression lines listed in Table 5.2. These observations suggest that the peaks are generated by a repeatable mechanism, such as by the exhaust pressure waves acting on the flow in the sampling tube.

The exact mechanism that generates this effect is unclear; however, some hypotheses can be examined:

- Firstly, enhanced Rayleigh scattering of gas molecules due to the passing of a pressure or shock wave can be considered. The average Rayleigh scattering due to exhaust gases at 200 °C, assuming a refractive index of 1.0002 [152], and an average molecular diameter of 0.4 nm [30], is only 1 - 3 nW on the photodetectors. Compressions by factors of 10 or more, only possible with strong shock waves, are required to justify the peaks observed in the experiments, which are unrealistic for engine exhaust.

- Secondly, a compressed gas front in a pressure wave increases the PM concentration due to a pressure ratio effect,

$$C_m^+ = C_{m,0} \frac{P^+}{P_0} \tag{5.8}$$

where P^+ is the increased pressure at the wave front, and P_0 is the background pressure inside the FEN chamber. This effect, however, implies a scaling relation between $P_{45,peak}(i)$ and $P_{45,tail}(i-1)$, which is not consistent with the correlations observed in Figure 5.5 and Table 5.2, which indicate the two parameters are different by an offset and not a proportionality factor.

- Thirdly, a pressure wave at the tip of the sampling tube might enhance the aspiration efficiency by reducing the velocity ratio according to Equation 5.6 shown in Figure 5.6. Nonetheless, this effect, too, does not justify the offset relation between $P_{45,peak}(i)$ and $P_{45,tail}(i-1)$, and only affects super-micron particles that are uncommon for fresh HPDI soot (see Chapter 6). More importantly, this mechanism depends on the advection of the particles in the sampling tube, which, as discussed in Section 5.5.2, requires much longer delays compared to the EVO - $P_{45,peak}$ intervals observed in Figure 5.3.

A plausible mechanism that can generate the effects observed in Figure 5.5 is the resuspension of wall-deposited PM into the flow. This mechanism does not require unrealistically large pressure ratios observed only in strong shock waves, and can produce the offset-type correlations seen here. A repeatable, relatively strong, pressure wave resuspends approximately the same amount of deposited PM into the flow in each cycle, thereby producing a light scattering peak that has a constant offset from the tail of its preceding cycle (i.e., constant $P_{45,peak}(i) - P_{45,tail}(i-1)$ in Figure 5.3). The offset depends on the amount of freshly deposited soot on the walls which is likely correlated to the mean soot concentration during an operating point (i.e. $\bar{P}_{45}$ in Table 5.2). This effect can be observed in table 5.2, where the y-intercept of the correlations (i.e. average relative rise of the peaks) is smaller for point

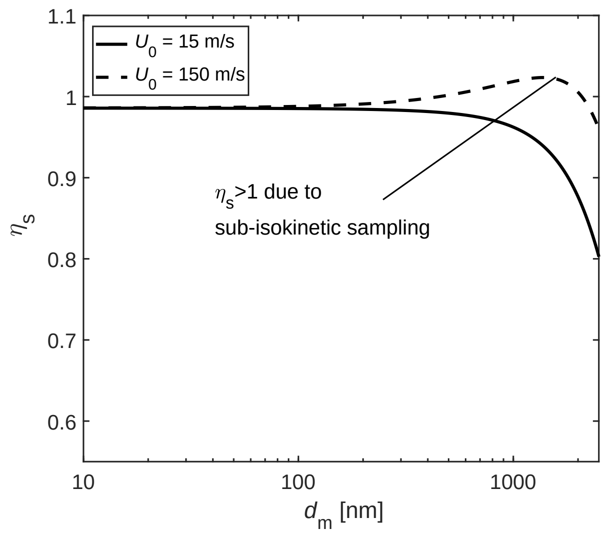

Figure 5.6: Exhaust-port overall PM sampling efficiency considering aspiration effects and wall impaction losses inside the FEN sampling tube, modeled in Equations 5.6 - 5.7.

6 which has a lower mean value of P_{45}, and large for point 8 with a higher mean P_{45}.

As shown in the next chapter (Figure 6.5), a sharp peak in $d_{m,g}$ coincident with the light-intensity peaks after EVO is consistent with the notion that these patterns are caused by resuspension of wall deposits, which tend to be larger. The particles that produce this artifact are presumably shed very close to the FEN measurement volume, and cannot be captured by means such as an impactor or a cyclone placed in the sampling line. Besides, such devices negatively impact the FEN response time, which is critical for this study. A redesigned sampling tube using a perforated inlet can attenuate the EVO pressure pulses, while maintaining the favourable fast sample transfer characteristics that are essential to our method, and is considered as a future modification to the FEN. These intra-cycle correlations are examined to better understand the underlying mechanisms that generate the observed patterns in the light scattering traces. The description provided here is complemented by considering the FEN response time during the transient skip-fired engine operation.

5.5.2 Response time of the exhaust-port measurement system

To verify that single-cycle information can, indeed, be obtained from the exhaust-port FEN light scattering measurements, a series of skip-firing tests are conducted, demonstrated in Figures 5.4 and 5.7. The exhaust transfer delay, t_0 in ms or θ_0 in CAD, is the time or crank-angle duration it takes the gases to travel from the exhaust valve to the FEN. Moreover, τ in ms, and δ in CAD, is the first-order time constant of the system, presumably due to mixing. These are obtained from least-square regression fitting of a delayed first-order response function, shown in Equation 5.9, to the light scattering signal.

$$P_{45}(\theta) = P_{45,0} \exp\left(-\frac{\theta-\theta_0}{\delta}\right) u(\theta-\theta_0) \tag{5.9}$$

Here, $P_{45,0}$ is the light scattering signal prior to the first motored cycle (defined similar to $P_{45,tail}(i-1)$ during continuous firing), and $u(\theta-\theta_0)$ is a unit step function (1 if $\theta < \theta_0$, and 0 otherwise) that models the flow transfer delay to the FEN. The crank-angle delay, θ_0, and time constant, δ in CAD, are marked in Figure 5.7. The original FEN P_{45} signal is the solid blue line and the fitted first-order response is shown with dashed red line for demonstration. Here, a skip-firing sequence containing 8 motored cycles (cycles 392 - 399) is shown, but only the first three cycles are considered for the least-square fit, so that the regression is not heavily influenced by the background tail. The measurement response, θ_{resp} or t_{resp}, is the exhaust transfer delay plus two time constants, defined in Equation 5.10.

$$\theta_{resp} = \theta_0 + 2\delta \tag{5.10}$$

Here, crank-angle definitions are provided, as the least-square regression is carried out on the crank-angle-resolved FEN signals. The time-based

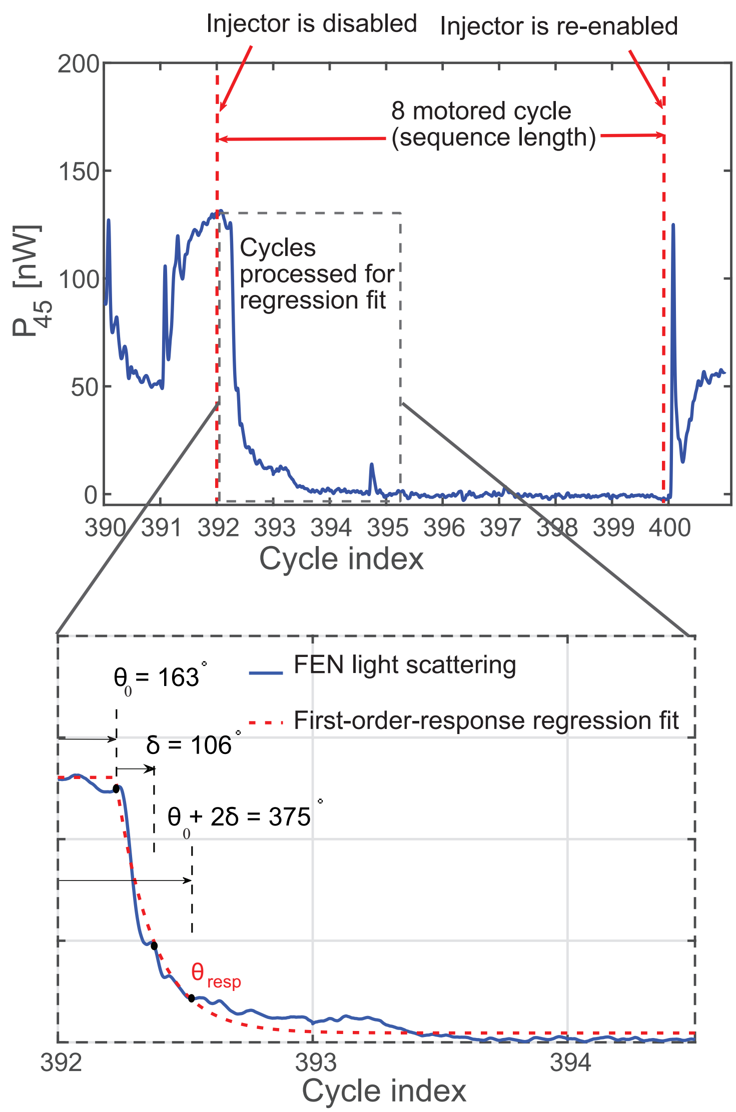

Figure 5.7: FEN light scattering signal during a skip-firing sequence. Fuel injection is turned off during cycles 392 - 399, and the FEN light scattering drops to zero shortly after. The transfer delay (θ_0) and time constant (δ) are obtained based on least-square fitting a delayed first-order function to the light scattering signal.

parameters, t_0, τ, and t_{resp} are calculated from the corresponding crank-angle parameters considering the engine speed. By this definition, the light scattering after θ_{resp} is mostly from the current engine cycle (more than 90%), as the remaining gases from previous cycles inside the FEN are purged out. The mean value and standard deviation of θ_{resp} is determined based on multiple ($n \approx 15$) skip-firing sequences repeated at each operating point. The delays and time constants and their uncertainty based on one standard deviation of the repeated skip-firing sequences are summarized in Table 5.3.

Table 5.3: The sample transfer delay (t_0, θ_0) and time constant (τ, δ) of the exhaust-port FEN measurement system in units of CAD and time (milliseconds).

Engine point	Speed	P_{exh}	crank-angle-based results		Time-based results	
	[RPM]	[bar-a]	θ_0 [CAD]	δ [CAD]	t_0 [ms]	τ [ms]
2	1350	285	177±30	152±39	22±4	19±5
3	1350	270	196±39	121±48	24±5	15±6
5	1350	268	192±21	113±21	24±3	14±4
6†	1500	222	235±14 (75)	80±23 (89)	26±2 (8.5)	9±3 (10)
7	1200	196	182±32	168±103	25±4	24±14
8†	890	223	160±20 (91.5)	109±51 (69)	30±4 (17)	21±10 (12.8)

†Numbers in brackets are from the GT-Power modeling study of [185].

The sample transfer delay, t_0 in milliseconds, is similar for different operating points, as it mostly depends on the distance of the sampling tube from the exhaust valve and the length of the sampling tube. Other factors such as engine speed, and in-cylinder and exhaust pressures have secondary and tertiary effects. The time constant, τ, however, depends largely on the measurement volume of the FEN and its flow rate. The longer τ for point 7, for instance, is likely due to the low SCRE exhaust pressure reducing the sample flow rate, while large τ for point 8 is likely due to a low engine speed and increased mixing time inside the SCRE exhaust. The extent to which τ depends on the SCRE conditions vs the FEN is not clear and cannot be determined from these tests, especially given the large error bars.

Points 6 and 8 had been numerically studied using a GT-Power simulation toolkit, where the transfer delay and time constants were obtained by tracking artificially injected tracer gas in the exhaust [185]. The advantage of this approach is that, unlike the experiments, the response times may be determined for fired engine operating points. The GT-Power results, nevertheless, predicted t_0 values that are 2 - 3 times shorter than their corresponding measured skip-fired values. Increased cylinder pressure and stronger blow-down events during the fired operation may have contributed to this discrepancy. The difference is also partly due to higher velocities predicted by the model, evident from the 20% - 30% over-predicted exhaust flowrate from the GT-Power results compared to the experimental data reported in [185]. The time constant values do not follow similar trends between the two points, i.e. the GT-Power τ and δ are similar to the experimental vales for point 6, but are 40% smaller for point 8.

Based on the results in Table 5.3, the experimental θ_{resp} and t_{resp} are in the range 380 - 520 CAD and 45 - 70 ms, respectively. The response times are less than the single-cycle time threshold (t_{sc} in Equation 5.1), which is in the range 80 - 130 ms for the engine speeds tested here, confirming that measuring single-cycle soot concentration is feasible. The numerically determined GT-Power θ_{resp} and t_{resp} are considerably smaller, and are in the range 230 - 255 CAD and 29 - 43 ms, respectively. The response times from the skip-firing (SF), the numerical GT-Power model (GT) [185], and the iso-thermal model (IT) of [28] (Equations 5.3 and 5.5) are compared for points 6 and 8 in Figure 5.8. The experimentally measured $\theta_{resp,SF}$ is longer than the corresponding modeling results, likely due to lower cylinder pressure during motored operation, as pointed out earlier. The GT-Power $\theta_{resp,GT}$, on the other hand, is located earlier than the signal plateau for point 6, and thus seems to underestimate the response time at higher engine speeds. The formulation used to calculate the iso-thermal response time only considers the flow inside the sampling tube based on Equations 5.3 - 5.5. For

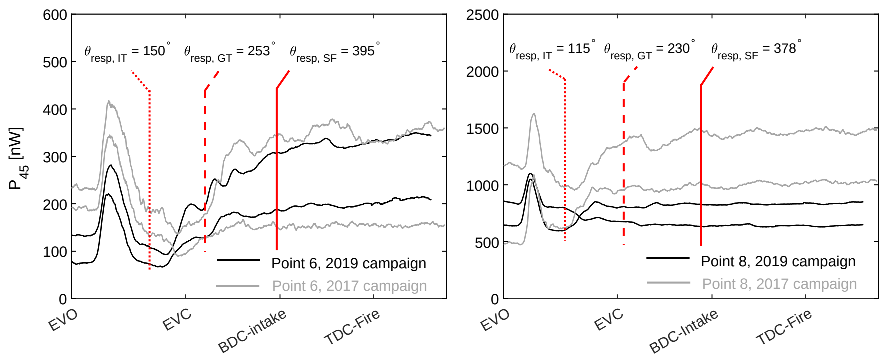

Figure 5.8: Response times based on the skip-firing results (SF, Equation 5.10), the GT-Power model (GT) [185], and the iso-thermal model (IT, Equations 5.3 and 5.5) marked on the crank-angle light scattering traces for points 6 (left), and 8 (right).

a pressure ratio of 2, typically observed between the exhaust port and the FEN measurement volume and the dimensions of the sampling tube, $t_{resp,IT}$ is 10 ms, too short compared to other results, since the delay in the exhaust pipe is not considered. This is addressed by considering an additional delay based on a mean exhaust gas velocity calculated from the mean piston speed. The modified $t_{resp,IT}$ shown in Figure 5.8, is still considerably shorter than $t_{resp,SF}$ and $t_{resp,GT}$.

Lastly, cycle-based soot mass concentration, $C_m(i)$, is calculated by averaging its corresponding crank-angle-resolved series over the $\theta_{resp} - \theta_{EVO}$ period,

$$C_m(i) = \frac{\int_{\theta_{resp}}^{\theta_{EVO}} C_m(\theta)\, d\theta}{\theta_{EVO} - \theta_{resp}} \tag{5.11}$$

where θ_{resp} is the experimentally-derived value from the skip-firing tests. Starting the averaging interval from $\theta_{resp,SF}$ guarantees that variations due to early transitions in FEN light scattering do not affect the average. Since the light scattering traces are steady in this interval, a uniform averaging, similar to [93, 110], is considered appropriate to determine the cycle-specific soot concentrations. Applications of the procedures developed here are demonstrated in Chapter 6 to characterize the cycle-to-cycle variations of engine-out soot concentration and investigate its correlations with cycle-specific in-cylinder parameters.

5.6 Summary and conclusions

In this chapter, we developed a method for determining a single-cycle soot concentration based on light-scattering signals from the exhaust-port FEN measurements. To develop a signal-averaging procedure, first, the crank-angle-resolved FEN light scattering traces are phenomenologically analyzed during continuous and skip-fired engine operations. With this analysis, the characteristics of the light scattering signatures are correlated with the exhaust-port sampling conditions, and are utilized to determine the transient response time of the sampling and measurement system implemented with the FEN.

The crank-angle-resolved FEN signals are divided in two distinct regions, an initial dynamic segment starting from the EVO through the middle of the cycle, followed by a relatively steady tail for the remainder of the cycle. The timing and magnitude of the light-scattering peaks after EVO resembled the repeatable peaks in the exhaust pressure traces. These light-scattering peaks are shown to rise by a same amount above the light-scattering intensity during their preceding cycle, for all cycles during an operating point. After critically examining several mechanisms for generating such patterns, it is believed that exhaust pressure waves, generated by the EVO, resuspends the wall-deposited particles into the sampled flow causing a repeatable spike in the light scattering signal. The shed particles are close to the FEN measurement volume and cannot be removed by a cyclone or impactor in the sampling line, instead, modified sampler inlets that attenuate the pressure pulses are considered and will be tested in the future FEN rebuilds.

A response time of 40 - 70 ms, equal to 380 - 520 CAD, based on analyzing the transient light-scattering traces during skip-fired engine operation was noted for the FEN. These experimentally-determined response times are compared with the numerical and analytical models in the literature and is shown to give more conservative estimates for fired engine operation. It is concluded that the measured response times are shorter than the engine cycle time period, and hence are suitable for single-cycle measurements. Practical applications of the single-cycle method developed here is demonstrated for studying cycle-to-cycle variability of the engine-out soot concentration and its correlations with the underlying combustion processes in the next chapter.

Chapter 6

Cycle-resolved engine-out soot concentrations from a pilot-ignited direct-injection natural gas engine[1]

6.1 Overview

Cycle-resolved measurement of engine-out particulate matter (PM) enables quantifying the cycle-cycle variations and their impacts on emissions. Here, a methodology for cycle-specific soot concentration (C_m) measurement is developed to characterize the cycle-cycle variability of engine-out soot and its correlations with the in-cylinder processes. To achieve the fast response times necessary for this study, soot is sampled with the Fast Exhaust Nephelometer (FEN) near the exhaust valve of a single-cylinder research engine (SCRE) for light-scattering mass concentration and size measurements.

[1]This chapter is based on a manuscript authored by Kheirkhah P, Kirchen P, and Rogak S., entitled "Measurement of cycle-resolved engine-out soot concentration from a diesel-pilot assisted natural gas direct-injection compression-ignition engine", accepted for publication in the International Journal of Engine Research. Parts of this manuscript were presented in Chapter 5, and necessary modifications are made for the flow of the thesis.

Exhaust-port FEN measurements are validated with gravimetric soot mass concentration and mobility diameter measurements of diluted soot. The condition of the diluted sample is important and must be considered. In particular, while the soot concentration and sizes of the diluted exhaust-port sample is similar to the measurements obtained from the FEN, samples extracted downstream of the exhaust system have 50 - 70 nm larger mean mobility diameters and different morphology due to coagulation.

By considering at least 1500 cycles per operating point, cycle-specific GIMEP and C_m are negatively correlated ($R^2 \sim 0.2$ - 0.7), implying that cycles with lower GIMEP emit more soot; however, the physical causes of this association deserve further investigation. The mean concentrations obtained by averaging the FEN signals, are similar to those obtained from diluted gravimetric filter measurements, but the cycle-to-cycle variations can only be detected with the FEN. This property can be utilized in future to characterize the transient real-world engine emissions, or to interpret the in-cylinder variabilities observed in optical research engines.

6.2 Introduction

The real-world motor vehicle soot emissions are affected by the transient engine operation, especially the variability of the in-cylinder combustion. A significant fraction of the total engine-out PM is produced during the transient events, where peak concentrations tenfold the steady state amounts are experienced [70]. Regular PM instruments are too slow to measure these excursions which might last only for a few cycles [69]. The cycle-specific gaseous emissions and their correlations with the in-cylinder combustion is demonstrated in research studies. For instance, the nitrogen oxides (NO_x) concentration measured with a Cambustion CLD-500 is shown to be positively correlated to the peak cylinder pressure, presumably due to the enhanced NO_x formation rate brought about by higher cylinder temperatures [110]. The exhaust-stream soot emissions, however, have not been studied on a cycle by cycle basis. This topic deserves further research, primarily due to the large sensitivity of soot formation and oxidation to the combustion conditions.

Studies of cycle-resolved engine PM are scarce and mostly limited to in-cylinder optical measurements. Pyrometry technique, for instance, estimates the in-cylinder soot concentrations by measuring the crank-angle-resolved optical thickness of the soot cloud (KL) from natural luminosity [102, 197]. Obtaining cycle-specific soot concentrations, however, is prone to noise due to weak natural luminosity late in the cycle, and has large variations from cycle to cycle. The cycle-specific in-cylinder soot is characterized by KL_{end} defined at the latest crank angle where solutions to the multi-colour pyrometry equations exist, typically 40° to 60° aTDC.

$$\lambda_1^{\alpha}\left[1-\frac{e^{C/\lambda_1 T}-1}{e^{C/\lambda_1 T_{a,1}}-1}\right]=\lambda_2^{\alpha}\left[1-\frac{e^{C/\lambda_2 T}-1}{e^{C/\lambda_2 T_{a,2}}-1}\right] \tag{6.1}$$

where, λ_1 and λ_2 are the pyrometry wavelengths, $C = 1.43\times10^{-2}$ mK, and T_a is the apparent soot temperature [100]. It is not clear whether the large variations in KL_{end} are physical or an artifact of the method. This is particularly challenging when such variabilities are manifested during seemingly stable pressure and heat-release traces. Examining these requires quantitative single-cycle measurements in the exhaust port, which are rare in the literature, and in the few existing cases, are limited to qualitative demonstrations[154].

Here, we use the Fast Exhaust Nephelometer (FEN) characterized for quantitative steady-state soot measurement, and shown to be capable of detecting the single-cycle changes in exhaust-port soot concentrations. Cycle-specific soot concentrations are correlated with the cycle-specific gross indicated mean effective pressure (GIMEP), which showcases how the FEN can be utilized to capture the effects of in-cylinder variabilities on the exhaust soot. FEN light scattering measurements are converted to soot mass concentration and mass-mean mobility diameters using the inverse RDGFA model introduced in Chapter 4, and the quantitative results are validated with diluted engine soot measurements in Section 6.4.1. Lastly, the correlations between the cycle-resolved exhaust soot and in-cylinder combustion

GIMEP are explored for the engine operating points introduced in Chapter 3 (reviewed here in Table 6.1), and its results are presented in Section 6.4.2.

6.3 Research methodology

The work presented here is carried out on the experimental facility, namely the SCRE and the in-cylinder and exhaust instrumentation, described earlier in Chapter 3. The results from the previous chapters, particularly the inversion methodology for the FEN in Chapter 4 and its crank-angle-resolved response times in Chapter 5 are applied to obtain quantitative soot concentrations at the exhaust-port with a single-cycle resolution. Here, the experimental procedures and data post-processing methods are explained.

6.3.1 Experimental setup

The FEN is mounted for exhaust-port sampling from SCRE, shown in Figure 6.1. The engine is operated in a steady-state continuous fashion without disruptions to the injection. The signals from the FEN photodetectors, the in-cylinder piezo-electric pressure sensor, and the intake- and exhaust-port pressures are recorded on the fast DAQ with 0.5° CAD resolution, and processed to characterize the in-cylinder combustion and exhaust-port soot emission, as described in Section 6.3.2.

PM characterization

In addition to the raw exhaust-port FEN measurements, the SCRE PM is characterized based on diluted gravimetric mass concentration with filters, mobility diameter with the SMPS, and morphology based on TEM samples. Two sampling points are considered for the diluted measurements, shown in Figure 6.1. A sampling point located after the exhaust surge tank (denoted post-surge-tank or PST sample) allows for a controllable dilution ratio, which was utilized during the FEN calibration in Chapter 4. A second sampling point is located at the exhaust of the FEN and has a constant ratio of $\sim$ 20:1, denoted exhaust-port or EXP sample. Both samples are diluted with HEPA-filtered air using ejector nozzles, and measured for mass concentration, mobility diameter, and the soot morphology, to determine the effects of particle coagulation in the exhaust system and ensure that proper parameters are used for the FEN light scattering inversion. The layout of the experimental system is shown in Figure 6.1.

As mentioned in Chapter 3, the gravimetric filters are placed before the thermodenuder, due to flow rate restrictions, and may be affected by the condensed volatile and semi-volatile compounds (VOC and SVOC). The PM concentration time series from the Dusttrak are used to track the time variation of soot concentration during the filter loading, that could occur due to variabilities in the engine operating condition. It is also used to measure the pre- and post-thermodenuder PM concentration to determine the mass removal rate in the thermodenuder. As the Dusttrak measures soot indirectly from light scattering, it is not used for validating the FEN, and its time-series are provided in Appendix I; nevertheless, its implications for the validation of the FEN measurements are discussed in Section 6.4.1.

6.3.2 Data analysis methods

The cycle-resolved soot concentrations and in-cylinder combustion parameters are calculated based on the recorded crank-angle-resolved data. The in-cylinder combustion is characterized based on the gross indicated mean effective pressure (GIMEP) and the combustion phasing (θ_{50}), calculated from in-cylinder pressure and heat release rates.

The crank-angle-resolved light scattering intensities measured with the FEN, P_{45}, P_{90}, and P_{135}, are filtered using a 10° moving average, and inverted into soot mass concentration C_m, geometric mass-mean mobility diameter $d_{m,g}$, and geometric standard deviation $\sigma_{m,g}$ of the polydisperse samples, based on the method of Chapter 4. The crank-angle-resolved signals are processed according to the flowchart in Figure 6.2, with the light scattering inversion block shown in the top and mid sections of the Figure. The morphological parameters needed for the inversion of the light scattering signals are obtained from TEM image processing, described in Chapter 4. The de-

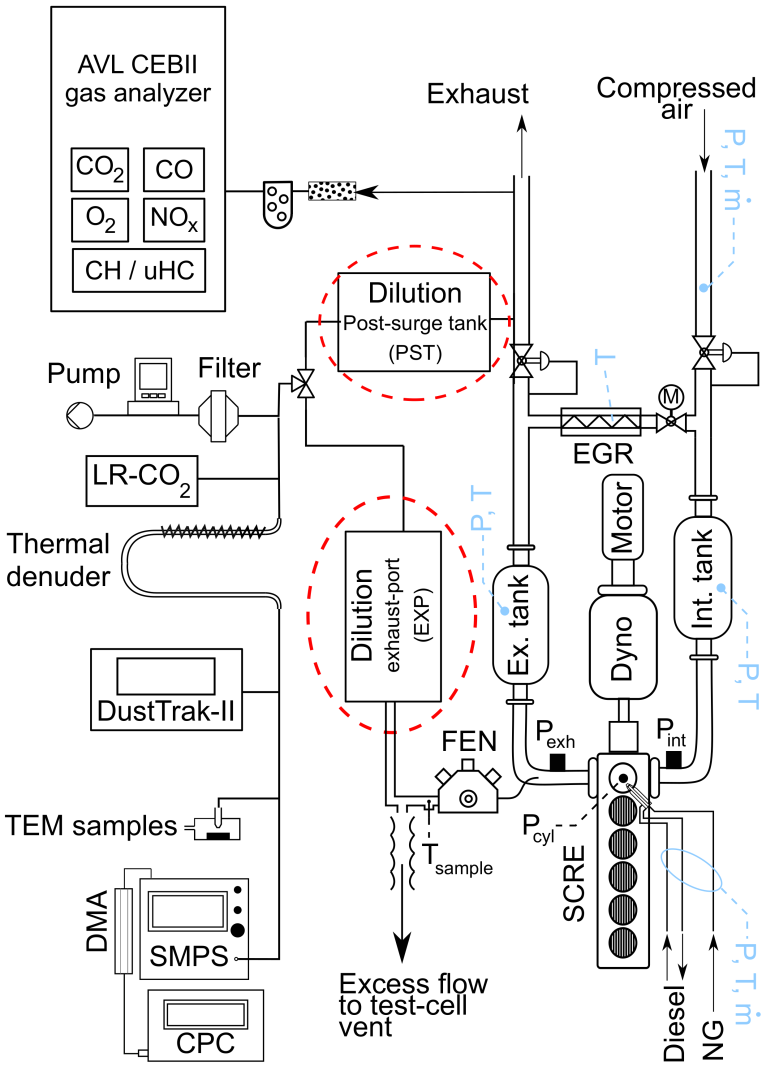

Figure 6.1: The SCRE PM measurement layout. The engine operation is characterized based on fuel and air path measurements (light blue), and high-speed manifold and in-cylinder pressure (black) sensors. The post-surge-tank (PST) and the exhaust-port (EXP) PM sampling locations are marked with dashed ellipses.

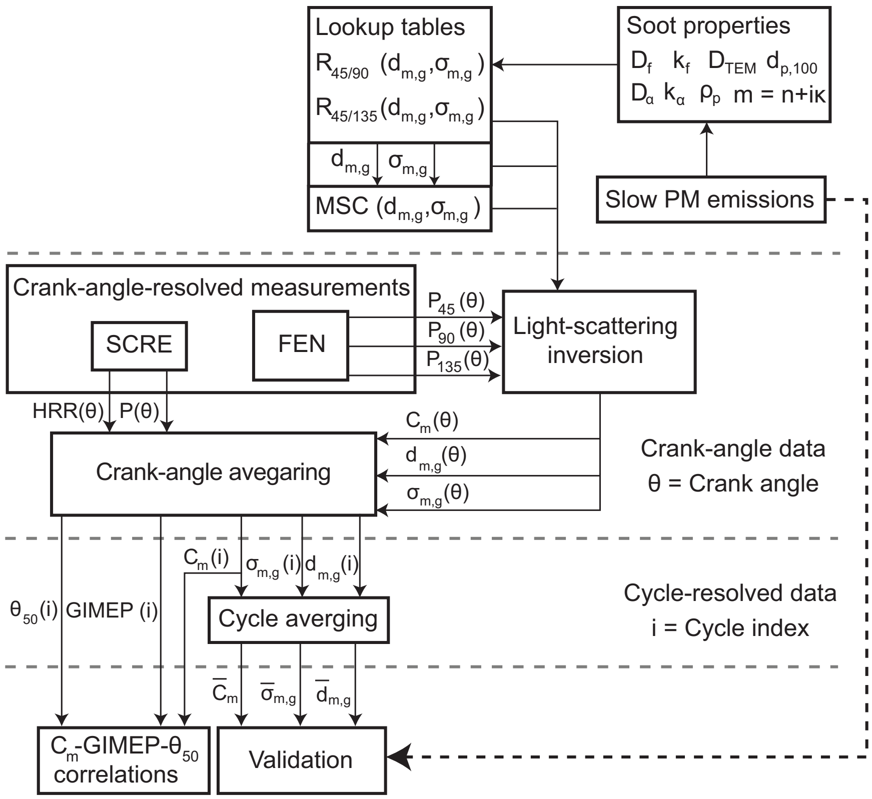

Figure 6.2: The flowchart for converting the raw outputs of the in-cylinder and exhaust sensors into the crank-angle and cycle-specific quantities.

tails of the morphology analysis and the resulting pre-factors and exponents (D_{TEM}, $d_{p,100}$, D_f, and k_f) are provided in Appendix G for the PST and EXP samples. The morphological parameters used for the results presented here are based on the EXP samples. Other parameters used in the inversion are similar to Chapter 4 Table 4.1. The crank-angle-resolved in-cylinder pressure and heat-release-rate and the inverted FEN results are processed to give the cycle-specific quantities, namely the GIMEP, θ_{50} (Equations 3.1-3.3), and the soot C_m, $d_{m,g}$, and $\sigma_{m,g}$ (Equation 5.11), and are discussed below.

6.4 Results and discussion

The cycle-resolved variability of the exhaust soot emission and the correlations between the in-cylinder combustion and cycle-resolved C_m are investigated over the engine operating conditions listed in Table 6.1. The operating points are similar to Table 3.4 in Chapter 3, except that point 9 is removed due to excessively high equivalence ratio. The averaged exhaust-port FEN results are validated against diluted PM measurements, and the cycle-resolved FEN concentrations are compared against the in-cylinder combustion parameters.

Table 6.1: SCRE operating points tested for the FEN single-cycle exhaust-port measurement.

Engine point	Engine speed [RPM]	GIMEP [bar]	θ_{50} [°aTDC]	ϕ [-]	EGR [%]	P_{exh} [kPa-a]
1	1335	16.0	12.7	0.65	19	276
2	1350	16.0	12.7	0.55	12	285
3	1350	15.5	15.5	0.54	13	270
4	1350	15.5	20.0	0.75	22	275
5	1350	16.0	20.0	0.65	15	268
6	1500	11.8	11.2	0.55	20	222
7	1200	12.2	10.0	0.70	0	196
8	890	9.9	11.3	0.53	46	223

6.4.1 Validation of the FEN exhaust-port measurements

To validate the exhaust-port C_m and $d_{m,g}$ measured with the FEN, diluted samples from the post-surge-tank (PST) and exhaust-port (EXP) locations are measured and compared with the FEN. The soot at the PST location can be different from the exhaust-port samples due to particle coagulation inside the exhaust pipes. This is investigated by measuring a diluted EXP soot sample taken from the exhaust of the FEN. The two sampling and dilution configurations are schematically shown in Figure 6.1 and the results are explained here.

The results for the gravimetric soot C_m and the SMPS $d_{m,g}$ and $\sigma_{m,g}$ from the EXP and PST samples are shown in Table 6.2. The exhaust C_m

reported in Table 6.2 is based on the diluted filter masses corrected by the dilution factor (Equation 3.4), and the $d_{m,g}$ values are calculated from the original SMPS number scans using the soot effective density [47]. The light scattering from soot is weighted by higher moments of mobility diameter similar to particle mass; therefore, the mass-mean instead of the number-mean mobility diameter is considered for validating the FEN light scattering soot diameters, similar to [98].

The morphological parameters D_f, k_f, D_{TEM}, and $d_{p,100}$ are based on the TEM samples collected for points 1, 2, and 7 and are provided in Appendix G, and the rest of RDGFA parameters are similar to Table 4.1. In the absence of TEM samples for other SCRE points, the morphological parameters from points 1 and 2 are averaged and used. As point 7 is run with 0% EGR, its morphological parameters are remarkably different from points 1 and 2. Therefore, the TEM parameters obtained for point 7 are used only for the inversion of the signals collected at this point.

The results in Table 6.2 show that $d_{m,g}$ of the exhaust-port soot is smaller than the post-surge tank samples by 50 - 70 nm, confirming that particle coagulation in the engine exhaust path increases the $d_{m,g}$. The two sampling locations have different morphological parameters as well, which is provided in Appendix G. Samples from points 1 and 2 indicate that PST mass concentrations are lower than the EXP concentrations, and the difference is significant compared to the variability of the engine operating point. Points 4 and 5, on the other hand, show similar mass concentrations for both the PST and EXP samples. The reason for this dissimilarity is not completely clear; it is possible that discrepancies are due to the run-to-run or day-to-day variability and is further discussed in Section 6.4.3.

The mean cycle-specific C_m and $d_{m,g}$ are evaluated for each operating point based on the FEN data and compared to the corresponding metrics from the SMPS and gravimetric instruments. The measurements are repeated multiple times to ensure the results are not biased and the conclusions are statistically valid.

The SMPS mobility diameters measured from both the EXP and the PST samples are compared with the exhaust-port FEN $d_{m,g}$ in Figure 6.3.

Table 6.2: Gravimetric filter mass concentration and SMPS mobility diameter measurement results. Filters from the post-surge-tank (PST) sample are collected for all points, while the diluted exhaust-port (EXP) filters are only collected for points 1, 2, 4, and 5. The ranges are based on the recorded minima and maxima.

Engine point	PM sample	Gravimetric C_m [mg/m^3]	SMPS $d_{m,g}$ [nm]	SMPS $\sigma_{m,g}$ [-]
Point 1	PST	55-75	195-210	1.60-1.65
	EXP	86-100	126-140	1.47-1.56
Point 2	PST	16-22	150-170	1.50-1.55
	EXP	27	115-120	1.45-1.48
Point 3	PST	9.4	155-170	1.42-1.45
	EXP	-	-	-
Point 4	PST	23-30	145-170	1.57-1.60
	EXP	30	94-100	1.50-1.55
Point 5	PST	9-10	130-160	1.40-1.50
	EXP	9-10	85-100	1.45-1.50
Point 6	PST	27-31	160-170	1.55-1.60
	EXP	-	-	-
Point 7	PST	17-19	140-170	1.55-1.60
	EXP	-	90-97	1.50-1.60
Point 8	PST	96	300-325	1.90
	EXP	-	-	-

The $d_{m,g}$ measured using the two instrument generally agree for the EXP sampling location, while the soot particles sampled downstream of the SCRE exhaust path are 50-70 nm larger. The particle coagulation rates expected based on the undiluted exhaust concentrations (a coagulation time constant of $\sim$ 8 - 10 s is calculated for 100 nm aggregates assuming a typical raw exhaust concentration of 2×10^8 cm^{-3}) are considered the cause of this difference [172]. The FEN-inferred engine-out soot diameters are in the same range as the EXP SMPS measurements; nonetheless, small changes in the mean soot diameter from one operating condition to another cannot be resolved with the FEN. It could be that the variabilities in the engine affects the FEN, EXP, and PST samples differently, as the PST and EXP measurements are not simultaneous, and both have different sample transit times

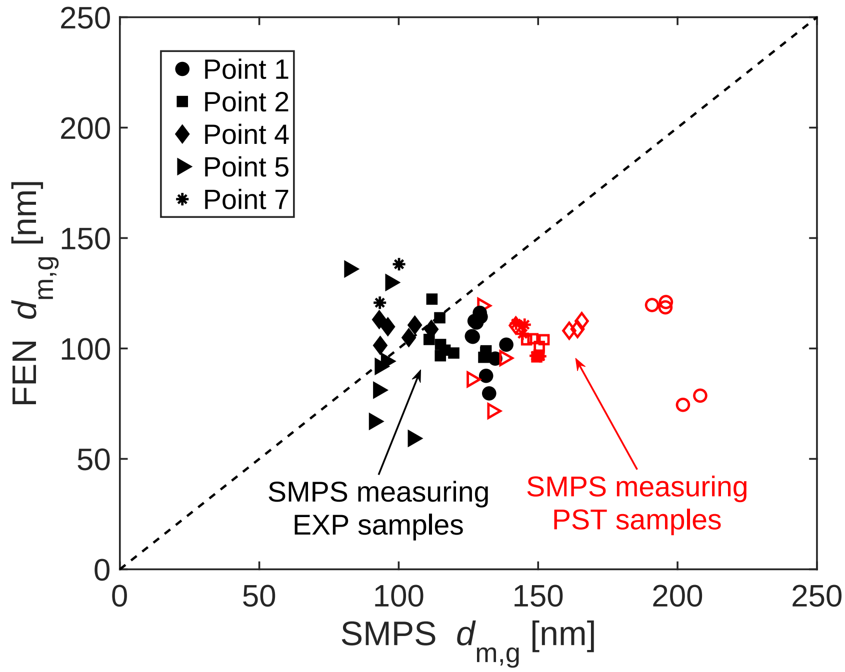

Figure 6.3: The averaged FEN $d_{m,g}$ compared with the diluted SMPS $d_{m,g}$ of the exhaust-port (EXP, filled [black] symbols) and the post-surge-tank (PST, open [red] symbols) samples. Engine operating points are shown with different symbols, and the dashed line is the 1:1 guideline.

compared to the FEN.

Similarly, the averaged FEN C_m for different engine tests is compared with the gravimetric soot mass concentration measured from the diluted samples at EXP and PST in Figure 6.4. The gravimetric mass concentrations in Figure 6.4 are based on the diluted EXP samples when available, and otherwise based on the PST samples (points 3, 6, 7, and 8), as the two are considered to be similar as discussed earlier. The vertical scatter of similar symbols for a given operating point indicates a changing exhaust-port soot concentration while collecting a filter sample ($\sim$ 15-20 minutes). The Dusttrak time-resolved data (provided in Appendix I) indicates similar variations in the diluted PM concentration for points with substantial vertical

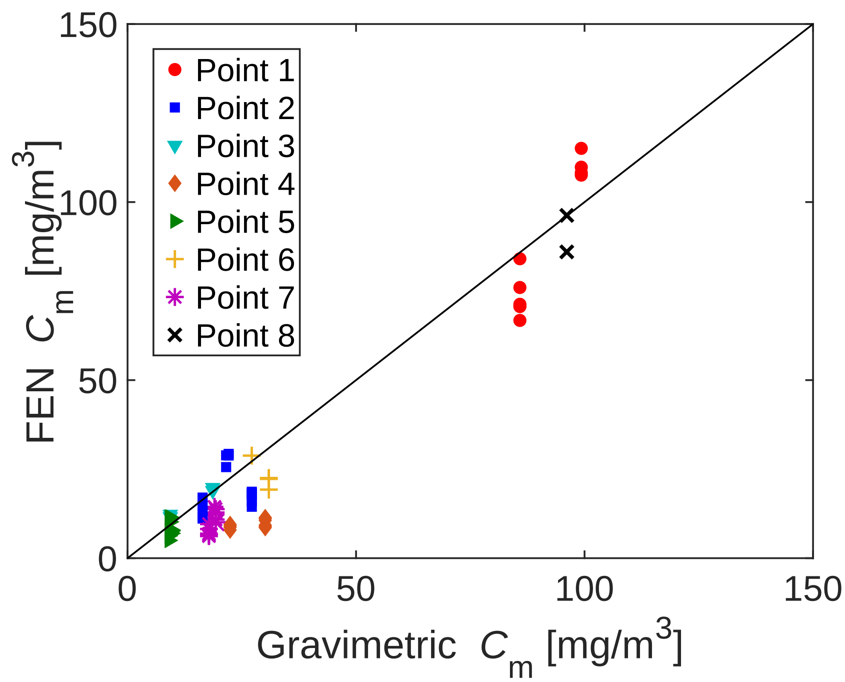

Figure 6.4: The averaged exhaust-port (EXP) FEN compared with the gravimetric C_m. The gravimetric filter masses are corrected for the dilution ratio. Different operating points are segregated by different colors and symbols. Gravimetric mass concentrations are based on the EXP samples when available, and otherwise based on the PST samples.

scatter, likely due to variabilities in the engine operating condition.

The mass concentration from the FEN depends on the measured light scattering and the parameters used in its inversion. Deviations from the unity line in Figure 6.4 indicate a difference between the exhaust-port light-scattering C_m and the diluted gravimetric mass concentration. The normalized root-mean-square deviation (NRMSD) of the FEN C_m for the gravimetric datum is defined in Equation 6.2, and is close to 30%.

$$NRMSD = \frac{1}{\bar{C}_{m,grav}} \sqrt{\frac{\sum \left(C_{m,FEN} - C_{m,grav}\right)^2}{N}} \tag{6.2}$$

The sample population (N in Equation 6.2) is 63, considering the measurement repetitions for different operating points, as shown in Figure 6.4. Differences in the range of 25% - 30% might be attributable to the uncertainty of FEN inversion as it is sensitive to the physical and morphological properties of soot [98, 123, 143]. It can also be attributed to the VOC and SVOC material condensed onto filters or the variability of the engine operating point as discussed earlier. Based on the Dusttrak measurements before and after the thermodenuder (provided in Appendix I), and the estimated particle losses (provided in Appendix C), it is possible that some samples (e.g. point 4) contain up to 25% condensed SVOC, which explains some of the discrepancy between the gravimetric and exhaust-port light-scattering measurements in Figure 6.4. This is consistent with previous research on the same engine that operating conditions similar to points 4 and 7 could contain more than 20% volatile and semi-volatiles in the total PM mass [155].

6.4.2 Cycle-specific soot emissions

The cycle-specific soot concentration series may be constructed from the procedures laid out in Chapter 5 to characterize the cycle-to-cycle variation of engine-out soot emissions, correlated with the single-cycle in-cylinder combustion.

The crank-angle-resolved C_m and $d_{m,g}$, shown in Figure 6.5 over a single-cycle 720 CAD period indexed at the exhaust valve opening (EVO), are derived from the inversion of the crank-angle light scattering intensities (top panel). Larger soot diameters shortly after the EVO are coincident with the peaks of the light scattering. Occasionally, the $d_{m,g}$ was unrecoverable from the inversion process in the peaked intervals, as the ratios were outside the valid bounds of the RDGFA model. The description given in Chapter 5 for the light scattering traces and the sampling flow in the FEN, attributes these peaks to the resuspension of wall-deposited particles due to the passing pressure waves. The crank-angle $d_{m,g}$ plots shown here are consistent with this description, indicating that the light scattering signals correspond to larger particles, which tend to be different from fresh engine soot.

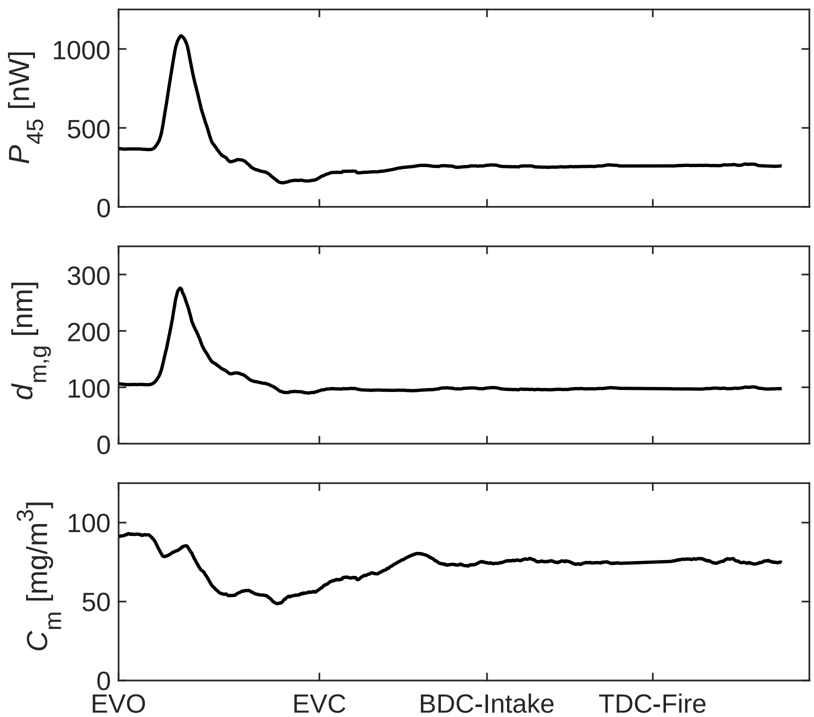

Figure 6.5: The crank-angle-resolved light scattering P_{45} (top), the inverted $d_{m,g}$ (middle) and the C_m (bottom) traces during one engine cycle period, indexed at EVO. The data corresponds to point 1 operating condition.

Exhaust port cycle-specific soot concentrations ($C_m(i)$) are shown for 2000 cycles in Figure 6.6, where each point in the series represents an engine cycle based on the crank-angle-averaging procedure in Equation 5.11, also illustrated in the bottom right panel of Figure 6.6. The series of soot C_m and $d_{m,g}$ and combustion GIMEP and θ_{50} between cycles 400 and 600 for this engine point are shown in the left panel of Figure 6.6. During the empty sections in the series, the laser is turned off to cool the diode and extend its longevity. The overlaid solid red line on the C_m series is a 10-cycle moving average, applied to the series to simulate the measurement from an instrument with a response time of 0.5 s, such as the instruments listed in Chapter 2 Table 2.1.

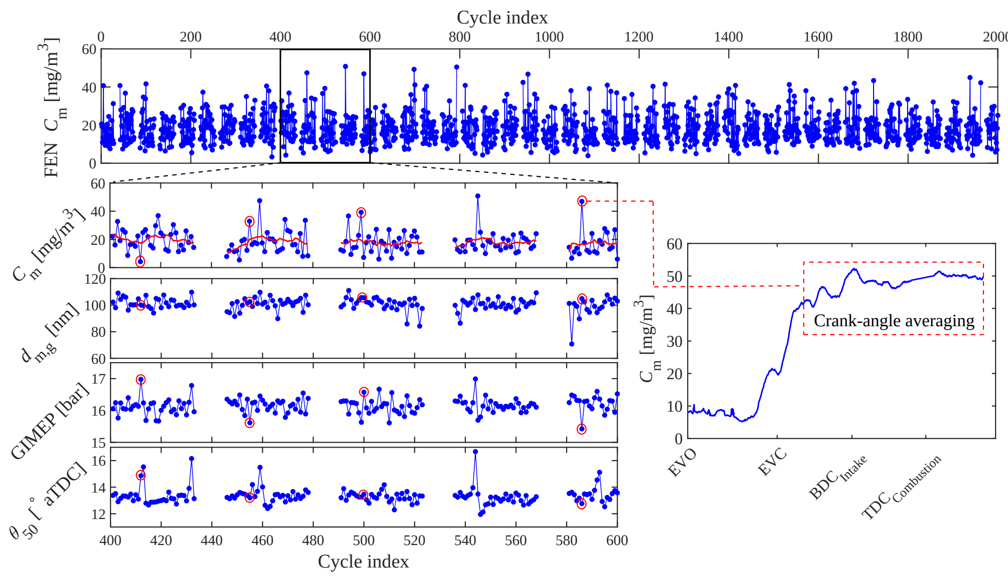

Figure 6.6: The cycle-resolved concentration series for 2000 consecutive cycles for steady-state operation at point 2 (top). Each point in the series is constructed based on Equation 5.11, demonstrated in the right panel. The soot C_m and $d_{m,g}$ and the combustion GIMEP and θ_{50} are plotted between cycles 400 and 600. The solid red line is a 10-cycle moving-average filter applied to the original C_m series. High and low soot concentrations (marked with circles) are coincident with low and high GIMEP respectively.

The FEN reveals significant variations in cycle-specific soot during steady operations, denoted by the difference between the cycle-resolved and the filtered series. Until now, sudden changes to the engine-out soot was observed only during transient engine operations [70]. Optical measurements in the past have shown similar cycle-cycle variations based on the in-cylinder pyrometry measurements in diesel engines, but had not been validated with any exhaust-stream reference.

The cycle-to-cycle variations of soot concentration, shown in Figure 6.6, is significant as the range of variations is comparable to the mean. Here, for instance, the variations of C_m are in the ranges 5-35 mg/m^3 while its mean is 20 mg/m^3. Furthermore, cycles with significantly higher or lower C_m correspond to cycles with lower or higher GIMEP, respectively. Such cycles are indicated in Figure 6.6 (numbers 412, 455, 499, and 586, the single-cycle crank-angle series shown on the right belongs to the latter). The combustion phasing, θ_{50} (the bottom panel) do not seem to indicate any particular trend in the exhaust soot series, as cycles 412, 455, 499, and 586 have different combustion timings. The correlations between the engine-out soot mass concentration and the combustion GIMEP are further investigated in the next section.

The mean value and the coefficient of variation (COV, standard deviation divided by the mean) for the cycle-resolved FEN soot mass concentration, and the combustion GIMEP and θ_{50} are summarized in Table 6.3, and correspond to repeated tests on multiple days. The COV of the C_m are in the range 30% - 50%[2]. The COV of the GIMEP is 1.2 %, and do not seem to explain the changes in the COV of C_m between different operating points or repetitions of the same operating point. While their COV is not correlated, there are correlations between the single-cycle GIMEP and C_m, as pointed out in Figure 6.6, and further discussed in the next section. It is also noticed that the engine operating points could vary due to the day-to-day variability, which explains the differences between the mean value of FEN C_m for different repetitions.

6.4.3 Correlations between the soot emission and the in-cylinder combustion

The cycle-specific soot C_m are correlated with the cycle-specific combustion GIMEP, shown in Figure 6.7, where each dot in the scatter plots represents an individual cycle. The lines shown in the figure are the linear least-square fits to the cluster of dots for each engine operating point, typically containing 1300-1600 cycles. Same colors are used for repeated points in the same day

[2] The repetition of point 5 on day 5 has close to 100% variations

Table 6.3: The mean and the standard deviation of the cyclic variations of the FEN C_m, the combustion GIMEP and θ_{50}. Results from repeated operating points on different days are presented, and are consistent with Figure 6.7.

Engine Point	Test day	C_m [mg/m^3] mean	C_m COV_{cyclic}	$GIMEP$ [bar] mean	$GIMEP$ COV_{cyclic}	θ_{50} [°aTDC] mean [°]	θ_{50} σ_{cyclic} [°]
1	3	111.2	35 %	16.6	1.6 %	13.1	0.42
	7	73.3	29 %	15.8	1.3 %	14.2	0.31
2	1	27.2	49 %	16.5	1.2 %	12.9	0.30
	2	29.1	45 %	16.0	1.2 %	13.2	0.29
	4	15.7	43 %	16.1	1.9 %	13.3	0.53
	6	18.7	56 %	15.8	1.2 %	14.1	0.37
3	1	12.0	54 %	14.9	0.9 %	15.0	0.22
	2	19.4	46 %	15.7	1.0 %	16.8	0.25
4	5	9.5	39 %	15.4	1.8 %	21.4	0.96
5	1	7.5	56 %	16.6	0.7 %	20.2	0.23
	5	8.0	100 %	15.9	1.6 %	20.6	0.85
6	1	21.3	41 %	11.6	1.6 %	11.5	0.26
	2	28.8	36 %	11.9	1.2 %	11.5	0.29
7	1	11.9	35 %	11.7	1.2 %	10.0	0.29
	2	14.4	33 %	12.4	1.2 %	10	0.3
	7	6.8	56 %	11.8	1.2 %	10.8	0.25
8	1	91.1	23 %	9.9	1.0 %	11.6	0.33

and are distinguished from operating points repeated on different days. A correlation between the cycle-specific soot mass concentration and GIMEP is evident from Figure 6.7, with more details summarized in Table 6.4.

Possible correlations between the cycle-resolved exhaust soot concentration and combustion phasing, characterized based on CA_{50} and CA_{90}, were considered too, but indicated weak correlations (with R^2 less than 0.1), and are not further discussed here. The negatively correlated C_m and GIMEP indicates that cycles with lower GIMEP tend to emit higher soot mass. This is while a positive correlation factor between the GIMEP and soot emissions is evident in the literature [128]. Those studies, however, track changes in the mean-value of soot emissions between operating points with different mean GIMEP, likely due to different fueling and combustion parameters. Here, the variations within the operating points are studied which might be

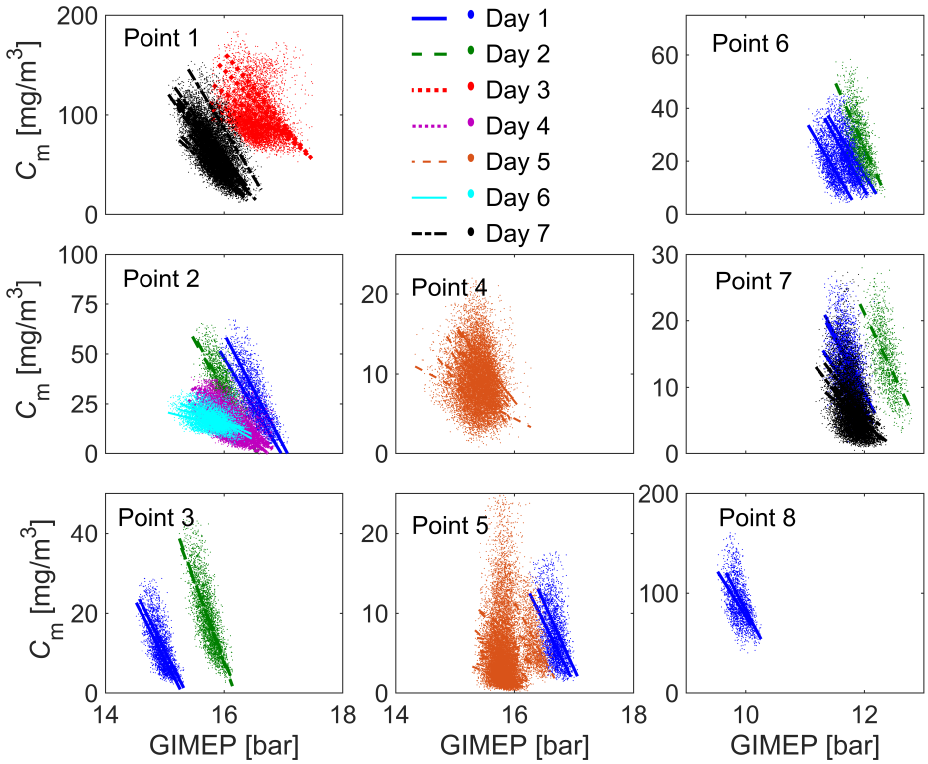

Figure 6.7: Correlations between the cycle-specific soot mass concentration C_m and combustion GIMEP. Different operating points are shown in separate panels, each is repeated on the same day and in different days. The lines show the linear least square fits to clusters from each repetition. Repeated operating points on different days are shown with different colors and line styles.

caused by variabilities in air-fuel mixing [87, 109], injector shot-to-shot variations [69], or early ignition processes [164]. The increased soot concentration at lower GIMEP could be due to changes in the soot oxidation processes, which are also subject to significant cycle-cycle variabilities based on the in-cylinder measurements [87, 102, 197]. Such effects, however, were not manifested in the thermodynamically calculated combustion phasing (θ_{50} or θ_{90}) in this study. In-cylinder optical diagnostic tools and cycle-resolved exhaust gas measurements are needed alongside the FEN to investigate these effects, which are beyond the scope of this work.

Table 6.4: Examining the correlations between the cycle-resolved exhaust soot C_m and the combustion GIMEP. The number of cycles per operating point, and the R^2 and the slopes of the C_m-GIMEP correlations from repeated tests are shown.

Engine Point	Test day	No. of repeats	No. of cycles per repeat	C_m-GIMEP $R^2 \pm \sigma$	slope $\pm\sigma$ [mg/m^{3}bar]
1	3	6	1480	0.24 ± 0.21	-37.9 ± 23.0
	7	6	1640	0.68 ± 0.01	-82.6 ± 8.4
	7*	3	1608	0.66 ± 0.01	-55.8 ± 2.3
2	1	2	1444	0.65 ± 0.02	-53.2 ± 3.2
	2	2	1498	0.67 ± 0.01	-53.7 ± 0.5
	4	12	1361	0.56 ± 0.06	-21.7 ± 2.9
	6	4	1478	0.21 ± 0.11	-11.4 ± 3.7
3	1	2	1497	0.51 ± 0.01	-29.5 ± 0.3
	2	2	1504	0.59 ± 0.01	-40.1 ± 1.3
4	5	10	1495	0.21 ± 0.08	-8.7 ± 2.1
5	1	3	1473	0.31 ± 0.01	-15.3 ± 1.1
	5	11	1506	0.04 ± 0.07	-2.8 ± 2.7
6	1	3	1641	0.44 ± 0.03	-38.2 ± 2.0
	2	1	1682	0.52 ± -	-50 ± -
7	1	4	1414	0.28 ± 0.04	-14.9 ± 2.6
	2	1	1316	0.36 ± -	-18.6 ± -
	7	7	1478	0.14 ± 0.07	-8.9 ± 2.3
8	1	2	970	0.29 ± 0.22	-134.4 ± 56.6

* A drift in the last three runs of point 1 was observed.

The R^2 and slopes of the cycle-specific C_m-GIMEP correlations are summarized in Table 6.4, and vary across different operating points. Different R^2 and slopes exist for the repetitions of same operating points too, likely due to variations in the engine set-point (e.g. mean GIMEP) between different days as previously discussed. The variability in the engine set-points might be due to seasonal changes in the natural gas and diesel fuel composition, or intake air temperature and humidity, since tests are done over a one-year period.

Strongest correlations are observed for points with high GIMEP and early θ_{50} (points 1, 2, and 3) with R^2 values in the range 0.5 - 0.7, and the weakest correlations are observed for point 4 with late θ_{50}, and point 7 operated without EGR, where the R^2 values are in the range 0.2 - 0.3. In the past, correlations between the cycle-specific exhaust NO_x and cylinder P_{max} had been observed with positive NO_x-P_{max} slopes [10, 93]. Such correlations are important for characterizing the cycle-to-cycle variabilities, and suggests that the overall emission factors can be improved by minimizing the variations.

6.5 Summary and conclusions

The single-cycle engine-out soot emissions from a pilot-ignited direct-injection natural gas (PIDING) single-cylinder research engine (SCRE) is measured with the Fast Exhaust Nephelometer (FEN) at the exhaust-port. The light scattering intensities of the FEN are converted to soot mass concentration (C_m) and mass-median mobility diameter ($d_{m,g}$) using the RDGFA light scattering lookup tables. The parameters of the RDGFA model are determined from analyzing the TEM soot images, and from the literature. Using these parameters, the exhaust-port soot concentration and sizes are validated with diluted gravimetric filter mass and SMPS mobility diameter measurements. It is noted that the soot aggregate growth can be significant (50-70 nm) between exhaust-port and downstream soot sampling points.

Using the cycle-resolved FEN measurements, the single-cycle soot mass concentrations are shown to be negatively correlated with the in-cylinder combustion gross indicated mean effective pressure (GIMEP). The correlation R^2 are in the range 0.2 - 0.7, which is significant given the large number of engine cycles per operating point ($n_c \sim 1500$). Moreover, the correlation slopes are negative, indicating that cycles with low GIMEP are prone to increased soot. Variations are noted in the repetitions of the engine points, which affect the GIMEP-C_m correlations as well. Cycle-specific correlations between the in-cylinder combustion and the exhaust emissions have been previously shown for gaseous species, but is for the first time demonstrated between exhaust soot and GIMEP. This information is relevant for evaluating PM control strategies in transient operations, especially in real-drive emissions (RDE) measurements.

The methods demonstrated here are useful to other applications, where the cycle-resolved variations are important and must be characterized. These include research applications such as the in-cylinder optical diagnostics to better understand the variability of soot oxidation processes. The FEN can also be implemented on single- or multi-cylinder engines during transient operations to provide insight into the short-lived transient soot excursions and cylinder imbalances that are critical to engine optimization.

Chapter 7

Conclusions and recommendations

Development of PM instruments suited for fast exhaust measurement of transient engine emissions is critically necessary given the recent trends in regulatory requirements and competition for cleaner engines. In this work, a method for measuring the engine-out soot size and concentration with a single-cycle time resolution based on a Fast Exhaust Nephelometer (FEN) was demonstrated. The FEN was implemented for exhaust-port sampling from a single-cylinder research engine (SCRE) on a dynamometer testbed, and revealed patterns in soot emissions that had been obscure in the past, due to lack of a sufficiently fast instrument for single-cycle exhaust-stream soot measurement. The results of this work were discussed throughout the thesis, and conclusions specific to each segment of the research were presented in the corresponding chapters. Here, a summary of the key findings and overall conclusions are provided, and is followed with a subsequent discussion about the future research applications of the method.

7.1 Summary of the research findings and conclusions

Based on the objectives set out for this work, a method was developed and implemented on a pilot-ignited direct-injection natural gas (PIDNIG) research engine to measure its exhaust soot concentration and size. In order to employ such a method for quantitative measurements, it was validated with steady diluted exhaust soot, and its response to fast transients was characterized during "skip-firing" engine operation. The development and characterization of this method was tackled in two steps. First, an inversion algorithm was developed to convert the steady-state FEN light-scattering signals into soot concentration and polydisperse size distribution parameters, which were validated against reference instruments. Second, a signal-processing toolkit for single-cycle measurements based on the characteristics of exhaust-port sampling was developed and incorporated with the validated inversion model. A key feature of this methodology is its ability to measure quantitative cycle-resolved soot concentrations that can be correlated with other cycle-resolved engine parameters, most importantly, those related to the underlying in-cylinder combustion processes. Below, the key findings and overall conclusions of the work based on a holistic view of the previous chapters are discussed.

7.1.1 The three-angle light scattering soot measurement

Light scattering measurements were carried out with the FEN, consisting of three silicon photodetectors, a 405 nm laser system, and the necessary focusing optics. It was shown that the FEN responds to concentrations of diluted exhaust soot similarly to a commercially available light scattering photometer, the Dusttrak DRX. Nonetheless, to obtain concentrations and particle sizes that are comparable with gravimetric mass and mobility measurements, the FEN light scattering intensities were processed with an inversion tool-kit. The inversion procedure is based on lookup tables generated with a RDGFA model, containing 9 parameters (D_f, k_f, D_{TEM}, $d_{p,100}$, D_α, k_α, $\mathbf{m} = n + i\kappa$, and ρ_p) that model the properties of soot, and a coefficient,

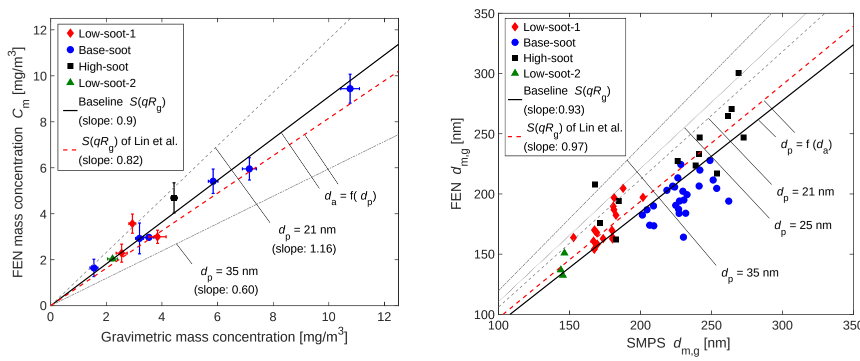

(a) **(b)**

Figure 7.1: The mass concentration and mean mobility diameter results from the inversion of FEN light-scattering intensities compared to gravimetric mass concentration (left), and SMPS mobility diameter measurements (right).

Λ_{FEN}, for the optical properties of the FEN. The effects of primary particle polydispersity based on the external mixing hypothesis (EMH) were considered in the RDGFA model for a more realistic description of light scattering from polydisperse samples.

The inverted mass concentration (C_m) and geometric mass-mean mobility diameter ($d_{m,g}$) of the measured soot samples were, on average, within a $\sim$ 10% range of the gravimetric mass concentration and SMPS mobility diameter measurements. Such small differences between the FEN and gravimetric filters are justified based on an analysis of particle losses in a thermodenuder placed between the two instruments. Differences in the measured diameters, however, are likely attributed to our aggregate modeling assumptions, namely the equality between the mobility and projected-area diameters, which is only valid in the molecular and parts of the transition regimes. Despite such close agreements, the inversion results were sensitive to the morphological and physical parameters of the RDGFA model. Namely, C_m could vary by more than $\pm$40% due to its sensitivity to the model parameters, most notably the soot absorption coefficient (κ, imaginary part of the refractive index), the primary particle diameter (d_p), and the fractal pre-factor (k_f), or due to approximations inherent in the RDGFA model. By implementing the primary particle-aggregate correlations derived from the EMH model, these variations are reduced to within $\sim \pm 25\%$ of the reference measurements. The findings here improved our understanding of the comparison between the gravimetric and light-scattering soot concentration measurements and can be applied in other applications where indirect optical methods are used for measuring soot.

The diluted exhaust calibrations have demonstrated the validity of our light-scattering inversion procedure, they have also highlighted the significance of the inversion variabilities due to the uncertainty of the underlying RDGFA parameters. This must be considered when conducting exhaust-port measurements, as soot morphology changes in the exhaust system. Using morphological parameters obtained from down-stream samples were shown to generate gross discrepancies, whereas D_f, D_{TEM}, $d_{p,100}$, and k_f determined from exhaust-port samples produced FEN results that were similar to diluted mass and mobility measurements, with variations of less than 30%. To measure exhaust-port soot concentrations with the FEN, the inversion toolkit was applied to crank-angle-recorded FEN signals with provisions based on the exhaust-port sampling conditions.

7.1.2 The cycle-resolved exhaust-port soot measurement

In order to minimize the measurement delays and realize the goal of developing a single-cycle measurement methodology, the FEN was implemented at the exhaust-port of SCRE to characterize the engine-out soot. The light scattering signals demonstrated consistent characteristics, but their intensity varied during and between cycles. By considering intra-cycle correlations between different segments of the light-scattering signals, relevant characteristics of the exhaust-port sampling system was extracted. Pressure waves emanated from the engine during exhaust valve opening (EVO), resuspended PM wall deposits into the sampled flow which crossed the laser beam and generated a strong light-scattering peak shortly after EVO. Inverted crank-angle-resolved $d_{m,g}$ histories during this period also indicated

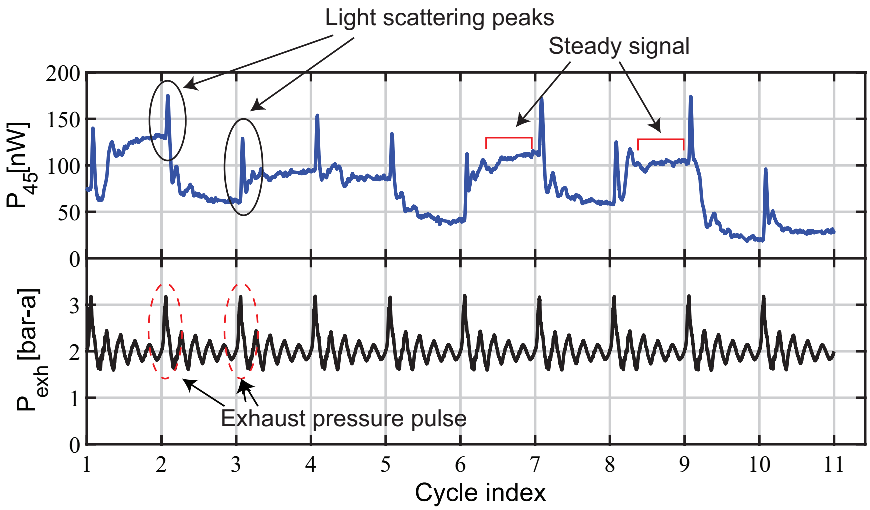

Figure 7.2: The FEN light scattering and the exhaust pressure histories during consecutive engine cycles, showing the coherent features repeated in every cycle.

larger particles, supporting our phenomenological understanding of early fluctuations in light-scattering signals. This is, however, separate from the engine exhaust gases which are transported convectively, and reach the FEN much later. The arrival of fresh exhaust gases is coincident with a relatively constant segment of the light-scattering signals, indicating a homogenous mixture inside the FEN.

The response time of the FEN is defined based on the arrival of the fresh exhaust charge determined from the skip-firing tests. The decaying light-scattering traces caused by disabling the fuel injection were analyzed to give the flow transfer delay (t_0, θ_0) and the time constant of the system (τ, δ). The measured response times based on the delay and time constants from the skip-firing tests are in the 45 ms - 70 ms range, and are sufficiently shorter than the duration of an engine cycle (80-130 ms), permitting single-cycle soot measurement at the exhaust port. Correspondingly, the cycle-specific soot concentrations and mean diameters were obtained based on a crank-angle averaging scheme that considers the steady portion of the crank-angle-resolved signals, marked in Figure 7.2.

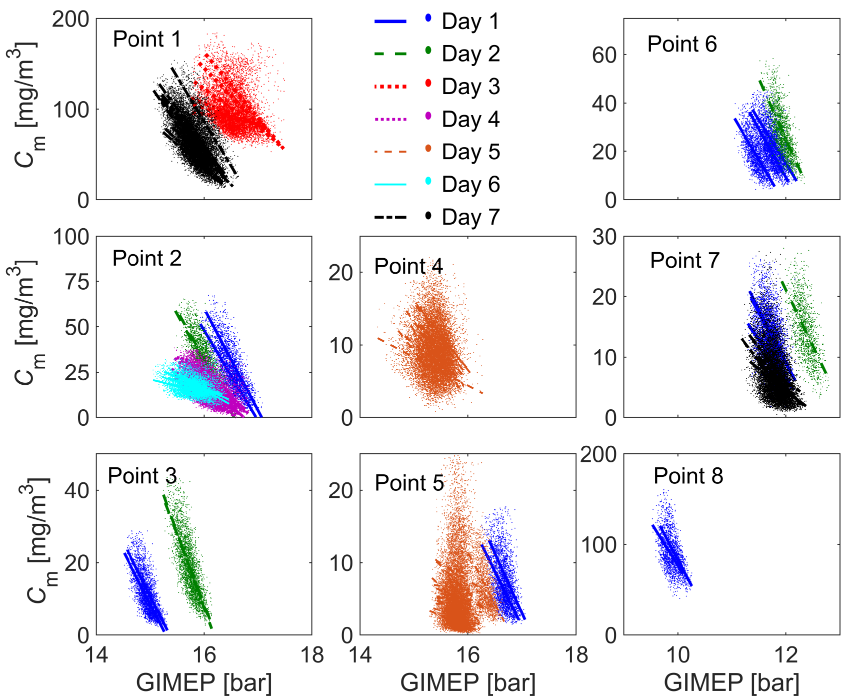

Figure 7.3: The correlations between the cycle-specific exhaust-port soot mass concentration and the in-cylinder GIMEP.

The averaged exhaust-port measurements were validated against diluted samples. The condition of the diluted sample was critical to this validation, demonstrated by collecting two samples along the exhaust path, one close to the exhaust port and the other down-stream of a surge tank. The down-stream samples were affected by particle coagulation due to residence times in the exhaust system, affecting their morphology and size, as mentioned earlier. The raw (FEN) and diluted (filters) exhaust-port mass concentrations were similar, where differences of less than ∼30% could exist for some operating points. The observed differences are believed to be due to factors such as semi-volatile condensation, different physicochemical soot properties, or variability of the engine operating points coupled with the time difference between the raw and diluted measurements.

The single-cycle method developed in this work can assist engine developers during the calibration procedures, where single-cycle events during transient operation could negatively affect the soot emissions and must be detected. As demonstrated here, it was made possible with this method to investigate the correlations between the cycle-resolved exhaust-port soot concentration and the in-cylinder combustion processes. After considering different metrics characterizing the in-cylinder combustion, the exhaust soot C_m is found to be negatively correlated with the gross indicated mean effective pressure (GIMEP). The R^2 value of the cycle-resolved GIMEP-C_m least-square regression fits can be as high as 0.7 for points with high equivalence ratio (ϕ) and early combustion phasing (θ_{50}), or as low as 0.2 for points operated without exhaust gas recirculation (EGR) or with late θ_{50} ($\sim$21 °aTDC), due to low concentrations or disparate soot morphology for these operating conditions. The negative correlations indicate that cycles with lower GIMEP tend to produce more soot, the causes of this association deserve further investigation, but are believed to be due to poor combustion in locally fuel-rich regions.

The PM emissions from internal combustion engines depend on the air-fuel mixing and combustion processes, which may vary from cycle to cycle due to effects induced by the fuel and air components. Deconvoluting the effects of these parameters on the net soot emissions is impeded by the rapid variation of exhaust soot concentration, which demands high-speed instruments and methodologies capable of single-cycle measurements. The methodology developed in this work based on the FEN multi-angle light-scattering measurements is fast, quantitatively validated against other instruments, and can be implemented for exhaust-port sampling from internal combustion engines. By applying this new tool to a PIDING research engine, new patterns were uncovered between the in-cylinder GIMEP and exhaust soot concentration that were not known before. This demonstrates a utility of this method for engine experiments, and can be implemented on other, applied or fundamental-level, engine setups as well. Some applications can include researching engine transient emissions on dynamometer or during on-road testing, or on optical research engines to support the in-cylinder soot measurement diagnostics. Application of this method in transient emissions research, on testbeds or during on-road measurements, can help identify the high-emitting cycles, further our understanding of the transient soot emissions results, and guide the design of new test cycles for soot emission research.

7.2 Recommendations

The findings of this work highlight the benefits of cycle-resolved exhaust-stream soot measurement. This method can be enhanced by making appropriate modifications to the FEN or the inversion method, and may be used in other applications, as discussed below.

7.2.1 Modifications to the FEN

By using the FEN in the reported experiments, areas where its design and operation can be improved are identified. Firstly, the FEN requires a laser assembly that is well-aligned with optical passages to avoid stray light reflections from internal surfaces. This tedious process can be improved by a rig designed and engineered to facilitate the laser calibration, alignment, and polarization measurement. Additionally, the residual stray light reflections from the beam entrance and exit bores can be avoided by increasing the bore sizes to allow wider beam diameters.

The quality and accuracy of the inverted C_m, $d_{m,g}$, and $\sigma_{m,g}$ can also be enhanced by considering more angles for light scattering measurements, or multiple lasers with different wavelengths. Higher angular resolution is useful to recover the morphology parameters, such as the fractal dimension, or to improve the quality of the recovered polydispersity parameters such as $\sigma_{m,g}$ which had poor inversion results. Multiple wavelengths can be utilized to recover, or narrow down, the range of the soot refractive indices based on optical dispersion models [17].

To enhance the dynamic range of the FEN for PM concentration, specifically to extend its lower detection limit, the light scattering from gas molecules needs to be considered. Unfortunately, these can produce 1 - 3 nW on the photodetectors, depending on the temperature and the chemical composition of exhaust gases. This interferes with the PM measurement, especially on the 135° detector where soot light intensity is ~ 3 times weaker than on the 45° detector, and its effect is equivalent to ~ 1 mg/m^3 of soot concentration. The minimum detection limit of the FEN is critically limited by the uncertainty of light scattering from exhaust gases, especially due to the variability of exhaust temperature and chemical composition between different operating points. It might be possible to remedy this by accurately controlling the sample delivery temperature, thereby eliminating a source of variability and possibly expanding the FEN detection limit to ~ 0.1 - 0.2 mg/m^3.

7.2.2 Engine operating space

The conclusions here are based on the engine tests over a limited operating space, and does not investigate the effect of individual engine parameters on cycle-cycle soot concentration variations. An expanded test matrix must be designed to study the isolated effect of different engine parameters, such as the mean GIMEP, θ_{50}, ϕ, EGR, and injection pressure, to name a few. Due to the challenges of adjusting a single engine parameter without affecting the others, and the prohibitive size of a test matrix that considers all factorials, here we recommend investigating the effects of θ_{50}, and EGR, as these were found to have the largest impact on the C_m-GIMEP correlations.

A key area where fast-response soot measurement is beneficial is during the transient single or multi-cylinder engine operation, where the specific cycles or cylinders responsible for high soot emissions can be isolated and probed. Such information can be compared to other cycle-resolved parameters, such as the commanded injection duration, or the in-cylinder combustion metrics to investigate the root-cause of the anomalies.

7.2.3 Complementary in-cylinder and exhaust diagnostics

The underlying mechanisms responsible for the C_m-GIMEP correlations observed in this work are unknown and require further investigation. Complementary information available from optical research engines, such as the pyrometric soot optical thickness, KL, can further our understanding of the correlations between the in-cylinder and exhaust soot. It is known that crank-angle-resolved in-cylinder KL vary substantially from cycle to cycle, and the variations are larger during the oxidation process [102, 197]. The KL_{end} metric used in the literature to characterize the cycle-specific soot, needs to be compared to the single-cycle exhaust-port C_m to evaluate its suitability as a cycle-specific metric, and understand the impacts of late-cycle oxidation on the overall soot emission rates.

Further insights into cycle-cycle variability may be gained from gaseous exhaust emissions, namely from the cycle-resolved concentrations of CH_4, unburned hydrocarbons (uHC), carbon monoxide (CO), and NO_x. It is speculated that the in-cylinder combustion variations responsible for the negative C_m-GIMEP correlations, produces similar correlations with other emissions such as uHC or CO. A low-GIMEP cycle coincident with high uHD and CO can imply poor fuel conversion which exacerbates the PM, CO, and uHC emissions simultaneously. It is likely that the cycle-resolved NO_x and GIMEP correlate positively, assuming that cycles with higher GIMEP have higher temperatures that accelerate the NO_x thermal reactions. The overall effect of the cycle-cycle combustion variability on the engine PM and gaseous emissions is important in the low-emission combustion strategies and can guide the development of new combustion regimes.

7.2.4 Transient measurements and real-world applications

So far, the applications described here include fundamental-level research configuration, such as using the FEN in conjunction with single-cylinder all-metal or optical engines. The FEN, however, can be implemented to measure the exhaust soot from multi-cylinder engines operated under transient conditions. Such implementations can assist engine designers to determine the impacts of real-world transient operating conditions, cylinder imbalances, or engine controls strategies on cycle-resolved soot emissions. The FEN is particularly well-suited for real-world applications as it is designed to handle harsh conditions at the exhaust port, such as vibrations and high exhaust pressures and temperatures. This is a critical advantage of this method, as most PM instruments cannot endure the demanding real-drive measurement requirements, or require extra care for uncertainties associated with exhaust dilution and conditioning, whereas one need not worry about such artefacts with FEN raw exhaust measurements.

Bibliography

[1] I. S. Abdul-Khalek and D. B. Kittelson. Real time measurement of volatile and solid exhaust particles using a catalytic stripper. *SAE transactions*, pages 462–478, 1995. → page 28

[2] E. A. M. A. (ACEA). Passenger car fleet by fuel type, 2018. URL https://www.acea.be/statistics/article/Passenger-Car-Fleet-by-Fuel-Type. → page 1

[3] M. Altenhoff, S. Aßmann, C. Teige, F. J. Huber, and S. Will. An optimized evaluation strategy for a comprehensive morphological soot nanoparticle aggregate characterization by electron microscopy. *Journal of Aerosol Science*, 139:105470, 2020. → pages 32, 84, 93, 94

[4] S. Amanatidis, M. M. Maricq, L. Ntziachristos, and Z. Samaras. Application of the dual pegasor particle sensor to real-time measurement of motor vehicle exhaust pm. *Journal of Aerosol Science*, 103:93–104, 2017. → page 36

[5] S. Amanatidis, L. Ntziachristos, P. Karjalainen, E. Saukko, P. Simonen, N. Kuittinen, P. Aakko-Saksa, H. Timonen, T. Rönkkö, and J. Keskinen. Comparative performance of a thermal denuder and a catalytic stripper in sampling laboratory and marine exhaust aerosols. *Aerosol Science and Technology*, 52(4):420–432, 2018. → page 93

[6] H. M. Amin and W. L. Roberts. Soot measurements by two angle scattering and extinction in an N_2-diluted ethylene/air counterflow

diffusion flame from 2 to 5 atm. *Proceedings of the Combustion Institute*, 36(1):861–869, 2017. → pages 7, 8, 196

[7] S. Bai, G. Chen, Q. Sun, G. Wang, and G.-x. Li. Influence of active control strategies on exhaust thermal management for diesel particular filter active regeneration. *Applied Thermal Engineering*, 119:297–303, 2017. → page 30

[8] A. Baldelli and S. N. Rogak. Morphology and Raman spectra of aerodynamically classified soot samples. *Atmospheric Measurement Techniques*, 12(8), 2019. → pages 19, 76

[9] A. Baldelli, U. Trivanovic, and S. N. Rogak. Electron tomography of soot for validation of 2D image processing and observation of new structural features. *Aerosol Science and Technology*, 53(5):575–582, 2019. → page 70

[10] J. Ball, C. Stone, and N. Collings. Cycle-by-cycle modelling of NO formation and comparison with experimental data. *Proceedings of the Institution of Mechanical Engineers, Part D: Journal of Automobile Engineering*, 213(2):175–189, 1999. → pages 4, 142

[11] C. Barro, P. Obrecht, and K. Boulouchos. Development and validation of a virtual soot sensor: Part 1: steady-state engine operation. *International Journal of Engine Research*, 15(6):719–730, 2014. → pages 6, 16, 45

[12] C. Barro, P. Obrecht, and K. Boulouchos. Development and validation of a virtual soot sensor: Part 2: Transient engine operation. *International Journal of Engine Research*, 16(2):127–136, 2015. → pages 16, 45

[13] J. N. Bates. Nitric oxide measurement by chemiluminescence detection. *Neuroprotocols*, 1(2):141–149, 1992. → page 54

[14] H. Beck, R. Niessner, and C. Haisch. Development and characterization of a mobile photoacoustic sensor for on-line soot emission moni-

toring in diesel exhaust gas. *Analytical and Bioanalytical Chemistry*, 375(8):1136–1143, 2003. → page 5

[15] M. Beck and K. Hinterhofer. Direct high dynamic flow measurement in the exhaust of combustion engines. *SAE Technical Paper*, (980880), 1998. → page 100

[16] L. Benbrahim-Tallaa, R. A. Baan, Y. Grosse, B. Lauby-Secretan, F. El Ghissassi, V. Bouvard, N. Guha, D. Loomis, K. Straif, on behalf of the International Agency for Research on Cancer Monograph Working Group, and I. A. for Research on Cancer Monograph Working Group. Carcinogenicity of diesel-engine and gasoline-engine exhausts and some nitroarenes. *The lancet oncology*, 13(7):663–664, 2012. → page 1

[17] A. Bescond, J. Yon, F.-X. Ouf, C. Rozé, A. Coppalle, P. Parent, D. Ferry, and C. Laffon. Soot optical properties determined by analyzing extinction spectra in the visible near-UV: Toward an optical speciation according to constituents and structure. *Journal of Aerosol Science*, 101:118–132, 2016. → pages 72, 77, 151, 188

[18] G. Blair and J. Goulburn. The pressure-time history in the exhaust system of a high-speed reciprocating internal combustion engine. *SAE Transactions*, pages 1725–1732, 1968. → page 100

[19] C. F. Bohren and D. R. Huffman. *Absorption and scattering of light by small particles*. John Wiley & Sons, 2008. → pages 23, 24, 74

[20] T. C. Bond and R. W. Bergstrom. Light absorption by carbonaceous particles: An investigative review. *Aerosol Science and Technology*, 40 (1):27–67, 2006. → pages 18, 19, 76, 188

[21] T. C. Bond, S. J. Doherty, D. W. Fahey, P. M. Forster, T. Berntsen, B. J. DeAngelo, M. G. Flanner, S. Ghan, B. Kärcher, D. Koch, et al. Bounding the role of black carbon in the climate system: A scientific assessment. *Journal of Geophysical Research: Atmospheres*, 118(11): 5380–5552, 2013. → pages 1, 2

[22] A. Brasil, T. L. Farias, and M. Carvalho. A recipe for image characterization of fractal-like aggregates. *Journal of Aerosol Science*, 30 (10):1379–1389, 1999. → pages 17, 57, 70, 71, 93, 188, 194

[23] R. D. Brook, S. Rajagopalan, C. A. Pope III, J. R. Brook, A. Bhatnagar, A. V. Diez-Roux, F. Holguin, Y. Hong, R. V. Luepker, M. A. Mittleman, et al. Particulate matter air pollution and cardiovascular disease: an update to the scientific statement from the american heart association. *Circulation*, 121(21):2331–2378, 2010. → page 1

[24] D. Burr, K. Daun, O. Link, K. Thomson, and G. Smallwood. Determination of the soot aggregate size distribution from elastic light scattering through Bayesian inference. *Journal of Quantitative Spectroscopy and Radiative Transfer*, 112(6):1099–1107, 2011. → pages 7, 9, 40, 41

[25] H. Burtscher, U. Baltensperger, N. Bukowiecki, P. Cohn, C. Hüglin, M. Mohr, U. Matter, S. Nyeki, V. Schmatloch, N. Streit, et al. Separation of volatile and non-volatile aerosol fractions by thermodesorption: instrumental development and applications. *Journal of Aerosol Science*, 32(4):427–442, 2001. → pages 28, 56

[26] J. Cai, N. Lu, and C. M. Sorensen. Analysis of fractal cluster morphology parameters: Structural coefficient and density autocorrelation function cutoff. *Journal of Colloid and Interface Science*, 171:470–473, 1995. → pages 25, 188

[27] C. Caumont-Prim, J. Yon, A. Coppalle, F.-X. Ouf, and K. F. Ren. Measurement of aggregates' size distribution by angular light scattering. *Journal of Quantitative Spectroscopy and Radiative Transfer*, 126: 140–149, 2013. → pages 68, 69

[28] W. K. Cheng, T. Summers, and N. Collings. The fast-response flame ionization detector. *Progress in Energy and Combustion Science*, 24 (2):89–124, 1998. → pages 101, 102, 104, 119

[29] S. K. Cheung, S. T. Elder, and R. R. Raine. Diesel particulate measurements with a light scattering photometer. *SAE Technical Paper*, (2000-01-1136), 2000. → pages 7, 37

[30] S. Colin. Single-phase gas flow in microchannels. *Heat transfer and fluid flow in minichannels and microchannels*, pages 9–86. → page 113

[31] N. Collings and J. Willey. Cyclically resolved HC emissions from a spark ignition engine. *SAE Technical Paper*, (871691), 1987. → pages 8, 101

[32] R. Dastanpour. *Characterization of primary particle size variation and its influence on measurable properties of aerosol soot*. PhD thesis, University of British Columbia, 2016. → page 18

[33] R. Dastanpour and S. N. Rogak. Observations of a correlation between primary particle and aggregate size for soot particles. *Aerosol Science and Technology*, 48(10):1043–1049, 2014. → page 8

[34] R. Dastanpour, J. M. Boone, and S. N. Rogak. Automated primary particle sizing of nanoparticle aggregates by TEM image analysis. *Powder Technology*, 295:218–224, 2016. → pages 32, 57, 70, 82, 202

[35] R. Dastanpour, S. N. Rogak, B. Graves, J. Olfert, M. L. Eggersdorfer, and A. M. Boies. Improved sizing of soot primary particles using mass-mobility measurements. *Aerosol Science and Technology*, 50(2): 101–109, 2016. → pages 71, 94, 188, 202, 203

[36] R. Dastanpour, A. Momenimovahed, K. Thomson, J. Olfert, and S. Rogak. Variation of the optical properties of soot as a function of particle mass. *Carbon*, 124:201–211, 2017. → pages 19, 69, 76

[37] P. Davis and M. S. Peckham. Measurement of cycle-by-cycle AFR using a fast response NDIR analyzer for cold start fuelling calibration applications. *SAE Technical Paper*, (2006-01-1515), 2006. → page 4

[38] S. De Iuliis, F. Cignoli, S. Benecchi, and G. Zizak. Determination of soot parameters by a two-angle scattering–extinction technique in an ethylene diffusion flame. *Applied Optics*, 37(33):7865–7874, 1998. → pages 7, 68

[39] P.-J. De Temmerman, E. Verleysen, J. Lammertyn, and J. Mast. Semi-automatic size measurement of primary particles in aggregated nanomaterials by transmission electron microscopy. *Powder Technology*, 261:191–200, 2014. → page 32

[40] J. E. Dec. A conceptual model of DI diesel combustion based on laser-sheet imaging. *SAE transactions*, pages 1319–1348, 1997. → page 16

[41] Diesel Technology Forum. Climate change and diesel technology, 2018. URL https://www.dieselforum.org/policy/climate-change-and-diesel-technology. → page 1

[42] Dieselnet. Emission Standards, EU: Heavy-Duty Truck and Bus Engines, 2019. URL https://dieselnet.com/standards/eu/hd.php. → pages 3, 28

[43] Dieselnet. Emission Test Cycles, 2019. URL https://dieselnet.com/standards/cycles/index.php#eu-hd. → page 2

[44] R. A. Dobbins and C. M. Megaridis. Absorption and scattering of light by polydisperse aggregates. *Applied Optics*, 30(33):4747–4754, 1991. → pages 25, 26, 73, 74, 89, 90, 92

[45] B. T. Draine and P. J. Flatau. Discrete-dipole approximation for scattering calculations. *Journal of the Optical Society of America. A, Optics, image science, and vision*, 11(4):1491–1499, 1994. → page 38

[46] M. D. Durham and D. A. Lundgren. Evaluation of aerosol aspiration efficiency as a function of stokes number, velocity ratio and nozzle angle. *Journal of Aerosol Science*, 11(2):179–188, 1980. → page 34

[47] M. L. Eggersdorfer, A. J. Gröhn, C. Sorensen, P. H. McMurry, and S. E. Pratsinis. Mass-mobility characterization of flame-made ZrO_2 aerosols: Primary particle diameter and extent of aggregation. *Journal of Colloid and Interface Science*, 387(1):12–23, 2012. → pages 35, 72, 84, 131

[48] E. Faghani. *Effect of injection strategies on particulate matter emissions from HPDI natural-gas engine*. PhD thesis, University of British Columbia, 2015. → page 49

[49] E. Faghani, P. Kheirkhah, C. W. Mabson, G. McTaggart-Cowan, P. Kirchen, and S. Rogak. Effect of injection strategies on emissions from a pilot-ignited direct-injection natural-gas engine-part i: Late post injection. *SAE Technical Paper*, (2017-01-0774), 2017. → page 30

[50] E. Faghani, P. Kheirkhah, C. W. Mabson, G. McTaggart-Cowan, P. Kirchen, and S. Rogak. Effect of injection strategies on emissions from a pilot-ignited direct-injection natural-gas engine-part ii: Slightly premixed combustion. *SAE Technical Paper*, (2017-01-0763), 2017. → page 30

[51] T. L. Farias, Ü. Ö. Köylü, and M. d. G. Carvalho. Range of validity of the Rayleigh–Debye–Gans theory for optics of fractal aggregates. *Applied Optics*, 35(33):6560–6567, 1996. → page 39

[52] I. Finlay, D. Boam, J. Bingham, and T. Clark. Fast response FID measurement of unburned hydrocarbons in the exhaust port of a firing gasoline engine. *SAE Technical Paper*, (902165), 1990. → page 101

[53] R. C. Flagan. Differential mobility analysis of aerosols: a tutorial. *KONA Powder and Particle Journal*, 26:254–268, 2008. → page 33

[54] R. C. Flagan and J. H. Seinfeld. *Fundamentals of air pollution engineering*, chapter 5, pages 290–357. Courier Corporation, 2012. → page 33

[55] S. Forrest and T. Witten Jr. Long-range correlations in smoke-particle aggregates. *Journal of Physics A: Mathematical and General*, 12(5): L109, 1979. → page 24

[56] M. Frenklach. Reaction mechanism of soot formation in flames. *Physical Chemistry Chemical Physics*, 4(11):2028–2037, 2002. → page 14

[57] S. Friedlander and C. Wang. The self-preserving particle size distribution for coagulation by Brownian motion. *Journal of Colloid and Interface Science*, 22(2):126–132, 1966. → page 27

[58] Gamma Technologies. Gt-suite overview, 2020. URL https://www.gtisoft.com/gt-suite/gt-suite-overview/. → page 103

[59] E. G. Giakoumis. *Driving and engine cycles*. Springer, 2017. → pages 28, 29

[60] B. Giechaskiel. Solid particle number emission factors of Euro VI heavy-duty vehicles on the road and in the laboratory. *International journal of environmental research and public health*, 15(2):304, 2018. → page 29

[61] B. Giechaskiel, M. Maricq, L. Ntziachristos, C. Dardiotis, X. Wang, H. Axmann, A. Bergmann, and W. Schindler. Review of motor vehicle particulate emissions sampling and measurement: From smoke and filter mass to particle number. *Journal of Aerosol Science*, 67:48–86, 2014. → pages 3, 5, 17, 27, 29, 31

[62] M. Gilbert and N. Clark. Measurement of particulate matter from diesel engine exhaust using a tapered element oscillating microbalance. *International Journal of Engine Research*, 2(4):277–287, 2001. → page 35

[63] W. Glewen, D. Heuwetter, D. Foster, M. Andrie, and R. Krieger. Analysis of deviations from steady state performance during transient operation of a light duty diesel engine. *SAE International Journal of Engines*, 5(3):909–922, 2012. → page 3

[64] N. F. González, J. C. Kindelán, J. M. L. Martí, et al. Methodology for instantaneous average exhaust gas mass flow rate measurement. *Flow Measurement and Instrumentation*, 49:52–62, 2016. → page 100

[65] B. Graves, J. Olfert, B. Patychuk, R. Dastanpour, and S. Rogak. Characterization of particulate matter morphology and volatility from a compression-ignition natural-gas direct-injection engine. *Aerosol Science and Technology*, 49(8):589–598, 2015. → pages 27, 35, 74, 79, 82, 83, 215

[66] A. P. Grieshop, C. C. Reynolds, M. Kandlikar, and H. Dowlatabadi. A black-carbon mitigation wedge. *Nature Geoscience*, 2(8):533–534, 2009. → page 2

[67] I. Grishin, K. Thomson, F. Migliorini, and J. J. Sloan. Application of the hough transform for the automatic determination of soot aggregate morphology. *Applied Optics*, 51(5):610–620, 2012. → page 32

[68] B. Guan, R. Zhan, H. Lin, and Z. Huang. Review of the state-of-the-art of exhaust particulate filter technology in internal combustion engines. *Journal of Environmental Management*, 154:225–258, 2015. → pages 3, 30

[69] J. Hagena, D. Assanis, and Z. Filipi. Cycle-resolved measurements of in-cylinder constituents during diesel engine transients and insight into their impact on emissions. *Proceedings of the Institution of Mechanical Engineers, Part D: Journal of Automobile Engineering*, 225(9):1103–1117, 2011. → pages 4, 124, 140

[70] J. R. Hagena, Z. Filipi, and D. N. Assanis. Transient diesel emissions: analysis of engine operation during a tip-in. *SAE Technical Paper*, (2006-01-1151), 2006. → pages 3, 4, 28, 124, 137

[71] D. E. Hall and C. J. Dickens. Measurement of the numbers of emitted gasoline particles: Genuine or artefact? *SAE transactions*, pages 3000–3008, 2000. → page 29

[72] A. Hansen and R. Schnell. The aethalometer. *Magee Scientific Company, Berkeley, California, USA*, pages 1–209, 2005. → page 36

[73] S. J. Harris and M. M. Maricq. Signature size distributions for diesel and gasoline engine exhaust particulate matter. *Journal of Aerosol Science*, 32(6):749–764, 2001. → page 27

[74] E. Helmers, J. Leitão, U. Tietge, and T. Butler. CO_2-equivalent emissions from European passenger vehicles in the years 1995–2015 based on real-world use: Assessing the climate benefit of the European "diesel boom". *Atmospheric Environment*, 198:122–132, 2019. → page 2

[75] C. Henry. Product review: Measuring the masses: Quartz crystal microbalances. *Analytical Chemistry*, 68(19):625A–628A, 1996. → page 35

[76] J. B. Heywood. *Internal Combustion Engine Fundamentals*. McGraw-Hill, 1988. → page 55

[77] D. J. Holve. Two-angle ratio scattering (STAR) method for real-time measurement of agglomerate soot concentration and size: Theory. *Aerosol Science and Technology*, 45(11):1388–1399, 2011. → pages 7, 89, 188

[78] D. J. Holve, J. Chapman, and R. Graze. Two-angle ratio scattering (STAR) method for real-time measurement of agglomerate soot concentration and size: Experimental measurements. *Aerosol Science and Technology*, 45(11):1400–1407, 2011. → pages 8, 42, 69, 89, 196

[79] Y. Hotta, M. Inayoshi, K. Nakakita, K. Fujiwara, and I. Sakata. Achieving lower exhaust emissions and better performance in an HSDI diesel engine with multiple injection. *SAE Technical Paper*, (2005-01-0928), 2005. → page 30

[80] F. J. Huber, S. Will, and K. J. Daun. Sizing aerosolized fractal nanoparticle aggregates through bayesian analysis of wide-angle light

scattering (wals) data. *Journal of Quantitative Spectroscopy and Radiative Transfer*, 184:27–39, 2016. → pages 9, 41

[81] E. Huestis, P. A. Erickson, and M. P. Musculus. In-cylinder and exhaust soot in low-temperature combustion using a wide-range of EGR in a heavy-duty diesel engine. *SAE Transactions*, pages 860–870, 2007. → page 6

[82] H. C. Hulst and H. C. van de Hulst. *Light scattering by small particles*. Courier Corporation, 1981. → pages 21, 22, 74

[83] A. J. Hurd and W. L. Flower. In situ growth and structure of fractal silica aggregates in a flame. *Journal of Colloid and Interface Science*, 122(1):178–192, 1988. → page 68

[84] A. Isenstadt, J. German, M. Dorobantu, D. Boggs, and T. Watson. Downsized, boosted gasoline engines. *The International Council on Clean Transportation*, 2016. → page 2

[85] D. Jaggard, C. Hill, R. Shorthill, D. Stuart, M. Glantz, F. Rosswog, B. Taggart, and S. Hammond. Light scattering from particles of regular and irregular shape. *Atmospheric Environment*, 15(12):2511–2519, 1981. → pages 24, 61, 183

[86] A. Järvinen, M. Aitomaa, A. Rostedt, J. Keskinen, and J. Yli-Ojanperä. Calibration of the new electrical low pressure impactor (ELPI+). *Journal of Aerosol Science*, 69:150–159, 2014. → page 35

[87] J. Jeon, N. Bock, D. B. Kittelson, and W. F. Northrop. Correlation of nanoparticle size distribution features to spatiotemporal flame luminosity in gasoline direct injection engines. *International Journal of Engine Research*, 21(7):1107–1117, 2020. → pages 4, 6, 140

[88] J. Jimenez, C. Claiborn, T. Larson, T. Gould, T. W. Kirchstetter, and L. Gundel. Loading effect correction for real-time aethalometer measurements of fresh diesel soot. *Journal of the Air & Waste Management Association*, 57(7):868–873, 2007. → page 5

[89] T. Johnson, R. Caldow, A. Pöcher, A. Mirme, and D. Kittelson. A new electrical mobility particle sizer spectrometer for engine exhaust particle measurements. *SAE Technical Paper*, (2004-01-1341), 2004. → pages 5, 34

[90] H. L. Jones. Source and characterization of particulate matter from a pilot-ignited natural gas fuelled engine. Master's thesis, University of British Columbia, 2004. → page 49

[91] Z. Juranyi, M. Loepfe, M. Nenkov, and H. Burtscher. Multi-angle, dual wavelength scattering measurement chamber for the structural measurement of combustion generated particles. *Journal of Aerosol Science*, 103:83–92, 2017. → page 68

[92] G. A. Karim. *Dual-fuel diesel engines*, chapter Dual-fuel engine performance. CRC Press, 2015. → page 30

[93] A. Karvountzis-Kontakiotis, A. Dimaratos, L. Ntziachristos, and Z. Samaras. Exploring the stochastic and deterministic aspects of cyclic emission variability on a high speed spark-ignition engine. *Energy*, 118:68–76, 2017. → pages 120, 142

[94] G. A. Kelesidis and S. E. Pratsinis. Soot light absorption and refractive index during agglomeration and surface growth. *Proceedings of the Combustion Institute*, 37(1):1177–1184, 2019. → pages 19, 77, 188

[95] M. K. Khair. A review of diesel particulate filter technologies. *SAE Technical Paper*, (2003-01-2303), 2003. → pages 3, 29

[96] I. A. Khalek, T. L. Bougher, P. M. Merritt, and B. Zielinska. Regulated and unregulated emissions from highway heavy-duty diesel engines complying with US Environmental Protection Agency 2007 emissions standards. *Journal of the Air & Waste Management Association*, 61(4):427–442, 2011. → page 17

[97] P. Kheirkhah. CFD modeling of injection strategies in a High-Pressure

Direct-Injection (HPDI) natural gas engine. Master's thesis, University of British Columbia, 2015. → page 16

[98] P. Kheirkhah, A. Baldelli, P. Kirchen, and S. Rogak. Development and validation of a multi-angle light scattering method for fast engine soot mass and size measurements. *Aerosol Science and Technology*, 54. → pages 25, 41, 63, 67, 131, 135

[99] P. Kheirkhah, P. Kirchen, and S. Rogak. Fast exhaust nephelometer (FEN): A new instrument for measuring cycle-resolved engine particulate emission. *SAE Technical Paper*, (2016-01-2329), 2016. → pages 7, 8, 62, 64, 91, 106, 107, 108

[100] M. Khosravi and P. Kirchen. Refinement of the two-color pyrometry method for application in a direct injection diesel and natural gas compression-ignition engine. *Proceedings of the Institution of Mechanical Engineers, Part D: Journal of Automobile Engineering*, 233(14): 3787–3800, 2019. → page 125

[101] M. Khosravi, J. Rochussen, J. Yeo, P. Kirchen, G. McTaggart-Cowan, and N. Wu. Effect of fuelling control parameters on combustion characteristics of diesel-ignited natural gas dual-fuel combustion in an optical engine. In *ASME 2016 Internal Combustion Engine Division Fall Technical Conference*. American Society of Mechanical Engineers Digital Collection, 2016. → page 16

[102] P. Kirchen. *Steady-state and transient diesel soot emissions: Development of a mean value soot model and exhaust-stream and in-cylinder measurements*. PhD thesis, ETH Zurich, 2008. → pages 4, 6, 125, 140, 153

[103] P. Kirchen, P. Obrecht, and K. Boulouchos. Soot emission measurements and validation of a mean value soot model for common-rail diesel engines during transient operation. *SAE international journal of engines*, 2(1):1663–1678, 2009. → page 16

[104] P. Kirchen, P. Obrecht, K. Boulouchos, and A. Bertola. Exhaust-stream and in-cylinder measurements and analysis of the soot emissions from a common rail diesel engine using two fuels. *Journal of Engineering for Gas Turbines and Power*, 132(11), 2010. → page 6

[105] Kistler. *ThermoCOMP type 6067C water-cooled precision cylinder pressure sensor*. Kistler, 2012. → page 50

[106] D. Kittelson and M. Stenitzer. A new catalytic stripper for removal of volatile particles. In *Proceedings of 7th ETH Conference on Combustion Generated Nanoparticles, ZUrich*, 2003. → page 28

[107] U. Koeylue, Y. Xing, and D. E. Rosner. Fractal morphology analysis of combustion-generated aggregates using angular light scattering and electron microscope images. *Langmuir*, 11(12):4848–4854, 1995. → page 188

[108] Ü. Ö. Köylü, G. Faeth, T. L. Farias, and M. d. G. Carvalho. Fractal and projected structure properties of soot aggregates. *Combustion and Flame*, 100(4):621–633, 1995. → pages 18, 71, 188

[109] P. Kyrtatos, C. Brückner, and K. Boulouchos. Cycle-to-cycle variations in diesel engines. *Applied Energy*, 171:120–132, 2016. → page 140

[110] P. Kyrtatos, A. Zivolic, C. Brueckner, and K. Boulouchos. The effect of cycle-to-cycle variations on the NOx-SFC tradeoff in diesel engines under long ignition delay conditions. *SAE International Journal of Engines*, 10(5):2451–2460, 2017. → pages 4, 120, 124

[111] M. Lapuerta, F. J. Martos, and M. D. Cárdenas. Determination of light extinction efficiency of diesel soot from smoke opacity measurements. *Measurement Science and Technology*, 16(10):2048, 2005. → page 37

[112] J. S. Lighty, J. M. Veranth, and A. F. Sarofim. Combustion aerosols: Factors governing their size and composition and implications to hu-

man health. *Journal of the Air & Waste Management Association*, 50 (9):1565–1618, 2000. → page 31

[113] J.-S. Lin and C.-J. Tsai. Thermophoretic deposition efficiency in a cylindrical tube taking into account developing flow at the entrance region. *Journal of Aerosol Science*, 34(5):569–583, 2003. → page 190

[114] M. Lin, R. Klein, H. Lindsay, D. A. Weitz, R. C. Ball, and P. Meakin. The structure of fractal colloidal aggregates of finite extent. *Journal of Colloid and Interface Science*, 137(1):263–280, 1990. → pages 25, 26, 74, 89, 90, 91, 92

[115] C. Liu, S. Teng, Y. Zhu, M. A. Yurkin, and Y. L. Yung. Performance of the discrete dipole approximation for optical properties of black carbon aggregates. *Journal of Quantitative Spectroscopy and Radiative Transfer*, 221:98–109, 2018. → page 38

[116] F. Liu and G. Smallwood. The effect of particle aggregation on the absorption and emission properties of mono-and polydisperse soot aggregates. *Applied Physics B*, 104(2):343–355, 2011. → page 36

[117] F. Liu, J. Yon, and A. Bescond. On the radiative properties of soot aggregates–part 2: Effects of coating. *Journal of Quantitative Spectroscopy and Radiative Transfer*, 172:134–145, 2016. → pages 38, 79

[118] F. Liu, J. Yon, A. Fuentes, P. Lobo, G. J. Smallwood, and J. C. Corbin. Review of recent literature on the light absorption properties of black carbon: Refractive index, mass absorption cross section, and absorption function. *Aerosol Science and Technology*, 54(1):33–51, 2020. → pages 19, 77, 93

[119] A. C. Lloyd and T. A. Cackette. Diesel engines: environmental impact and control. *Journal of the Air & Waste Management Association*, 51 (6):809–847, 2001. → page 2

[120] D. W. Mackowski and M. I. Mishchenko. Calculation of the T matrix and the scattering matrix for ensembles of spheres. *Journal of the

Optical Society of America. A, Optics, image science, and vision, 13 (11):2266–2278, 1996. → pages 37, 38

[121] A. Mamakos, L. Ntziachristos, and Z. Samaras. Evaluation of the Dekati mass monitor for the measurement of exhaust particle mass emissions. *Environmental Science & Technology*, 40(15):4739–4745, 2006. → page 35

[122] M. M. Maricq. Chemical characterization of particulate emissions from diesel engines: A review. *Journal of Aerosol Science*, 38(11):1079–1118, 2007. → page 17

[123] M. M. Maricq. Monitoring motor vehicle PM emissions: An evaluation of three portable low-cost aerosol instruments. *Aerosol Science and Technology*, 47(5):564–573, 2013. → pages 7, 37, 68, 135

[124] M. M. Maricq, N. Xu, and R. E. Chase. Measuring particulate mass emissions with the electrical low pressure impactor. *Aerosol Science and Technology*, 40(1):68–79, 2006. → page 35

[125] M. Marjamäki, J. Keskinen, D.-R. Chen, and D. Y. Pui. Performance evaluation of the electrical low-pressure impactor (ELPI). *Journal of Aerosol Science*, 31(2):249–261, 2000. → pages 5, 35

[126] N. A. Marley, J. S. Gaffney, J. C. Baird, C. A. Blazer, P. J. Drayton, and J. E. Frederick. An empirical method for the determination of the complex refractive index of size-fractionated atmospheric aerosols for radiative transfer calculations. *Aerosol Science & Technology*, 34(6): 535–549, 2001. → page 188

[127] J. May, D. Bosteels, and C. Favre. An assessment of emissions from light-duty vehicles using PEMS and chassis dynamometer testing. *SAE International Journal of Engines*, 7(3):1326–1335, 2014. → page 3

[128] G. McTaggart-Cowan, H. Jones, S. Rogak, W. Bushe, P. Hill, and S. Munshi. The effects of high-pressure injection on a compression-ignition, direct injection of natural gas engine. In *Internal Combustion*

Engine Division Fall Technical Conference, volume 47365, pages 161–173, 2005. → pages 81, 139

[129] G. McTaggart-Cowan, S. Rogak, S. Munshi, P. Hill, and W. Bushe. The influence of fuel composition on a heavy-duty, natural-gas direct-injection engine. *Fuel*, 89(3):752–759, 2010. → page 30

[130] G. McTaggart-Cowan, K. Mann, J. Huang, A. Singh, B. Patychuk, Z. X. Zheng, and S. Munshi. Direct injection of natural gas at up to 600 bar in a pilot-ignited heavy-duty engine. *SAE International Journal of Engines*, 8(3):981–996, 2015. → page 30

[131] G. P. McTaggart-Cowan. *Pollutant formation in a gaseous-fuelled, direct injection engine.* PhD thesis, University of British Columbia, 2006. → pages 49, 56

[132] P. Meakin. Fractal aggregates. *Advances in Colloid and Interface Science*, 28:249–331, 1987. → pages 17, 24, 73

[133] S. T. Moghaddam, P. J. Hadwin, and K. J. Daun. Soot aggregate sizing through multiangle elastic light scattering: Influence of model error. *Journal of Aerosol Science*, 111:36–50, 2017. → pages 40, 73

[134] G. Mordas, H. Manninen, T. Petäjä, P. Aalto, K. Hämeri, and M. Kulmala. On operation of the ultra-fine water-based CPC TSI 3786 and comparison with other TSI models (TSI 3776, TSI 3772, TSI 3025, TSI 3010, TSI 3007). *Aerosol Science and Technology*, 42(2):152–158, 2008. → page 31

[135] S. Mosbach, M. S. Celnik, A. Raj, M. Kraft, H. R. Zhang, S. Kubo, and K.-O. Kim. Towards a detailed soot model for internal combustion engines. *Combustion and Flame*, 156(6):1156–1165, 2009. → page 15

[136] G. W. Mulholland, A. Hamins, and T. Kashiwagi. Comparisons of the soot volume fraction using gravimetric and light extinction techniques. *Combust Flame*, 102:161–169, 1995. → page 188

[137] M. P. Musculus, P. C. Miles, and L. M. Pickett. Conceptual models for partially premixed low-temperature diesel combustion. *Progress in Energy and Combustion Science*, 39(2-3):246–283, 2013. → pages 16, 30

[138] G. Myhre, D. Shindell, F. Bréon, W. Collins, J. Fuglestvedt, J. Huang, D. Koch, J. Lamarque, D. Lee, B. Mendoza, et al. *Climate Change 2013 – The Physical Science Basis: Working Group I Contribution to the Fifth Assessment Report of the Intergovernmental Panel on Climate Change*, chapter 8, pages 659–740. Cambridge University Press, 2014;2015;. → page 2

[139] C. Myung, A. Ko, and S. Park. Review on characterization of nano-particle emissions and PM morphology from internal combustion engines: Part 1. *International Journal of Automotive Technology*, 15(2): 203–218, 2014. → page 17

[140] H. Nakamura, I. Asano, M. Adachi, and J. Senda. Analysis of pulsating flow measurement of engine exhaust by a pitot tube flowmeter. *International Journal of Engine Research*, 6(1):85–93, 2005. → page 100

[141] K. Nishida and H. Hiroyasu. Simplified three-dimensional modeling of mixture formation and combustion in a di diesel engine. *SAE transactions*, pages 276–293, 1989. → pages 6, 15

[142] W. F. Northrop, S. V. Bohac, J.-Y. Chin, and D. N. Assanis. Comparison of filter smoke number and elemental carbon mass from partially premixed low temperature combustion in a direct-injection diesel engine. *Journal of Engineering for Gas Turbines and Power*, 133(10), 2011. → page 36

[143] W. F. Northrop, D. Zarling, and X. Li. Considerations in using photometer instruments for measuring total particulate matter mass concentration in diesel engine exhaust. *Journal of Engineering for Gas Turbines and Power*, 140(11), 2018. → pages 7, 135

[144] L. Ntziachristos, S. Amanatidis, Z. Samaras, K. Janka, and J. Tikkanen. Application of the Pegasor particle sensor for the measurement of mass and particle number emissions. *SAE International Journal of Fuels and Lubricants*, 6(2):521–531, 2013. → pages 6, 35

[145] C. Oh and C. Sorensen. The effect of overlap between monomers on the determination of fractal cluster morphology. *Journal of Colloid and Interface Science*, 193(1):17–25, 1997. → pages 18, 84, 93, 188

[146] J. Olfert and S. Rogak. Universal relations between soot effective density and primary particle size for common combustion sources. *Aerosol Science and Technology*, 53(5):485–492, 2019. → pages 8, 18, 27, 69, 71, 94, 188

[147] H. Oltmann, J. Reimann, and S. Will. Wide-angle light scattering (WALS) for soot aggregate characterization. *Combustion and Flame*, 157(3):516–522, 2010. → pages 68, 69

[148] H. Oltmann, J. Reimann, and S. Will. Single-shot measurement of soot aggregate sizes by wide-angle light scattering (WALS). *Applied Physics B*, 106(1):171–183, 2012. → pages 8, 59, 69

[149] Omega engineering. *Silicon on sapphire pressure transmitter*. Omega engineering. → page 50

[150] H. Omidvarborna, A. Kumar, and D.-S. Kim. Recent studies on soot modeling for diesel combustion. *Renewable and Sustainable Energy Reviews*, 48:635–647, 2015. → page 15

[151] F.-X. Ouf, J. Vendel, A. Coppalle, M. Weill, and J. Yon. Characterization of soot particles in the plumes of over-ventilated diffusion flames. *Combustion Science and Technology*, 180(4):674–698, 2008. → pages 72, 188

[152] J. C. Owens. Optical refractive index of air: dependence on pressure, temperature and composition. *Applied Optics*, 6(1):51–59, 1967. → page 113

[153] K. Park, D. B. Kittelson, and P. H. McMurry. Structural properties of diesel exhaust particles measured by transmission electron microscopy (TEM): Relationships to particle mass and mobility. *Aerosol Science and Technology*, 38(9):881–889, 2004. → page 188

[154] J. Parks, B. Partridge, and V. Prikhodko. An optical backscatter sensor for particulate matter measurement. *SAE Technical Paper*, (2009-01-0687), 2009. → pages 7, 42, 125

[155] B. Patychuk and S. N. Rogak. Particulate matter emission characterization from a natural gas fuelled high pressure direct injection engine. In *Internal Combustion Engine Division Fall Technical Conference*, volume 55096, pages 447–455. American Society of Mechanical Engineers, 2012. → pages 49, 135

[156] B. D. Patychuk. Particulate matter emission characterization from a natural-gas high-pressure direct-injection engine. Master's thesis, University of British Columbia, 2013. → pages 56, 62, 68

[157] PCB group. *Test and measurement sensors and instrumentation.* → page 50

[158] R. Pearson. *Numerical methods for simulating gas dynamics in engine manifolds.* PhD thesis, University of Manchester, Institute of Science and Technology, 1994. → page 102

[159] L. Pelkmans and P. Debal. Comparison of on-road emissions with emissions measured on chassis dynamometer test cycles. *Transportation Research Part D: Transport and Environment*, 11(4):233–241, 2006. → page 3

[160] A. Petzold and R. Niessner. Photoacoustic soot sensor for in-situ black carbon monitoring. *Applied Physics B*, 63(2):191–197, 1996. → pages 5, 36

[161] P. Price, R. Stone, T. Collier, M. Davies, and V. Scheer. Dynamic particulate measurements from a DISI vehicle: a comparison of DMS500,

ELPI, CPC and PASS. *SAE Transactions*, pages 410–422, 2006. → page 41

[162] D. Y. Pui, F. Romay-Novas, and B. Y. Liu. Experimental study of particle deposition in bends of circular cross section. *Aerosol Science and Technology*, 7(3):301–315, 1987. → page 105

[163] K. Reavell, T. Hands, and N. Collings. A fast response particulate spectrometer for combustion aerosols. *SAE Transactions*, pages 1338–1344, 2002. → pages 5, 34, 42, 43

[164] J. Rochussen, G. McTaggart-Cowan, and P. Kirchen. Parametric study of pilot-ignited direct-injection natural gas combustion in an optically accessible heavy-duty engine. *International Journal of Engine Research*, 21(3):497–513, 2020. → pages 16, 140

[165] S. N. Rogak, R. C. Flagan, and H. V. Nguyen. The mobility and structure of aerosol agglomerates. *Aerosol Science and Technology*, 18 (1):25–47, 1993. → page 72

[166] R. Rossman and W. Smith. Density of carbon black by helium displacement. *Industrial & Engineering Chemistry*, 35(9):972–976, 1943. → page 188

[167] L. Rubino, P. R. Phillips, and M. V. Twigg. Measurements of ultrafine particle number emissions from a light-duty diesel engine using SMPS, DMS, ELPI and EEPS. *SAE Technical Paper*, (2005-24-015), 2005. → pages 41, 42, 43

[168] W. Schindler, C. Haisch, H. A. Beck, R. Niessner, E. Jacob, and D. Rothe. A photoacoustic sensor system for time resolved quantification of diesel soot emissions. *SAE transactions*, pages 483–490, 2004. → page 36

[169] S. Schraml, C. Heimgärtner, S. Will, A. Leipertz, and A. Hemm. Application of a new soot sensor for exhaust emission control based on

time resolved laser induced incandescence (TIRE-LII). *SAE transactions*, pages 2629–2638, 2000. → pages 5, 36

[170] S. Schraml, S. Schrami, S. Will, A. Leipertz, T. Zens, and N. D'Alfonso. Performance characteristics of TIRE-LII soot diagnostics in exhaust gases of diesel engines. *SAE Transactions*, pages 1935–1942, 2000. → page 36

[171] C. Schulz, B. F. Kock, M. Hofmann, H. Michelsen, S. Will, B. Bougie, R. Suntz, and G. Smallwood. Laser-induced incandescence: Recent trends and current questions. *Applied Physics B*, 83(3):333, 2006. → page 5

[172] J. H. Seinfeld and S. N. Pandis. *Atmospheric chemistry and physics: from air pollution to climate change.* John Wiley & Sons, 2016. → page 132

[173] B. Semlitsch, Y. Wang, and M. Mihăescu. Flow effects due to pulsation in an internal combustion engine exhaust port. *Energy Conversion and Management*, 86:520–536, 2014. → pages 6, 100

[174] W. G. Shin, J. Wang, M. Mertler, B. Sachweh, H. Fissan, and D. Y. Pui. The effect of particle morphology on unipolar diffusion charging of nanoparticle agglomerates in the transition regime. *Journal of Aerosol Science*, 41(11):975–986, 2010. → pages 31, 34

[175] M. Shupler, P. Hystad, A. Birch, D. Miller-Lionberg, M. Jeronimo, R. E. Arku, Y. L. Chu, M. Mushtaha, L. Heenan, S. Rangarajan, et al. Household and personal air pollution exposure measurements from 120 communities in eight countries: results from the pure-air study. *The Lancet Planetary Health*, 4(10):e451–e462, 2020. → pages 79, 88

[176] W. Singer, W. Schindler, and H. Friedl. High sensitive smoke measurement for dynamic engine tests. *SAE Technical Paper*, (1999-01-3077), 1999. → page 37

[177] A. P. Singh. Characterization and system level study of air addition in a pilot ignited direct injection natural gas engine. Master's thesis, University of British Columbia, 2019. → page 50

[178] T. A. Sipkens, P. J. Hadwin, S. J. Grauer, and K. J. Daun. General error model for analysis of laser-induced incandescence signals. *Applied Optics*, 56(30):8436–8445, 2017. → page 36

[179] K. C. Smyth and C. R. Shaddix. The elusive history of m = 1.57–0.56 i for the refractive index of soot. *Combustion and Flame*, 107(3): 314–320, 1996. → page 188

[180] A. Soewono. *Morphology and optical properties of coated aggregates*. PhD thesis, University of British Columbia, 2013. → page 24

[181] A. Soewono and S. N. Rogak. Morphology and optical properties of numerically simulated soot aggregates. *Aerosol Science and Technology*, 47(3):267–274, 2013. → page 38

[182] C. Sorensen. Light scattering by fractal aggregates: a review. *Aerosol Science & Technology*, 35(2):648–687, 2001. → pages xvi, 7, 17, 25, 26, 90

[183] C. Sorensen. The mobility of fractal aggregates: a review. *Aerosol Science and Technology*, 45(7):765–779, 2011. → pages 33, 72, 94

[184] C. M. Sorensen, J. Yon, F. Liu, J. Maughan, W. R. Heinson, and M. J. Berg. Light scattering and absorption by fractal aggregates including soot. *Journal of Quantitative Spectroscopy and Radiative Transfer*, 217:459–473, 2018. → pages 39, 198, 199, 200

[185] P. Steiche. Cycle resolved mass averaged sampling of engine particulate emissions: A combination of optical instrumentation and 1-D flow modeling. Master's thesis, Technische Universität München, Lehrstuhl für Thermodynamik, 2017. → pages xvii, 103, 104, 106, 107, 110, 118, 119, 120

[186] a. C. J. Sternberg, W. S. Gallaway, and D. T. Jones. *The mechanism of response of flame ionization detectors*. Academic Press, 1962. → page 54

[187] M. Svartengren, R. Falk, L. Linnman, K. Philipson, and P. Camner. Deposition of large particles in human lung. *Experimental Lung Research*, 12(1):75–88, 1987. → page 34

[188] J. Swanson and D. Kittelson. Evaluation of thermal denuder and catalytic stripper methods for solid particle measurements. *Journal of Aerosol Science*, 41(12):1113–1122, 2010. → page 93

[189] A. Sydbom, A. Blomberg, S. Parnia, N. Stenfors, T. Sandström, and S. Dahlen. Health effects of diesel exhaust emissions. *European Respiratory Journal*, 17(4):733–746, 2001. → page 1

[190] Thorlabs. *PDA36A Si Switchable Gain Detector User Guide*, 2013. → pages 59, 60

[191] D. R. Tree and K. I. Svensson. Soot processes in compression ignition engines. *Progress in Energy and Combustion Science*, 33(3):272–309, 2007. → pages 4, 15

[192] TSI. *Series 3080 Electrostatic Classifiers, Operation and Service Manual*, . → pages 34, 181

[193] TSI. *Model 3025A Ultrafine Condensation Particle Counter, Instruction Manual*, . → page 31

[194] TSI. *Dusttrak DRX Aerosol monitor, Model 8533/8534/8533EP*, 12 2014. → pages 37, 61

[195] R. L. Vander Wal and A. J. Tomasek. Soot nanostructure: dependence upon synthesis conditions. *Combustion and Flame*, 136(1-2):129–140, 2004. → pages 18, 19

[196] R. Viskup, D. Alberer, K. Oppenauer, and L. del Re. Measurement of transient PM emissions in diesel engine. *SAE Technical Paper*, (2011-24-0197), 2011. → pages 6, 7, 36, 42, 43

[197] P. Vögelin, P. Obrecht, and K. Boulouchos. Experimental investigation of multi-in-cylinder pyrometer measurements and exhaust soot emissions under steady and transient operation of a heavy-duty diesel engine. *SAE International Journal of Engines*, 6(3):1855–1865, 2013. → pages 6, 125, 140, 153

[198] S. von der Weiden, F. Drewnick, and S. Borrmann. Particle loss calculator–a new software tool for the assessment of the performance of aerosol inlet systems. *Atmospheric Measurement Techniques*, 2(2): 479–494, 2009. → pages 105, 190, 191

[199] J. Wang, R. C. Flagan, and J. H. Seinfeld. Diffusional losses in particle sampling systems containing bends and elbows. *Journal of Aerosol Science*, 33(6):843–857, 2002. → page 190

[200] A. Wiedensohler. An approximation of the bipolar charge distribution for particles in the submicron size range. *Journal of Aerosol Science*, 19(3):387–389, 1988. → page 33

[201] P. O. Witze, R. E. Chase, M. M. Maricq, D. H. Podsiadlik, and N. Xu. Time-resolved measurements of exhaust PM for FTP-75: Comparison of LII, ELPI, and TEOM techniques. *SAE Technical Paper*, (2004-01-0964), 2004. → page 41

[202] P. O. Witze, G. A. Payne, W. D. Bachalo, and G. J. Smallwood. Influence of measurement location on transient laser-induced incandescence measurements of particulate matter in raw diesel exhaust. *Annual Report of the International Energy Agency Program of Research in Energy Conservation and Emissions Reduction in Combustion Sub-Task*, 3, 2004. → pages 36, 42

[203] J.-S. Wu, S. Krishnan, and G. Faeth. Refractive indices at visible

wavelengths of soot emitted from buoyant turbulent diffusion flames. *Journal of Heat Transfer*, 119:230–237, 1997. → page 188

[204] Y.-l. Xu. Electromagnetic scattering by an aggregate of spheres: far field. *Applied Optics*, 36(36):9496–9508, 1997. → page 37

[205] J. Yon, A. Bescond, and F. Liu. On the radiative properties of soot aggregates part 1: Necking and overlapping. *Journal of Quantitative Spectroscopy and Radiative Transfer*, 162:197–206, 2015. → pages 38, 77, 188

[206] J. Yon, A. Bescond, and F.-X. Ouf. A simple semi-empirical model for effective density measurements of fractal aggregates. *Journal of Aerosol Science*, 87:28–37, 2015. → page 92

[207] H. Yun and W. Mirsky. Schlieren-streak measurements of instantaneous exhaust gas velocities from a spark-ignition engine. *SAE Transactions*, pages 3143–3158, 1974. → pages 6, 100

[208] F. Zhao, M.-C. Lai, and D. L. Harrington. Automotive spark-ignited direct-injection gasoline engines. *Progress in energy and combustion science*, 25(5):437–562, 1999. → page 2

Appendix A

FEN optical coefficient

The value of Λ_{FEN} is determined experimentally based on calibration with characterized aerosols. Here, the experimental procedure and the theoretical considerations for the data reduction are explained.

A.1 Experimental system

The characterized sodium chloride particles are used to measure the optical coefficient of the FEN. This involves atomizing a NaCl-water solution with an air-blast-assisted constant output TSI atomizer (model 3076) and then drying the droplets in a diffusion drier column. The aerosol stream is then diluted with clean particle-free air prior to measurement. The polydisperse sample is routed to the FEN for the light scattering measurement and then to the SMPS for the mobility size characterization. The SMPS has an upper size limit of 770 nm (for the sheath and sample flowrates used in this test [192]). Therefore, a cyclone particle separator was added just upstream of the atomizer to remove the large droplets, and thereby prevent the formation of the large NaCl particles.

A TSI OPS particle sizer is also used in tandem with the SMPS to verify that the sample does not contain large particles. Emfab filter samples are collected to characterize the gravimetric mass concentration of aerosol samples. Mid-high rates of dilution air is added to the main sample to make

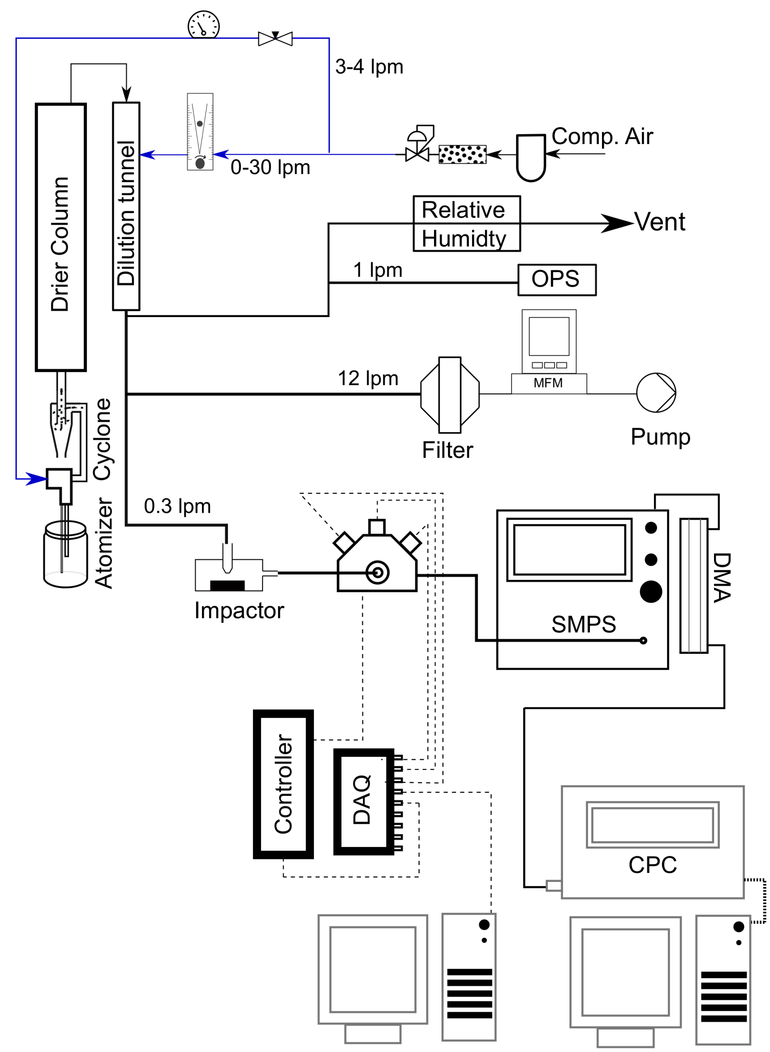

Figure A.1: The experimental setup for measuring the FEN optical coefficient. Tandem SMPS measurements are for the size characterization of the polydisperse NaCl sample. Emfab filter samples characterize the gravimetric mass concentration of the sample.

up for the required flow demand for all instruments. Figure A.1 shows a schematic layout of the measurement system.

Three different NaCl-water solutions with concentrations of 3, 5, and 10 g/L are used to generate the atomized droplets, which upon drying, generate different sizes of dry NaCl aerosol population. To change the particle mass concentration and their light scattering, while maintaining constant $d_{m,g}$ and $\sigma_{m,g}$, dilution air is added to the aerosol flow. The dry sodium chloride aerosols have a $d_{m,g}$ of 180 nm, 190 nm, 240 nm, generated from the 3 g/L, 5 g/L and 10 g/L water solutions respectively, and $\sigma_{m,g}$ is in the range 1.5 - 1.6 in all cases.

A.2 Theoretical framework

Although the sodium chloride aerosols are not spherical, the Mie model is reasonably accurate in describing the light scattering from the suspension of randomly oriented, irregularly shaped, polydisperse particles in air [85]. Unlike soot, the light scattering from a NaCl particle can be characterized with only three physical parameters, namely its area-equivalent diameter (equal to the mobility diameter for the sizes pertinent to this experiment), the refractive index, and the material density. The optical refractive index and density of sodium chloride are known ($\mathbf{m} = 1.56 + 0i$, $\rho_{mat} = 2160$ kg/m^3), and the mobility diameter could be accurately measured with the SMPS. The mobility size measurement of the polydisperse NaCl aerosols generated with the atomizer-drier system in figure A.1 shows the number and mass distributions may be characterized with lognormal functions, as shown in Figure A.2. That is, a polydisperse sample is characterized by its $d_{m,g}$, $\sigma_{m,g}$ and the total mass, similar to our approach for soot measurement. For pairs of $d_{m,g}$ and $\sigma_{m,g}$ in the range 80 - 500 nm and 1.4 - 2.0 respectively, the MSC of lognormal polydispersions of NaCl aerosols is calculated based on the Mie model. The variation of MSC as a function of $d_{m,g}$ for five different $\sigma_{m,g}$ values are shown in Figure A.3.

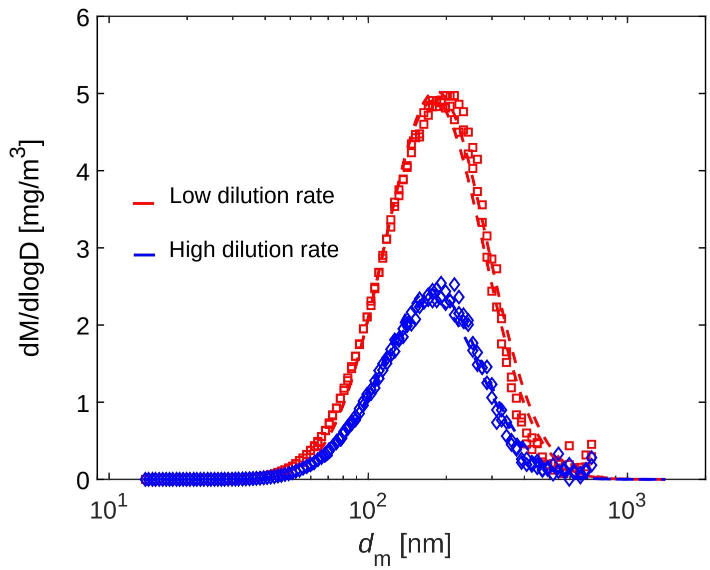

Figure A.2: The mass distribution of the NaCl aerosols generated with the 3 g/L sodium chloride in water solution. Two dilution rates (red [square] and blue [diamond] symbols and curves), with two SMPS scans per dilution, are shown. The $d_{m,g}$ and $\sigma_{m,g}$ values are 176 nm and 1.56 respectively for the high dilution case, and 181 nm and 1.57 for the low dilution case (values are averaged between the two scans).

A.3 Results and discussion

To calculate Λ_{FEN} for each light scattering cone (45°, 90°, and 135°), the measured light scattering power on the FEN photodetectors, P_θ, is compared with the gravimetric mass measured with the filters, $C_{m,grav}$, in Equation A.1. Here, the MSC values are are from the NaCl Mie scattering lookup tables. The critical difference with the signal inversion method for soot is that the retrieved MSC values are based on the $d_{m,g}$ and $\sigma_{m,g}$ measured with the SMPS, not the light scattering ratios. In other words, there is no data inversion error in $d_{m,g}$ and $\sigma_{m,g}$, as these are directly measured by the SMPS. Therefore, the optical coefficient is calculated based on the gravimetric mass, the light scattering intensity, and the MSC,

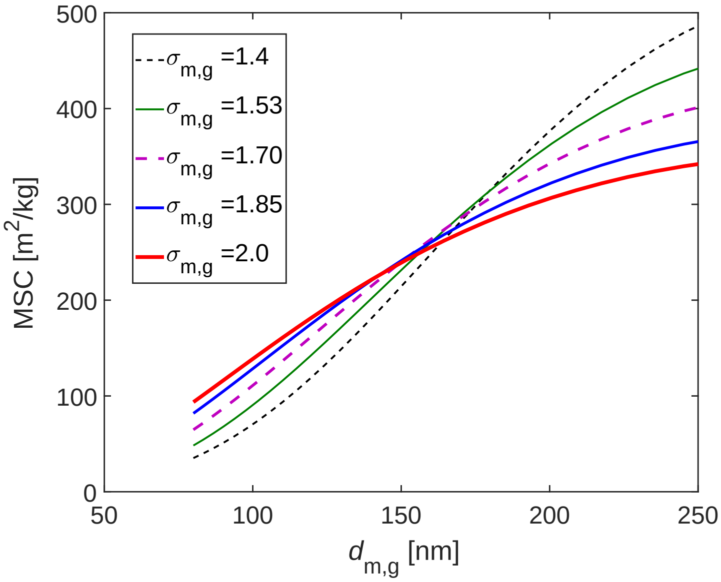

Figure A.3: The variation of the Mass-specific Scattering Cross-section (MSC) for the 45° detector with the $d_{m,g}$ for five different $\sigma_{m,g}$ values.

$$\Lambda_{FEN} = \frac{P_\theta}{(MSC)_\theta C_{m,grav}} \tag{A.1}$$

Table A.1 lists the calculated Λ_{FEN} from different tests. The mean value and the standard deviation of Λ_{45}, Λ_{90}, and Λ_{135} are $(8.6 \pm 1.1) \times 10^{-5}$, $(7.2 \pm 0.5) \times 10^{-5}$, and $(9.3 \pm 0.5) \times 10^{-5}$ Wm respectively. The optical parameters obtained with this calibration are used for the mass concentration calculations of the engine exhaust soot in this work.

Table A.1: The sample specifications at each test point and the calculated optical efficiencies Λ_{45}, Λ_{90}, and Λ_{135}.

Solution conentration	Dilution air [lpm]	$d_{m,g}$ [nm]	$\sigma_{m,g}$ [-]	$C_{m,grav}$ [mg/m^3]	$\Lambda_{FEN,45}$ [mWm]	$\Lambda_{FEN,90}$ [mWm]	$\Lambda_{FEN,135}$ [mWm]
3	12	183	1.58	3.17	76.8	73.8	93.0
		179	1.56		78.0	76.2	94.8
	20	176	1.56	2.00	88.2	75.6	91.8
		175	1.55		82.8	72.0	87.0
5	20	192	1.59	3.52	87.6	73.2	88.2
		188	1.57		87.0	73.8	90.0
10	12	241	1.61	10.93	101.0	77.4	102.0
		238	1.60		95.4	71.4	96.0
		240	1.60		101.0	78.0	104.0
	20	231	1.58	6.26	88.2	72.0	93.0
		237	1.57		57.6	75.6	99.0
		257	1.59		82.2	61.2	85.2
	30	255	1.59	3.89	79.8	60.0	85.2
		242	1.61		94.8	68.4	96.6
		242	1.61		91.8	67.2	93.6

Appendix B

Survey of the soot optical and morphological properties

Table B.1: The numerical value of the RDGFA parameters from various literature sources.

Parameter	Value	Sources
D_α, k_α	1.09 ± 0.02, 1.15 ± 0.18	[108]
	1.08 ± 0.003, 1.10 ± 0.005	[22] ($C_{ov} = 0$)
	1.11 ± 0.002, 1.20 ± 0.005	[22] ($C_{ov} = 0.15$)
	1.13 ± 0.002, 1.30 ± 0.006	[22] ($C_{ov} = 0.25$)
	1.07 ± 0.005, 1.17 ± 0.02	[145] (small overlap)
	1.19 ± 0.01, 1.81 ± 0.03	[145] (large overlap)
	1.1 ± 0.05, 1.13 ± 0.2	[35] (only HPDI soot)
D_f, k_f	1.65 ± 0.06, 2.71 ± 0.8	[108]
	1.86, 2.25	[107] (Light scattering from flame soot)
	1.75, 2.78	
	1.67, 2.39	[107] (TEM from flame soot)
	1.66, 3.25	
	1.80 ± 0.03, 1.30 ± 0.07	[145]
	1.78 ± 0.15, 2.44 ± 0.82	[151]
	1.75 ± 0.02, 1.95 ± 0.02	[17]
	1.74, 1.23	[26]
	1.81, 1.81	[22]
D_{TEM}, $d_{p,100}$	0.26 ± 0.1, 22 ± 4	[146] (only HPDI soot)[†]
	0.3 ± 0.1, 21 ± 5	[146] (various soot sources)[†]
$\mathbf{m} = n + i\kappa$	1.6 + 0.6i	[179]
	1.48 + 0.84i	[205]
	1.95 + 0.95i	[20]
	1.68 + 056i	[126]
	1.39 + 0.85i	[17] (Ethylene flame)
	1.8 + 0.9i	[77]
	1.65 + 0.75i	[94]
ρ_p [g/cc]	1.74	[136]
	1.82	[166]
	1.72	[151]
	1.87	[203]
	1.74	[17] (Ethylene flame)
	1.78	[153]

[†] Values are derived from soot TEM microscopy and image analysis. A mean D_{TEM} value of 0.38 ± 0.1 based on an effective density method is also reported in this source.

Appendix C

Particle loss calculations in the PM filter sampling and thermodenuder assemblies

C.1 Overview

The particle losses inside the thermodenuder and the gravimetric filter sampling systems are calculated. This facilitates the comparison between the measurements done after the thermodenuder with the gravimetric filters placed before the thermodenuder. The dominant loss mechanisms inside the thermodenuder are the diffusion and thermophoretic losses, and in the gravimetric sampling system are the inertial losses due to bending flow.

C.2 Background

When transferring aerosols to the measurement instruments, sample losses occur due to particles depositing on the walls of the sampling system. Large particles at higher flow velocities and Reynolds numbers are subject to inertial losses, such as impaction on tube walls inside the bends and flow branches. Smaller particles are subject to diffusional or thermophoretic losses due to the Brownian motion. Particle sampling losses due to these mechanisms are calculated based on the correlations recommended in [198] for inertial losses in bends as described in Chapter 5. The Gormley Kennedy formula for diffusional losses in straight lines is used for the diffusional losses,

$$\eta_{diff} = 8 \sum_{n=0}^{\infty} \frac{G_n}{\lambda_n^2} \exp\left(-\lambda_n^2 x\right) \tag{C.1}$$

where $x = (2L/d)\mathrm{Pe}$, L and d are the length and inner diameter of the sampling tube, and Pe is the particle Peclèt number $\mathrm{Pe} = \bar{\mathrm{U}}\mathrm{d}/\mathrm{D}$, and D is the Brownian diffusivity of the particles described by the Stokes-Einstein relation below, and the coefficients G_n and λ_n are given in [199].

$$D = \frac{kTC_c}{3\pi\mu d_a} \tag{C.2}$$

The thermophoretic wall deposition due to temperature gradients occurs when there is hot flow in a cold tube. The thermophoretic coefficient describes for the thermophoretic force and migration velocity in such a condition, and is expressed below,

$$K_{th} = \frac{2C_sC}{1+C_m(2\lambda/d_a)}\left(\frac{k_g/k_a + C_t(2\lambda/d_a)}{1+2(k_g/k_a)+2C_i(2\lambda/d_a)}\right) \tag{C.3}$$

where coefficients C_m, C_s, and C_t are 1.14, 1.17, and 2.18 [113]. The results of the particle losses calculated based on these methods are summarized below.

C.3 Results of loss calculation

The diffusion, thermophoretic and inertial losses are calculated and the PM mass transmission efficiency inside the thermodenuder are shown in Figure C.1. The inertial losses inside the thermodenuder are negligible for the flowrates used in our experiments. The results are provided for a flowrate of 0.3 lpm (the SMPS flowrate without the thermophoretic sampler) and 1.0 lpm (when running the thermophoretic sampler pump for TEM grid collection).

The total soot mass transmission efficiency of the thermodenuder for polydisperse soot population as a function of mass-mean mobility diameter,

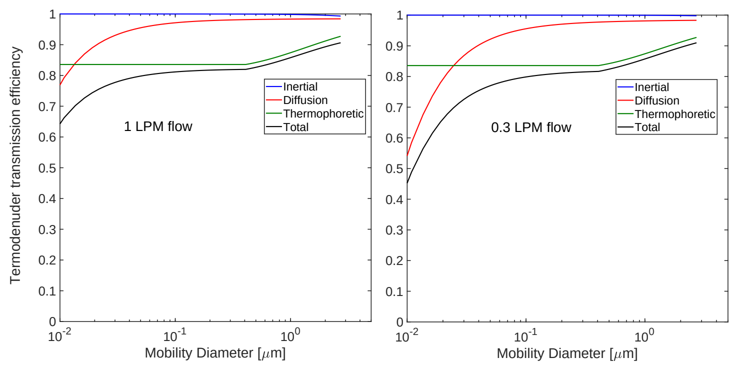

Figure C.1: The inertial, diffusion, and thermophoretic particle mass transmission efficiencies in the thermodenuder when the thermophoretic sampler pump is off (left) and on (right) for different particle mobility diameters.

$d_{m,g}$, in Figure C.2. Based on these calculations, an overall particle mass loss close to 16%-20% in the thermodenuder is expected (blue and red lines in Figure C.2). When comparing the FEN or SMPS results with the gravimetric filters, the losses that occur in the gravimetric line must be considered as well. Firstly, the flowrate through the gravimetric filter sampling system is much higher than the thermodenuder branch, 12 lpm compared to 0.3 lpm; therefore, inertial losses, such as in a branched Tee and a 90° elbow which exist in the filter sampling line are accounted for. The black line in Figure C.2 shows the sampling efficiency in the filter sampling tubing calculated based on the method of [198]. The ratio of the mass transmission efficiency of the thermodenuder to the gravimetric line for samples with $d_{m,g}$ of 200 nm and 250 nm are $0.83/0.94 = 0.88$ and $0.83/0.92 = 0.90$ respectively. This indicates that a 10% difference in mass between the thermodenuded sample and the gravimetric filter sample could exist due to particle losses.

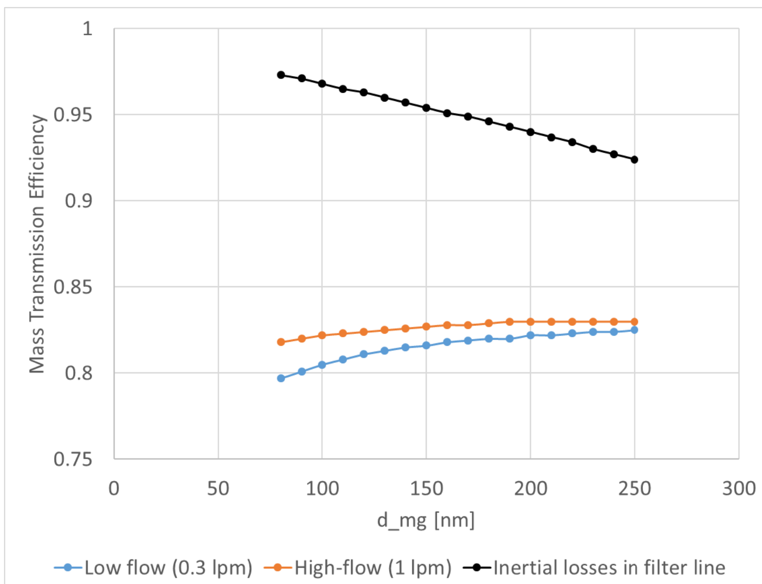

Figure C.2: Soot mass transmission efficiency as a function of polydisperse $d_{m,g}$ of lognormal soot for the low (0.3 lpm, blue line) and high (1 lpm, red line) flowrates inside the thermodenuder. The black line is the mass transmission efficiency in the gravimetric filter sampling line, mostly due to inertial losses in 90° bends.

Appendix D

Relations of characteristic aggregate lengths

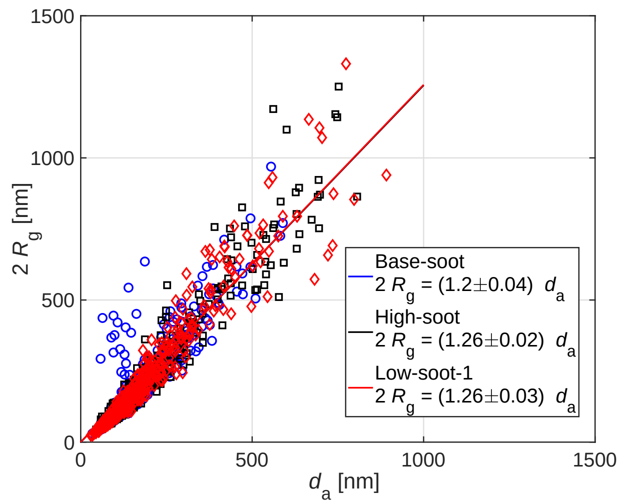

Figure D.1: Linear relationship between the diameter of gyration ($2R_g$) and the projected area diameter (d_a) based on the soot TEM images collected at the base, high, and low-soot engine operating points.

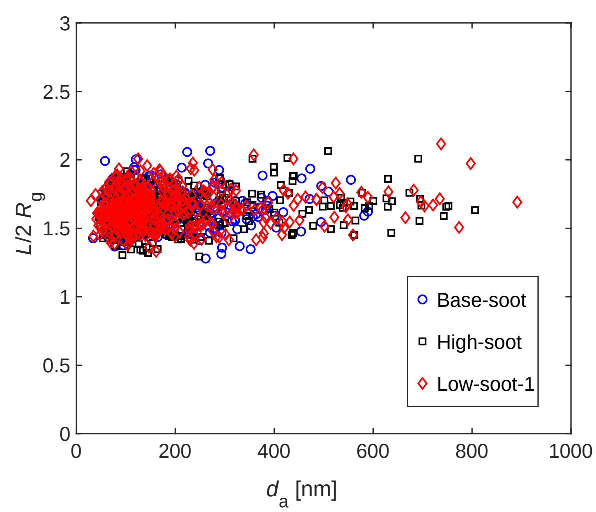

Figure D.2: The ratio of maximum length of aggregates to their diameter of gyration at different sizes. The mean value of the $L/2R_g$ ratio is ~ 1.7. Similar results are reported by [22].

Appendix E

Discussion of $\sigma_{m,g}$ from the FEN light scattering inversion

Figure E.1 shows the $\sigma_{m,g}$ inversion results using our FEN-RDGFA lookup table methodology (ordinate) compared with the SMPS $\sigma_{m,g}$ (abscissa). The lookup table search window for $\sigma_{m,g}$ is bounded to the 1.4 - 2.0 interval which covers the range of measured SMPS $\sigma_{m,g}$, and is implemented to avoid unphysical results, as mentioned in Chapter 4. The data points shown in Figure E.1 are the same as in Figure 4.9 in Chapter 4 for the baseline inversion model. Most inversion results land on the $\sigma_{m,g} = 1.4$ and $\sigma_{m,g} = 2.0$ limits, indicating that uncertainties in $\sigma_{m,g}$ inversion are large and its measurement with the FEN is poor. The errors in calculating $d_{m,g}$ from the lookup tables, however, are small as $d_{45/90}$ and $d_{45/135}$ are averaged to give $d_{m,g}$ (step 5 in the inversion process).

The impact of the $\sigma_{m,g}$ inversion on other parameters, namely $d_{m,g}$ and C_m, are further investigated in Figure E.2. The linear trend lines to the baseline inversion results using the two ratios (solid black line) is compared to the light scattering inversion aided by $\sigma_{m,g}$ directly measured with the SMPS, while obtaining $d_{m,g}$ once from the $R_{45/90}$ (red dashed) and once from $R_{45/135}$ (red dotted). By using the two-ratio method in the 5-step inversion

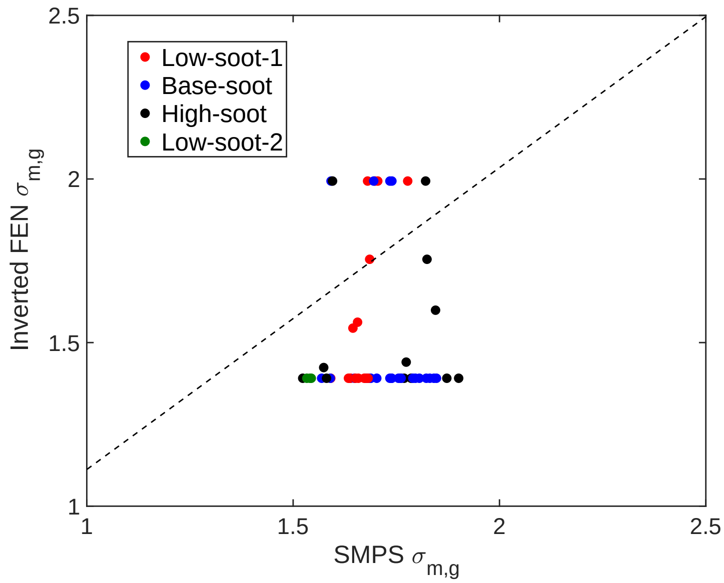

Figure E.1: The $\sigma_{m,g}$ from FEN light scattering inversion compared with the SMPS $\sigma_{m,g}$. Different colors show different engine operating conditions, similar to Figure 4.9 in Chapter 4. The inversion results are from the baseline RDGFA lookup table. The $\sigma_{m,g}$ is bounded between 1.4 and 2.0 by the lookup table search algorithm (top and bottom horizontal clusters).

algorithm, the FEN results lie in the middle of the two red lines (close to their average), and are less sensitive to errors in $\sigma_{m,g}$. This indicates while the $\sigma_{m,g}$ inversion is poor, averaging $d_{45/90}(\sigma_{m,g})$ and $d_{45/135}(\sigma_{m,g})$ in step 5 of the inversion algorithm reduces the errors due to incorrect $\sigma_{m,g}$, highlighting the benefit of using three, instead of two, light scattering angles (e.g. [78] or [6] used two angles and relied on a constant σ), where in the latter, errors due to wrong $\sigma_{m,g}$ are not corrected by a second light scattering ratio and could result in large systematic errors in size and mass concentrations. Furthermore, it is observed that variations due to $\sigma_{m,g}$ (even when using only one light scattering ratio) are still less than uncertainties in the primary particle diameter using constant d_p RDGFA models.

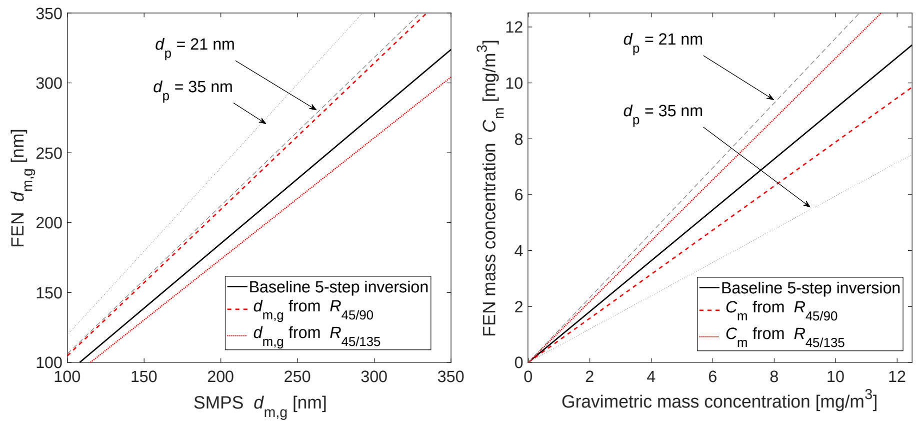

Figure E.2: Linear trend lines for the FEN C_m and $d_{m,g}$ with 2-ratio inversion (5-step inversion algorithm, solid black line), inversion aided by SMPS $\sigma_{m,g}$, using the $R_{45/90}$ or $R_{45/135}$ tables, dashed and dotted red lines respectively, and inversion with the constant-d_p morphology models, grey dashed and dotted lines.

Appendix F

RDGFA structural errors based on comparisons with a T-matrix light scattering model

Sorensen et al. investigated the structural errors in RDGFA compared to a detailed multi-sphere T-Matrix (MSTM) light scattering model. Here, we use Figures 3 and 6 in [184] to determine the errors embedded in the RDGFA inversion lookup tables used in this work. We analyze a small ($\sim$ 100 nm) and a large ($\sim$ 400 nm) aggregate and given that all of the soot samples in our work have $d_{m,g}$ in the range 150-250 nm, the two proposed aggregate sizes provide a fair estimate of the structural RDGFA errors in the lookup tables used for inversion of light scattering in our work. Table F.1 summarises the properties of the 100-nm and 400-nm aggregates analysed here. These are also mapped onto Figures 3 and 6 of [184], adapted here as Figures F.1 and F.2. The baseline refractive index of $\mathbf{m}$=1.6+0.8i and laser wavelength of 405 nm (k = 0.0155 nm^{-1}, thus q at the 45° detection angle is 0.012 nm^{-1}) are used for the analysis. In Table F.1, a is the radius of the primary particles, ka is the normalized primary particle diameter, and ρ'_{agg}

is modified phase-shift parameter used in [184].

Table F.1: The properties of two sample aggregates for the study of the RDGFA structural errors based on the work of [184].

d_a [nm]	d_p [nm]	ka	N_p	ρ_{agg}	R_g	$q_{45}R_g$
100	19.7	0.156	39	0.24	49	0.58
400	33	0.256	275	0.46	256	3.05

The location of the two aggregates chosen for the analysis of the RDGFA lookup table errors are marked in Figures F.1 and F.2. The ratio of the MSTM light scattering intensity at the forward direction to the RDGFA light scattering (the same as the Rayleigh scattering intensity for $\theta = 0$) for different aggregates and refractive indices are shown as a function of the aggregate optical phase shift parameter ρ'_{agg}. The location of the 100-nm and 400-nm are shown on the bundle of lines corresponding to $\mathbf{m} = 1.5 + 0.8i$ (dark red). The MSTM-to-RDGFA ratio is close to unity for the 100-nm aggregate and is close to 0.92 for the 400-nm aggregate. This ratio is, however, expected to be even closer to one (e.g 0.95), as the actual position of the two crosses is between the dark red and dark blue lines, corresponding to $\mathbf{m} = 1.5 + 0.8i$ and $\mathbf{m} = 1.9 + 0.8i$ respectively. The RDGFA error at the 45° scattering angle is determined by combining the information obtained from Figure F.1, and estimating the error in the RDGFA structure factor $S(qR_g)$ at 45° based on Figure F.2.

Errors in the RDGFA structure factor are characterized by examining the ratio of the MSTM to the RDGFA structure factor for different values of qR_g in Figure F.2, adapted from [184]. The qR_g values corresponding to the 100-nm and 400-nm soot aggregates at the 45° scattering angle are marked on the left and right panels of the figure respectively. Based on Figure F.2, errors in the RDGFA structure factor for the 100-nm aggregate is expected to be less than 3% and for the 400-nm aggregate is around 20%. Combining the errors in the RDGFA forward light scattering (Figure F.1) and the errors in the RDGFA structure factor at 45° angle (Figure F.2), and considering that the soot aggregates measured in this work have $d_{m,g}$ values smaller than 270 nm, We expect that errors due to RDGFA approximations are less than

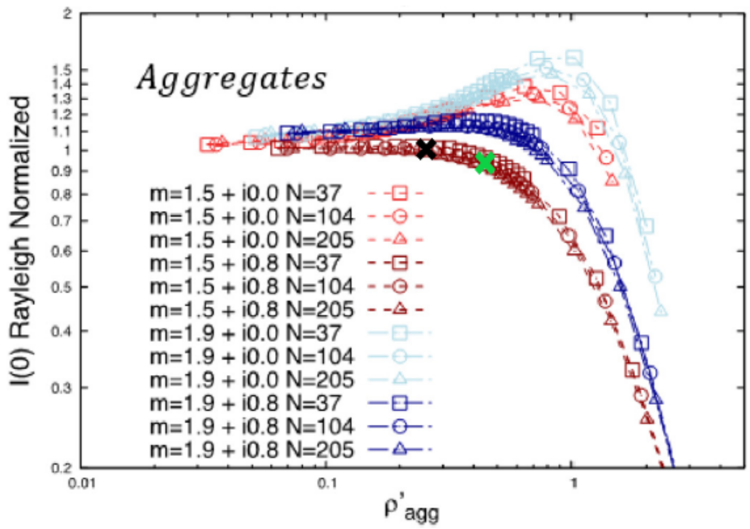

Figure F.1: The forward (θ=0) light scattering intensity based on MSTM normalized by the RDGFA forward scattering intensity. The dark red bundle of lines and symbols are similar to the soot refractive index used in this work and are used to determine the RDGFA structural errors. The black and green crosses mark a 100 nm and 400 nm aggregate respectively. Figure is adapted from [184].

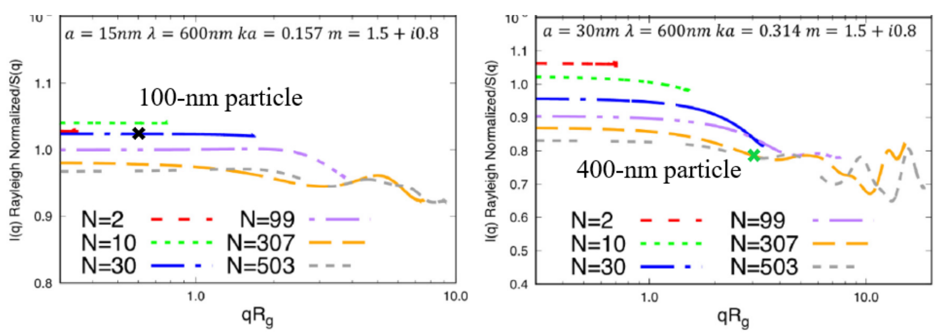

Figure F.2: The ratio of the MSTM to the RDGFA structure factor as a function of qR_g for various aggregate sizes and two different primary particle normalized ka values of 0.157 (left) and 0.314 (right), representing the errors in the RDGFA structure factors for the 100 nm (black cross, left panel) and 400 nm (green cross, right panel) aggregates considered in this analysis. Figure is adapted from [184].

15% for the larger aggregates and is less than 5% for the smaller aggregates in the light scattering lookup tables used for FEN inversion.

Appendix G

TEM soot image processing

G.1 Methodology

Soot samples collected on carbon-coated copper grids are imaged under TEM. The soot images are processed to give the morphological and scaling parameters needed for the FEN light scattering inversion. A TEM soot image, shown in Figure G.1-top panel, is processed with an in-house MatLab code to determine its projected area (A), area-equivalent diameter (d_a), length and width (L and W), radius of gyration (R_g), and primary particle diameter (d_p). A binary image is first produced by applying an intensity threshold to the gray-scale soot image for determining A, d_a, L, W, and R_g, shown in Figure G.1-mid panel. The averaged primary particle diameter of the aggregate is obtained from a pair correlation method (PCM) explained in [34]. Figure G.1-bottom panel shows the raw and processed image of a soot aggregate, showing its d_a and d_p.

The number of primary particles in the aggregate is determined based on its projected-area and primary particle diameters in Equation G.1, where D_α and k_α are aggregate shielding exponent and pre-factor with values of 1.1 and 1.13 respectively [35].

$$N_p = k_\alpha \left(\frac{d_a}{d_p} \right)^{2D_\alpha} \tag{G.1}$$

Soot fractal dimension (D_f) and pre-factor (k_f) are needed for the RDGFA lookup table calculations and are defined based on Equation G.2. By processing a sufficiently large number of soot aggregates, a function of the form shown in Equation G.2 is fitted to the N_p and $2R_g/d_p$ data obtained from TEM soot image-processing to determine the parameters D_f and k_f.

$$N_p = k_f \left(\frac{2R_g}{d_p}\right)^{D_f} \tag{G.2}$$

$$d_p = d_{p,100} \left(\frac{d_a}{100}\right)^{D_{TEM}} \tag{G.3}$$

Using this procedure, four of the nine parameters needed for light scattering lookup tables are determined from the SCRE soot. It might be possible to determine D_α and k_α from the TEM data set, but since the difference in their numerical values from different sources is small, here we use literature values [35]. The FEN calibration and baseline inversion lookup tables are based on the soot parameters from TEM analysis of exhaust-port (EXP) soot samples explained in section, and are compared with the TEM parameters of the more easily accessible post-surge tank (PST) sample. The two samples differ mainly due to particle coagulation in the exhaust piping system, which alters their morphology and light scattering parameters.

G.2 The results of the soot morphology analysis

In addition to particle mass and mobility size from the EXP and PST samples discussed in the paper, the morphology of the soot samples are compared here. Figures G.2 and G.3 show the changes in the primary particle-aggregate size correlation parameters due to aging effects in the SCRE exhaust system. It is notable that more dots are present on the left side of the EXP figures, consistent with the observation that the SMPS mobility diameter of the exhaust-port soot is smaller. Particle coagulation in the engine exhaust piping affects soot morphology, in particular the primary particle-aggregate scaling exponent, D_{TEM}. The difference between the exhaust-port and post-surge tank D_{TEM} is highest for point 7 with no EGR. The scaling

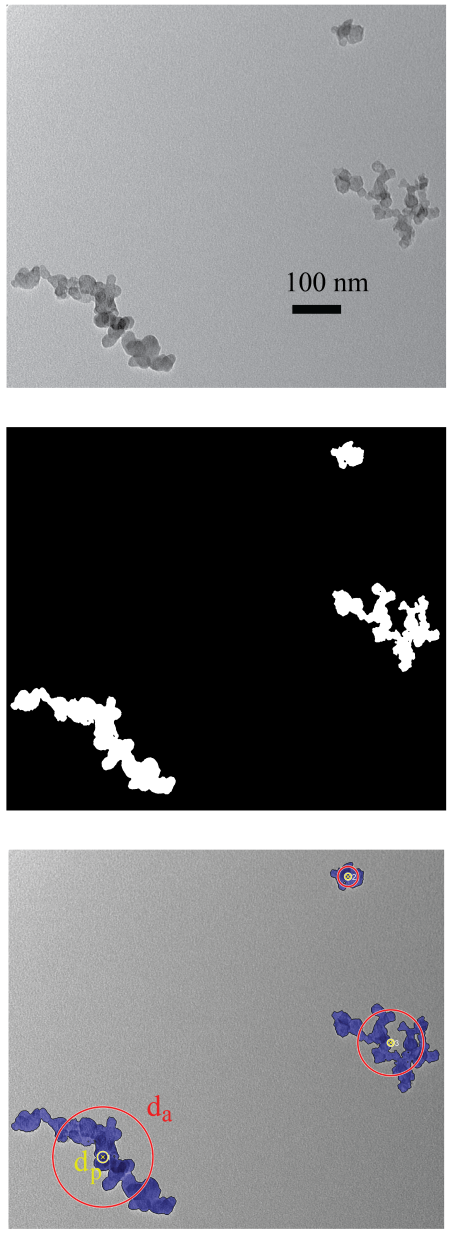

Figure G.1: TEM image of three soot aggregates sampled from SCRE exhaust port. The raw TEM image (top), the binary thresholded image (middle), and processed imaged showing the diameters of aggregates and primary particles (bottom).

and morphological parameters, D_{TEM}, $d_{p,100}$, D_f, and k_f are compared for these three cases in Table G.1.

Table G.1: The fractal soot D_{TEM}, $d_{p,100}$, D_f, and k_f parameters obtained from TEM soot imaging of the exhaust-port (EXP) and post-surge tank (PST) samples.

		D_{TEM}	$d_{p,100}$	D_f	k_f
Point 1	EXP	0.29	19.5	1.69	2.9
	PST	0.23	19.8	1.63	3.2
Point 2	EXP	0.27	18.7	1.75	2.6
	PST	0.31	18.2	1.64	3.2
Point 7	EXP	0.40	17.6	1.69	2.8
	PST	0.16	16.9	1.72	2.7

The soot morphological parameters, obtained here from TEM analysis, are used to generate lookup tables for the RDGFA light scattering inversion of the FEN signals into C_m and $d_{m,g}$.Variations in parameters D_{TEM}, $d_{p,100}$, D_f, and k_f affect the light-scattering inversion. In this work, the EXP parameters are used to carry out the light scattering inversion, as they are more representative of the soot particles inside the FEN.

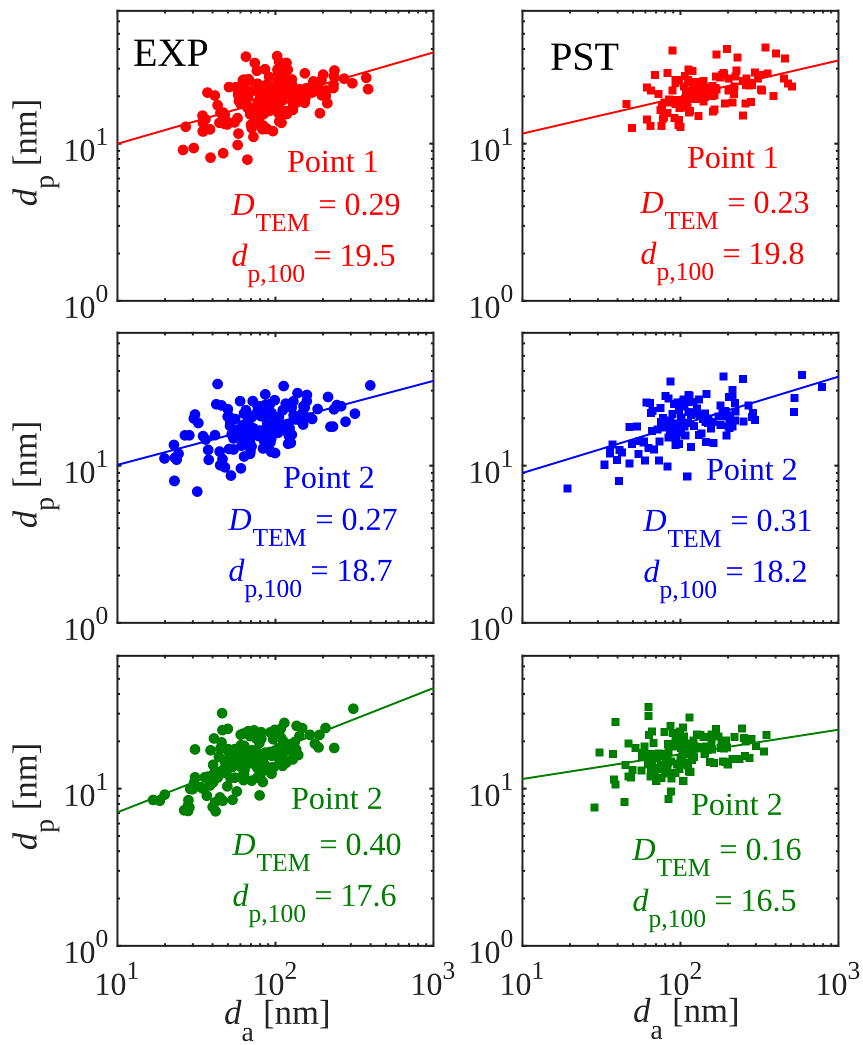

Figure G.2: Variation of the primary particle diameter with the aggregate diameter examined from the TEM analysis. Each aggregate is represented with a dot in the scatter plot and the d_p-d_a least-square regression fits are shown with solid lines. The D_{TEM} and $d_{p,100}$ are extracted from the regression coefficients.

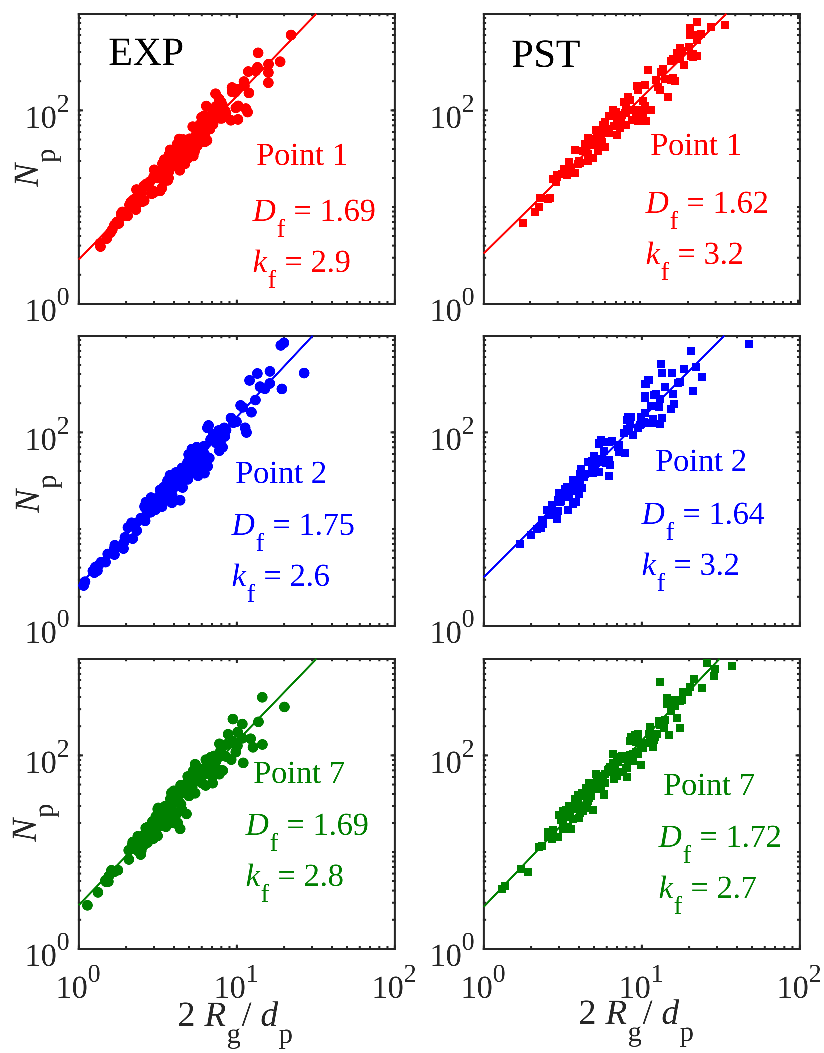

Figure G.3: Variation of the number of primary particles with $\frac{2R_g}{d_p}$ from the TEM analysis. The corresponding D_f and k_f are determined from the regression coefficients.

Appendix H

Soot polydisperse population measurements with SMPS

As pointed out in Chapter 4, samples of soot number distribution and their corresponding mass distribution based on SMPS mobility diameter measurements for a SCRE soot sample are provided in Figure H.1-H.4, and support the lognormal hypothesis. The dashed line indicates the corresponding lognormal least-square fits to the number ($\frac{dN}{d\log d}$) and mass ($\frac{dM}{d\log d}$) distributions. The mass distribution is calculated from effective density based on Equations 4.4-4.6 with morphology parameters obtained from the TEM analysis. Deviations from the lognormal mass distribution observed for d_m larger than 500 nm is believed to be due to reaching the upper size limit of the SMPS scan, and the Condensation Particle Counter (CPC) counting noise for low particle numbers, rather than actual deviations from lognormal distribution. Discrepancies in the order of 10% between the SMPS and gravimetric mass concentration are expected due to these artefacts, as further discussed in Chapter 4.

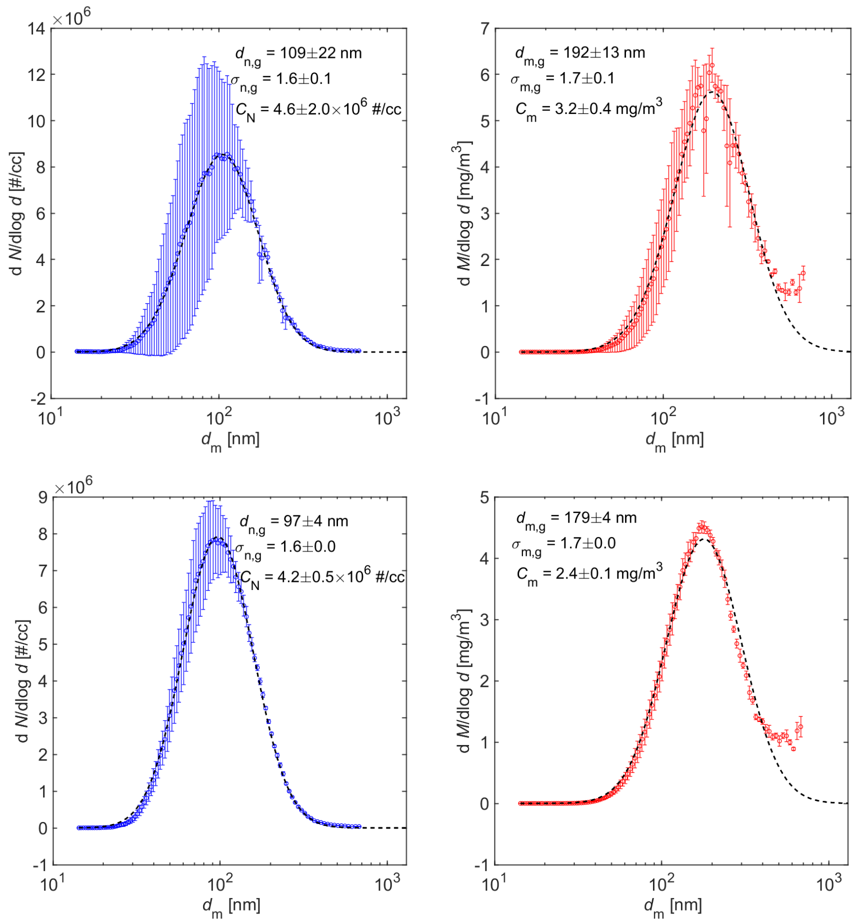

Figure H.1: Number (left) and mass (right) concentration distributions versus soot mobility diameter for two low-soot-1 (point 4) diluted SCRE exhaust samples (top and bottom), discussed in Chapter 4. The number distribution is directly measured with an SMPS-3080 during the tests, and the mass concentration is constructed from soot effective density with parameters obtained from TEM analysis. Error bars are based on multiple repeats of the measurements.

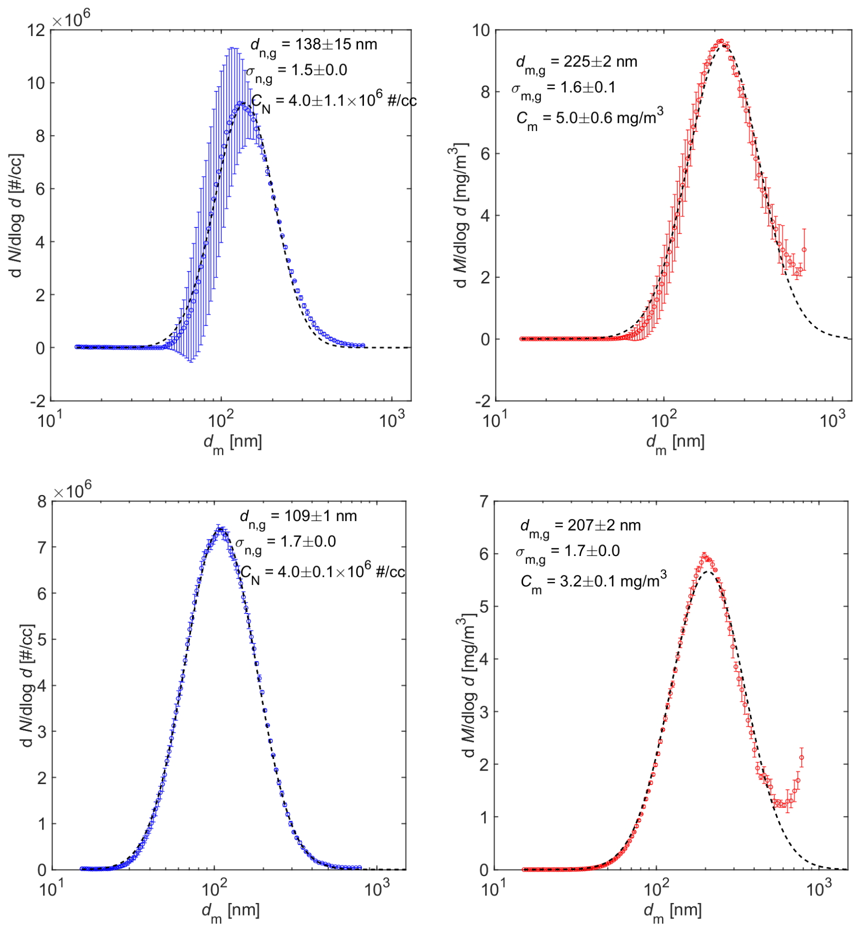

Figure H.2: Number (left) and mass (right) concentration distributions versus soot mobility diameter for two base-soot (point 1) diluted SCRE exhaust samples (top and bottom), discussed in Chapter 4. The number distribution is directly measured with an SMPS-3080 during the tests, and the mass concentration is constructed from soot effective density with parameters obtained from TEM analysis. Error bars are based on multiple repeats of the measurements.

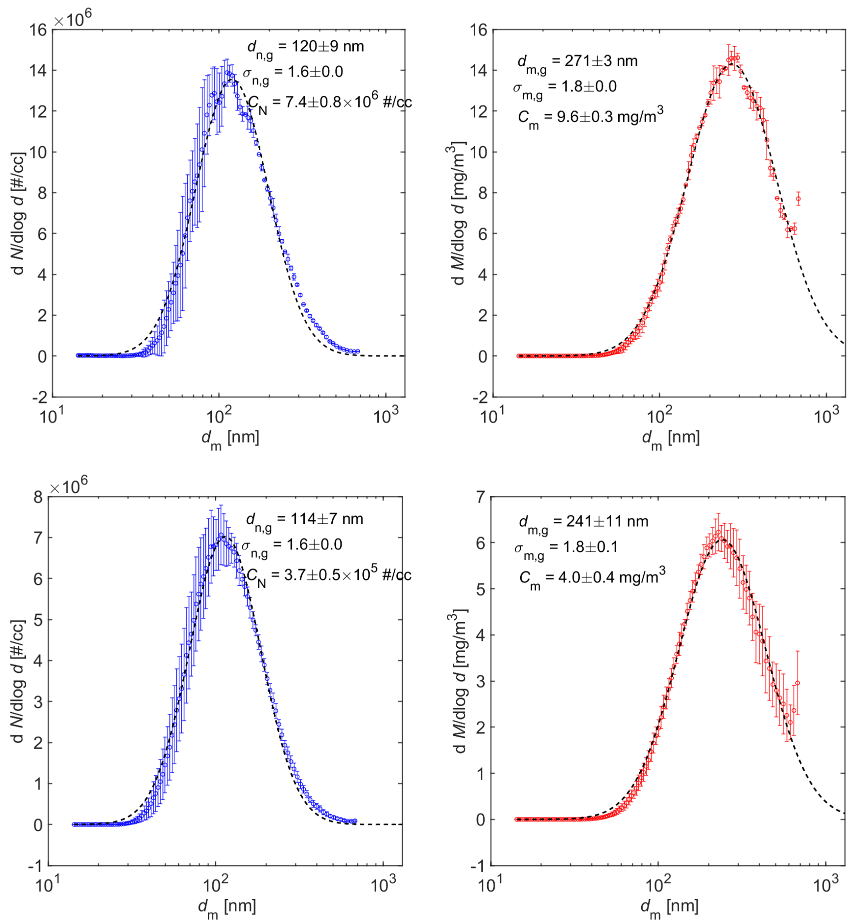

Figure H.3: Number (left) and mass (right) concentration distributions versus soot mobility diameter for two high-soot (point 9) diluted SCRE exhaust samples (top and bottom), discussed in Chapter 4. The number distribution is directly measured with an SMPS-3080 during the tests, and the mass concentration is constructed from soot effective density with parameters obtained from TEM analysis. Error bars are based on multiple repeats of the measurements.

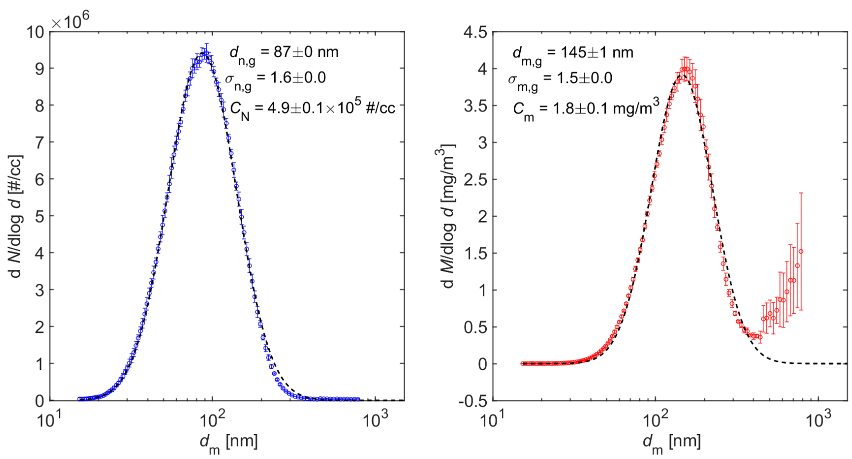

Figure H.4: Number (left) and mass (right) concentration distributions versus soot mobility diameter for two low-soot-2 (point 2) diluted SCRE exhaust samples (top and bottom), discussed in Chapter 4. The number distribution is directly measured with an SMPS-3080 during the tests, and the mass concentration is constructed from soot effective density with parameters obtained from TEM analysis. Error bars are based on multiple repeats of the measurements.

Appendix I

Time-resolved diluted Dusttrak PM measurement

The Dusttrak-II instrument is used for measuring diluted samples and providing time-resolved data to monitor the variation of exhaust soot concentration while collecting filter samples and making SMPS measurements. The Dusttrak is also used to sample the pre- and post-thermodenuder PM to estimate the combined particle loss and SVOC removal rates in the thermodenuder. Dilution-corrected PM mass concentration time-series from the Dusttrak during point-2 and point-4 engine operation is presented in the middle and bottom panels of Figure I.1, corresponding to the time-averaged data used for the FEN validation, shown on the top panel.

The mid-panel in Figure I.1 showcases two instances when the soot concentration undergoes transient changes, at times 17:12 and near the end of the measurement at 17:30. These transitions are likely due to variabilities in the engine operating conditions caused by, e.g. fuel pressure changes due to the operation of the natural gas compressor. The variation of the symbols corresponding to the point 2 test in the parity plot (labeled 1-6 in the top panel) are consistent with the time series in the mid-panel of Figure I.1.

The Dusttrak inlet can be easily switched between the pre- and post-thermodenuder samples and shows a decreased PM concentration after the thermodenuder, due to loss of the solid particles and the removal of volatile

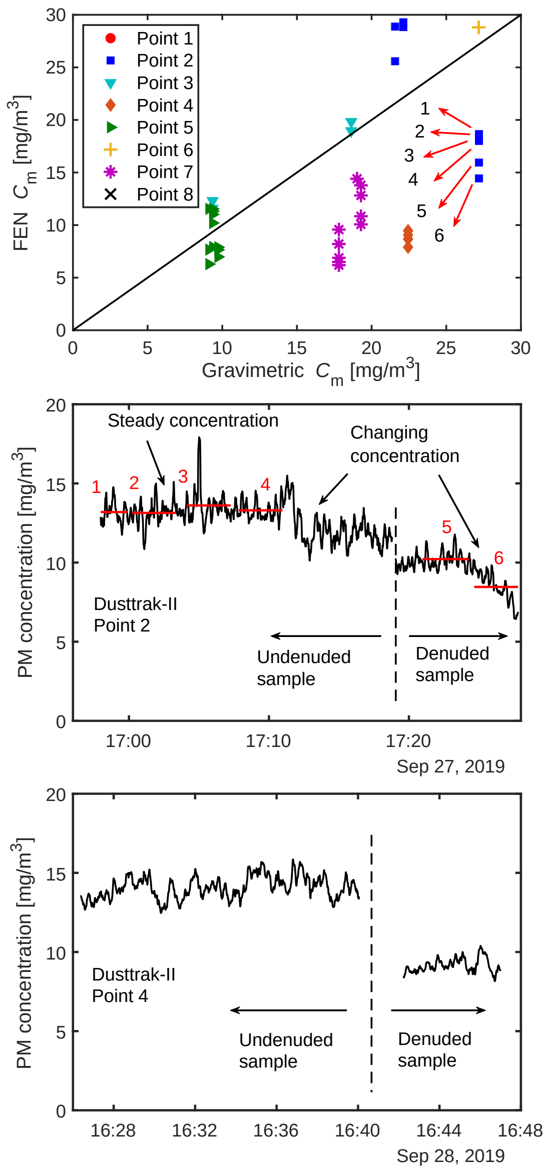

Figure I.1: Top: A close-up view of the concentration parity plot discussed in the main paper, shown in the 0-30 mg/m^3 range. Middle: PM concentration time series from Dusttrak-II during the point-2 engine operation marked on the parity plot. Bottom: The denuded and undenuded Dusttrak mass concentration time series for point 4, showing a 35% reduced PM mass after the thermodenuder.

and semi-volatile material. It cannot, however, be determined exactly what fraction of the losses is due to the removal of SVOC material and what fraction is due to soot particle loss. A particle loss rate of $\sim$15% in the thermodenuder is expected based on thermophoretic and diffusional loss calculations in Appendix C, which is similar to the difference between the pre- and post-thermodenuder concentrations observed for point 2 (mid-panel). This also indicates a low (few percent) mass volatile fractions which is consistent with the data reported in [65] for a similar operating point. The denuded-to-undenuded mass concentration ratio for point 4 is close to 65% based on the Dusttrak time series in the bottom panel of Figure I.1. This suggests a considerable VOC and SVOC fraction for this point, which could justify the discrepancy between the light-scattering FEN and gravimetric mass concentrations observed for point 4 in the parity plot.